Spin and Valley Physics in a Si/SiGe Quantum Dot

SPIN AND VALLEY PHYSICS IN A SI/SIGE QUANTUM DOT

Proefschrift

ter verkrijging van de graad van doctor
aan de Technische Universiteit Delft,
op gezag van de Rector Magnificus prof. ir. K.C.A.M. Luyben,
voorzitter van het College voor Promoties,
in het openbaar te verdedigen op maandag 1 februari 2016 om 12:30 uur

door

Pasquale SCARLINO

Master of Science in Physics,
Universita' del Salento, Lecce, Italië,
geboren te Gagliano del Capo (LE), Italië.

Dit proefschrift is goedgekeurd door de

promotor: prof. dr. ir. L. M. K. Vandersypen

Samenstelling promotiecommissie:

Rector Magnificus,	voorzitter
Prof. dr. ir. L. M. K. Vandersypen,	Technische Universiteit Delft, promotor

Onafhankelijke leden:

Prof. dr. ir. R. Hanson,	Technische Universiteit Delft
Prof. dr. C. M. Marcus,	University of Copenhagen, Denmark
Prof. dr. S. N. Coppersmith,	University of Wisconsin, USA
Dr. ir. F. A. Zwanenburg,	Universiteit Twente
Dr. R. Ishihara,	Technische Universiteit Delft
Prof. dr. Y. M. Blanter,	Technische Universiteit Delft, reservelid

Printed by: Proefschriftmaken.nl-Uitgeverij BOXPress

Cover by: Paolo Poti'

Casimir PhD series Delft-Leiden 2015-38

An electronic version of this dissertation is available at www.library.tudelft.nl/dissertations

CONTENTS

SUMMARY

This Thesis describes a series of experiments aimed at the optimization of the coherence properties of a single electron spin confined in a solid-state environment. The motivation behind this work is the promising prospect of using a single electron spin as a quantum bit. Thanks to its charge, we can confine a single electron in a nanoscale island, called a quantum dot. In the presence of an external magnetic field the two spin states of the electron (aligned with or opposed to an external magnetic field) can be easily distinguished thanks to their different energies. In this work, the two spin states of an electron represent the 0 and 1 of the qubit. Therefore, we explore how to store and manipulate the quantum information given by the spin state.

An important challenge in building a future quantum computer is to realize quantum bits that are both robust and scalable. This first property is the focus of the first part of the thesis. In previous experiments with spin qubits in III-V semiconductors, the electron spins were strongly affected by the presence of many nuclear spins in their surroundings. In silicon, only 5% of all atomic nuclei carry a spin, so their influence is expected to be much smaller, allowing us to observe a longer-lived spin qubit. The first generation of SiGe/Si/SiGe devices made use of intentionally doped heterostructures, providing free electrons. We decided to focus on a new generation of devices without intentional doping. This dramatically improves the charge stability of the devices but it complicates the device fabrication, as described in Chapter 4. Still, given that this system is compatible with CMOS technology, large-scale integration of many quantum bits may one day be possible.

For spin manipulation we create a magnetic field gradient at the location of the quantum dot using of a microfabricated magnetic film. Thanks to the magnetic field gradient the electron will be subject to a different magnetic field depending on its position. Microwave excitation applied to one of the confining gates, oscillates the electron back and forth spatially. If the oscillation frequency matches the precession frequency of the spin in the magnetic field gradient, we can flip the spin and drive Rabi oscillations. In the first experimental chapter of this Thesis, we report a Rabi frequency of the order of 1 MHz. The interaction with the remaining nuclear spins in natural Si limits the dephasing time of the electron spin to around 1 μs (a factor of $\sim$100 times longer than the typical dephasing time observed for a single electron spin in GaAs/AlGaAs depletion quantum dots). Further improvements in the spin dephasing time are possible by isotopically purifying the silicon, so that only Si atoms without spin remain. These results strongly boosted the prospects for semiconductor quantum bits.

The energy level structure of a spin-1/2 particle is extremely simple, consisting of just the spin-up and spin-down levels. Therefore, when performing spectroscopy on an electron spin, only a single resonance is expected corresponding to the energy separation between the two spin levels. However, the experiments reported in the central part of the thesis reveal a much more complex response than this simple picture suggests:

when varying the applied microwave frequency, we observe five distinct spin resonance peaks.

This rich spectrum goes back to the symmetry of the Si crystal structure, which leads to an additional degree of freedom, called the valley. In quantum dots, two of the valley states have an energy far below the other four but close to each other. If the energy difference between the two valleys is very small, both will be thermally populated. This leads to two closely spaced intra-valley spin resonance peaks, one for each of the two lowest-lying valley states, because of valley-orbit coupling combined with spin-orbit coupling (from the micromagnet gradient). Furthermore, the same two resonances can be driven at half the Larmor frequency by second harmonic generation, as showed by the second experimental Chapter of this Thesis. Remarkably, these transitions can be driven coherently too, with Rabi frequencies comparable to those for the fundamental harmonic. Combined with the lower demands on microwave circuitry when operating at half the qubit frequency, second harmonic driving can be a useful technique for future quantum computation architectures. Moreover, in the next chapter we show that it is possible to drive not just intra-valley spin resonances but also an inter-valley spin transition, i.e. where the valley and the spin degree of freedom are flipped simultaneously. We observed that the coherence of the inter-valley spin resonance is degraded compared to the intra-valley spin resonances, due to the unavoidable coupling between the valley and the charge degrees of freedom. Finally, we present a unified model to explain the presence and the magnetic field dependence of all five observed spin resonances. This model consists of just a driven four-level system comprising of two valley-orbit and two spin states.

In the next part of the thesis we report a study on the anisotropy of the spin-orbit (SO) interaction strength by making use of an electron spin confined in a GaAs quantum dot. Whereas spin-orbit coupling intrinsic to the substrate is weak in silicon (and we introduced a micromagnet to enhance coupling of electric fields to the electron spin), there are two sizable SO contributions for electrons in GaAs. One comes from the crystal itself and the other is generated by the electric field along the growth direction of the structure. The interplay of these two contributions results in a SO interaction that can be anisotropic with respect to the magnetic field direction. We probe the SO anisotropy by measurements of the electron spin relaxation time, which is a sensitive probe of the SO strength. Rotating the magnetic field in the plane of the 2DEG, we observed a striking 180 degree periodicity in the SO strength, in agreement with theoretical predictions of 10 years ago. We can take advantage of this understanding for designing new spin qubit devices, in order to maximize or minimize the spin lifetime (according to the specific goal) and the strength of the spin driving.

An important next step for the future of the solid-state spin qubit architectures consists in building larger quantum dot systems comprising many more qubits. Therefore, it is important to find a way to couple spins over large distances (micrometer scale). The last experiment reported in this Thesis pursues the idea to achieve strong coupling between a single-electron spin and the electric field of a superconducting microwave cavity, mediated by a natural or artificial SO coupling. We designed and measured microwave-frequency resonators based on NbTiN nanowires, displaying magnetic field resilience as needed for spin qubit experiments. The large kinetic inductance of the strongly dis-

ordered superconducting nanowires increases their impedance by nearly two orders of magnitude compared to conventional coplanar waveguide resonators used in typical circuit quantum electrodynamics devices. This results in a ten times stronger cavity-qubit coupling, which makes these resonators well suited for coupling to systems with small electric dipole moments, such as electrons in single or double quantum dots.

SAMENVATTING

Dit proefschrift beschrijft een reeks experimenten gericht op het optimaliseren van coherentie van een enkele elektronspin gevangen in de vaste stof. De motivatie voor dit werk is het veelbelovende vooruitzicht van het gebruik van een enkele elektronspin als quantumbit (qubit). We kunnen, dankzij zijn lading, een enkel elektron opsluiten in een eilandje met afmetingen op de nanoschaal dat zich bevindt in een halfgeleideromgeving. Dit eilandje wordt een quantumdot genoemd. In de aanwezigheid van een extern magneetveld kunnen de beide spintoestanden van het elektron (parallel of antiparallel aan het extern magneetveld) gemakkelijk onderscheiden worden als gevolg van het verschil in hun energie. In dit werk representeren de spintoestanden van het elektron de 0 en 1 toestand van een qubit. Derhalve verkennen we hoe quantuminformatie in de spintoestand van elektronen opgeslagen en gemanipuleerd kan worden.

Een belangrijke uitdaging bij het bouwen van een toekomstige quantumcomputer is het realiseren van qubits die zowel robuust als schaalbaar zijn. In het eerste deel van dit proefschrift ligt de focus op de eerste eigenschap. In voorgaande experimenten met spinqubits in III-V-halfgeleiders werd de elektronspin sterk beïnvloed door de aanwezigheid van een grote hoeveelheid kernspin in de omgeving. In silicium bezit slechts 5% van de atoomkernen een spin, dus de verwachte invloed hiervan is veel kleiner. Dit maakt het mogelijk lang levende spinqubits te observeren. De eerste generaties SiGe/Si/SiGe-devices maakten gebruik van gedoteerde heterostructuren die voor vrije elektronen zorgden. Wij hebben besloten ons te focussen op een nieuwe generatie devices zonder opzettelijke doping. De ladingsstabiliteit wordt hierdoor enorm verbeterd, maar de fabricage is ingewikkelder, zoals beschreven in hoofdstuk 4. Echter, doordat dit materiaalsysteem compatibel is met CMOS-technologie, zijn geïntegreerde schakelingen van vele qubits wellicht ooit mogelijk.

Om de spin te manipuleren creëren we een gradiënt in het magneetveld op de locatie van de quantumdot door gebruik te maken van een micromagneet. Dankzij deze gradiënt ondervindt het elektron een verschillend magneetveld afhankelijk van zijn positie. Microgolfexcitatie van een van de elektrodes waarmee het elektron op z'n plaats wordt gehouden laat het elektron ruimtelijk oscilleren. We kunnen de spin van richting laten veranderen en Rabi-oscillaties aandrijven als de frequentie van de ruimtelijke oscillatie overeenkomt met de precessiefrequentie van de spin in het magneetveld. In het eerste experimentele hoofdstuk van dit proefschrift rapporteren we een Rabi-frequentie in de orde van 1 MHz. De interactie met de nog aanwezige kernspin in natuurlijk Si limiteert de defaseringstijd van de elektronspin tot zo'n 1 μs (een factor ~100 langer dan de typisch geobserveerde defaseringstijd van een enkele elektronspin in GaAs/AlGaAs depletie-quantumdots). Verdere verbetering van de spindefaseringstijd is mogelijk door silicium isotopisch te verrijken, waardoor enkel Si atomen zonder kernspin overblijven. Deze resultaten stimuleren de vooruitzichten voor halfgeleiderquantumdots.

De structuur van energieniveaus voor spin-1/2-deeltjes is extreem simpel en bestaat

slechts uit de spin-op- en spin-neer-niveaus. Bij spectroscopie van een elektronspin verwacht men daarom slechts een enkele resonantie corresponderend met het verschil in energie tussen deze niveaus. Echter, de experimenten in het centrale deel van dit proefschrift onthullen een veel complexere respons dan gesuggereerd door dit simpele model: vijf afzonderlijke spinresonantiepieken worden waargenomen wanneer we de aangeboden microgolffrequentie variëren.

De oorsprong van dit rijke resonantiespectrum ligt in de symmetrie van het siliciumkristal. Dit leidt tot een extra vrijheidsgraad, welke vallei wordt genoemd. In quantumdots hebben twee valleitoestanden een vergelijkbare energie, maar veel lager dan de andere vier toestanden. Wanneer het energieverschil tussen deze twee laag gelegen valleien klein is, zijn beide thermisch bezet. Dit leidt tot twee intra-vallei-spinresonantiepieken dicht bij elkaar, één voor elke van de laag gelegen valleien, als gevolg van vallei-baankoppeling gecombineerd met de spin-baankoppeling door de magneetveldgradiënt gevormd door de micromagneet. Dezelfde resonanties kunnen tevens aangedreven worden op de halve Larmor-frequentie door middel van het genereren van tweede harmonischen, zoals aangetoond in het tweede experimentele hoofdstuk van dit proefschrift. Het is opmerkelijk dat ook deze overgangen coherent aangedreven kunnen worden met Rabi-frequenties vergelijkbaar met die van de fundamentele harmonischen. Gecombineerd met de minder strikte eisen aan de microgolfelektronica bij gebruik van de halve qubitfrequentie, kan het genereren van tweede harmonischen een bruikbare techniek zijn voor toekomstige ontwerpen om toe te passen in quantumberekeningen. In het volgende hoofdstuk laten we zien dat het niet alleen mogelijk is om intra-vallei-, maar ook inter-valleispinresonanties, aan te drijven, d.w.z. een overgang waarbij zowel spin als vallei van het elektron tegelijk veranderen. We observeren dat de coherentie van inter-valleispinresonanties kleiner is vergeleken met intra-valleispinresonanties, vanwege de onvermijdelijke koppeling tussen de vallei- en ladingsvrijheidsgraad. Tenslotte presenteren we een compleet model om de magneetveldafhankelijkheid van alle vijf de spinresonanties te verklaren. Dit model bestaat slechts uit een aangedreven vierniveausysteem bestaande uit twee vallei-baantoestanden en twee spintoestanden.

In het volgende deel van dit proefschrift rapporteren we anisotropie van de sterkte van de spin-baaninteractie door gebruik te maken van een elektronspin gevangen in een GaAs-quantumdot. Terwijl in silicium de spin-baankoppeling intrinsiek zwak is (waardoor we gebruik maken van een micromagneet om de koppeling van de elektronspin met elektrische velden te versterken), zijn er twee aanzienlijke bijdragen aan de spin-baankoppeling in GaAs. Eén komt van het kristal zelf en de ander is het gevolg van het elektrisch veld in de groeirichting van de structuur. Het samenspel van deze bijdragen zorgt ervoor dat de spin-baankoppeling anisotroop kan zijn ten opzichte van de richting van het magneetveld. We onderzoeken de spin-baananisotropie door middel van het meten van de relaxatietijd van de elektronspin, welke een gevoelige maat is voor de sterkte van de spin-baankoppeling. We observeren, in overeenstemming met theoretische voorspellingen van 10 jaar terug, een duidelijke periodiciteit van 180 graden in de spin-baansterkte wanneer we het magneetveld roteren in het vlak van het 2-dimensionaal elektronengas. We profiteren van dit begrip bij het ontwerpen van nieuwe spinqubit-devices om zo de spinlevensduur (in overeenstemming met een specifiek doel) en de kracht van het aandrijven van de spin te maximaliseren of minimaliseren.

Een belangrijke stap voor de toekomst van spinqubit-ontwerpen in de vaste stof bestaat uit het bouwen van grotere systemen van quantumdots bestaande uit meerdere qubits. Het is daarom van belang om een methode te vinden om spins over grotere afstand (micrometers) aan elkaar te koppelen. Het laatste experiment dat besproken wordt in dit proefschrift volgt het idee om sterke koppeling te realiseren tussen een enkele elektronspin en het elektrisch veld van een supergeleidende microgolftrilholte gemedieerd door natuurlijke of kunstmatige spin-baankoppeling. We ontwerpen en karakteriseren microgolfresonatoren gebaseerd op NbTiN nanodraden die bestand zijn tegen een magneetveld, zoals vereist voor spinqubit-experimenten. De grote kinetische inductie van sterk wanordelijke supergeleidende nanodraden vergroot hun impedantie met bijna twee ordes van grootte in vergelijking tot conventionele vlakke plaatresonatoren die typisch gebruikt worden in circuit-quantumelektrodynamica. Dit resulteert in een tien maal sterkere koppeling tussen trilholte en qubit, waardoor de resonator erg geschikt is voor het koppelen aan systemen met een klein elektrisch dipoolmoment, zoals elektronen in enkele of dubbele quantumdots.

1

INTRODUCTION

1.1. SEMICONDUCTOR TECHNOLOGY

Advances in solid-state semiconductor technology allow the fabrication of well-defined nanostructures in very narrow two-dimensional systems with high homogeneity and relatively low disorder. From this starting point, it is possible to define an electrostatic potential by using depletion gate, which leads to the confinement in the other dimensions, creating one-dimensional [1, 2] or zero-dimensional systems [3, 4]. These systems show quantum behaviour due to the confinement on a scale comparable to the de Broglie electron wavelength in the host semiconductor material [5]. The real potential of the depletion gate technology comes from the possibility to tune many parameters of the system Hamiltonian (energy levels, tunnel couplings, interference phases,...) individually, by changing the gate voltages.

The first step to create a nanostructured device consists in isolating a 2-dimensional electron gas (2DEG), where electrons are free to move in two dimensions. A 2DEG can be realized by combining layers of semiconductor materials with similar crystal structure and different bandgap, like GaAs/AlGaAs or Si/SiGe. For GaAs/AlGaAs systems the confinement is due to the edge in the electron bandstructure that is created at the interface between GaAs and $Al_xGa_{1-x}As$ (typically $x \sim 0,3$), sketched in the inset of Fig. 1.1(a). As explained in Chapter 4, for Si/SiGe system, the confinement is realized by creating a Si quantum well (QW), sandwiched between $SiGe_x$ layers (typically $x \sim 0,3$). If the temperature is low enough, the dynamics of the electron is localized in a few nm along the heterostructure growth direction (z-direction), in a way that it can be considered effectively two-dimensional [6].
In the next Chapter we will mainly focus on GaAs/AlGaAs heterostructures, to describe the fabrication and physics of quantum dots (QDs), which can be easily extended to Si/SiGe systems (described in Chapter 4). The most relevant differences between those two electron spin hosting systems are discussed in Chapter 3.

For GaAs/AlGaAs heterostructures, the modulation doping technique is usually implemented. It consists of separating the dopant region, which provides the free electrons

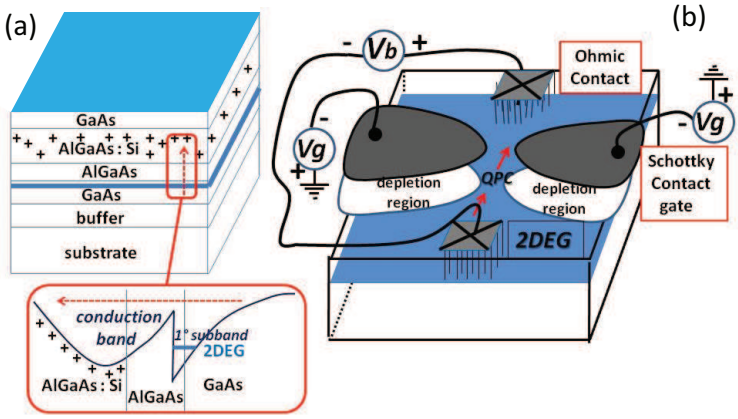

Figure 1.1: (a) The diagram shows the different layers of the GaAs heterostructure. Usually the 2DEG is created in the first 100 nm from the surface. A triangular potential well is formed at the GaAs/AlGaAs interface, with only one subband below the Fermi level. Other subbands are energetically inaccessible. (b) The schematic depicts the depletion principle, operated by applying a negative electric potential to a surface gate. Regions with the 2DEG are shown in blue. Metallic gates, defined by electron beam lithography, are deposited on the surface of the heterostructure. Wires, bonded to the gates, connect them with external voltage sources V_g. Ohmic contacts are made on both sides of the mesoscopic structure, allowing current to flow through the system defined by depletion technique.

and constitutes the main electron scattering source, from the 2DEG. This technique limits the amount of disorder introduced in the 2DEG. Hence, by also controlling the stress and strain accumulated in the heterostructure, caused by the lattice mismatch between the different layers of semiconductors alloys, it is possible to achieve very low density of epitaxial defects and a smooth potential in the 2DEG plane with high charge mobility and mean free paths (as high as $100\,\mu m$).

The specific layout of the metallic gates on the surface of the heterostructure, which will be used to create the nano-device in the 2DEG, is implemented by electron beam lithography (resolution of tens of nanometers). The depletion of the 2DEG with metallic gates is schematically depicted in Fig. 1.1(b). A Schottky barrier is formed between the metallic gate and the heterostructure, forbidding direct tunneling of electrons from the gates into the semiconductor heterostructure[1]. Therefore, by applying a negative voltage to the gates, we can locally raise the Fermi level of the 2DEG above the first z-subband minimum, depleting all the electrons from the regions below the gates. As a result, we obtain the electron confinement also in x-y-directions, transferring the gate geometry from the surface of the heterostructure to the 2DEG.

A general measurement on a mesoscopic system consists in recording the current and voltage characteristics between various regions of the 2DEG. Therefore, good electrical ohmic contacts (represented by the crossed squares in Fig. 1.1(b)) between the heterostructure surface and the confined 2DEG are also necessary. These can be realized by

[1] This is a common rectifying structure, thus if we measure the current flowing from a gate to the 2DEG as a function of the applied voltage bias, we will find a characteristic exponential behaviour.

annealing of a metal alloy (such as Au, Ni, and Ge layers for GaAs systems) previously deposited on top of the heterostructure or by implanting dopants in the hosting semiconductor (see Chapter 4).

1.2. QUANTUM COMPUTATION

The idea to create and control a physical system, whose dynamics is entirely dominated by quantum processes, comes from the effective impossibility to realize a complete simulation of a generic quantum system by classical computation techniques. In 1980s Feynman introduced the concept of a 'quantum simulator', a well controlled quantum system, whose dynamics is entirely governed by Quantum Mechanics, to simulate the behaviour of any Quantum Hamiltonian. The natural evolution of this concept led to the creation of Quantum Computation Science [7].

The philosophy of quantum computation is fundamentally different from the classical case. In fact, the calculations follow the rules of quantum mechanics in every respect. The fundamental computation unit of a classical computer is the bit, which represents a discrete value 0 or 1. Nowadays, the transistor channel length of modern integrated components are of the order 25-15 nm, therefore quantum mechanics becomes necessary in order to properly model the transistor behaviour. However, all the logic devices built with those transistors are subject to classical Boolean logic. Instead, quantum computers encode, manipulate, and store the information using qubits. Contrary to a classical binary digits $(0-1)$, a qubit is a two level quantum system, which we can describe using the basis states $|0\rangle$ and $|1\rangle$.

The incredible power of a qubit comes from two main characteristics, intimately related to its quantum nature: (i) every superpositions of the two basis states can be created and used; (ii) the correlation between qubits is non-local (entanglement). Considering two qubits interacting, the bipartite wavefunction is not necessary separable into two independent wavefunctions. In fact, a qubit can hold a superposition, $a|0\rangle + b|1\rangle$, with probability of $|a|^2$ for the state $|0\rangle$ and $|b|^2$ for the state $|1\rangle$. According to the superposition principle, the coherent state of two qubits is the superposition of 2^2 states $|00\rangle, |01\rangle, |10\rangle, |11\rangle$ and, in general, a n-qubit system is represented by a superposition of 2^n states. Therefore, in order to simulate a single step of a quantum processor, a classical computer would need a number of steps that scales exponentially with n (parallelism) [7]. To have a schematic picture of a qubit it is possible to build a correspondence between the state of the qubit and the surface of a sphere, known as Bloch sphere. Any superposition can be mapped onto the Bloch sphere with $|0\rangle$ coinciding with the north pole and $|1\rangle$ with the south pole [7]. Unitary evolution of the qubit (no dephasing and relaxation) can be represented as a rotation on the surface of the Bloch sphere.

Being a computational process, every quantum operation performed on a qubit may develop errors. One important ingredient for the realization of a quantum computation is the creation of efficient error-correcting codes [7, 8]. The trick of quantum error correction consists in encoding a logical qubit by using multiple physical qubits, allowing the detection of the error without affecting the encoded state. It has been demonstrated that, even in the presence of finite decoherence, it is possible to implement universal quantum computation on an arbitrarily large quantum Hilbert space if the error rate per operation is lower than an 'accuracy threshold' [9]. Therefore, it is necessary to realize

fast unitary operation with relatively high fidelity in order to successfully implement a complete quantum algorithm. The Surface Code [10] is a very powerful quantum error correcting code that can be defined on a 2D architecture of qubits laid out in a square lattice with only nearest neighbour interactions. The nodes of the lattice are alternatively represented by either syndrome or data qubits. Errors affecting the data qubits are detected by repeatedly measuring the syndrome qubits. To realize this detection, each syndrome qubit needs to interact with each of its four neighbouring data qubits and single- and two-qubit gates need to be performed with sufficiently high fidelity (higher than 99%).

1.3. DIVINCENZO CRITERIA

Every good quantum hardware candidate has to fulfil five general and fundamental criteria, written down by D. P. DiVincenzo in [11, 12]:
1) Control of the Hilbert space: the two states of the qubit have to be precisely identified and experimentally characterized. Furthermore, in order to implement multiple qubits operations and extend the Hilbert space, we need a scalable system.
2) State initialization: we want to be able to initialize the state of the qubit in a deterministic way with the highest possible accuracy. Experimentally, one way to realize this is to initialize the system in the ground state, by waiting a time longer than the relaxation time. This requires that the thermal energy is far smaller than the qubit energy splitting (see Chapter 8). Another possible qubit initialization protocol (used in Chapters 5, 6 and 7) is through the qubit read out process.
3) Low decoherence: the coupling between the two-level system and the rest of the environment should be small enough to be able to implement error-correcting codes, before the qubit loses completely its coherence. However, there also needs to be coupling between the qubit and the external world to perform some unitary operation and readout the final result of the computation. Therefore, it is fundamental to identify good two-state systems weakly coupled to environment, but which can still be manipulated and read out efficiently.
4) Controlled unitary transformations: elementary quantum gates consist of unitary operations on one single qubit and between qubits. The unitary operations need to be implemented with high accuracy and much faster than the decoherence time of the qubit. It is convenient to define and implement a set of universal quantum gates, which we can combine to realize all the possible algorithms. In this perspective it has been demonstrated that the combination of certain one and two qubit operations constitute a universal set [7].
5) State-specific read out: at the end of a computational process, it is important to be able to measure the final state of each qubit separately and with the highest possible fidelity.

In this thesis, we realize all of the DiVincenzo criteria (except the 2-qubit gate) using the spin of a single electron hosted in GaAs and Si environments.

1.4. THESIS OUTLINE

Finally, we give a brief outline of this thesis:

- **Chapter 2** gives a brief introduction to the main theoretical concepts, focusing on GaAs-AlGaAs depletion QD systems, as well as experimental techniques used in the later chapters.
- **Chapter 3** describes the theory background for electron spin qubits, focusing on the properties of spin hosted in a silicon environment.
- **Chapter 4** represents an introduction to the properties of a Si/SiGe heterostructure and describes the fabrication process for accumulation QDs in Si/SiGe undoped systems.
- **Chapter 5** describes the first experimental realization of electrical dipole mediated spin resonance for a single electron confined in a single QD, built in a Si/SiGe QW. We demonstrated a coherence time $T_2^* \sim 1\ \mu$s and perform universal control and spin echo. Surprisingly, we observed two spin resonances that we attribute to the presence of an almost valley degeneracy in our system. In fact, in the presence of a valley energy splitting comparable to the electron thermal energy, both of the valley states get populated during the spin initialization stage.
- **Chapter 6** presents measurements of the second harmonic driving of intra-valley spin resonances. This is a not trivial result for a single QD confinement potential. Furthermore, we demonstrate the possibility to use the second harmonic driving, not just to perform spin spectroscopy but also to realize coherent spin oscillations.
- **Chapter 7** reports the first observation of an inter-valley spin resonance. We present also a detailed study of the coherence property of this resonance, which we demonstrate to be dominated by electric noise. We also present a simple model that takes into account simultaneously all the 5 spin resonances observed.
- **Chapter 8** discusses a result regarding the interplay between Rashba (R) and Dresselhaus (D) spin-orbit (SO) fields, obtained for a single spin confined into a GaAs/AlGaAs single depletion-mode QD. We use the spin relaxation time (T_1) as a probe for the intensity of the total SO field and finally correlate the anisotropy measured for T_1 with the anisotropy generated by the R and D SO interplay and the shape anisotropy of the QD confinement potential.
- **Chapter 9** reports the realization of a high impedance superconducting resonator, based on NbTiN nanowires, compatible with high magnetic field (up to 6 T applied in plane). This resonator shows a resonance frequency around 3 GHz and intrinsic quality factors above 10^5 in the few photon regime. The fabrication and characterization of this high impedance resonator represents an important step toward the realization of a strong coupling between microwave (MW) photons and the small dipole moment of a single electron spin confined into a double quantum dots (DQD).

REFERENCES

[1] T. J. Thornton, M. Pepper, H. Ahmed, D. Andrews and G. J. Davies, Phys. Rev. Lett. **56**, 1198 (1986).

[2] B. J. van Wees, H. van Houten, C. W. J. Beenakker, J. G. Williamson, L. P. Kouwenhoven, D. van der Marel and C. T. Foxon, Phys. Rev. Lett. **60**, 848 (1988).

[3] L. P. Kouwenhoven, D. G. Austing and S. Tarucha, Rep. Prog. Phys. **64**, 701 (2001).

[4] M. A. Kastner, Rev. Mod. Phys. **64**, 849 (1992).

[5] T. Ihn, 'Semiconductor Nanostructures: Quantum states and electronic transport', Oxford Scholarship Online (2010).

[6] C. Weisbuch and B. Vinter, 'Quantum Semiconductor Structures', Accademic Press, Inc., New York (1991).

[7] M. A. Nielsen and I. L. Chuang, 'Quantum Computation and Quantum Information', Cambridge University Press (2000).

[8] A. R. Calderbank and P. W. Shor, Phys. Rev. A **54**, 1098 (1996).

[9] D. Aharonov and M. Ben-Or, arXiv:quant-ph/9906129.

[10] A. Fowler, M. Marlantoni, J. M. Martinis, and A. N. Cleland, Phys. Rev. A **86**, 032324 (2012).

[11] D. P. DiVincenzo, Science **270**, 255 (1995).

[12] D. P. DiVincenzo and D. Loss, Superlattices and Microstructures **23**, 419 (1998).

2

SPIN QUBITS IN QUANTUM DOTS

2.1. QUBITS IN QUANTUM DOTS

In this thesis we will analyze spin quantum bits, encoded using the spin of single electrons confined in depletion QDs in a solid-state environment. Solid-state devices are, in principle, possible to scale up by using the fabrication process of integrated electronics. Furthermore, we can easily integrate such qubits with classical electronics to implement controlled operations and the read-out process. On the other hand, since a solid-state system presents a huge number of degrees of freedom, the qubits may strongly interact with their environment quickly loosing their coherence [1]. As a result, it is crucial to find an optimal two-level system whose coupling with the environment represents the ideal trade off between the preservation of coherence and the requirements for manipulation and readout.

Even restricting our discussion to the case of qubits defined by using spin and charge degrees of electrons confined in QDs (hosted in semiconductors), different encoding schemes have been proposed and explored. We will summarize those in the following[1].

Charge Qubit

A charge qubit is conceptually the simplest and consists of a single electron shared by two tunnel coupled QDs (double quantum dot (DQD)). The two-level system for the charge qubits is represented by the electron confined on either the left (QD_L) or right (QD_R) QD. The transfer of electrons between the QDs is allowed, and it is described by the tunnel coupling t. The ground state of the system can be $|L\rangle$ ($|R\rangle$), meaning that the single electron is positioned at QD_L (QD_R), depending on the combination of voltages V_L or V_R applied at electric gates controlling the electrochemical potential of each QD [3, 4]. The charge degree of freedom naturally couples with the electric field, so it can be easily accessed in experiments. The qubit can be, in this way, initialized by fast charge relaxation processes and read out by using charge sensing. As a consequence, the charge qubit is also very sensitive to electric field fluctuations [4, 6] because it is directly

[1] For a more detailed analysis see [2].

coupled to the charge fluctuations via the Coulomb interaction. In fact, even though coherent manipulation has been achieved [3–6], the electric field fluctuations in semiconductors make the charge qubit usually lose its phase coherence within ~1 ns [3]. In [5] authors have used shaped electrical pulses to create Landau–Zener–Stückelberg interference and demonstrated x-rotation and dynamic phase-gate operations in a few tens of picoseconds. The coherent dynamics of two spatially separated electrons in a coupled DQD have been investigated in [7] and recently a conditional rotation of two capacitively coupled charge qubits has been realized in [8].

The main advantage in using the spin as a qubit in a semiconductor host environment comes from the fact that major sources of noise in those systems usually have an electric origin [1]. Electric or charge fluctuations are not directly coupled to the spin, but the coupling is indirect, mediated for instance by spin-orbit interaction [9, 10]. Instead, the main source of spin decoherence is represented by fluctuations of the nuclear-spin configuration of the host environment, coupled via the hyperfine interaction with the electron spin [11].

Considering a pair of electrons whose electron wavefunctions partially overlap, their spins are coupled by the exchange interaction, which results from the combination of the Pauli exclusion principle and the Coulomb interaction. In the absence of a magnetic field, the spin sector of the ground state of two electrons confined in coupled quantum dots usually presents a singlet nature, while the first excited state is a spin triplet. The low-energy dynamics of such a system is described by the Heisenberg spin Hamiltonian, $H_S(t) = J(t)S_L \bullet S_R$, where $J(t)$ describes the exchange coupling strength between the left (L) and right (R) electron (confined in QD_L and QD_R), with the spins S_L and S_R [12, 13]. The exchange coupling represents the energy difference between the triplet and the singlet states. The exchange interaction can be rapidly and precisely controlled in experiments by using voltage pulses on the metallic gates to control the tunnel barrier between the QDs [14]. This control makes it appealing to encode quantum information using qubits that can be manipulated with the exchange interaction. Three such implementations have been demonstrated and are summarized below.

ST_0 Qubit

A ST_0 is realized by defining a DQD with one electron in each QD and focusing on the $S_z = 0$ subspace, where S_z represents the component along the quantization direction of the total spin. In the presence of a large enough external magnetic field, the energy states $S_z = \pm 1$ are energetically well separated from the $S_z = 0$ subspace. The logical qubit states are the $S_z = 0$ triplet (T_0) and singlet (S) states, therefore the qubit is known as the ST_0 qubit [14, 15]. To realize universal qubit control in addition to the S-T_0 exchange interaction, a magnetic field gradient in the direction parallel to the global magnetic field is required [15]. A magnetic field gradient can be created by polarizing the nuclear spin bath [17] or by using micro magnets [19][2]. The readout uses Pauli spin-blockade [20], which allows the singlet and triplet component of the spin sector to be correlated with the charge state of the DQD. Initialization of the ST_0 qubit relies on the fact that the singlet state is strongly favored in (2, 0) and (0, 2) configurations by relax-

[2] This is an indispensable choice for Si host material [18, 19]

ation processes [21]. ST_0 qubits have excellent coherence properties because the nuclear spins fluctuations, which cause local magnetic field fluctuations, are typically at low frequency, therefore relatively easy to mitigate by dynamical decoupling protocols [16, 17]. A realization of a two-qubit gate for ST_0 qubits based on capacitive coupling has been reported by [22] in a GaAs/AlGaAs system.

Exchange-Only Qubit

It is also possible to encode a qubit using three singly occupied QDs arranged in a linear design with nearest neighbour tunnel couplings. This system has been proposed by D. P. DiVincenzo [23] and has the advantage of providing universal control by the exchange interaction only, without the necessity to control local magnetic fields, which are difficult to implement experimentally. Single-qubit manipulations of the exchange-only qubit have been implemented experimentally tuning independently J_{12} and J_{23} [24], representing the exchange interactions between QD_1-QD_2 and QD_2-QD_3 respectively. Recently, this architecture has been demonstrated also in a ^{28}Si QW [25]. A possible alternative to pulsed gates is given by the resonant manipulation of the exchange interactions [26]. Two-qubit gates of the exchange-only qubit have not been realized so far.

Hybrid Qubit

The hybrid qubit [27, 28] is realized by confining three electrons (as for the exchange-only qubit) in a DQD. It is encoded by using the $S = 1/2$, $S_z = 1/2$ subspace of the 3 electrons in the (1,2) (or (2,1)) charge configuration. This qubit presents a larger energy difference Δ (so faster manipulation) between the two states representing the qubit basis if compared to the exchange only qubits, for which the energy difference is of the order of the QDs tunnel energy. The reason is that the ground $|0\rangle$ and excited $|1\rangle$ states of the hybrid system contain a singlet and a triplet component of two electrons inside one of the two dots. Usually $\Delta E_{ST} \sim \Delta E_{orb}$ (or E_{VS} in silicon), where ΔE_{ST} is the S-T energy difference, ΔE_{orb} the orbital excitation energy, and E_{VS} the valley energy splitting. The initialization processes can be based on the energy relaxation of all triplet configurations into the singlet configuration, which is energetically favoured. All single-qubit gates can be realized using fast modifications (faster than h/Δ ~sub-ns pulses) of the detuning ϵ [27]. Single-qubit gates have been recently demonstrated for the hybrid qubit [29] and characterized via tomography, also by using resonant a.c. microwave driving [30]. Ref. [31] proposes a realization of a two-qubit gate by Coulomb interactions between two DQD hybrid systems, but no experiment has been implemented yet. Furthermore, regarding the coherence properties, the hybrid qubit is affected by the charge noise, as already for a charge qubit.

Loss-DiVincenzo Qubit

Another quite promising spin qubit candidate is realized by a single electron confined in a single QD [1, 12]. Different from many other qubit encoding schemes, which constitute an effective pseudo-spin two-level system, a single electron spin system is a natural and archetypal qubit, with the computational quantum basis, $|\uparrow\rangle$ and $|\downarrow\rangle$, related to the spin sector of the Hilbert space of one electron.
Electron spin qubits proposed by D. P. DiVincenzo and D. Loss [12] are defined by using

a single excess electron confined in a quantum dot. The Loss-DiVincenzo qubit in GaAs and Si, being the focus of this thesis work, will be extensively described in the following.

2.1.1. REALIZATION OF DEPLETION QDS

The starting point for all the encoding schemes reported in the previous section consists in the confinement of the electrons in a small island, called Quantum Dot (QD). One can think about a QD as an 'artificial atom' in which the electrons are confined in all 3 spatial dimensions. In this perspective, the attractive Coulomb potential of a nucleus, which provides the electron confinement for a real atom, is replaced by an artificial repulsive confinement potential, created by the voltages applied to the surface gates. Physically, a QD presents discrete energy levels if the island size is of the order of the de Broglie wavelength of the electrons $\lambda = h/\sqrt{2m^* E_K}$ inside the hosting material, where m^* and E_K represent the effective mass and the kinetic energy of the electron, respectively.

There are many different experimental realizations of few-electron QDs, for example by vertical etched pillars [32] or self-assembled structures [33]. In addition, it is also possible to use electrons confined to single impurities hosted in semiconductors, such as silicon or carbon [34].

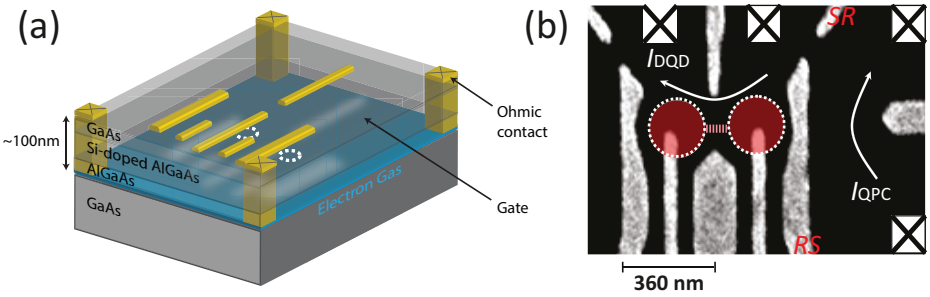

Figure 2.1: An example of depletion gates lateral DQD device in GaAs/AlGaAs 2DEG. (a) Schematic of the structure with all the surface gates (gold), the depleted region below them (white shadows) and the 2DEG (blue). (b) Scanning electron microscope picture of a real device, indicating the gates (light grey), the electron islands (red dots) connected via tunable tunnel barriers with a source and drain electron reservoir. The gate on the right can be used to create a charge sensor.

In this thesis we consider quantum dots that are tens of nanometers in size, defined by lateral depletion gate technology, in a semiconductor GaAs/AlGaAs or SiGe/Si/SiGe heterostructure. Fig. 2.1 shows a typical DQD structure, with a schematic of the depletion gates (panel (a)) and a scanning electron microscope picture of a DQD device (panel (b)). The main advantage of this type of QD, compared to self-assembled or etched structures, is the possibility to precisely control the number of electrons and height of the tunnel barriers by the voltages applied to the depletion gates. This can be done in-situ and independently, in principle, for every single QD, which is a useful property toward scalability. Furthermore, this last goal can be pursued by making use of the common fabrication facilities and techniques of the semiconductor industry.
By applying a voltage bias across the mesoscopic structure, the current flowing through

the QD can be put in relation with electron tunneling processes between the electron reservoirs and the quantum states of the electron confined in the QD (energy spectrum of the structure). Therefore, the transport current can reveal information on the energy level spectrum of the QD [1].
Alternatively, it is possible to measure the charge state (number of electrons) of the QD by an external, non invasive, charge detector, such as Single Electron Transistor (SET) [35] or a Quantum Point Contact (QPC) [4, 36, 37, 39]. For instance, the current through a QPC located in proximity to a dot can be influenced by the dot charge state [38, 40]. This charge detection mechanism has been demonstrated to be quite sensitive, allowing the real time detection of electron tunneling events [41] and the single-shot read-out of electron spin qubit states [42], as we will describe in the 'Charge Detector' subsection 2.3.

2.2. TRANSPORT THROUGH QUANTUM DOTS

The conventional way to perform electrical studies of the physical properties of a depletion QD consists of measuring electron transport between two electron reservoirs (source and drain), through the two tunnel barriers defining the QD.
In order to use single or multiple coupled QD systems it is useful to understand how the voltage applied on the surface gates defines, influences, and modifies the QD energies and transport properties[3].

2.2.1. SINGLE QD

In order to understand the transport measurements we can refer to the 'constant-interaction (CI) model', which is based on two main assumptions:
(i) the interactions between the electron confined in the dot and the environment around it, can be represented, as depicted in the schematic of Fig. 2.2(a), by a constant capacitance $C = C_{QD-S} + C_{QD-D} + C_{QD-g}$, where C is the total capacitance, C_{QD-D} is the capacitance of the dot to the drain, C_{QD-S} is that to the source, and C_{QD-g} indicates the capacitive coupling with all the gates.
(ii) the interaction between electrons confined inside the dot does not modify the discrete single particle energy spectrum.
The total energy $U(N)$ of an N-electron quantum dot can be defined as

$$U(N) = \frac{[e(N-N_0) + C_{QD-S}V_{SD} + C_{QD-g}V_g]^2}{2C} + \sum_{n=1}^{N} E_n(B), \tag{2.1}$$

where N_0 is the number of electrons inside the dot when $V_g = 0$, e is the fundamental electron charge, V_g is the gate voltage, and V_{SD} is the source drain voltage bias where the drain is kept on ground. The capacitive coupling allows the charge stored in a dot to be tuned via either C_{QD-g} or C_{QD-S} by varying the V_g or V_{SD}, respectively. The index n in the sum in eq. 2.1 labels all the single-particle energy levels $E_n(B)$ of the quantum dot, which can be a function of the external magnetic field B. Their distribution and separation in energy, $\triangle E_n = E_n - E_{n-1}$, is determined by the dot confinement potential.

[3] For this section and the next one, we mostly follow Chapter 1 of the PhD Thesis of J.M. Elzerman [43], and the article of W. G. van der Wiel et al. [44].

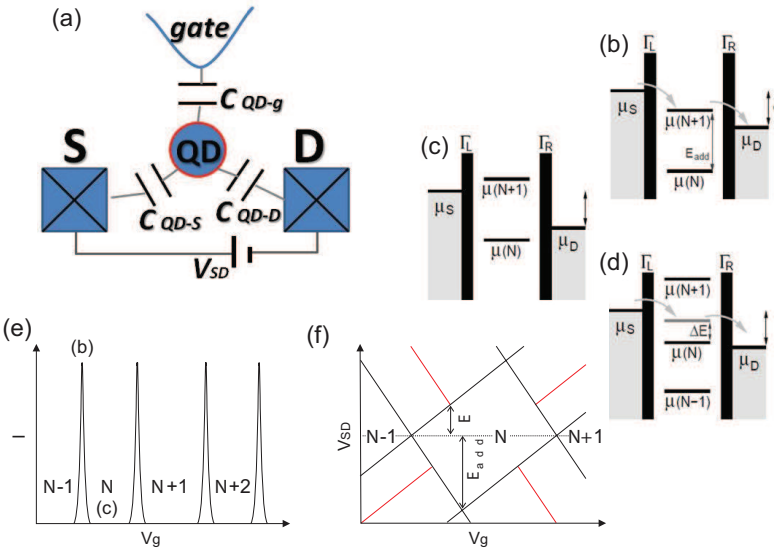

Figure 2.2: (a) Schematic diagrams of a single Quantum Dot (QD) structure with the main capacitive coupling between metallic structures and QD (we are neglecting the cross-coupling capacitances). Tunneling processes for a QD occupied by N electrons (from ref.[43]): (b) since the electrochemical potential for (N+1) electrons in the QD is inside the bias window (V_{SD}), determined by the difference between Source and Drain electrochemical potentials (black arrow), the sequential tunneling of electrons is allowed. (c) If there is no QD energy state (neither for N nor for N+1 stored electrons) inside the useful bias window, the sequential tunneling of electrons is forbidden (Coulomb blockade). (d) When the ground and an excited states of a QD with N-electrons are inside the bias window, both contribute to the final current. (e) Typical $I\ vs\ V_g$ characteristic of Coulomb blockade oscillations. The current (I) through the QD flows with a typical peaks structure, being suppressed for gate voltage values (V_g) in between each peak. In this situation the number of the electrons stored in the QD cannot change. (f) Typical Coulomb diamonds diagram showing the differential conductance versus both V_{SD} and V_g. In the region inside each diamond the QD charge configuration is stable. The red lines, parallel to the diamond edges, represent transport through excited states (adapted from ref.[43]).

To interpret transport measurements, sometimes it is more convenient to refer the energy scale to the electrochemical potential $\mu(N)$ instead of the total energy $U(N)$. The electrochemical potential can be defined as the amount of energy needed to supply to the system to allow the transition between $N-1$ and N electrons inside the dot:

$$\mu(N) \equiv U(N) - U(N-1) = (N - N_0 - \frac{1}{2})E_C - \frac{E_C}{|e|}(C_{QD-S}V_{SD} + C_{QD-g}V_g) + E_N, \quad (2.2)$$

where $E_C = e^2/C$ is the charging energy of the dot.
Next, we can define a quantity that can be directly accessed experimentally, called the addition energy $E_{add}(N)$. This represents the energy separation between two consecutive electrochemical potentials in the dot $E_{add}(N) = \mu(N+1) - \mu(N) = E_C + \Delta E$. It is composed by two terms: E_C and ΔE, which represents the level spacing between two quantum states[4] (see Fig. 2.2(f)).

The main principle that determines the electron transport properties is energy conservation: by applying a bias V_{SD} we are able to move electrons only if tunneling, from the source to the dot and the dot to the drain, is energetically allowed.
To reach a current transport configuration the voltage applied to the QD gates is used to shift the dot electrochemical potential, with respect to the bias window $eV_{SD} = \mu_S - \mu_D$ between the source-drain electrochemical potentials, $\mu_S \leq \mu(N+1) \leq \mu_D$ (see Fig. 2.2(b)). If no allowed dot electrochemical potential levels are inside the bias window, the current is blocked (Fig. 2.2(c)) due to Coulomb interaction. This phenomenon is called 'Coulomb blockade' (see Fig. 2.2(e)).
In a measurement one can usually fix V_{SD} and change V_g. Therefore, we can change the number of electron confined in a dot, by tuning V_g: the more negative we make it, the more electrons leave the dot and at each transition we observe a Coulomb oscillation (Fig. 2.2(e)). If we also vary V_{SD} we obtain a typical 'Coulomb diamond diagram', for the current flowing through the dot (Fig. 2.2(f)).
When not only the ground state but also excited states are inside the bias window, they contribute to the transport process by effectively increasing the tunnel rate, and therefore the tunneling current (Fig. 2.2(d) and color line in Fig. 2.2(f)). As a result, the current through the QD, as a function of the bias applied across it, provides a spectroscopic tool that we can employ to obtain information about the energetic structure of the QD.

2.2.2. DOUBLE QD

In analogy to the properties of a single QD, one can characterize the main properties of a DQD system by investigating its stability diagram, i.e. the map representing the number of the electrons confined in each QD as a function of the voltage applied to two of the gates (or any combinations of them). The transport properties of a DQD can be understood by analyzing the schematic of a DQD system, depicted in Fig. 2.3(a) with all the main capacitive couplings.
For a double dot structure one can define the electrochemical potentials $\mu_1(N_1, N_2)$ and

[4] Therefore, if for example $B = 0$ and we add two electrons to the same energy level, which is spin degenerate, we will have $\Delta E = 0$.

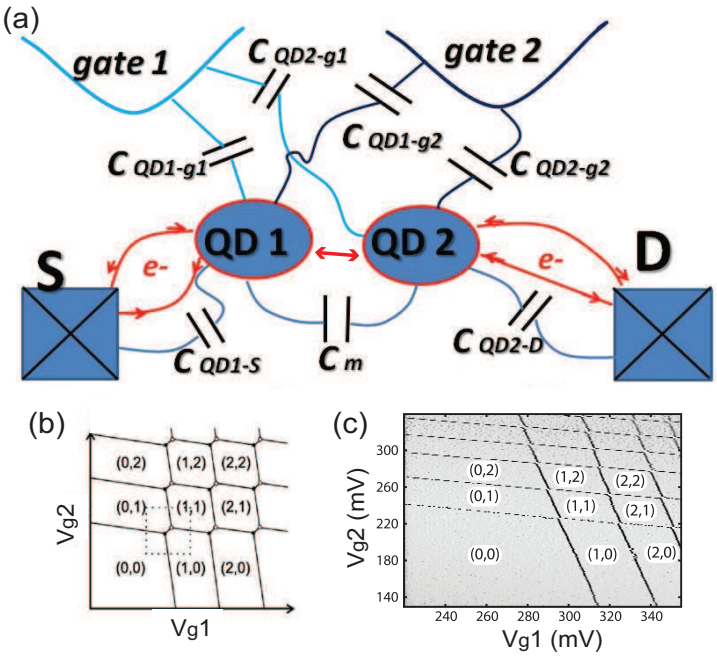

Figure 2.3: (a) Schematic of the main capacitive coupling for a Double Quantum Dot system. There are also depicted, with red arrows and lines, electron tunneling events between QDs and reservoirs. Different coupling regimes determine different shapes of the stability diagram. (b) Schematic of a DQD charge stability diagram in the presence of an inter-dot couplings; it takes an hexagonal shape (honeycomb diagram) (adapted from [44]). (c) Measurement of a honeycomb charge stability diagram of a DQD device in GaAs/AlGaAs.

$\mu_2(N_1,N_2)$, where N_1 and N_2 are the electron numbers on dot 1 and 2 respectively, as

$$\begin{aligned}\mu_1(N_1,N_2) &= U(N_1,N_2)-U(N_1-1,N_2)= \\ &= (N_1-1/2)E_{C1}+N_2E_{Cm}-(1/|e|)(C_{g1}V_{g1}E_{C1}+C_{g2}V_{g2}E_{Cm}),\end{aligned} \tag{2.3}$$

$$\begin{aligned}\mu_2(N_1,N_2) &= U(N_1,N_2)-U(N_1,N_2-1)= \\ &= (N_2-1/2)E_{C2}+N_1E_{Cm}-(1/|e|)(C_{g1}V_{g1}E_{Cm}+C_{g2}V_{g2}E_{C2}),\end{aligned} \tag{2.4}$$

where E_{Ci} is the charging energies for the dot-i. Physically, E_{Cm} describes the electrostatic energy modification generated on one dot when an extra electron is added or removed to the other one. C_{gi} ($\equiv C_{QD_i-g_i}$ in Fig. 2.3(a)), represents the capacitive coupling between gate-i and QD-i and C_m the capacitance between the two QDs.

The charge stability diagram is determined by the expressions for the electrochemical energies $\mu_1(N_1,N_2)$ and $\mu_2(N_1,N_2)$. Fig. 2.3(b) is a diagrammatic representation of the equilibrium electron numbers on QD1 and QD2 as a function of the gate voltages V_{g1} and V_{g2}. If both $\mu_1(N_1,N_2)$ and $\mu_2(N_1,N_2)$ are less than zero but $\mu_1(N_1+1,N_2)$ and $\mu_1(N_1,N_2+1)$ are larger than zero, we have that the charge configuration (N_1,N_2) on the dot represents the equilibrium situation. This creates the typical hexagonal shape of the regions of charge stability diagram (Fig. 2.3(b,c)) that we can use to identify the DQD charge configuration we want to use to start an experiment or to move between different charge configurations.
Measuring the conductance through the whole DQD structure, we will find a peak in the current every time an electron is allowed to tunnel through both dots from source to drain. This condition, for an elastic sequential tunneling process with $V_{SD}\sim 0$, is fulfilled only at the triple points of the stability diagram, namely where the electrochemical potentials of each dot and the leads are degenerate [44].

2.2.3. TRIPLE QDS AND MORE

Solid-state qubits can be, in principle, scaled up in a straightforward way. The depletion gate technology is quite suited for this purpose because it allows an easy evolution of the metal surface gates toward the realization of confinement potentials for 3 or more QDs [56–60]. Each new QD introduces one (or more) control parameter, therefore dimension in the stability diagram of the system. This makes the final tuning process more involved. Figures 2.4(a) and (b) report two SEM pictures of a triple and quadruple QDs linear arrays (with nearest neighbour tunnel coupling only), with their stability diagram in panel (c) and (d). The charge states of each QD can be discriminated by using multiple QDs charge detectors (CDs) (see next section).

2.3. CHARGE DETECTOR

One very important ingredient to realize quantum computation (as clearly exposed by D. Loss and D. P. DiVincenzo [12]) is a high fidelity readout process. A direct measure of the single electron spin in real time is experimentally infeasible. Thus, the readout of the final spin state is an indirect measurement, during which the spin is unequivocally correlated to a specific charge state that we can easily determine by using a charge sensor, capacitively coupled to our QDs [1]. This indirect measurement consists of creating a

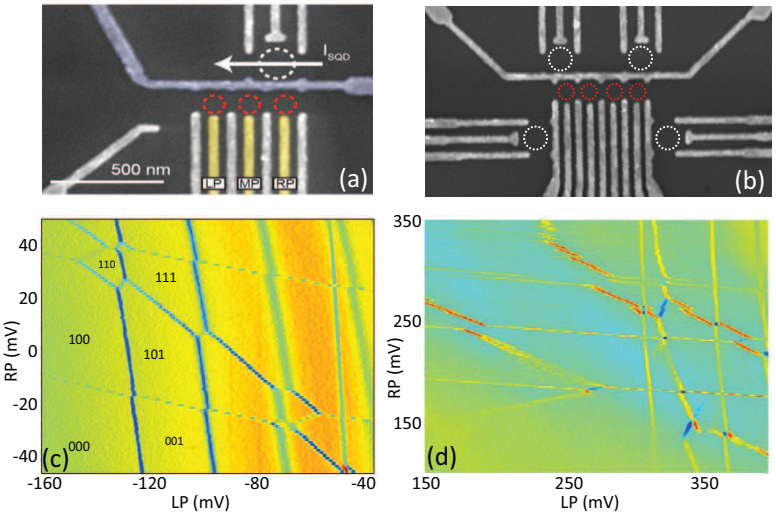

Figure 2.4: (a) Linear array of triple-QDs (TQD, red circles), with a QD CD on top (white circle) and a QPC CD on the left. (b) Linear array of quadruple-QDs (QQD, red circles), with four QD CDs (white circle). (c-d) Stability diagram for the TQD and QQD systems (partially adapted from [58]).

unique correlation between the final orientation of the electron spin and its position (inside or outside a single QD or in the left or right position in a DQD) and can be achieved in two main ways: (i) by the difference in tunnel rates from the different spin states of the dot to the reservoir (tunnel-selective readout) [45–48]; (ii) positioning the spin levels with respect to the electrochemical potential of the reservoir in such a way that only if the electron is in the spin excited state it is energetically allowed to tunnel out of the dot (energy-selective readout) [42, 49–51].

2.3.1. CHARGE SENSING

We refer to 'charge sensing' as the ability to use an electron conduction channel to test the electrostatic environment around the detector itself; thus we can employ this technique to infer the number and location of nearby charges in a QD system. The main figure of merit of a charge detector is its sensitivity to the local electrostatic environment, so that when a single electron moves inside-outside the dot, its conductance will appreciably change.

The working principle of the single electron charge detection is quite simple: the charge state of the QD (the electron number in each dot) affects the voltage profile of the conduction channel of the CD. We maximize the CD transconductance ($|dI/dV|$) by tuning the gate voltages defining the CD. In this configuration a 'small' modification in the electrostatic environment (related to the movement of a single electron) can appreciably change the CD conductance. Therefore, a macroscopic external low noise amplification system can be used to detect the CD impedance change, at low frequency (up to tens of kHz) or in radio frequency (RF, ~hundreds of MHz).

The working principle of this technique is conceptually identical to a field effect transistor (FET) for which the gating effect is realized by a single electron; thus one might consider a charge sensor as a 'single-electron FET' with very high gain.

The location of a single electron could in principle change the conductance of a channel between totally open or totally closed, generating a big change in the conductance of the detector. However, most of the charge sensors created in a solid-state system by depletion technique show a limited sensitivity, particularly because the sensed charge is screened by metallic gates between it and the sensor channel.

Even if QPCs are absolutely the most versatile and widely used charge detector in quantum electronics, due to its simplicity in realization and high sensitivity [4, 36–39], recently it has been demonstrated that a QD-charge sensor could provide a better sensitivity and signal-to-noise ratio (SNR). In [52] it has been shown an increment of ~30 times in terms of charge sensitivity and a three times greater SNR by using a QD-charge sensor embedded in a RF reflectometry circuitry. Furthermore, in this work, it has been pointed out that the key differences between a QD and a QPC as a charge sensor is in the reduced screening and smaller characteristic energy needed to change the current transmission in the QD compared to the QPC.

2.3.2. COMPARISON BETWEEN EXTERNAL DETECTION AND TRANSPORT MEASUREMENTS

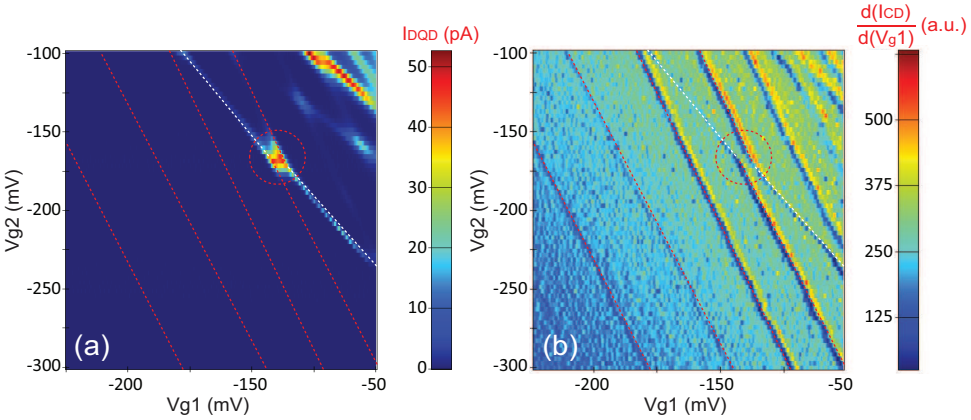

Figure 2.5: (a) Transport current through a DQD as a function of the voltage applied on 2 generic gates. The current inside the red circle represents the last triple points visible for this device. The red and white dashed lines are reported for comparison with panel (b). (b) Numerical derivative along the gate 1 of the CD current, registered simultaneously with panel (a).

In this subsection we want to clarify the advantages of the charge detection method compared to a standard current measurement. We can assume a background noise from the room temperature electronics of $\sim 10 fA/\sqrt{Hz}$ for a conventional current meter (limited by the amplifier noise). This value naturally sets a lower bound for the minimum detectable average transport current signal through the QD. This, on the other

hand, sets a lower bound to the tunneling rate of a QD tunnel barrier; it must be larger than $\Gamma > 10$ fA/e $\sim$ 60 kHz (in order to overcome the noise[5]).
In contrast, with a non invasive charge detector, it is possible to measure electron tunneling on much longer time-scales (slower tunnel rates ~Hz). In particular one can detect equilibrium fluctuations of the QD charge with just a single tunnel barrier open (the other tunnel barrier can be made completely opaque), thus having an electron interacting with a single electron reservoir, characterized by a single Fermi energy. This configuration does not generate electron current and it is used for the single-shot (energy selective) readout of the electron spin.
Fig. 2.5(a) displays a measurement of the current flowing through a DQD system in Si by applying a voltage bias across it. In transport measurements through lateral DQD, the main problem is that the gates used to deplete the dots (by applying a more negative voltage potential) also control the tunnel barriers. Thus, quite often, the few electron regime cannot be reached while keeping a sufficiently high current level. The current inside the red circle in panel (a) represents the last DQD triple point where transport current can be measured (for this specific device and gate configuration) before one of the three tunnel barriers, defining the DQD, will become too opaque.
Referring to the Fig. 2.1(b), the gate structure defining the DQD+charge sensors allows to drive a current through two separate electron paths by pinching-off the SR-RS channel (I_{QPC} and I_{DQD}). In Fig. 2.5(b) we report the differential conductance $\partial G_{QPC}/\partial V$ of the current through the QPC detected simultaneously while measuring panel (a). The red (white) lines in panel (b) correspond to the change in the number of electrons on Dot 1 (dot 2), which is most capacitively coupled to gate 1 (gate 2).
In addition to all of the features already present in panel (a) (look, for example, at the anti-crossing inside the dotted red circle), we can clearly follow both of the charge transitions between each QD and the respective electron reservoirs (white and red dotted lines). From the coincidence of the DQD transport current and QPC differential conductance peaks in these two graphs, we can see that whenever an electron is added to the quantum dot, the conductance of the quantum point contact is reduced by ΔG_{QPC} due to the repulsive Coulomb potential. Thus, we have a dip in the dG_{QPC}/dV_{gate} vs. V_{gate} curve in correspondence of the same gate voltage for the peak in the DQD transport current.

2.3.3. SIGNAL TO NOISE RATIO IN A CHARGE DETECTOR

The ratio between the change in the CD current ΔI_{CD} (the signal) and the noise I_{noise} is the most important figure of merit of a detector (SNR). If we want to maximize the fidelity of the readout process, and so the useful information that can be extracted from the measurements, we have to increase the signal and minimize the noise, as much as possible. The SNR ratio in the measured CD current can be partially improved by increasing the source drain bias voltage. However, there is a practical upper limit to the bias voltage applicable across a CD , which is typically of the order of 1 meV. In fact, it has also been observed that for a bias $V_{CD} > 1\,mV$ the tunneling statistics of the confining QD are significantly altered [41]. In practice, the maximum CD current is limited by heating or photons or phonons emission from the CD, which can influence the QD

[5] Both tunnel barriers with the two leads have to be open enough in order to resolve a transport current.

system[6] [53–55].

If the electron tunnels out or moves faster than the detector measurement bandwidth (BW), the sensor will measure an average property, as it has been done in conventional transport measurements through a QD; on the contrary, if the electron tunnels slower than the measurement BW, every tunneling event may be recorded individually, allowing its real time detection [41][7]. This enables a variety of new measurements, for instance acquiring counting statistics of transport [61], tunneling spectroscopy [62] and single-shot read-out [42].

2.4. EXPERIMENTAL SETUP

A detailed description of the fabrication procedure is given in Chapter 4, with fabrication recipes reported in Appendix A. When the samples are finished (typically in the form of an array of identical device cells), they are diced to separate each individual devices.

2.4.1. SAMPLE PCB AND LASER DIODE

A single device is then glued on a printed circuit board (PCB). To be able to apply and control the voltages applied to the gates and ohmic contacts, electrical connections are realized by Al-wire bonds between contact pads on the PCB and bond pads on the device. Fig. 2.6 shows a PCB (printed by Eurocircuits) similar to the one used for the experiments presented in this thesis, mounted on top of a copper housing attached at the bottom of the cold finger. The PCB, embedded in the electronic circuit of the measurement setup (see Fig. 2.8), is equipped with DC connectors (for 32 DC lines) and with four RF connectors (SMA), used to apply voltage pulses or microwave (MW) bursts on the gates. Three of those connectors are visible in Fig. 2.6(a), mounted on top of the PCB, and the other, visible in Fig. 2.6(c), is mounted with a 90 degree SMA adapter on the back of the copper housing.

The combination of the voltage pulses and MW bursts with the DC voltages is realized by home made RC type bias-tees, mounted directly on the PCB. The bias-tees used to apply MW bursts and voltage pulses are realized with R=10 MΩ and C=47 nF (giving a time constant of ~500 ms). For a discussion about possible issues coming from pulse distortions and how to partially correct for those, see sec. 8.8.1.

For experiments with QWs in undoped Si/SiGe heterostructures we can benefit from the use of a laser diode [63]. Shining light using the laser diode releases charges from traps and effectively resets the charge configuration of the QW. The laser diode used in this experiment has a wavelength of 780 nm, a maximum optical output of 5 mW, and a maximum operating current of 35 mA. However, we limit the current below 1 mA to reduce fridge heating[8]. Three wires (a twisted pair and a single wire of one of the bun-

[6] If we have a CD bias energy larger than the QD single-particle energy level spacing, the CD can excite high energy (up to eV_{bias}) photons and phonons that will promote transitions in the measured system (back-action).

[7] With this non invasive charge technique it is also possible to detect, if the system is well designed, events that may not generate current at all, for example electrons rearranging inside the same QD (squeezing the electron wavefunction by gate voltages), or tunneling into a single electron reservoir.

[8] A wavelength of 790 nm can excite carriers over an energy gap of 1.59 eV. It is not exactly clear how the illumination affects the amount of carriers in the 2DEG. From the band structure of Si it can be seen that the energy

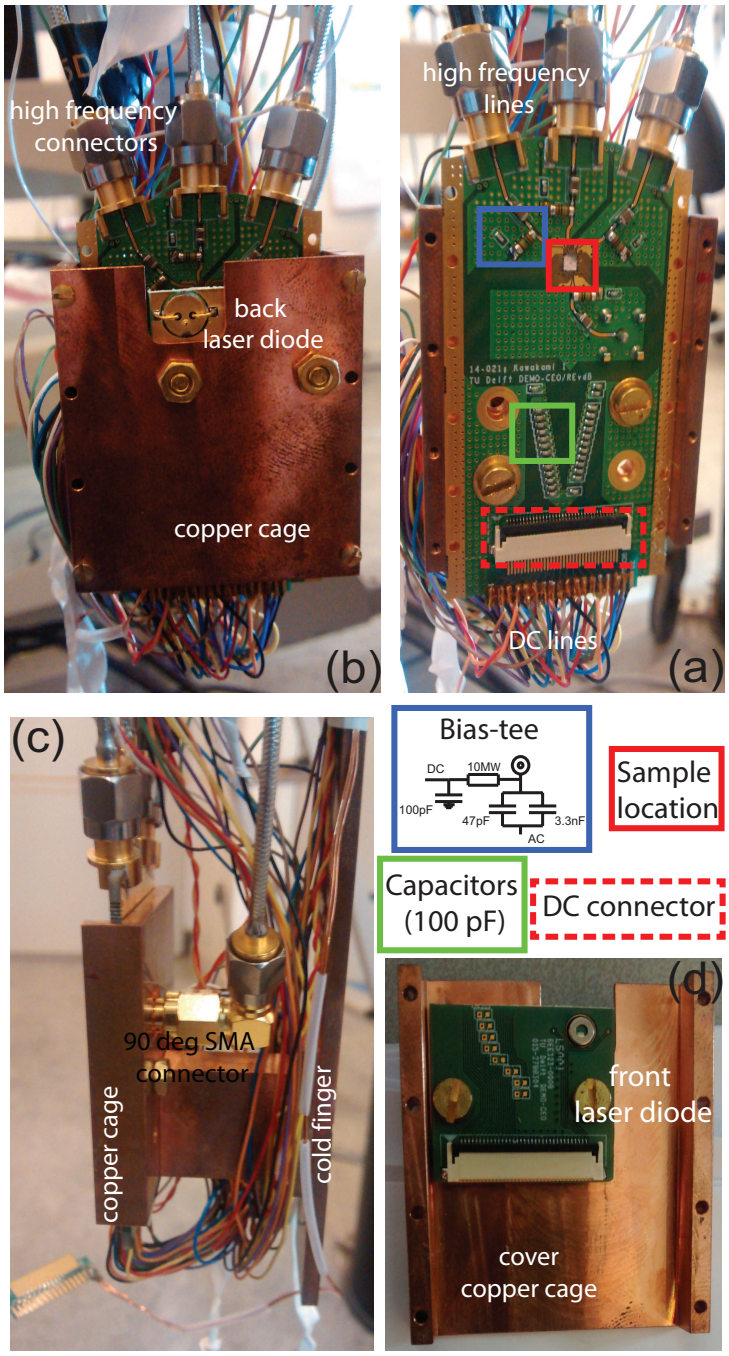

Figure 2.6: (a-b-c) Pictures of the PCB and copper housing (attached to the cold finger) used for the experiments described in the Thesis. The copper housing represents the extremity of the cold finger. (d) Cover of the copper housing with the attached PCB used to control the laser diode.

dles) are connected to the laser diode mounted on a separate PCB (see Fig. 2.6(d)) that is attached to the cover plate of the copper housing of the sample PCB. This solution has been chosen to have the diode directly facing the device, to optimize the excitation process. From room temperature to 4 K the wires are made out of copper (electrical resistance $\sim 1.72 \times 10^{-8}$ Ωm) to limit Joule heating when relatively high currents are sent to the laser diode.

2.4.2. DILUTION REFRIGERATOR

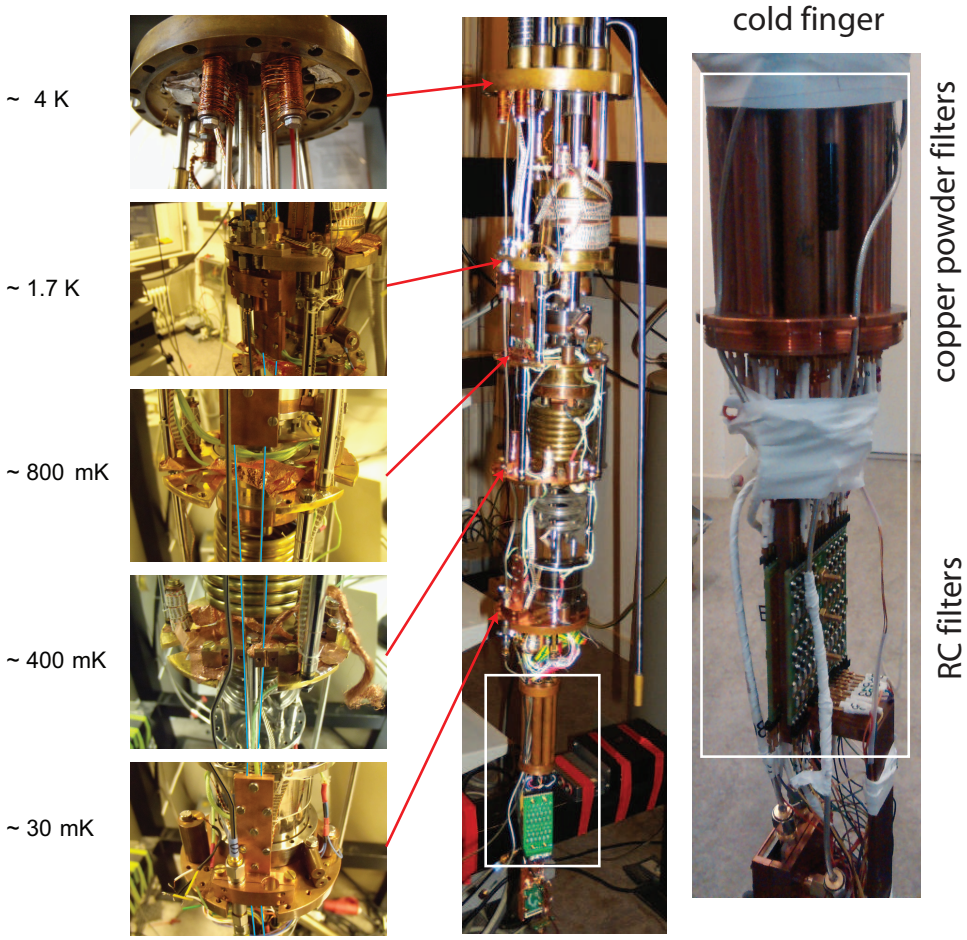

Figure 2.7: Pictures of the different stages of the dilution unit. Partially adapted from [63].

To limit the broadening effect of temperature and to create a well confined 2DEG and

of 1.59 eV is enough to cause carrier excitation over the indirect band gap. Another option would be that the illumination releases carriers from traps occasionally is formed on top of the sample.

a QD structure, we cool down the device to a temperature of ~ 20 mK, by using an Oxford Kelvinox 300 dilution refrigerator. The main cooling contribution to the electrons in the 2DEG comes from the DC/RF wires connected to the ohmic contacts of the device. The lowest refrigeration temperature will be close to the lattice (phonon) temperature of the sample, but the electrons in the 2DEG usually will be hotter (typically ~150 - 250mK). In fact, the electron-phonon interaction is drastically reduced at such low temperatures, therefore the electrons in the 2DEG cannot easily dissipate the extra thermal energy by re-equilibrating with the phonon bath (at 20 mK). This extra heating on the 2DEG is mainly produced by the thermal energy and electric noise, reaching the device from warmer stages of the dilution system through the dc measurement wires and high frequency coax lines.
The liquid helium around the inner vacuum chamber (IVC) of the dilution unit constitutes the 4 K thermal bath for the device, which, if not properly shielded, can cause heating by radiation. In our dilution system, we mount the device in a closed cylinder made out of copper ('copper can'), which is attached to the mixing chamber via a home made cold finger and it is not in thermal contact with the IVC. The 'copper can' absorbs the 4 K radiation from the IVC, suppressing the heating of the sample. Furthermore, the helium Dewar, in which the dilution unit is immersed, is equipped with a two axis superconducting vector magnet that can be used to apply magnetic fields up to 3 T along the transverse axis or up to 7 T along the main axis of the Dewar. The alignment of the PCB with the X-axis of the magnet has been realized manually and it has been tested to be precise within less than 5 degrees.

2.4.3. MEASUREMENT ELECTRONICS: DC WIRES AND FILTERING

The noise level of an electronic transport measurement (whether through quantum dots or charge sensor) depends on the quality of the electrical circuitry connecting the samples to the measurement instruments. Most of the measurement electronics, filters, and PCBs were designed and home-built by Raymond Schouten and the physics electronics workshop at the Delft University of Technology. Figure 2.8 shows a typical electrical circuit schematic with the different components (at different temperatures) of a typical measurement setup. One of the most important features is the galvanic isolation of the sample from a large part of the measurement equipment, including lab computers. This is realized through the use of opto-couplers, where the electrical signals are converted to an optical signal and back, respectively by an LED and by a photo-diode. Furthermore, all measurement electronics connected to the sample, namely the DC voltage sources, DACs and isolation amplifiers are battery-powered.
The gates of the device are voltage biased using 16-bit DACs providing voltages from -2V to +2V or from 0V to ±4V (0.06 mV resolution[9]). The rms voltage fluctuations of the DACs is estimated to be about 4 μV during an hour.

To connect the device (attached to the cold finger) to the room temperature electronics, 48 twisted pairs of wires run inside the dilution refrigerator from room temperature down to the mixing chamber. There are two types of wires, made of manganese (low thermal conductivity, but high electrical resistance) or copper (high thermal conductiv-

[9] This resolution can be increased, for some gates, up to ~600 nV by combining two 16-bit DACs, one of which is down-scaled with a voltage divider with a factor of 100.

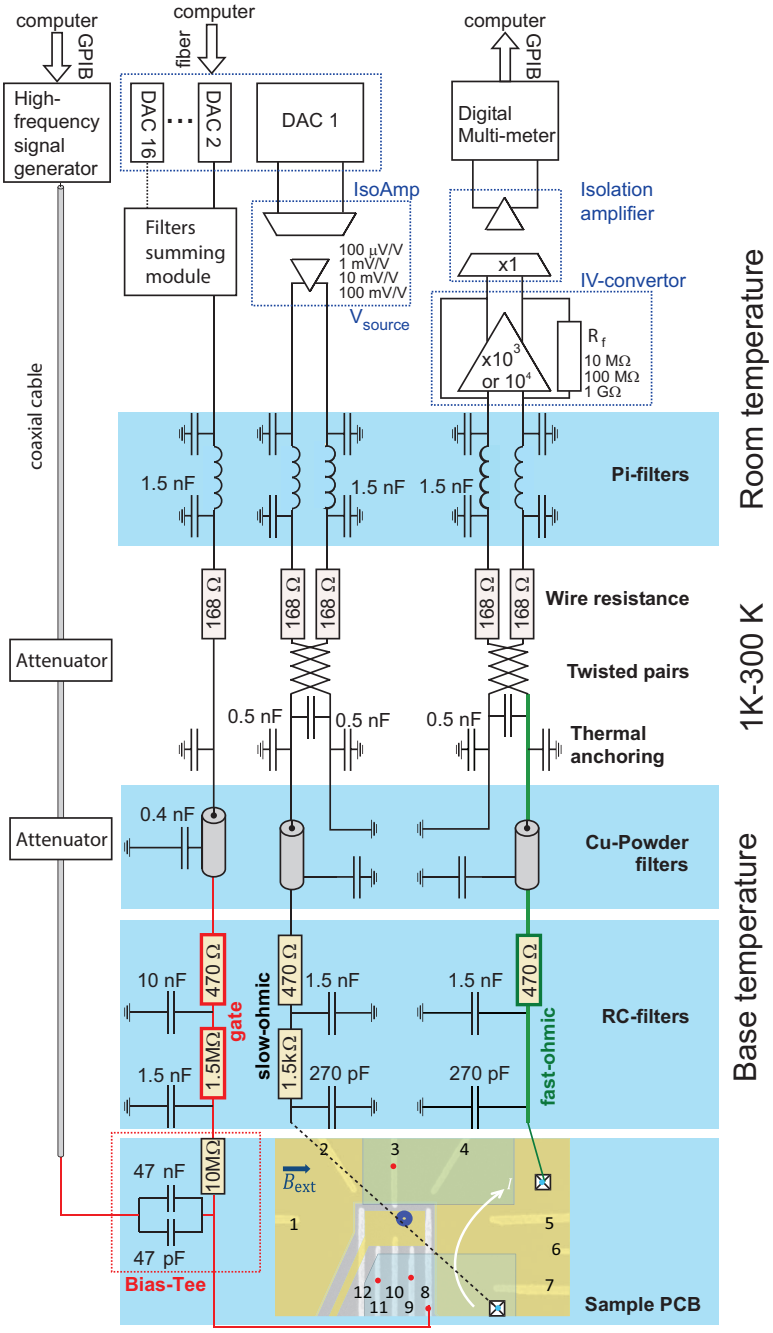

Figure 2.8: Schematic overview of the electronic part of a typical measurement setup.

ity but low resistance). The copper wires are usually used for fast ohmic lines, in order to implement real time single electron tunneling measurements with high-BW. All the wires are thermally anchored to the refrigerator (by wrapping them) at several temperature stages (4 K, 1 K and base temperature)[10]. To reduce the background electrical noise it is important to avoid the introduction of interference due to currents running through magnetic pickup loops in the measurement wires. This is achieved by using a twisted pair for each ohmic contact.

As observed above, thermal radiation (from hotter stages of the dilution system) and interference noise in the DC/RF wires will result in electron heating. Therefore, it is very important to properly filter and attenuate all the lines inside the cryostat to conveniently reduce the electric noise level. We filter all the DC lines, except the fast Ohmic lines, with three different stages, covering a large frequency range (from ~MHz up to ~100 GHz) [64]. i) Pi-filters (consisting of two capacitors and an inductor) in the matrix modules at room temperature filter out the middle frequency range (10 MHz - 10 GHz, attenuation 5 - 70 dB for a 50 Ω load). The rest of the filters are placed directly on the cold finger, at base temperature: ii) first the wires run through copper tubes filled with copper powder. This powder can absorb high frequency noise via eddy currents and provides attenuation of more than 60 dB for high frequencies (1 GHz - 50 GHz). The output of those filters is directly placed inside the 'copper can', which shields the last stage of the filter chain from the 4K radiation. iii) This consists of two-stage RC-filters to attenuate the lower frequency noise. We use RC-filters with different cutoff frequencies of ~30 Hz and ~150 kHz respectively for wires connecting to the gates and ohmic contacts, respectively. A very low cutoff frequency is implemented for the gates to suppress as much as possible gate voltage noise.

The low BW IV-converter has a low noise floor down to 5 fA/$\sqrt{Hz}$ and a variable feedback resistor. The signal from the IV-convertors is sent to an isolation amplifier (which can provide optionally more gain) and low-pass filtered. Finally, the voltage from the isolation amplifier is measured by a digital multimeter (Keithley 2700). The high frequency current fluctuations from the CD (presenting the signature of the single electron tunneling events) are measured via a fast IV-converter. The output voltage of the IV-converter can be read by using a Keithley 2700 for the low BW voltage measurements and a LeCroy WaveRunner 44Xi oscilloscope or a field-programmable gate array (FPGA) system for high BW measurements.
For the fast ohmic lines it is not possible to use the filters mentioned above, which will otherwise limits their BW. Therefore, on this line, the filtering capacitance to the ground is reduced: the pi-filters have been replaced with small capacitance (100 pF) and the capacitance of the first order RC filter inside the fridge is ~270 pF. In this way, the total capacitance of the line from room temperature to the sample is ~1 nF, which allows to keep the BW of the IV converter ~50 kHz. Finally, to obtain a sufficient SNR for the measurement, we further low-pass filter the CD signal, reducing the BW to around ~30-10 kHz.

[10] Note that there is a voltage difference (of several mV) between the cold ground and room temperature ground (thermal-voltage), which should be taken into account to avoid the application of a too high bias voltage across the device.

2.4.4. HIGH FREQUENCY SIGNALS

Our system is equipped with four coax lines, two with 2.4 mm connectors and two with 2.9 mm connectors (K-connectors), which can be accessed from room temperature via two SMA and two 2.4 feed-through connectors[11].
The 4 coax lines inside the cryogenic system consist of three parts:
(i) from room temperature to 1.7 K: semi-rigid Keycom ULT-05 coax cables (outer diameter 2.2 mm; inner conductor: silver-plated brass; outer conductor: stainless steel (SUS304) with a 5 mm layer of copper). The outer conductor has been thermally anchored at the 4K and 1K stages of the fridge by clamping the coax line. The additional use of a 20 dB attenuator at the 1K stage allows to thermally anchor also the inner conductor[12];
(ii) from the 1K plate to the mixing chamber plate: ~30 cm long superconducting Keycom Nb-Ti coaxes (with outer diameter of 2.2 mm; inner and outer conductor: niobium). The inner part is anchored at the mixing chamber plate by using a 10 dB attenuator;
(iii) from the mixing chamber to the sample printed circuit board: ~20 cm flexible tin-plated copper coaxes.

The detection of the electron tunneling events and the calculation of their statistics are done on the fly by the FPGA, as depicted in Fig. 2.9. The fast analysis using FPGA allows us to measure without waiting for transferring large amounts of real time traces to the PC for post analysis. The voltage pulses are generated by a Tektronix AWG (Arbitrary Wave function Generator) 5014C. The output of the AWG is low-pass filter by SBLP-300+ (Mini-circuits) filters. The phase-controlled MW sequences are generated by a Agilent MW vector source E8267D with internal I/Q controlled by two channels of AWG. The on/off ratio of the I/Q modulation is 40 dB. Even if the MW source is off, some MW signal can still leak out and arrive at the sample. If this MW signal is not sufficiently suppressed, it increases the effective electron temperature. This will result in lower read-out and initialization fidelities. Reduced fidelities were indeed observed when applying high power microwave excitation (> 15 dBm at the source) using I/Q modulation only. As a solution, we use the digital pulse modulation (PM) in parallel to the I/Q modulation, which gives a on/off ratio of 80 dB. A drawback of PM is that the turn on (off) speed of the MW burst becomes lower. We correct for this by turning on the PM 200 ns before the I/Q modulation (the inset of Fig. 2.9). Sometimes, in order to keep the read out and initialization fidelity constant even when we change the MW burst time, we apply an off-resonant MW burst (with MW frequency 30 MHz away from the resonance frequency) 2 μs after the on-resonance MW burst. For this rapid shift of the MW frequency, we used FM (Frequency Modulation) controlled by a channel of AWG. FM is turned on 1 μs after the on-resonant burst is switched off (the inset of Fig. 2.9). For the lines connected to the MW source, we use at room temperature DC blocks for both inner connector and outer conductor (0.1 to 40 GHz, Pasternack PE8227 DC block).

[11] The BW of the lines with 2.4 mm connectors is specified up to 50 GHz, nominally higher than the BW of lines with K-connectors (~ 40 GHz)

[12] In general, coax lines connecting two stages with a temperature ratio of ~100 have to be attenuated by using a 20 dB cryogenic attenuator. In this case, the high temperature Johnson noise is scaled down to the Johnson noise at the coldest plate out of the two.

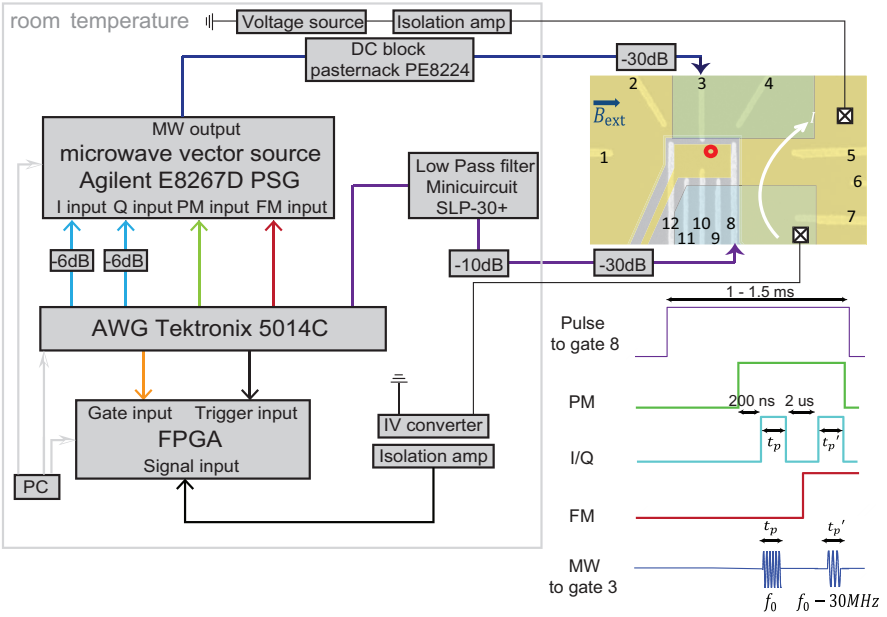

Figure 2.9: (a) Device schematic and block diagram depicting the generation of gate voltage pulses and phase-controlled microwaves, and scheme for the current detection and post analysis using an FPGA. There is a 20 dB attenuator at the 1 K plate and a 10 dB attenuator at the mixing chamber (MC) stage for each of two high frequency lines which are connected to gate 3 and gate 8. The I/Q modulation, PM (Pulse Modulation) and FM (Frequency Modulation) of the MW vector source are controlled by voltage pulses generated from different channels of the AWG. For the I/Q inputs, 6 dB attenuators are added to reduce the noise from the AWG. The 4 stage voltage pulse applied to gate 8 is generated by another channel of the AWG. In order to reduce the noise going to the sample from the AWG, the Minicircuits low pass filter SLP-30+ and 10 dB attenuator are added at room temperature. The microwaves are applied to gate 3 and the Pasternack DC block PE8224 is added at room temperature to reduce the low frequency noise. The current running through a sensing quantum dot is measured. The voltage signal converted from the current via the IV converter is plugged into the FPGA for post analysis (event detection) of each cycle and for making the statistics of these events over cycles. Gate pulses and trigger pulses are connected to the FPGA. Gate pulses define the part of the signal where the analysis should be done. The trigger pulse is applied before the whole sequence starts. The inset shows the voltage pulse applied to gate 8 (black line), voltage pulses for PM (green line), for gating the FPGA (orange line), for I/Q modulation (light blue line), and for FM (red line) of the microwaves applied to gate 3 (blue line) during the manipulation stage.

REFERENCES

[1] R. Hanson, L. P. Kouwenhoven, J. R. Petta, S. Tarucha, and L. M. K. Vandersypen, Rev. Mod. Phys. **79**, 1217 (2007).

[2] S. J. Mehl, 'Achieving quantum computation with quantum dot spin qubits', PhD thesis, RWTH Aachen University (2014).

[3] T. Hayashi, T. Fujisawa, H. D. Cheong, Y. H. Jeong, and Y. Hirayama, Phys. Rev. Lett. **91**, 226804 (2003).

[4] J. R. Petta, A. C. Johnson, C. M. Marcus, M. P. Hanson, and A. C. Gossard, Phys. Rev. Lett. **93**, 186802 (2004).

[5] G. Cao, H. O. Li, T. Tu, L. Wang, C. Zhou, M. Xiao, G. C. Guo, H. W. Jiang, and G. P. Guo, Nat. Commun. **4**, 1401 (2013).

[6] K. D. Petersson, J. R. Petta, H. Lu, and A. C. Gossard, Phys. Rev. Lett. **105**, 246804 (2010).

[7] G. Shinkai, T. Hayashi, T. Ota, and T. Fujisawa, Phys. Rev. Lett. **103**, 056802 (2009).

[8] H. O. Li, G. Cao, G. D. Yu, M. Xiao, G. C. Guo, H. W. Jiang, and G. P. Guo, Nat. Commun. **6**, 7681 (2015).

[9] T. Meunier, I. T. Vink, L. H. Willems van Beveren, K J. Tielrooij, R. Hanson, F. H. L. Koppens, H. P. Tranitz, W. Wegscheider, L. P. Kouwenhoven and L. M. K. Vandersypen, Phys. Rev. Lett. **98**, 126601 (2007).

[10] V. N. Golovach, A. Khaetskii and D. Loss, Phys. Rev. Lett. **93**, 016601 (2004).

[11] S. I. Erlingsson and Y. V. Nazarov, Phys. Rev. B **66**, 155327 (2002).

[12] D. Loss, and D. P. DiVincenzo, Phys. Rev. A **57**, 120 (1998).

[13] G. Burkard, D. Loss, and D. P. DiVincenzo, Phys. Rev. B **59**, 2070 (1999).

[14] J. R. Petta, A. C. Johnson, J. M. Taylor, E. A. Laird, A. Yacoby, M. D. Lukin, C. M. Marcus, M. P. Hanson, and A. C. Gossard, Science **309**, 2180 (2005).

[15] J. M. Taylor, J. R. Petta, A. C. Johnson, A. Yacoby, C. M. Marcus, and M. D. Lukin, Phys. Rev. B **76**, 035315 (2007).

[16] S. Foletti, H. Bluhm, D. Mahalu, V. Umansky, and A. Yacoby, Nature Phys. **5**, 903 (2009).

[17] H. Bluhm, S. Foletti, D. Mahalu, V. Umansky, and A. Yacoby, Phys. Rev. Lett. **105**, 216803 (2010).

[18] B. M. Maune, M. G. Borselli, B. Huang, T. D. Ladd, P. W. Deelman, K. S. Holabird, A. A. Kiselev, I. Alvarado-Rodriguez, R. S. Ross, A. E. Schmitz, M. Sokolich, C. A. Watson, M. F. Gyure, and A. T. Hunter, Nature (London) **481**, 344 (2012).

[19] X. Wu, D. R. Ward, J. R. Prance, D. Kim, J. K. Gamble, R. T. Mohr, Z. Shi, D. E. Savage, M. G. Lagally, Mark Friesen, S. N. Coppersmith, and M. A. Eriksson, Proceedings of the National Academy of Sciences **111**, 11938 (2014).

[20] F. H. L. Koppens, C. Buizert, K. J. Tielrooij, I. T. Vink, K. C. Nowack, T. Meunier, L. P. Kouwenhoven, and L. M. K. Vandersypen, Nature (London) **442**, 766 (2006).

[21] A. C. Johnson, J. R. Petta, J. M. Taylor, A. Yacoby, M. D. Lukin, C. M. Marcus, M. P. Hanson, and A. C. Gossard, Nature (London) **435**, 925 (2005).

[22] M. D. Shulman, O. E. Dial, S. P. Harvey, H. Bluhm, V. Umansky, A. Yacoby, Science **336**, 202 (2012).

[23] D. P. DiVincenzo, D. Bacon, J. Kempe, G. Burkard, and K. Whaley, Nature (London) **408**, 339 (2000).

[24] J. Medford, J. Beil, J. M. Taylor, S. D. Bartlett, A. C. Doherty, E. I. Rashba, D. P. DiVincenzo, H. Lu, A. C. Gossard, and C. M. Marcus, Nature Nanotech. **8**, 654 (2013).

[25] K. Eng, et al., Sci. Adv. **1** e1500214.

[26] J. Medford, J. Beil, J. M. Taylor, E. I. Rashba, H. Lu, A. C. Gossard, and C. M. Marcus, Phys. Rev. Lett. **111**, 050501 (2013).

[27] Z. Shi, C. B. Simmons, J. R. Prance, J. K. Gamble, T. S. Koh, Y. P. Shim, X. Hu, D. E. Savage, M. G. Lagally, M. A. Eriksson, M. Friesen, and S. N. Coppersmith, Phys. Rev. Lett. **108**, 140503 (2012).

[28] Z. Shi, C. B. Simmons, D. R. Ward, J. R. Prance, X. Wu, T. S. Koh, J. K. Gamble, D. E. Savage, M. G. Lagally, Mark Friesen, S. N. Coppersmith, and M. A. Eriksson, Nat. Commun. **5**, 3020 (2014).

[29] D. Kim, Z. Shi, C. B. Simmons, D. R. Ward, J. R. Prance, T. S. Koh, J. K. Gamble, D. E. Savage, M. G. Lagally, Mark Friesen, S. N. Coppersmith, and M. A. Eriksson, Nature (London) **511**, 70 (2014).

[30] D. Kim, D. R. Ward, C. B. Simmons, J. K. Gamble, R. B. Kohout, E. Nielsen, D. E. Savage, M. G. Lagally, Mark Friesen, S. N. Coppersmith, and M. A. Eriksson, Nature Nanotech. **10**, 243 (2015).

[31] T. S. Koh, J. K. Gamble, Mark Friesen, M. A. Eriksson, and S. N. Coppersmith, Phys. Rev. Lett. **109**, 250503 (2012).

[32] L. P. Kouwenhoven, D. G. Austing and S. Tarucha, Rep. Prog. Phys. **64**, 701 (2001).

[33] P. M. Petroff, A. Lorke, A. Imamoglu, Phys. Today **54**, 46 (2001).

[34] D. D. Awschalom, L. C. Bassett, A. S. Dzurak, E. L. Hu, J. R. Petta, Science **339**, 1174 (2013).

[35] W. Lu, Z. Ji, L. Pfeiffer, K. W. West and A. J. Rimberg, Nature **423**, 422 (2003).

[36] M. Field, C. G. Smith, M. Pepper, D. A. Ritchie, J. E. F. Frost, G. A. C. Jones and D. G. Hasko, Phys. Rev. Lett. **70**, 1311 (1993).

[37] A. W. Rushforth, C. G. Smith, M. D. Godfrey, H. E. Beere, D. A. Ritchie and M. Pepper, Phys. Rev. B **69**, 113309 (2004).

[38] C. Fricke, M. C. Rogge, B. Harke, M. Reinwald, W. Wegscheider, F. Hohls, and R. J. Haug, Phys. Rev. B **72**, 193302 (2005).

[39] J. M. Elzerman, R. Hanson, J. S. Greidanus, L. H. Willems van Beveren, S. De Franceschi, L. M. K. Vandersypen, S. Tarucha and L. P. Kouwenhoven, Phys. Rev. B **67**, 161308 (2003).

[40] R. Schleser, E. Ruh, T. Ihn, K. Ensslin, D. C. Driscoll and A. C. Gossard, Appl. Phys. Lett. **85**, 2005 (2004).

[41] L. M. K. Vandersypen, J. M. Elzerman, R. N. Schouten, L. H. W. van Beveren, R. Hanson, and L. P. Kouwenhoven, Appl. Phys. Lett. **85**, 4394 (2004).

[42] J. M. Elzerman, R. Hanson, L. H. Willems van Beveren, B. Witkamp, L. M. K. Vandersypen and L. P. Kouwenhoven, Nature **430**, 431 (2004).

[43] J. M. Elzerman, 'Electron spin and charge in semiconductor quantum dots', Ph.D. thesis, Delft University of Technology (2004).

[44] W. G. van der Wiel, S. De Franceschi, J. M. Elzerman, T. Fujisawa, S. Tarucha, and L. P. Kouwenhoven, Rev. Mod. Phys. **75**, 1 (2002).

[45] R. Hanson, L. H. Willems van Beveren, I. T. Vink, J. M. Elzerman, W. J. M. Naber, F. H. L. Koppens, L. P. Kouwenhoven and L. M. K. Vandersypen, Phys. Rev. Lett. **94**, 196802 (2005).

[46] S. Amasha, K. MacLean, I. P. Radu, D. M. Zumbühl, M. A. Kastner, M. P. Hanson, and A. C. Gossard, Phys. Rev. B **78**, 041306(R) (2008).

[47] P. Stano and P. Jacquod, Phys. Rev. B **82**, 125309 (2010).

[48] M. Thalakulam, C. B. Simmons, B. J. Van Bael, B. M. Rosemeyer, D. E. Savage, M. G. Lagally, Mark Friesen, S. N. Coppersmith, and M. A. Eriksson, Phys. Rev. B **84**, 045307 (2011).

[49] A. Morello et al., Nature (London) **467**, 687 (2010).

[50] K. C. Nowack, M. Shafiei, M. Laforest, G. E. D. K. Prawiroatmodjo, L. R. Schreiber, C. Reichl, W. Wegscheider, and L. M. K. Vandersypen, Science **333**, 1269 (2011).

[51] C. B. Simmons, J. R. Prance, B. J. Van Bael, T S. Koh, Z. Shi, D. E. Savage, M. G. Lagally, R. Joynt, Mark Friesen, S. N. Coppersmith, and M. A. Eriksson, Phys. Rev. Lett. **106**, 156804 (2011).

[52] C. Barthel, M. Kjaergaard, J. Medford, M. Stopa, C. M. Marcus, M. P. Hanson, and A. C. Gossard, Phys. Rev. B **81**, 161308(R) (2010).

[53] E. Onac, F. Balestro, L. H. Willems van Beveren, U. Hartmann, Y. V. Nazarov and L. P. Kouwenhoven, Phys. Rev. Lett. **96**, 176601 (2006).

[54] D. Harbusch, D. Taubert, H. P. Tranitz, W. Wegscheider, and S. Ludwig, Phys. Rev. Lett. **104**, 196801 (2010).

[55] G. Granger, D. Taubert, C. E. Young, L. Gaudreau, A. Kam, S. A. Studenikin, P. Zawadzki, D. Harbusch, D. Schuh, W. Wegscheider, Z. R. Wasilewski, A. A. Clerk, S. Ludwig and A. S. Sachrajda, Nature Phys. **8**, 522 (2012).

[56] L. Gaudreau, G. Granger, A. Kam, G. C. Aers, S. A. Studenikin, P. Zawadzki, M. Pioro-Ladrière, Z. R. Wasilewski and, A. S. Sachrajda, Nature Phys. **8**, 54 (2012).

[57] F. R. Braakman, P. Barthelemy, C. Reichl, W. Wegscheider and, L. M. K. Vandersypen, Nature Nanotech. **8**, 432–437 (2013).

[58] T. A. Baart, M. Shafiei, T. Fujita, C. Reichl, W. Wegscheider, L. M. K. Vandersypen, arXiv:1507.07991.

[59] R. Thalineau, S. Hermelin, A. D. Wieck, C. Bäuerle, L. Saminadayar, and T. Meunier, Appl. Phys. Lett. **101**, 103102 (2012).

[60] M. R. Delbecq, T. Nakajima, T. Otsuka, S. Amaha, J. D. Watson, M. J. Manfra, and S. Tarucha, Appl. Phys. Lett. **104**, 183111 (2014).

[61] S. Gustavsson, R. Leturcq, M. Studer, I. Shorubalko, T. Ihn, K. Ensslin, D. C. Driscoll, A. C. Gossard, Surface Science Reports **64**, 191 (2009).

[62] J. M. Elzerman, R. Hanson, L. H. Willems van Beveren, L. M. K. Vandersypen, and L. P. Kouwenhoven, Appl. Phys. Lett. **84**, 4617 (2004).

[63] S. N. Hendrichs, 'Si-SiGe quantum dots for highly coherent spin qubits', Master thesis, Delft University of Technology (2011).

[64] M. Shafiei, 'Electrical Control, Read-out and Initialization of Single Electron Spins', Ph.D. thesis, Delft University of Technology (2013).

3

THEORY OF VALLEY AND SPIN PHYSICS

The symmetry of the silicon (Si) crystal structure gives to the valence electrons an additional degree of freedom known as valley [1, 2]. It is known that the multi-valley structure of the conduction band in Si may constitute a challenge for spin quantum computing. In fact, the valley energy splitting, E_{VS}, can be of the same order or even smaller then both the Zeeman energy and orbital energy spacings [3–5]. If the valley energy splitting is smaller than the thermal energy or the Zeeman energy, the Hilbert space representing the quantum states of the confined electron cannot be anymore approximated with a simple two-level spin system. This can result in leakage of quantum information into the excited valley states, a process that directly limits the spin initialization fidelity and can also lead to faster spin relaxation and, therefore, errors in the spin manipulation.
Thus, for quantum dot (QD) spin qubits in silicon, it is necessary to lift the two-fold z-degeneracy of the two-dimensional electron gas to form a well isolated two-level system. If we assume a flat and defect-free heterostructure interface, with the growth direction of the heterostructure perfectly aligned with the [001] direction, the valley splitting is maximized with the valley eigenstates fully coupled (high valley-splitting) and with a predicted valley-energy-splitting of ~1 meV [4, 6, 7]. Instead, in most of the cases, the measured valley energy splitting varies from device to device and is, in general, 1-2 orders of magnitude smaller than the expected theoretical calculations considering an abrupt and disorder free interface [3, 6]. Today, for electron confined in SiGe/Si/SiGe heterostructure, such energy splittings are too small and too unpredictable for robust quantum computing applications.

3.1. VALLEY PHYSICS

Fig. 3.1(a) represents a schematic of a covalently bonded silicon crystal [9]. Silicon crystallizes in a diamond structure and its band structure (bulk) is indirect, as shown in Fig. 3.1(c). The minimum energy of electron states in the conduction band is not at

the same momentum (k-vector) as the maximum of the valence band (which is at $k = 0$), but rather at a point $k_0 \sim 0.85 \cdot 2\pi/a$ of the Brillouin zone (with a the Si lattice constant), as shown in Fig. 3.1(d). This minimum point presents a six-fold symmetry because of the cubic symmetry of bulk Si. As a consequence, there are six equivalent minima positioned at $(\pm k_0, 0, 0)$, $(0, \pm k_0, 0)$ and $(0, 0, \pm k_0)$ in the Brilluine zone, resulting in a 6-fold valley degeneracy of the conduction band minima.

Typically the valley degeneracy can be removed by three methods: strain, sharp (on atomic scale) confinement, and electric fields. Usually, building a nano-device deals with the creation of further electric potentials that realize the electron confinements which, if properly tailored, might generate a complete and robust lifting of this valley-degeneracy.

Already for conventional electronic devices, it has been shown that the presence of multiple degenerate valleys limits the electron mobility due to intra-valley scattering mechanisms [13, 14]; the mobility can be enhanced by partially removing this degeneracy by biaxial tensile strain. However, the remaining 2-fold-valley degeneracy can still play a critical role in quantum electronics due to the interference between different valley states and the coupling between valley and orbital degrees of freedom mediated by disorder potential. When valley degeneracy is completely lifted, the electrons populate only the ground valley state if the electron temperature is low enough. This simple picture represents the foundation of most of the conventional quantum computation schemes for electron spin in Si. The system, in this case, is analogous to a single electron spin hosted in the GaAs counterpart [9, 15].

A possible strategy for fabricating Si devices with lifted valley degeneracy consists in using a strained Si quantum wells (QW), grown on a relaxed $Si_{1-x}Ge_x$ substrate (see Chapter 4 for more details). The large tensile strain partially breaks the sixfold valley degeneracy, in four Δ_4-valley states with at an energy ~200 meV per 1% of accumulated strain above the two Δ_2-valleys, as shown in Fig. 3.2 [1]. Ideally, the confinement of electrons in a 2-dimensional electron gas (2DEG) against a sharp and flat interface lifts the remaining two-fold valley degeneracy in the z-direction[1]. Externally applied or internally built electric fields along the z-direction also break the inversion symmetry along z, thereby coupling the two z-valleys (if sufficiently abrupt) and providing a knob to tune, in-situ, the valley spitting [16].

However, real heterostructures do not present a clean abrupt interface; disorder and surface roughness hinder uniformity and homogeneity in the spectral properties of the final devices. Surface roughness, atomic steps in the Si QW or alloy disorder are omnipresent and play an important role in determining the magnitude of the valley-splitting [3, 4, 6, 7, 17]. Hence, breaking the two-fold valley degeneracy becomes very sensitive to atomic-scale details of the Si/SiGe interface and it is usually a function of the QD position, which naturally leads to valley-orbit coupling (see sections 3.4, 3.5 and 3.6) [17, 18]. What explained so far directly suggests that the study and the control (engineering) of the valley splitting is complex because the valley degree of freedom involves physics on a length-scale much smaller than typical control dimension that our fabrication skills allow us, corresponding to the typical quantum dot dimension ~20 nm. Indeed, E_{VS}

[1] A spatially sharp potential step in the z-direction provides the high-k momentum components that can couple the two lower energy z-valleys.

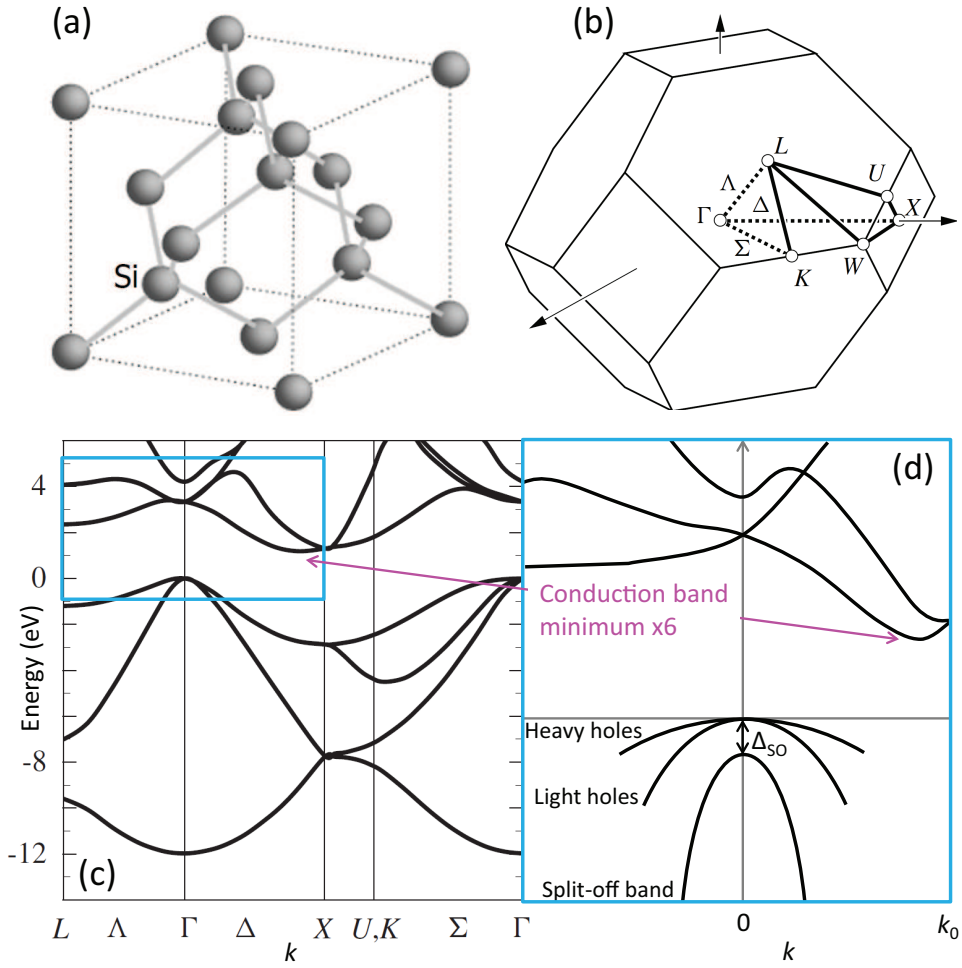

Figure 3.1: (a) Schematic of the crystal structure of bulk Si. (b) Brillouin zone for the electrons in the bulk (relaxed) Si, which presents a face centered cubic lattice. (c) Band structure for electrons in bulk Si. Notice how the maximum of the valence band is at the center of the Brilluin zone (Γ point) as opposed to to the minimum of the conduction band (indirect band gap). (d) Magnification of the band structure around of the band gap region. Adapted from [9].

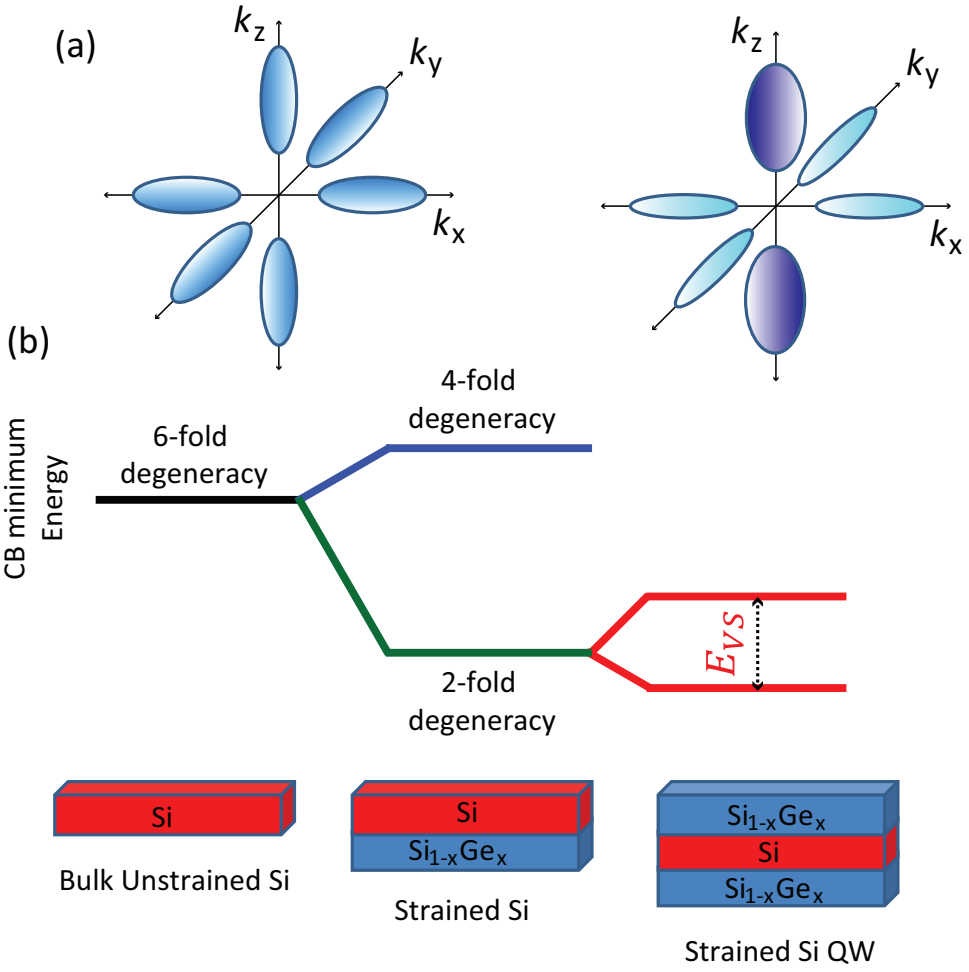

Figure 3.2: (a) Constant energy surface for relaxed (left) and biaxial strained (right) silicon. (b) Schematic of the evolution of the valley energy degeneracy by introducing strain and QW confinement with sharp interface.

depends on the atomic scale details of the disorder at the interface, so it will be, sample dependent. This is also the main reason why it is convenient to reduce the typical dot confinement radius.

In the context of quantum computing in a Si-based system, it is also important to consider valley-spin coupling, which can indirectly affect the spin state and lead to spin decoherence (as shown in [5]). In fact, spin-valley coupling has been predicted and measured for Si 2DEGs [16, 19, 20], with a magnitude proportional to the spin-orbit coupling. It is a second order effect that results form the combination of valley-orbit coupling and spin-orbit coupling. The latter can have a natural [16, 20] or artificial [5] origin, mediated by the stray magnetic field generated by a micromagnet [22, 23] (see sections 3.5 and 3.6).

3.2. ROLE OF THE VALLEY SPLITTING FOR DIFFERENT KINDS OF QUBITS

The study and the optimization of the valley physics (mainly of the valley energy splitting) is a very important task for all the different proposed physical implementations of qubits hosted in Si environment. In fact, the valley degree of freedom enriches the energy spectrum of electrons confined in Si QDs and makes them more difficult to control. Furthermore, we can look to this extra degree of freedom not only as a potential critical issue but also as a resource (if enough controllable) to encode and manipulate quantum information. We will limit our overview to depletion-accumulation QDs systems but similar considerations are also valid for electron confined by phosphorus impurities in Si, for which the valley splitting is usually much higher [24].

The typical example that shows how the additional valley degree of freedom can affect the spin physics and, therefore, spin qubits computation and read out schemes, refers to the exchange coupling. Controlling a non negligible exchange interaction is a fundamental requirement for implementing the two-spin gate for L-D qubit [25] or also the S-T_0 qubit [26] and exchange-only qubits [27] universal control. According to the Pauli exclusion principle, any two indistinguishable electrons must present different sets of quantum numbers, being fermions[2]. When the valley degree of freedom is introduced, the size of the Hilbert space doubles, providing to the electron an additional degree of freedom that can be used to build a final antisymmetric electron state, keeping the same orbital wavefunction. Therefore, a small valley energy splitting can result in an indirect spin effect, mediated by the Pauli principle, which makes ineffective the exchange coupling [28, 29]. The latter effect directly implies that if the valley energy splitting is smaller than the orbital energy splitting (for a given QD confinement potential), the triplet state can also present a lower energy than the singlet state [30, 31].

Furthermore, as we report more extensively in Chapter 5, the valley degree of freedom in Si plays an important role in determining the single electron spin initialization and manipulation fidelity (and Rabi oscillation visibility) [5]. In fact, in [5] it was possible to resolve 2 distinct spin resonances, one for each valley state. When both of the valleys are thermally populated, the visibility of spin rotations is reduced. Furthermore, switching between the two valleys limits the spin echo coherence time T_2 to around 40 μs, with

[2] the total wavefunction has to stay antisymmetric with respect to exchange of the fermions.

an exponential decay envelope as a function of the total waiting time (see Chapter 5)[3].

Regarding the relaxation time T_1 for Loss-DiVincenzo qubits, in [16] it has been demonstrated that, once the valley-orbit energy splitting equals the Zeeman splitting (condition also known as 'spin hot spot'), in the presence of spin-orbit coupling, fast spin relaxation occurs between the valley states via phonon emission, into an inter-valley scattering process.

Recently, a new kind of qubit, known as 'hybrid' qubit, has been proposed and experimentally realized by the M. A. Eriksson group and collaborators at University of Wisconsin [32, 33] (see section 2.1). The two logical states of the hybrid qubit consist of ground and excited states for a DQD configuration with a single electron in a QD and two electrons in the other, and the same total S^2 and S_z. The tailoring of the energy spectrum of the hybrid qubit system is strongly affected by the magnitude of the smallest valley splitting of one of the two QDs.

In 2012, a new quantum computation platform in Si QDs has been suggested in [34], by D. Culcer et al., based on the idea that the valley degree of freedom can be also used to encode and process quantum information. The task of this valley-based QC is to find two states with different valley compositions that can be rotated into each other by a tunable interaction. The proposed device consists in a DQD built in Si systems, and the tunneling between valley eigenstates is induced through the top gate, which tunes the magnitude of the valley-orbit coupling in each of the two quantum dots (QD). The decoherence times are set by inter-valley transitions, occurring on longer time scales than intra-valley transitions, allowing for longer coherence times if compared to a standard charge qubit. In Chapter 7 we will show how the experimental control of the valley degree of freedom can be quite problematic for a single electron confined in a SiGe QD, due to valley-orbit coupling generated by disorder potential. The spatial disuniformity of the wavefunctions between the two valley states makes a valley qubit inevitably a bit 'charge-like'. In this context it becomes clear that understanding and controlling the valley degree of freedom represents a fundamental goal for realizing any computation scheme dealing with electrons confined and energy spectrum in silicon QDs.

3.3. VALLEY DEGREE OF FREEDOM IN THE EXPERIMENTS

On the experimental side, it has been reported that the magnitude of the measured valley-orbit splitting ranges from vanishingly small to ~ 250 μeV in Si/SiGe systems. For Si/SiO_2 QDs it has been measured up to ~ 1 meV (see Table 3.1). Many experiments realized in 2DEG in the Quantum Hall configuration [38–41] have shown a quite small energy valley splitting (~ μeV). This suppression of the valley splitting is caused by an interference effect associated with the presence of an high density of randomly distributed atomic steps at the Si/SiGe interface, across which the electron wavefunction extends (as mentioned in the previous section).

One of the first clear demonstrations of valley-splitting energy tunability in a SiGe mesoscopic device has been realized in [42] by using a quantum point contact, created

[3] A possible explanation for this phenomenon is that the observed decoherence rate reflects the valley switching rate: as soon as the valley switches, the spin resonance frequency jumps by about 2 MHz (for the configuration used in our experiment), and the phase of the spin cannot be recovered anymore being randomized. This will make ineffective also the application of a more elaborated decoupling pulse scheme.

Table 3.1

Experiment	Valley Splitting (μeV)	System (technique)
[42]	up to 1500	Si/SiGe QPC
[31]	$\Delta E_V \sim 400$ mT=45	Si/SiGe QD-ΔE_{ST}
[30]	up to 270	Si/SiGe sQD
[16]	200-800	Si/SiO_2 single QD (spin hot spot)
[8]	~100	Si/SiO_2 single QD
[19]	~86	Si/SiO_2 DQD
[11]	~56	Si/SiGe DQD (PAT)
[12]	~35-70	Si/SiGe sQD
[10]	~150	Si/SiGe 2DEG (SdH oscill.)
Chapter 7	6 GHz~25	Si/SiGe sQD (spin-valley res.)

by depletion gate technology in a SiGe/Si/SiGe heterostructure grown on top a 2 degrees miscut Si substrate. The valley splitting (manifested in the QPC subband spectrum) has been significantly enhanced (up to 1.5 meV) by increasing the lateral confinement of the electron wavefunction by using a perpendicular magnetic field. In this way, the electron wavefuction will extend over fewer steps at the Si QW interface.

A clear experimental signature of valley physics in Si/SiO MOS structure, in the context of spin qubits, has been recently shown in [16]. In this work, the presence of the natural spin-orbit coupling in Si induces fast spin relaxation, mediated by phonon induced inter-valley mixing. This spin relaxation process is orders of magnitude faster than usual around the hot spot configuration ($\Delta E_z \sim \Delta E_{VS}$), where the Zeeman splitting matches the valley splitting. Furthermore, this experiment shows a controllable tuning of the valley-splitting from 200 μeV to 800 μeV, making use of the perpendicular electric field generated by a top accumulation gate very close to the QD [16, 43].

Another experiment showing a partial tunability of valley splitting in a Si/SiGe QD, which, even if unpredictable is controllable to a certain extent, makes use of the singlet-triplet (S-T) splitting of a two electron quantum dot [31]. S-T energy splittings ranging between 0 and 0.3 meV have been measured at zero-field [44–46] for similar systems. Since the triplet state involves the first single-electron excited state in the realization of an antisymmetric wavefunction [15], the S-T splitting provides a good estimate of the valley energy splitting (as already mentioned in the previous section). In [31] it has been observed that it is possible to clearly modify the S-T splitting by slightly shifting the QD position (by modifying the voltage on the depletion gates and trying to keep the QD dimensions more or less constant). The changing of S-T energy has been correlated to the dependence of the valley splitting from the electron position in the QW plane (valley-orbit coupling).

In [19], a DQD built in a silicon metal-oxide-semiconductor-system has been studied in transport, in the Pauli blockade regime, by driving the spin resonance using a stripline. By looking at the lifting of the blockade via ESR as a function of the applied magnetic field, it has been observed an anticrossing in the energy spectrum of the driven DQD, in coincidence of the Zeeman and valley energy splittings. The detected 60 MHz anticrossing splitting can be interpreted as a direct measure of spin-valley mixing. In fact, in

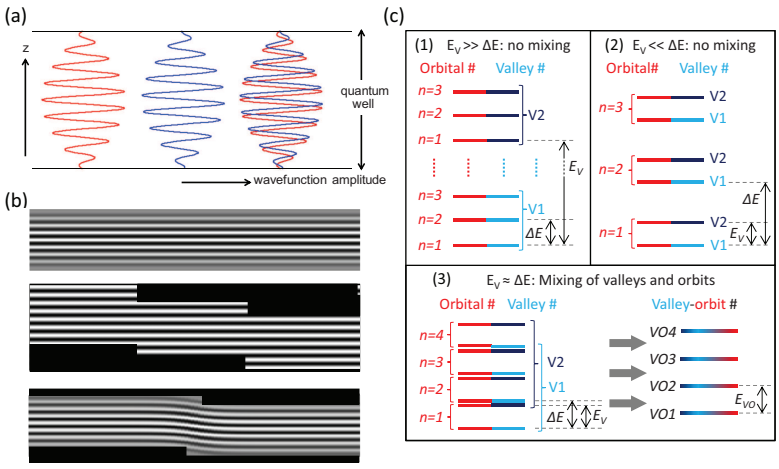

Figure 3.3: (a) Schematic representing an ideal Si QW with infinite SiGe barriers (no wavefunction penetration inside the SiGe layers) with the two lowest-energy valley states (from left to right: valley ground state, valley excited state, both superimposed). The valley degree of freedom results in fast oscillations of the wavefunctions but with similar envelopes. (b) Atomic steps at the Si/SiGe QW interface introduces valley-orbit coupling. (c) Interplay between orbital and valley degree of freedom. If the valley splitting and orbital level spacing are very different, the orbital and valley wavefucntions parts factorize and their eigenvalues represent good quantum numbers (no mixing). The valleys and orbits can also strongly hybridize in single-particle levels. Adapted from [9].

their model, the spin-valley coupling matrix element, resulting in an energy anticrossing in the spin-valley energy spectrum, is due to (i) spin-orbit coupling (SOC) in the 2DEG, which mixes spin and orbital states, and to (ii) the presence of interface disorder (so valley-orbit coupling) that generates a dipole moment between the 2 valley states [18] (see section 3.5). This can mediate the mixing between spin and valley states and also provides a channel to access higher valley states via ESR.

In the experiment described in Chapter 7, the same mechanism, reported above, allows also to address inter-valley transitions, driven by a Landau-Zener process, and a spin-valley resonance. The coherence properties of this inter-valley spin resonance are inferior compared to the intra-valley spin resonances. In fact, the inter-valley spin resonance does not show coherent spin oscillations and the estimated upper bound of T_2^* (extracted by the line width of the CW-peak) is ~100 ns (~ 10 times shorter compared to the intra-valley spin resonance). We ascribe this behavior to the difference of the spatial envelope of the wavefunction between the 2 driven valley-orbit states [18].

3.4. VALLEY INTERFERENCE AND VALLEY-ORBIT COUPLING

The wavefunction of an electron confined in a Si crystal varies spatially with fast oscillations over a length scale in correspondence of $\sim 2/|\mathbf{k}_v|$ (with $|\mathbf{k}_v| \sim 0.85 \cdot 2\pi/a = 2\pi/0.64$ nm^{-1}) [9], but with a phase difference between the 2 valley states. Since a large wave vector $2|\mathbf{k}_v|$ separates the two valleys, inter-valley coupling matrix elements are only appreciable for real-space interactions sharp in the z-direction. As reported in Fig. 3.3(a)

(representing the two valley eigenstates in an ideal infinite quantum well), the two valley eigenfunctions show very similar envelopes profiles. The energies of the 2 valleys states are different due to the different alignments of the phases of the fast oscillations with the interface of the quantum well. Due to disorder, the valley energy splitting will depend on the atomic-scale details at the interface [3, 17, 18], and will therefore change as a function of the position of the QD.

In fact, in order to build a confinement potential for the 2DEG, the Si is usually interfaced with either $Si_{1-x}Ge_x$ or SiO_2, which, even if technically well controlled, are far from atomically ordered. For example, in $Si_{1-x}Ge_x$ random alloy it is usually assumed that all atoms in the crystal alloy are separated from each other by an average bond length that is a function of the Ge content [35], resulting in a regularly ordered zincblende crystal. However, Si-Si, Ge-Ge, and Si-Ge bonds have different strengths, so different average interatomic distances; they move the respective bonding partners off the perfect zincblende lattice. There are 3 main critical unavoidable sources of alloy disorder to be considered: atom-type disorder, atom-position disorder, alloy concentration disorder [35–37]. In [36] the authors proposed that, even considering Ge-Si disordered random alloy barriers, the E_{VS} can be tuned over a wide energy range by realizing a Ge-Si layer by layer superlattice-like barrier. Furthermore, they identify a specific superlattice barrier with an optimum Ge-Si layering sequence that can provide, on average, an order of magnitude increment of the VS with respect to the normal alloy barrier (this prediction has not been experimentally explored yet).

Beside the alloy disorder, one other very important source of disorder is represented by random atomic steps at the Si/SiGe interface [17, 37]. Those locally modify the QW thickness and strongly couple the two valley states and the valley to the orbit degree, as schematically shown in Fig. 3.3(b). It is possible to interpret the suppression of valley splitting, due to the disorder at the Si-SiGe interface, as an interference effect caused by those multiple atomic steps experienced by the electron wavefunction confined in the Si QW. The phase of the fast valley oscillation of the electron wavefunction adjusts with respect the Si-SiGe interface and determines the valley energy splitting. Therefore, the presence of even a single atomic step at the heterostructure boundary can alter significantly this phase relation and consequently the valley splitting. As shown in Fig. 3.3(b), this kind of disorder realizes a coupling (known as 'valley-orbit coupling' [4]) between the phase of the fast valley-oscillations (along z) on the coordinates x and y (bottom panel) of the QW. For high step density at QW interface, the confined electron wavefunction will extend across multiple steps (center panel), suppressing the valley splitting [2, 3, 9].

The energy spectrum of the confined electron determines most of its dynamics properties. The presence of the valley degree of freedom makes the energy spectrum of electron confined in Si QD richer and more complicated. Different regimes can develop according to the relative magnitude of the orbital excitation energy ΔE_{orb} and valley energy splitting E_{VS} (for a $B_{ext} = 0 \Rightarrow \Delta E_z = 0$). The condition $\Delta E_{orb} > \Delta E_z$ is usually realized in a typical depletion QD built in semiconductors without the extra valley degree of freedom (such as GaAs). This also the case of a QD in Si with valley splitting E_{VS} much larger than the orbital level spacing ΔE_{orb}, for which electrons will occupy the different orbital states in the valley ground state V_1 (see Fig. 3.3(c-1)). On the contrary, if $\Delta E_{orb} > E_{VS}$,

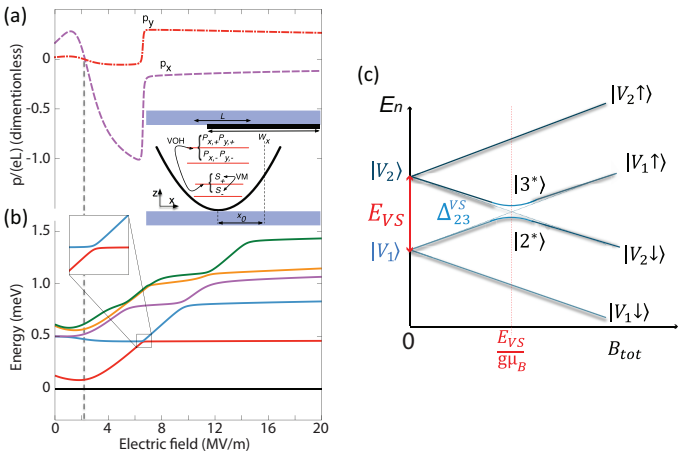

Figure 3.4: (a) Adapted from [18]. Calculation of low-lying energy eigenstates and electric dipole moments for a three-dimensional (3D) quantum dot in a quantum well with interface disorder, demonstrating that valley-orbit mixing induces a substantial dipole moment. The simulation geometry (inset) has a quantum well thickness of 10 nm and a barrier height of 150 meV. Disorder is introduced as a rectangular shaped bump (black region) in the quantum well barrier, with a height of a single atom. The top two curves show the components of the dipole moment **p** along the x (dashed) and y (dash-dotted) directions, as a function of the electric field applied along z. (b) Adapted from [18]. Energy spectrum of the lowest six energy levels in the quantum dot, measured relative to the ground state. (c) Schematic of energy level diagram of a spin-valley system (ground orbital state) as a function of the external magnetic field in plane.

the 2 valley states V_1 and V_2 present lower energy than the first excited orbital states, as shown in Fig. 3.3(c-2), and represent the first four states (2 valley states, each one with spin degeneracy) available for electrons. However, for $\Delta E_{orb} \sim E_{VS}$ (see Fig. 3.3(c-3)) orbit and valley degree of freedom are usually strongly hybridized [17].

Due to the omnipresence of the valley-orbit coupling in Si/SiGe QWs and the randomness of the disorder potential of the QW interface, it is more accurate to refer to the energy splitting between the lowest two QD eigenstates with the term 'ground state gap' instead of 'valley splitting' [17]. This is, in fact, the real energy difference relevant for quantum computing schemes. Due to valley-orbit coupling, the ground state gap cannot be strictly identified as purely orbital-like nor valley-like.
In the rest of this Chapter and Thesis we will, anyway, use indistinctly the term 'valley-orbit' splitting or, 'valley' splitting when referring to the 'ground state gap'.

3.5. VALLEY-ORBIT DIPOLE MOMENT

The dipole moment developed between the two valley-orbit states is a fundamental ingredient for most of the experimental evidences, reported in the previous section, in which the valley degree couples with electric field. For instance, [16] and [19] estimated a dipole moment of ~2-5 nm (bigger for lower valley splitting) and 15-55 nm (valley splitting ~85 μeV) respectively [4].

[4] the QD size in [16] is smaller than in [19]: $\Delta_{ST} \sim 8$ meV against a $\Delta_{ST} \sim 0.35$ meV.

In [18] the authors build a model considering the specific QD geometry shown in the inset of Fig. 3.4(a), consisting of a 2D parabolic confinement potential for the QD with an energy level spacing of ~ 0.5 meV (dot size of $L \approx 28.3$ nm). Furthermore, they consider the presence of a bump in the Si QW in the QD region (see Fig. 3.4(a) inset). The height of the bump is taken to be a single atom, the quantum well width and energy confinement barrier height are 10 nm and 150 meV (~ 25% Ge content), the lateral dimensions of the bump perturbation has been chosen to be of order of L and $W_x = 2L$ and $W_y = 4L$.

The results of this single-dot calculations are reproduced in Fig. 3.4(a) as a function of the perpendicular electric field. The p_x and p_y curves at the top of the plot, are the x and y components of the electric dipole moment $\mathbf{p} = e\int d^3\mathbf{r}(\left|\psi_{VO2}(\mathbf{r})\right|^2 - \left|\psi_{VO1}(\mathbf{r})\right|^2)\mathbf{r}$, where ψ_{VOi} are the spatial wavefunction of the $i-$valley-orbit state[5]. For the device specifications used in this simulation, the dipole moment is typically comparable to eL. Fig. 3.4(b) reports the energies of the lowest six energy eigenstates of the QD. The disorder potential can introduce mixing between states in the same valley doublet which gives rise to the energy anticrossing highlighted in the inset of Fig. 3.4(b). In correspondence of those valley-mixing anticrossings the dipole moments are strongly suppressed, as shown in Fig. 3.4(a), although its magnitude is never zero. In the limit of large orbital energy spacing, ΔE_{orb}, the dipole moment scales approximately as $1/\Delta E_{orb}$.

The inter-valley dipole moment represents a direct channel for the electric field (in the form of either driving MW $E_{a.c.}$ either charge or electric noise (phonons or electronic noise)) to get coupled with the valley-orbit states, enabling electrical driving and charge noise dephasing. Two methods can be applied that help to suppress the unwanted dipole moment: realizing smaller QDs (higher confinement means also less extension across atomic steps at the Si-SiGe interface) and working at electric fields corresponding to the valley-mixing anticrossing (this last condition can be used only if the valley-orbit energy spectrum is precisely known). This model is also considered in Chapter 7 to estimate the variation of E_{VS} as a function of the position of the confined electron across a single atomic step at the Si/SiGe interface. This results into a change of the valley-orbit energy splitting, reaching a minimum when the wave function is centered around the atomic step.

3.6. SPIN-VALLEY MIXING

As showed by experiments, the valley and spin degree of freedom can be coupled. The coupling mechanism is a second order process that results from the combination of the valley-orbit coupling (due to the presence of the interface disorder) and of the spin-orbit coupling. The spin-valley mixing process has been studied by [16, 20] in the context of the spin relaxation mechanism for electrons confined in Si QDs. A similar study has been realized in [19], applied to the S-T mixing mechanism in the Pauli blockade con-

[5] For a charge qubit, **p** is in correspondence of the DQD dipole axis. For an orbital qubit, **p** represents the lateral separation of the center of mass of the two orbital states. For a pure valley qubit, **p** presents a vertical (along z) component, in correspondence of the separation of the even and odd states (~0.16 nm). For a complicated system like a valley-orbit qubit with interface disorder, **p** will have lateral and vertical components, with the lateral component being usually much larger than the vertical one. In this last case the exact magnitude and orientation of **p** will depend on the specifics of the interface disorder; a reasonable guess would be p ~0.5-5 nm.

figuration. They found that the mixing between spin and valley degrees is particularly effective when the Zeeman energy E_z is comparable with the valley splitting E_{VS} (at the anticrossing in Fig. 3.4(c)). We will also refer to this model in the Chapter 7, where we report evidence of inter-valley spin resonance. Here we provide a simple model to take into account this coupling.

The model presented in this section refers partially to the work reported in [20, 47]. As reported in [20, 47], we can consider a single electron confined in a gate-defined quantum dot in Si (growth direction [001]). If the intra-valley orbital energy spacing, due to the lateral QD confinement, is sufficiently strong ($\sim 1-0.1$ meV), we can neglect the intra-valley excitations and focus on the spin-valley (inter-valley) physics, especially in the condition $E_z \sim E_{VS}$. In this limit, the spectrum and the dynamics of the system can be described considering four-levels, the 2 spin states and the 2 valleys states (in the orbital ground state), reported in Fig. 3.4(c).
Defining the valley-orbit ground $|V_1\rangle$ and excited $|V_2\rangle$ states, we can denote those 4 states with $|V_1\downarrow\rangle$, $|V_1\uparrow\rangle$, $|V_2\downarrow\rangle$, $|V_2\uparrow\rangle$. Confining the evolution of the electron in this Hilbert space (neglecting the leakage into higher orbital sectors), we can write the following Hamiltonian [20]:

$$H = \sum_i \frac{\epsilon_i}{2}|i\rangle\langle i| + \left[\frac{\Delta_{23}}{2}|V_1\uparrow\rangle\langle V_2\downarrow| + \frac{\Delta_{14}}{2}|V_1\downarrow\rangle\langle V_2\uparrow|\right]. \tag{3.1}$$

The first term in the Hamiltonian describes the non interacting spin and valley physics for the 4 product states introduced above, in the absence of the spin-orbit interaction. $\epsilon_i/2$ ($i = 1,2,3,4$) represent the energies of those product states (Fig. 3.4(c)):

$$\begin{aligned}\epsilon_4 &= -\epsilon_1 = E_{VS} + g\mu_B B,\\ \epsilon_3 &= -\epsilon_2 = E_{VS} - g\mu_B B.\end{aligned} \tag{3.2}$$

The other 2 terms in the Hamiltonian represent the spin-valley mixing mediated by an effective SO interaction. The spin-valley mixing energy is given by the terms

$$\Delta_{23} = 2\langle V_1\uparrow|H_{SO}|V_2\downarrow\rangle, \tag{3.3}$$

$$\Delta_{14} = 2\langle V_1\downarrow|H_{SO}|V_2\uparrow\rangle. \tag{3.4}$$

If we choose x and y axis along [110] and [-100] crystal directions (in the 2DEG plane), we can write a generic SO-interaction as

$$H_{SO} = \alpha_- p_y\sigma_x + \alpha_+ p_x\sigma_y, \tag{3.5}$$

where $\alpha_\pm = (\alpha_D \pm \alpha_R)$ represents the SO-interaction strength given by Dresselhaus (D) and Rashba (R) SO interplay (see 3.7.3 for a discussion about D and R SOI and their interplay)[6].

As we can see from Fig. 3.4(c), the states $|V_1\downarrow\rangle$ and $|V_2\uparrow\rangle$ are always well separated in energy so the contribution of Δ_{14} mixing can be neglected. Conversely, this is not valid

[6] In the presence of a magnetic field gradient (as in our experiment), we should add to the Hamiltonian an extra term $H_{SL} = -g\mu_B b_{SL}^{x,y}(x,y)\sigma_z$, where $b_{SL}^{x,y}$ represents the magnetic field gradient along in plane directions (x,y) and σ_z is the z-Pauli matrix operating on the spin sector.

for the states $|V_1\uparrow\rangle$ and $|V_2\downarrow\rangle$, which will be mixed by the spin-valley coupling term Δ_{23}, particularly close to $E_z \sim E_{VS}$, where the hybridization is maximal and an energy anticrossic of magnitude $2\Delta_{23}$ will develop.
Writing $\Delta_{23} = \Delta_1 + i\Delta_2$, we can get a more explicit expression for the new eigenstates:

$$|2\rangle^* = -sin(\gamma/2)e^{-i\delta/2}|V_2\downarrow\rangle + cos(\gamma/2)e^{i\delta/2}|V_1\uparrow\rangle, \tag{3.6}$$

$$|3\rangle^* = cos(\gamma/2)e^{-i\delta/2}|V_2\downarrow\rangle + sin(\gamma/2)e^{i\delta/2}|V_1\uparrow\rangle, \tag{3.7}$$

where we used $\gamma = arctan[(\Delta_1^2 + \Delta_2^2)/\epsilon_3]$ and $\delta = arctan(\Delta_2/\Delta_1)$.
The energy splitting between the new eigenstates $|2\rangle^*$ and $|3\rangle^*$ will be $\epsilon_3^* = \sqrt{\epsilon_3^2 + \Delta^2}$, with $\Delta^2 = \Delta_1^2 + \Delta_2^2$.

The spin valley mixing matrix element Δ_{23} can also present a dependence as a function of the magnetic field orientation, due to the SO anisotropy introduced by the angular dependence of the D and R SO fields [20, 48].

3.7. ELECTRON SPIN PHYSICS: COMPARISON BETWEEN GAAS AND SI

In this section we will focus on some physical properties of Si and GaAs quantum dots and on the main differences between them in the context of electron spin confinement and control, relaxation and dephasing for spin qubit.

Table 3.2

Property	(nat.) Si/SiGe	GaAs/AlGaAs
Crystal structure	Diamond	Zincblende
Band gap (eV)	(Indirect) 1.12	(Direct) 1.42
Valley degeneracy	2	1
Max alloy lattice mismatch	4.7%	0.05%
Effective mass (m_0)	0.19 ($m_{//}$); 0.98 ($m_\perp$)	0.067
Typical QD Δ_{orb}	~0.5 meV	~5 meV
g-factor	~+2	-0.44
2DEG mobility (cm^2/Vs)	$\sim 10^5 - 10^4$	$\sim 10^6$
Dielectric constant	11.7	12.9
Spin-Orbit (m/s)	45-60(R) [16, 19]	230 (R); 300 (D)
T_1 (s@1T)	~1	~0.01
Fraction nuclear spin	4.7%	100%
max B_{nucl} (T)	0.002	5
HF fluctuation (σ_{HF} mT)	0.008	1
T_2^*	$\sim 1\ \mu s$	~ 10 ns
T_2^{echo}(single spin)	$\sim 70\ \mu s$ [21]	$\sim 1\ \mu s$

3.7.1. HYPERFINE INTERACTION

The key motivation of the recent interest in developing and optimizing single electron confinement in Si arises from the possibility to drastically reduce, or even completely

eliminate, the nuclear spin environment of the electron spin qubits. This important achievement has been recently demonstrated by [43] and [49] for a single electron spin[7], making use of an accumulation MOS-QD and of a P-atom respectively as confinement system, in an isotopically purified Si epilayer [50]. This semiconductor constitutes the ideal hosting system for the single electron spin, known as 'spin or silicon vacuum' [52]. In this case the electron spin, being almost unperturbed by the nuclear spin fluctuations of hosting environment, can keep the coherence of a superposition state for hundreds of μs (T_2^* of 120 μs [43] and of 240 μs [49]), to compare with the T_2^* of ~ 350 ns and ~ 1 μs measured in natural Si QW [5, 53]. Furthermore, the removal of the hyperfine (HF) mediated dephasing allows to get electron spin control fidelity of 99.5 % [43], far beyond those obtained before in GaAs systems.

The main HF field contribution between the nuclear and the electron spin ($\mathbf{S}$) comes from the contact term, which has the form

$$H_{HF} \propto \mu_0 g_0 \mu_B \gamma_N \hbar \sum_{i=1}^{N} \left|\psi(\mathbf{r}_i)\right|^2 \mathbf{I}_i \bullet \mathbf{S}, \tag{3.8}$$

where g_0 is the free electron g-factor, γ_N the nuclear gyromagnetic ratio, $\mathbf{I}_i$ represents the nuclear spin at position $\mathbf{r}_i$ in the crystal lattice and $|\psi(\mathbf{r}_i)|^2$ denotes the magnitude of the electron wave function at the position of the nucleus [15]. It is possible to rewrite the previous equation as

$$H_{HF} \propto \sum_{i=1}^{N} A_i \mathbf{I}_i \bullet \mathbf{S} \equiv g\mu_B \mathbf{B}_N \mathbf{S}, \tag{3.9}$$

expression which defines $\mathbf{B}_N$, the so called Overhauser field, which can be approximated as a random classical field acting on the electron spin.

The nuclear gyromagnetic factor is ~1000 times smaller than the electron one; then, for the typical magnetic field used in the experiment the Zeeman splitting of the nuclear spin is of the order of ~neV, so well below the typical $k_B T_{el}$ of cryogenic environment (~ μeV). This implies, according to the Boltzmann distribution, that just a small fraction of the nuclei is polarized; the polarization direction is not stationary but fluctuates in time, resulting in a Gaussian distribution of the HF field in all of the 3 spatial directions, with spread $\sigma_{HF} \propto N^{-1/2}$ (N the number of the nuclei that overlap with the electron wavefunction). As a result, confining an electron into a bigger QD will reduce, overall, the magnitude of σ_{HF}, and therefore it results in longer T_2^*. This random field makes the Larmor frequency of a single electron spin ($\omega_L = E_z/\hbar$) fluctuate in time during the experiment. Considering, for example, a Rabi oscillation experiment [5], the typical time required for single shot data acquisition is of the order of ms and usually statistics (for a specific MW burst time) are averaged over multiple single shot read out cycles. This implies that the measurement of spin excited state probability for each data point is effectively an averaged measurement on a time-ensemble of the different HF field configurations; this results into a Gaussian damping over time of the Rabi oscillations (see Chapter 5 for more formal relations).

During the last 10 years, there has been an extensive experimental study of spin qubits realized in few-electron system hosted in GaAs/AlGaAs heterostructures, due to

[7] It was already known for ensemble P-systems [51].

their high quality and relatively easy fabrication process. But all the stable isotopes of common III-V semiconductor elements carry a nonzero nuclear spin. As explained above, those nuclear spins interact, via hyperfine interaction, with the electron spin and constitute the main noise source which dramatically limits its intrinsic coherence time (~ 10 ns) [15]. On the other hand, the most commonly occurring isotopes of group IV elements C, Si, and Ge all have zero nuclear spin and, furthermore, they can also be used to build a semiconductor environment, necessary to electrostatically confine the electron. The silicon isotope ^{29}Si (the only naturally occurring isotope with non-zero spin) represents only 4.7% of total natural amount of Si atoms; furthermore, it has spin 1/2, that is smaller than the spin of Ga and As isotopes, 5/2.

In [54, 55] it is reported an estimation for the dephasing time considering a QD (with $2r \sim 50$ nm, containing ~10^5 nuclei) in GaAs and Si

$$T_2^* = (10^{11}\hbar)/(4.3eV \bullet \sqrt{10^5 s}),$$

with s representing the atomic fraction of ^{29}Si. The estimated T_2^* is of the order ~ 7 ns (total HFI ~ 90 μeV ≃ 3.6 T), 0.22 μs (total HFI ~ 200 neV ≃ 2 mT) and 5 μs (total HFI ~ 0.4 neV ≃ 4 μT) respectively for GaAs, natural and 0.01% isotopically purified Si systems. With three orders of magnitude difference in the total HFI, the variance of the random hyperfine field and the intrinsic T_2^* in GaAs and natural Si differs of about two orders of magnitudes, as we experimentally confirmed in [5] (see Chapter 5), measuring a $T_2^* \sim 1$ μs (in a QD of ~50 nm diameter).

It is worth mentioning one fundamental difference between P-atoms, MOS Si/SiO_2 confining systems and depletion QDs in Si/SiGe heterostructures. As pointed out in [56], in the latter system, the electron wavefuncion is in close proximity and partially overlaps with the Ge atoms randomly distributed in the SiGe alloy of the buffer (mainly the top one, due to the high accumulation electric field which pulls up the electron). Almost 8% of the natural occurring atoms of Ge carry nonzero nuclear spin. For the 30% Ge content (the typical value in our heterostructures) the maximal estimated electron wavefucntion penetration into the SiGe barrier is of the order of 5% (for high pulling electric field) and this will limits the T_2^{echo} around 3 ms. In the same work, it has been also predicted that T_2 will increase rapidly as a function of the Ge enrichment level; then a ^{73}Ge concentration lower than 200 ppm will be already sufficient to get a T_2^{echo} limited by decoherence processes taking place in the Si QW.

3.7.2. EFFECTIVE MASS

The effective mass of electrons in Si is higher than in GaAs (~ $3m^*_{GaAs}$. with $m^*_{GaAs} \sim 0.067\ m_0$) and highly anisotropic, having the value 0.92 m_0 and 0.19 m_0, with m_0 the free electron mass, in the direction perpendicular and parallel to the Bloch vector respectively [1]. In a SiGe QW at low temperatures the electrons are tightly confined in the direction perpendicular to the heterostructure growth direction (z). The in-plane effective mass is ~0.19 m_0. This is the effective mass responsible for the transport or orbital spectral properties of electron hosted in Si at low temperature. In fact, to first order, the electron tunnelling rate across a tunnel barrier is proportional to $exp(-m^* E_B)$, where, for depletion gate technology, the height of the tunnel barrier E_B is proportional to the applied gate voltages. Therefore, the higher effective electron mass also influences

the electron tunnel rate, which in Si becomes more susceptible to changes in gate voltage and is, in general, lower (compared to GaAs) [57]. Furthermore, the higher effective mass in silicon compared to GaAs also implies a confinement potential a factor $\sim 1/\sqrt{3}$ tighter (compared to that of the GaAs QD) to achieve a comparable orbital confinement energy ($\Delta_{orb} \propto \hbar^2/(m^* r_{dot}^2)$). As a result, in Si QD is very difficult to approach the 'few electrons' regime by keeping all the tunnel barriers transparent enough; a charge sensor is very often essential[8].

3.7.3. SPIN-ORBIT COUPLING

The dynamics of a single electron moving in a electrical potential **V**, is captured by the Dirac equation [60]. In the non-relativistic approximation, a correction term representing the spin-orbit interaction (SOI) is introduced in the Hamiltonian, with expression

$$H_{SO} = \frac{-\hbar\vec{\sigma} \bullet \mathbf{p} \times \bigtriangledown \mathbf{V}}{4m^2c^2}, \tag{3.10}$$

where $\sigma_{x,y,z}$ represent the Pauli matrices and **p** the momentum operator [60].
In general, any electric field arising from some asymmetries in the electric potential is felt as an effective magnetic field by the moving electron on its reference frame.
Considering a generic Coulomb electrostatic potential with expression $V(r) = -Ze^2/r$, where Z is the atomic number of the nucleus, it is possible to evaluate [60] that the SO correction scales as Z^4, which directly suggests that materials composed by high Z-atoms are candidates to present a strong SO interaction.

In general for 2DEGs, the SOI can be generated by lack of inversion symmetries. Those can be related to asymmetries of the crystal unit cell of the hosting semiconductor (bulk inversion asymmetry, Dresselhaus (D)) [58], or to electric fields developed at the interface between two different semiconductor, typically used in heterostructure band offset engineering (structural inversion asymmetry, Rashba (R)) or due to the applied electric field to top or bottom gates; also lateral asymmetry in 2DEG, generated by the asymmetric voltage applied to depletion gates [59], can induce a consistent SO field.
Intuitively, the spin of an electron moving[9] in the electric field, generated by one of those mechanisms listed above, will feel an effective magnetic field $\mathbf{B}_{SO}$ and start to precess around it (in the reference frame of the moving electron).

In order to get a more explicit expression, we can consider a 2DEG confined at the interface between GaAs/AlGaAs. The bulk GaAs crystal presents a zincblende structure that, by breaking the bulk inversion asymmetry, gives rise to a D-SO-correction to the free electron Hamiltonian that can be expressed in the Kane model [60, 61] as:

$$H_D = \frac{2\Delta_{SO}}{3\sqrt{2mE_g}m_{cv}E_g}\vec{\sigma} \bullet \vec{\kappa}, \tag{3.11}$$

where Δ_{SO} is the SO-splitting energy of the conduction band, E_g is the band gap, $\kappa_x =$

[8] This directly translates into a more demanding electron-beam fabrication resolution for the depletion QDs, in terms of surface metallic gates width and separation, in order to shrink further their dimensions.

[9] which for free electron means really moving with momentum **p** and for electrons in the ground orbital state of a QDs means getting the coupling with higher orbital excited states, with opposite orbital wavefunction parity.

$p_x(p_y^2 - p_z^2)$ and m_{cv} are some parameters coming from the Kane model [60][10].
For a 2D-system, the Hamiltonian can be further reduced due to the strong confinement along the z-axis (the final form of the D-SOI strongly depends on the specific grown direction). The effective D-SO correction acting on a free 2DEG electron is obtained integrating along the growth direction [001] ($\langle p_z \rangle = 0$, $\langle p_z^2 \rangle \neq 0$):

$$H_D^{2D} = \beta(p_y\sigma_y - p_x\sigma_x), \tag{3.12}$$

where $\beta = \frac{2}{3}\langle p_z^2 \rangle \frac{\Delta_{SO}}{\sqrt{2mE_g m_{cv} E_g}}$ [61].
Notice that the dependence of β on $\langle p_z^2 \rangle$ means that this prefactor can be also partially influenced by a top gate voltage that can modify the confinement along z or by changing the QW confining properties [60]. Furthermore, besides linear SO terms as a function of momentum, in zincblende structures with (001) grown direction, terms cubic in momentum are possible (they derive from the D SOI) but they can be usually neglected.

In order to get a intuition for the Rashba SO term we can directly consider the generic expression for a relativistic SO correction of the energy of a free electron in the presence of an electric potential **V**.

$$H_R = \frac{\hbar}{4m^2c^2} \nabla \mathbf{V} \bullet (\vec{\sigma} \times \mathbf{p}) = \alpha \bullet (\vec{\sigma} \times \mathbf{p}). \tag{3.13}$$

For an electron confined in a 2DEG (built in a QW, at the interface between 2 semiconductors, or between a semiconductor and a dielectric) the Rashba constant α results by the band structure of the hosting semiconductor and electric field perpendicular to the 2DEG.
Considering a confinement along the z-(001)-direction we can rewrite H_R as

$$H_R^{2D} = \alpha(p_y\sigma_x - p_x\sigma_y), \tag{3.14}$$

where the coefficient α is tunable in strength by the external gate voltage perpendicular to the plane of the two-dimensional electron gas.
It is worth noting that H_D and H_R are equivalent under the unitary transformation $\sigma_{x(y)} \rightarrow \sigma_{y(x)}$ and $\sigma_z \rightarrow -\sigma_z$, suggesting that the spectral properties of a conduction band electron subject to those SO interactions are the same [62].

The combined spin-orbit Hamiltonian for a free electron confined in a 2DEG can be written as

$$H_{SO} = \alpha(\sigma_x p_y - \sigma_y p_x) + \beta(\sigma_x p_x - \sigma_y p_y). \tag{3.15}$$

We can re-write the equation above using the transformations (45 degree axis rotation) $p_{x^*} = \frac{1}{\sqrt{2}}p_x - \frac{1}{\sqrt{2}}p_y$, $p_{y^*} = \frac{1}{\sqrt{2}}p_x + \frac{1}{\sqrt{2}}p_y$, $\sigma_{x^*} = \frac{1}{\sqrt{2}}\sigma_x - \frac{1}{\sqrt{2}}\sigma_y$ and $\sigma_{y^*} = \frac{1}{\sqrt{2}}\sigma_x + \frac{1}{\sqrt{2}}\sigma_y$ as

$$H_{SO} = (\alpha - \beta)p_{y^*}\sigma_{x^*} - (\alpha + \beta)p_{x^*}\sigma_{y^*}. \tag{3.16}$$

The relative orientations of the R and D SO-field are, in general, different (see Chapter 8). More specifically, the SOI Hamiltonians H_D and H_R (eq. 3.12 and eq. 3.14) can

[10] Here we assume the definition of the x and y directions along the crystal axises [100] and [010] respectively.

be viewed as a result of an effective B field ($\mathbf{B}_{SO}$), whose amplitude and direction depends on the electron momentum. We can define $\mathbf{B}^R_{SO} = (\alpha/g\mu_B)(-P_y, P_x)$ and $\mathbf{B}^D_{SO} = (\beta/g\mu_B)(-P_x, P_y)$, with g the electron g-factor, μ_B the Bohr magneton and $\mathbf{P}$ the electron kinematic momentum. For the R term, the effective SO field $\mathbf{B}_{SO}$ is always perpendicular to the momentum. For the D term the $\mathbf{B}_{SO}$ is aligned with the momentum for the motion along [010] but is opposite for the [100] crystal directions (see Chapter 8)[11]. A convenient way to characterize the magnitude of this B_{SO} is introducing the SO length, defined as the distance associated with a π rotation of the spin subject to the action of $\mathbf{B}_{SO}$ (typically 1-10 μm in GaAs), $l^{SO}_{\alpha,\beta} = \hbar^2/(2m\alpha, \beta)$. The total SOI comes from the vectorial sum of those two contributions, and is a function of the in plane momentum direction. In many systems those 2 anisotropic SO contributions can interfere, and the result of this interplay is particularly visible if the magnitude of R and D fields are comparable (see Chapter 8) because they can completely add or cancel for specific in-plane directions [48].

The SO interaction mediates a coupling between different spin states by admixing the Zeeman-split ground orbital-ground spin state ($|g\uparrow\rangle$, referring to GaAs) with excited orbital states (presenting a different charge parity, so a dipole moment) with opposite spin ($|e\downarrow\rangle$). The magnitude of this coupling can be expressed as

$$\epsilon_+ = \frac{\langle e\downarrow|H_{SO}|g\uparrow\rangle}{E_{orb}+E_z}, \quad \epsilon_- = \frac{\langle e\uparrow|H_{SO}|g\downarrow\rangle}{E_{orb}-E_z}, \tag{3.17}$$

where E_{orb} represents the energy difference between $|g\uparrow\rangle$ and $|e\downarrow\rangle$. This expression is valid for $E_{orb} > E_z$ and shows that the degree of admixing between the two opposite spin states scales linearly with the strength of the SOI and it is inversely proportional to the orbital energy splitting. As a result, in the presence of SOI each spin state is no longer a pure spin state. Therefore, when we will refer to a state as spin down or spin up we just refer to the majority component of the spinor part of the electron wavefunction.
Spin-orbit coupling renormalizes the electronic g-factor in semiconductors [63]; this explains the difference in g-factor between silicon (1.99 [5], very close to the free-electron value of 2.002), and GaAs (-0.44 [15]). Notice also the difference in the sign: in Si, the excited spin state has a spin aligned with the magnetic field ($\uparrow$) and the ground state is anti-parallel ($\downarrow$); in GaAs, this is reversed because the g-factor is negative.

Si, Ge and SiGe relaxed alloy crystals present a cubic structure that preserves inversion symmetry. Therefore, the Dresselhaus SO contribution is expected to be negligible (but for the biaxial strain introduced in the Si QW this is not valid anymore) for electrons confined in Si systems. However, it has been shown [20, 64, 65] that the breaking of inversion symmetry by the interfaces can give rise to a Dresselhaus-like term. Also the presence of the Ge into the lattice of the SiGe alloy breaks the inversion symmetry and increases the SOI (also due to the higher atomic number of Ge). In QDs realized in

[11] For spin qubit design optimization it is very important to understand the effects of the SO anisotropy in the plane of heterostructure and try to benefit from it. There are, for example situations where it is useful to get long relaxation time or, in the contrary, one would like to make the relaxation process as fast as possible, for example in order to initialize the spin at the beginning of a pulse protocol. So the typical goal during the device fabrication would be to choose an optimum gate geometry respect to the crystal orientation in order to maximize T_1 (minimize the SOI) and maximize also the B_{SO} for EDSR [48] (maximize the SOI in the direction of the manipulating a.c. electric field).

SiGe/Si/SiGe heterostructures and in MOSFET-type systems, either by modulation doping or by a top-gate induced electric field QDs, there is a structural inversion asymmetry that comes from the fact that the symmetry $z \leftrightarrow -z$ is broken. The magnitude of the Rashba coefficient in a Si 2DEG is much smaller than for a GaAs 2DEG ($\alpha_{GaAs} \sim 230$ m/s [60] against $\alpha_{Si} \sim 6$ m/s [20, 66–68]. Actually, in [16] and [19] authors make use of a SO parameter of magnitude ~ 50 m/s, remarkable large due to the presence of a large perpendicular accumulation electric field ($\sim 10^7$ V/m).

3.7.4. SPIN-ORBIT INDUCED SPIN RELAXATION

In lateral quantum dots hosted in a semiconducture structure, the effect of SOI causes relaxation of the spin excited state, splitted in energy from the ground state due to the presence of a static magnetic field. For an electron confined in a QD, the SOI does not directly couple Zeeman splitted sublevels but it couples states with different orbital and spin (see eq. 3.17).Together with a generic electric field fluctuation, that can arise from external electrical noise or from phonons, the SO mediated spin mixture opens a spin decay channel [70].

The interplay of R and D SO coupling can give rise to an anisotropy in the direction and magnitude of the total $\mathbf{B}_{SO}$ and of the spin relaxation rate. However, another possible source of anisotropy can come from the dot confinement potential shape itself (if not circular). In fact, as it has been shown in [69], the shape of the QD, and accordingly the confinement potential, plays an important role in the electron spin relaxation time. The degree of SOI mediated mixing between spin opposite states scales $\propto 1/E_{orb}^4$ [70]. The more elongated is the dot, the lower the energy of the first excited state, the higher the coupling to the ground state and the faster the relaxation rate. As we will explore in Chapter 8, both of anisotropy mechanisms should be considered together to obtain a complete picture of the final spin relaxation anisotropy.

Usually, phonons dominate spin relaxation. In polar crystals, such as GaAs, the distortion of the lattice is associated also to a large internal electric field (piezoelectric interaction). Silicon is a non-polar and centrosymmetric crystal so it has no piezoelectric phonons, and the main scattering processes are dominated by deformational phonons that are present in every kind of crystal. For this reason, the spin-flip rate of electron confined in Si QDs is proportional to the 7th power of the magnetic field [20], different from the 5th power dependence for GaAs QDs [20]. In GaAs we find also a contribution of acoustic phonons which gives a 7th power dependence, but this is completely masked by the interaction with piezoelectric phonons, much more efficient in mediating the relaxation process. Quantitatively, the spin relaxation rates in Si are typically two orders of magnitude smaller than in GaAs, due to the absence of the piezoelectric phonon potential and generally weaker spin-orbit interactions. For the same reason, the phonon mediated back-action of a remote charge sensor on a qubit, which has been observed in GaAs based QDs [71, 72], is expected to be much weaker in Si.

3.7.5. ESR AND MAGNETIC FIELD GRADIENT AS AN ARTIFICIAL SO

As schematically reported in Fig. 3.5(a), the majority of the implemented spin resonance schemes relies on the application of an external static magnetic field (B_{ext}), which removes the initial spin degeneracy, and on the application of an a.c. magnetic field ($B_{a.c.}$),

perpendicular to the static field. When $B_{a.c.}$ is applied at the Larmor frequency $\omega_{Larmor} = \Delta E_z/\hbar$ it can coherently drive spin oscillations (Rabi oscillations) in case $f_{Rabi} \geq 1/T_2^*$, with T_2^* the dephasing time of the electron spin. For a confined single electron spin in semiconductors, many different ways to implement ESR have been proposed and demonstrated [23, 73, 76–78][12]. Fig. 3.5 summarizes them, except for the HF mediated ESR.

The first demonstration of single electron spin resonance has been realized in Delft by F. Koppens [73] and makes use of a stripline antenna for the generation of the driving $B_{a.c.}$ field (see Fig. 3.5(b)). The same technique has been recently optimized in order to achieve MW driving up to 40 GHz, by the Morello group [74]. If the magnitude of this oscillating current is high enough (i.e., the antenna is well matched in order to reduce reflection loss) and the stripline has been fabricated close enough to the confining QD, the magnitude of $B_{a.c.}$ will be high enough to drive fast Rabi oscillations ($f_{Rabi} \propto B_{a.c.}$). Although it is quite straightforward to implement, the use of the stripline antenna may present some limitations looking towards scalable systems. In fact, considering an array of QDs (or atom-impurities), in an ideal situation we would like to perform a fast and high fidelity manipulation of just one single spin, leaving the rest unaffected. A single stripline cannot achieve enough addressability and driving of all the electrons with high Rabi frequency. The necessary integration of multiple striplines on the same device can be extremely challenging because an Au stripline is quite bulky compared to the the QD (~300 nm thick and 300 nm wide in the closest point to the QD [75]).
Furthermore, another limitation can be related to the heating of the electron reservoirs generated by dissipation in the stripline, usually made out of gold (though it could be also realized by high T_c superconducting thin films). In [75] we explore the use of a d.c. current applied to the antenna for generating local, tunable magnetic field gradients at the position of the dots. A magnetic field gradient of around 1μT/nm can be achievable with a 2 mA d.c. current through the antenna. This gradient is necessary to detect ESR using transport measurements in the spin blockade regime. Based on numerical simulations of the magnetic field profile generated by the antenna, we estimate that a 4 mA d.c. current produces a ~40 μT field difference between two dots that are 30 nm apart and separated from the antenna by 200 nm (the lateral distance between the center of the two dots and the end of the on-chip antenna). The d.c. current that can be applied is ultimately limited by Joule heating[13].

As clarified above, the technological limitation relevant for single electron spin manipulation consists in the difficulty in generating localized $B_{a.c.}$, possible by using antennas (stripline, coplanar waveguide,...). On the contrary, it is quite easy to generate a local high frequency electric field by using the same surface depletion gates technology that already defines the QD confinement potential.
However, the electric field does not couple directly to the electron spin. This is the main reason why the electron spin confined in semiconductor environment preserves long relaxation and coherence times, despite the many electrical noise sources (piezoelectric or deformation potential phonons, charge noise, electrical noise from control electron-

[12] The mechanism reported in [78] is not included in the following overview because not relevant in the silicon environment.
[13] This increases the temperature of the electron reservoirs.

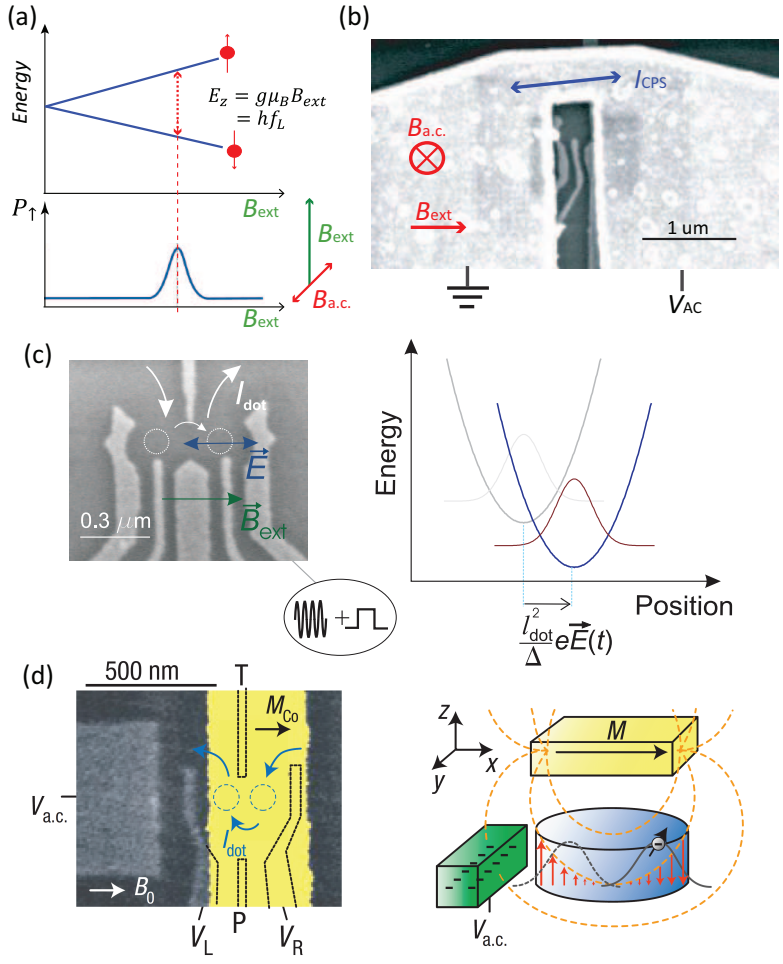

Figure 3.5: (a) Energy level schematic for a single spin 1/2 as a function of the static external magnetic field B_{ext}. Bottom: schematic of the spin resonance; the line width of the resonance gives information on the magnetic field noise. (b) SEM picture of the device used in [73, 76]; the stripline is fabricated on top of the DQD realized in GaAs/AlGaAs. (c) Left: SEM picture of a similar DQD device used in [73] before the stripline deposition. Right: schematic of the shifting of the center of mass of the electron wavefunction determined by the electric field $E(t)$ (adapted from [76]). (d) Left: SEM picture of the device used in [23]. Right: schematic of the stray magnetic field generated by the micromagnet on the electron wavefunction; its center of mass can be shifted by the oscillating voltage $V_{a.c.}$ applied on a gate capacitively coupled to the confined electron. Adapted from [23].

ics,...) [15]. Neverthless, as shown in the previous section, in systems where some inversion symmetry is broken, SO-interaction appears. Thanks to this coupling mechanism an a.c. electric field, applied to the confined electron, can be converted into an effective a.c. magnetic field that, in general, provides some driving component perpendicular to the static external magnetic field (usually the case for R and D SO fields). If applied at the Larmor frequency, this allows an efficient spin rotation driving process by purely electrical means (EDSR).

The principle of EDSR has been demonstrated, for the first time, for a single electron spin confined in GaAs/AlGaAs, in Delft by K. Nowack (see Fig. 3.5(c)) [76] . The effective $B_{a.c.}^{SO}$ driving the spin Rabi oscillations is given by

$$B_{a.c.}^{SO} = \frac{2eE_{a.c.}l_{orb}^2|B_{ext}|}{\Delta E_{orb} l_{SO}}, \tag{3.18}$$

where ΔE_{orb} and $l_{orb} \propto (\Delta E_{orb})^{-1/2}$ are the quantum dot confinement energy and orbital wavefunction spread and l_{SO} is the effective SO length. Due to the SO anisotropy, the magnitude of the $B_{a.c.}^{SO}$ should also depend on the relative orientation of B_{ext} and $E_{a.c.}$ (the latter defined by the gate geometry). SO-driven spin qubits have been also realized in DQD in III-V nanowires [77], for which the SOI has been shown to be almost 20 times stronger than for GaAs according to the smaller band gap. For InSb systems a record ~100 MHz Rabi frequency has been demonstrated [79].

The efficiency in the spin driving using SOI relies on the magnitude of the SO coupling. As already reported in the previous section, in silicon 2DEGs, the natural SO interaction is almost 1-2 orders of magnitude smaller than in GaAs. This, therefore, makes the application of SO mediated EDSR scheme extremely inefficient[14].

A solution to this issue has been suggested by Tokura in [22], realized for the first time experimentally in [23] and consists in creating an artificial coupling between the local electron Zeeman splitting and the electron position, via a nonzero magnetic field gradient (see Fig. 3.5(d) adapted from [23]). This can be interpreted as an 'artificial' SO field. The ESR will be electrically achieved by periodically displacing the electron around its equilibrium position in the slating magnetic field. The oscillatory motion induced by the $E_{a.c.}$ (in the same way as for the SO counterpart) in the magnetic field gradient generates an effective $\mathbf{B}_{a.c.}^{slanting}$ acting on the electron spin, which, if properly tailored, will present components perpendicular to the static B_{ext}.
Defining b_{SL} the z-magnetic field gradient along the driving direction (parallel to $E_{a.c.}$), we have that

$$B_{a.c.}^{slanting} = \frac{eE_{a.c.}l_{orb}^2|b_{SL}|}{\Delta E_{orb}} \propto \frac{eE_{a.c.}|b_{SL}|}{\Delta E_{orb}^2}. \tag{3.19}$$

Comparing the expressions for $B_{a.c.}^{SO}$ and $B_{a.c.}^{slanting}$, we can realize a remarkable analogy between the slanting magnetic field and the SO field[15]; in fact it is possible to consider the SO field as an intrinsic slanting magnetic field with 'gradient' $2B_{ext}/l_{SO}$ or we can consider the slanting Zeeman field as an artificial SO field of effective SO length

[14] in [16] and [19] systems it has been estimated to be ~ 15 m/s and 15-45 m/s respectively.
[15] This analogy cannot be arbitrarily extended further, without proper care, because the magnetic field from the micromagnet breaks also the time reversal symmetry which is, instead, preserved by the SO field.

$l_{SO}^{slanting} = |b_{SL}|/(2B_{ext})$.
As described in [22], the perturbation term coming from the variation of the slanting magnetic field component along the z-direction (for a static B_{ext} applied in the x-y plane), mixes the electron spin in the ground orbital state with higher orbital states with opposite spin. The degree of this mixing is proportional to the gradient b_{SL} (in analogy with what already observed for the SO coupling).
As observed previously for the SO field, the magnetic field gradient also renormalizes the bare electron Zeeman splitting $E_{0z} = g_0\mu_B B$. The degree of renormalization is proportional to b_{SL} but also depends on the ΔE_{orb} in the following way [22]:

$$E_z = g^*\mu_B B \sim G_+ - G_- \sim E_{0z}[1 - 0.5c^2(g\mu_B b_{SL} l_{orb})^2/(\Delta E_{orb}^2 - E_{0z}^2)]. \tag{3.20}$$

In [5] (see Chapter 5) it has been clearly reported that the two valley-orbit states present slightly different g-factors, which can be attributed to the different envelope wavefunctions of the two valley-orbit states, due to the valley-orbit coupling (see sections 3.5 and 3.6 for a more detailed discussion).

REFERENCES

[1] F. Schäffler, Semicond. Sci. Technol. **12**, 1515 (1997).

[2] T. Ando, Phys. Rev. B **19**, 3089 (1979).

[3] Mark Friesen, M. A. Eriksson, S. N. Coppersmith, Appl. Phys. Lett. **89**, 202106 (2006).

[4] Mark Friesen, S. Chutia, C. Tahan, and S. N. Coppersmith, Phys. Rev. B **75**, 115318 (2007).

[5] E. Kawakami, P. Scarlino, D. R. Ward, F. R. Braakman, D. E. Savage, M. G. Lagally, Mark Friesen, S. N. Coppersmith, M. A. Eriksson and L. M. K. Vandersypen, Nature Nanotech. **9**, 666 (2014).

[6] T. B. Boykin, G. Klimeck, M. A. Eriksson, Mark Friesen, S. N. Coppersmith, P. von Allmen, F. Oyafuso and S. Lee, Appl. Phys. Lett. **84**, 115 (2004).

[7] S. Srinivasan, G. Klimeck and L. P. Rokhinson, Appl. Phys. Lett. **93**, 112102 (2008).

[8] W. H. Lim, C. H. Yang, F. A. Zwanenburg, and A. S. Dzurak, Nanotechnology **22**, 335704 (2011).

[9] F. A. Zwanenburg, A. S. Dzurak, A. Morello, M. Y. Simmons, L. C. L. Hollenberg, G. Klimeck, S. Rogge, S. N. Coppersmith, and M. A. Eriksson, Rev. Mod. Phys. **85**, 961 (2012).

[10] X. Mi, T. M. Hazard, C. Payette, K. Wang, D. M. Zajac, J. V. Cady, and J. R. Petta, Phys. Rev. B **92**, 035304 (2015).

[11] K. Wang, C. Payette, Y. Dovzhenko, P. W. Deelman, and J. R. Petta, Phys. Rev. Lett. **111**, 046801 (2013).

[12] D. M. Zajac, T. M. Hazard, X. Mi, K. Wang, J. R. Petta, Appl. Phys. Lett. **106**, 223507 (2015).

[13] S. F. Nelson, K. Ismail, J. O. Chu, and B. S. Meyerson, Appl. Phys. Lett. **63**, 367 (1993).

[14] P. Basu and S. K. Paul, J. Appl. Phys. **71**, 3617 (1992).

[15] R. Hanson, L. P. Kouwenhoven, J. R. Petta, S. Tarucha, and L. M. K. Vandersypen, Rev. Mod. Phys. **79**, 1217 (2007).

[16] C. H. Yang, A. Rossi, R. Ruskov, N. S. Lai, F. A. Mohiyaddin, S. Lee, C. Tahan, G. Klimeck, A. Morello and A. S. Dzurak, Nat. Commun. **4**, 2069 (2013).

[17] Mark Friesen and S. N. Coppersmith, Phys. Rev. B **81**, 115324 (2010).

[18] J. K. Gamble, M. A. Eriksson, S. N. Coppersmith, Mark Friesen, Phys. Rev. B **88**, 035310 (2013).

[19] X. Hao, R. Ruskov, M. Xiao, C. Tahan, and H. W. Jian, Nat. Commun. **5**, 3860 (2014).

[20] C. Tahan and R. Joynt, Phys. Rev. B **89**, 075302 (2014).

[21] E. Kawakami, T. Jullien, P. Scarlino, D. R. Ward, D. E. Savage, M. G. Lagally, V. V. Dobrovitski, Mark Friesen, S. N. Coppersmith, M. A. Eriksson, L. M. K. Vandersypen, 'Gate fidelity and coherence time of an electron spin in a Si/SiGe quantum dot', in preparation.

[22] Y. Tokura, W. G. van der Wiel, T. Obata, and S. Tarucha, Phys. Rev. Lett. **96**, 047202 (2006).

[23] M. Pioro-Ladrière, T. Obata, Y. Tokura, Y. S. Shin, T. Kubo, K. Yoshida, T. Taniyama, and S. Tarucha, Nature Phys. **4**, 776 (2008).

[24] A. K. Ramdas, and S. Rodriguez, Rep. Prog. Phys. **44**, 1297 (1981).

[25] K. C. Nowack, M. Shafiei, M. Laforest, G. E. D. K. Prawiroatmodjo, L. R. Schreiber, C. Reich, W. Wegscheider, L. M. K. Vandersypen, Science **333**, 1269 (2011).

[26] J. R. Petta, et al., Science **309**, 2180 (2005).

[27] D. P. DiVincenzo, D. Bacon, J. Kempe, G. Burkard, and K. Whaley, Nature (London) **408**, 339 (2000).

[28] B. Koiller, X. Hu and S. das Sarma, Phys. Rev. Lett. **88**, 027903 (2002).

[29] Q. Li, Ł. Cywiński, D. Culcer, X. Hu, and S. Das Sarma, Phys. Rev. B **81**, 085313 (2010).

[30] M. G. Borselli, et al., Appl. Phys. Lett. **98**, 123118 (2011).

[31] Z. Shi, C. B. Simmons, J. Prance, J. K. Gamble, Mark Friesen, D. E. Savage, M. G. Lagally, S. N. Coppersmith, and M. A. Eriksson, Appl. Phys. Lett. **99**, 233108 (2011).

[32] Z. Shi, C. B. Simmons, J. R. Prance, J. K. Gamble, T. S. Koh, Y. P. Shim, X. Hu, D. E. Savage, M. G. Lagally, M. A. Eriksson, Mark Friesen, and S. N. Coppersmith, Phys. Rev. Lett. **108**, 140503 (2012).

[33] D. Kim, Z. Shi, C. B. Simmons, D. R. Ward, J. R. Prance, T. S. Koh, J. K. Gamble, D. E. Savage, M. G. Lagally, Mark Friesen, S. N. Coppersmith, and M. A. Eriksson, Nature **511**, 70 (2014).

[34] D. Culcer, A. L. Saraiva, B. Koiller, X. Hu and Das Sarma, Phys. Rev. Lett. **108**, 126804 (2012).

[35] Z. Jiang, N. Kharche, T. Boykin and G. Klimeck, Appl. Phys. Lett. **100**, 103502 (2012).

[36] L. Zhang, J. W. Luo, A. Saraiva, B. Koiller, A. Zunger, Nat. Commun. **4**, 2396 (2013).

[37] N. Kharche, M. Prada, T. B. Boykin and G. Klimeck, Appl. Phys. Lett. **90**, 092109 (2007).

[38] V. S. Khrapai, A. A. Shashkin, and V. P. Dolgopolov, Phys. Rev. B **67**, 113305 (2003).

[39] S. J. Koester, K. Ismail, and J. O. Chu, Semicond. Sci. Technol. **12**, 384 (1997).

[40] K. Lai, W. Pan, D. C. Tsui, S. Lyon, M. Mühlberger, and F. Schäffler, Phys. Rev. Lett. **93**, 156805 (2004).

[41] P. Weitz, R. Haug, K. von Klitzing, and F. Schäffler, Surf. Sci. **361**, 542 (1996).

[42] S. Goswami, K. A. Slinker, Mark Friesen, L. M. McGuire, J. L. Truitt, C. Tahan, L. J. Klein, J. O. Chu, P. M. Mooney, D. W. van der Weide, R. Joynt, S. N. Coppersmith and M. A. Eriksson, Nature Phys. **3**, 41 (2007).

[43] M. Veldhorst, J. C. C. Hwang, C. H. Yang, A. W. Leenstra, B. de Ronde, J. P. Dehollain, J. T. Muhonen, F. E. Hudson, K. M. Itoh, A. Morello and A. S. Dzurak, Nature Nanotech. **9**, 981 (2014).

[44] M. G. Borselli, et al., Appl. Phys. Lett. **99**, 063109 (2011).

[45] C. B. Simmons, J. R. Prance, B. J. Van Bael, T. S. Koh, Z. Shi, D. E. Savage, M. G. Lagally, R. Joynt, Mark Friesen, S. N. Coppersmith, and M. A. Eriksson, Phys. Rev. Lett. **106**, 156804 (2011).

[46] M. Thalakulam, C. B. Simmons, B. J. Van Bael, B. M. Rosemeyer, D. E. Savage, M. G. Lagally, Mark Friesen, S. N. Coppersmith, and M. A. Eriksson, Phys. Rev. B **84**, 045307 (2011).

[47] P. Huang and X. Hu, Phys. Rev. B **90**, 235315 (2014).

[48] P. Scarlino, E. Kawakami, P. Stano, M. Shafiei, C. Reichl, W. Wegscheider, and L. M. K. Vandersypen, Phys. Rev. Lett. **113**, 256802 (2014).

[49] J. T. Muhonen, J. P. Dehollain, A. Laucht, F. E. Hudson, R. Kalra, T. Sekiguchi, K. M. Itoh, D. N. Jamieson, J. C. McCallum, A. S. Dzurak and A. Morello, Nature Nanotech. **9**, 986 (2014).

[50] K. M. Itoh and H. Watanabe, MRS Communications **4**, 143 (2014).

[51] A. M. Tyryshkin, S. Tojo, J. J. L. Morton, H. Riemann, N. V. Abrosimov, P. Becker, H.-J. Pohl, T. Schenkel, M. L. W. Thewalt, K. M. Itoh and S. A. Lyon, Nature Mater. **11**, 143 (2012).

[52] M. Steger, K. Saeedi, M. L. W. Thewalt, J. J. L. Morton, H. Riemann, N. V. Abrosimov, P. Becker, and H. J. Pohl, Science **336**, 1280 (2012).

[53] B. M. Maune, et al., Nature **481**, 344 (2012).

[54] L. V. C. Assali, H. M. Petrilli, R. B. Capaz, B. Koiller, X. Hu, and S. Das Sarma, Phys. Rev. B **83**, 165301 (2011).

[55] J. Y. Li, C. T. Huang, L. P. Rokhinson, and J. C. Sturm, Appl. Phys. Lett. **103**, 162105 (2013).

[56] W. M. Witzel, R. Rahman, and M. S. Carroll, Phys. Rev. B **85**, 205312 (2012).

[57] A. Wild, J. Sailer, J. Nutzel, G. Abstreiter, S. Ludwig, and D. Bougeard, New J. Phys. **12**, 113019 (2010).

[58] G. Dresselhaus, Phys. Rev. **100**, 580 (1955).

[59] Y. A. Bychkov and E. I. Rashba, J. Phys. C **17**, 6039 (1984).

[60] R. Winkler, 'Spin-Orbit Coupling effects in Two-Dimensional Electron and Hole Systems' (Springer, 2003).

[61] C. G. Tahan, 'Silicon in the Quantum Limit: Quantum Computing and Decoherence in Silicon Architectures', PhD Thesis, University of Wisconsin (2005).

[62] P. Lucignano, R. Raimondi, and A. Tagliacozzo, Phys. Rev. B **78**, 035336 (2008).

[63] M. Borhani and X. Hu, Phys. Rev. B **85**, 125132 (2012).

[64] M. O. Nestoklon, E. L. Ivchenko, J. M. Jancu, and P. Voisin, Phys. Rev. B **77**, 155328 (2008).

[65] M. Prada, G. Klimek, and R. Joynt, New J. Phys. **13**, 013009 (2011).

[66] Z. Wilamowski, W. Jantsch, H. Malissa, U. Rossler, Phys. Rev. B **66**, 195315 (2002).

[67] Z. Wilamowski, W. Jantsch, Physica E **12**, 439–442 (2002).

[68] C. Tahan and R. Joynt, Phys. Rev. B **71**, 075315 (2005).

[69] S. Amasha, K. MacLean, I. P. Radu, D. M. Zumbühl, M. A. Kastner, M. P. Hanson, and A. C. Gossard, Phys. Rev. Lett. **100**, 046803 (2008).

[70] V. N. Golovach, A. Khaetskii, and D. Loss, Phys. Rev. Lett. **93**, 016601 (2004).

[71] D. Harbusch, D. Taubert, H. P. Tranitz, W. Wegscheider, and S. Ludwig, Phys. Rev. Lett. **104**, 196801 (2010).

[72] G. Granger, D. Taubert, C. E. Young, L. Gaudreau, A. Kam, S. A. Studenikin, P. Zawadzki, D. Harbusch, D. Schuh, W. Wegscheider, Z. R. Wasilewski, A. A. Clerk, S. Ludwig and A. S. Sachrajda, Nature Phys. **8**, 522 (2012).

[73] F. H. L. Koppens, C. Buizert, K. J. Tielrooij, I. T. Vink, K. C. Nowack, T. Meunier, L. P. Kouwenhoven, and L. M. K. Vandersypen, Nature **442**, 766 (2006).

[74] J. P. Dehollain, J. J. Pla, E. Siew, K. Y. Tan, A. S. Dzurak and A. Morello, Nanotechnology **24**, 015202 (2013).

[75] E. Kawakami, P. Scarlino, L. R. Schreiber, J. R. Prance, D. E. Savage, M. G. Lagally, M. A. Eriksson and L. M. K. Vandersypen, Appl. Phys. Lett. **103**, 132410 (2013).

[76] K. C. Nowack, F. H. L. Koppens, Y. V. Nazarov, and L. M. K. Vandersypen, Science **318**, 1430 (2007).

[77] S. Nadj-Perge, S. M. Frolov, E. P. A. M. Bakkers, and L. P. Kouwenhoven, Nature (London) **468**, 1084 (2010).

[78] E. A. Laird, C. Barthel, E. I. Rashba, C. M. Marcus, M. P. Hanson, and A. C. Gossard, Phys. Rev. Lett. **99**, 246601 (2007).

[79] J. van den Berg, S. Nadj-Perge, V. Pribiag, S. Plissard, E. Bakkers, S. M. Frolov, and L. P. Kouwenhoven, Phys. Rev. Lett. **110**, 066806 (2013).

4

FABRICATION PROCESS

The two-dimensional electron gas (2DEG) represents one of the most versatile low dimensional platforms used in the last 25 years for the study of solid-state condensed matter physics [1, 2]. One of the most important features of a 2DEG is its high electron mobility, reached, in most of the cases, using the so-called 'modulation-doping' technique. By separating the electron supply layer (which is usually the major source of scattering) from the region (interface, quantum well (QW)) where the electrons are confined, it is possible to reduce the scattering contribution of those impurities that otherwise would limit the carrier mobility [1].
As explained in Chapter 1, we realize depletion quantum dots (QDs) starting from an electron gas confined along the z-direction (2DEG) and using lateral gates to produce the confinement in the other dimensions. By applying a negative voltage to a metallic gate deposited on the surface of the structure we deplete the 2DEG below and define islands where the electrons are confined, separated from the rest of the 2DEG (electron reservoirs) by tunable tunnel barriers. The quality and tunability of the confining potential defining the QDs or the charge sensor is dramatically affected by the disorder in the semiconductor. There are indeed many possible sources of disorder, such as doping impurities, dangling bonds, impurities and defects at the surface of the structure or at the interface between different layers. All those sources define an effective potential landscape in the QW, thus increasing the charge scattering events or even trapping electrons in local potential minima. As a result, at cryogenic temperatures the system is insulating if not populated above a specific electron density[2]. Increasing the electron density results in a better screening of the disorder potential and, as a result, in increased 2DEG conductivity.

The key parameter used to estimate the amount of electric disorder in a semiconductor system is the carrier mobility. It is believed and widely verified that samples with

[1] In a modulation doped QW the mobility is, in principle, limited by remote ionized impurity from the δ-doping layer.
[2] The critical electron density of the insulator-metal transition is related to the amount and the nature of disorder present in the QW.

higher mobility provide better tunability and stability, and thus are more suited for quantum device technology based on electron confinement. However, it is not trivial to establish a priori how 2DEG mobility correlates with quantum dot device performance[3]. As a matter of fact, QD devices built on structures with low mobility present, quite often, the creation of 'unintentionally created QDs' that can hinder device tunability. These form at the local minima of the electrostatic disorder potential, that will behave effectively as QDs (positioned in random places), but with much less control and tunability than a real QD structure.

For Si/SiGe 2DEG systems, during the past 5 years very interesting experiments on single and two electron spins have been realized on devices with electron mobility around 4-12$\times 10^4$ cm^2/(Vs) [3–7]. As a general guide for quantum computation experiments in semiconductor devices, the aim is to realize a shallow 2DEG embedded in a heterostructure with high electron mobility at low charge density. If we want to set a boundary to a 'reasonable' mobility, necessary for quantum technology applications, we can refer to a threshold mobility level of ~40 000 cm^2/(Vs) at a charge carrier density of ~4×10^{11} cm^{-2} as a minimum quality metric for qubit device fabrication citeLi153.

4.1. HIGH MOBILITY IN UNDOPED SI SYSTEMS

Nowadays, the high mobility record in 2DEG has been demonstrated in a modulation-doped GaAs structure at $T < 1K$ [8], reaching 3.2 $\times 10^7$ cm^2/(Vs) with an electron density of 3×10^{11} cm^{-2}.
Silicon systems, in general, have electron mobilities 1-2 order of magnitude lower for comparable 2D electron density. In silicon, a high quality 2D electron confinement has been achieved for the first time in an inversion layer of a Si MOS structure, at a Si/SiO_2 interface, already in 1966 [9] and it was used to demonstrate quantum Hall effect for the first time [10]. However, in those inversion layers, strong scattering from the impurity charges, at the Si-SiO_2 interface, limited the electron mobility to around ~ 10^3 cm^2/(Vs). Recently, Kane proposed and demonstrated the use of vacuum gating of Si (111) [11], getting a peak electron mobility of 35×10^4 cm^2/(Vs) [13], but realization of such devices is still technologically challenging. Nowadays the best Si-SiO_2 MOS devices exhibit mobilities around 4×10^4 cm^2/(Vs), limited by interface roughness between amorphous SiO_2 and crystalline Si [12].

Another strategy for creating a 2DEG hosted in Si relies on heterostructure technology, which combines Si and SiGe alloy crystal layers to effectively realize a Si QW that, once populated with free electrons, can confine a high-mobility 2DEG [14]. Here we review the main achievements for Si/SiGe heterostructure technology in the context of mesoscopic physics (mobility improvement).

In 1985 the possibility to confine electrons in a strained Si layer sandwiched between relaxed SiGe alloys was demonstrated [15]. In this experiment, the authors showed, for the first time, lifting of the six-fold conduction band degeneracy of the strained Si QW. However, the $SiGe_{0.5}$ buffer layers were grown by a single step technique, resulting in a constant composition SiGe layer with a thickness higher than the critical value (see

[3] We usually assume that higher mobility means lower disorder, but the scattering mechanisms that define the 2DEG mobility may not be the same of the one that creates binding sites which confine the electrons.

section 4.1.1). This growing technique results in high dislocation density (10^9 cm^{-2}), due to the large lattice mismatch between Si and SiGe layers. Those defects penetrate through the grown SiGe buffer until the interface with the Si QW; as a result, the mobility obtained in this case was fairly low ($\sim 2\times10^3$ cm^2/Vs).

The use of virtual (relaxed) substrate layers (constant composition $SiGe_x$ relaxed buffer layer grown on top of a graded $SiGe_x$ buffer) has led to a remarkable improvement in the quality of the SiGe buffer, reducing the density of dislocations, and consequentially to a significant enhancement of the mobility [16] and stability of the quantum dot devices[4]. Reducing the threading dislocation densities to a value lower than 10^5 cm^{-2} [16, 17] greatly reduces their contribution as a primary scattering mechanism, which is then dominated by the following (with different dependence on the carrier density): background impurity scattering ($\mu \propto n^1$) and remote impurity scattering ($\mu \propto n^{1.5}$) [18].

In a linear grading virtual substrate germanium composition is increased gradually with the layer thickness. A thick layer with constant composition is added to ensure a complete relaxation of the final composition SiGe layer. Subsequently, using this technique, already in 1991, authors of [19] demonstrated the realization of a substrate with a concentration of dislocations in the active Si layer in between 10^5 and 10^6 cm^{-2}. Subsequently, authors of [20] demonstrated a much improved mobility of 5.35×10^5 cm^2/Vs by using a thick graded $Si_{1-x}Ge_x$ substrate ($0 < x < 0.3$) of several microns, grown on a Si substrate followed by a relaxed $Si_{0.7}Ge_{0.3}$ layer. A higher electron mobility of 8×10^5 cm^2/(Vs) was reported in 1998 in [21] with a combination of MBE and solid phase epitaxy to provide an atomically flat interface, reducing further interface roughness scattering.

In 2009 [22] the observation of a mobility of 1.6×10^6 cm^2/Vs was reported, for an electron density $n \approx 1.5\times10^{11}$ cm^{-2} in a 20% Ge insulated-gate field effect transistor (IGFET), with 150 nm Al_2O_3 dielectric and with a 15 nm strained Si QW 66 nm below the heterostructure surface. The same group reported, in the 2012, a mobility enhancement up to 2×10^6 (at 0.3 K), reached in a similar device with a 15 nm Si QW and a 530 nm $SiGe_{0.14}$ barrier layer [23]. In this work they also clearly show how the reduction of Ge concentration in the SiGe barrier layer (and relative buffer) reduces the lattice mismatch at the Si-SiGe interface, thereby reducing the threading dislocation density and interface roughness, effectively enhancing the 2DEG mobility.

For threading dislocation density lower than 10^5 cm^{-2}, the electron mobility inside the Si QW can be limited by other sources that can be discriminated by studying the dependence of the mobility on the carrier density [18]. A power law dependence close to $\mu \propto n^{1.5}$ was observed in [24]. Here, remote impurity charges from ionized dopants, presumably bounded at the Si cap-Al_2O_3 interface, were believed to limit the electron mobility around 5.2×10^5 cm^2/(Vs) for undoped Si/SiGe heterostructures [18]. In fact, the top-gate dielectric can contain many fixed charges that will constitute scattering centers for the 2DEG. A possible solution to attenuate the effect of this specific mobility limiting factor is increasing the thickness of the SiGe spacing layer between the Si cap-dielectric interface and the 2DEG [25]. However, this possibility is partially limited by the need of tight electrostatic lateral gate confinement for few-electron QDs devices, which can be achieved in shallow 2DEGs. This is especially important in Si as hosting material due to

[4] Strained silicon is indeed more active electrically: the dense dislocations act as diffusion pathway, and allow charges to flow through them, thereby increasing leakage current.

its high effective electron mass (see section 3.7.2).

The most remarkable result in terms of electron mobility has been reported in a recent work in [26, 27], with a record mobility for a strained Si QW of about 2.2×10^6 $cm^2/(Vs)$ at an electron density $n \approx 1.8\times10^{11}$ cm^{-2}. This work is based on undoped heterostructure with a graded $SiGe_{0.18}$ buffer on (100) Si substrate, with a 1 μm constant composition $SiGe_{0.18}$ buffer, a 15 nm Si QW, ~100 nm $SiGe_{0.18}$ barrier and 1 nm Si cap. The ohmic connections to the 2DEG are realized by thermally evaporated and subsequently annealed AuSb alloy contacts[5]. The mobility was found to be limited by small-angle scattering due to short range random potential.

Recently, in [28], the authors performed a detailed study of 2DEGs formed in undoped Lawrence Semiconductor Research Laboratory (LSRL) Si/SiGe heterostructures in order to identify their electron mobility limiting mechanisms. By analyzing data from 26 wafers with different heterostructure growth profiles they observed a strong correlation between the background oxygen concentration in the Si quantum well and the maximum mobility. Secondary Ion Mass Spectroscopy (SIMS) analysis of the heterostructures showed a clear correlation between the decrease in oxygen concentration and the increase in the mobility. In fact, ionization of even a small amount of the oxygen atoms in Si QW can lead to a significant impurity charge concentration directly inside the Si QW. In high quality samples (low oxygen content in the Si QW) the mobility was $\sim 1.6\times10^5$ cm^2/Vs at a density of $\sim 2.17\times10^{11}$ cm^{-2}. For these structures the charge mobility is limited by remote impurity scattering. Furthermore, they also were able to measure a valley splitting of ~150 meV for the high mobility heterostructure, by recording the perpendicular magnetic field at which it is possible to resolve clearly the removal of the valley degeneracy in the Landau levels spectrum[6].

Another promising attempt to improve the electrical performance of 2DEGs confined in Si/SiGe heterostructures, is to use structures grown on fully relaxed SiGe single crystal nanomembranes[7] [29, 30]. This approach aims to create defect-free, elastically relaxed, SiGe single crystals, eliminating the formation of dislocations. In [31], a charge mobility above 40 000 $cm^2/(Vs)$ was measured at a charge carrier density of 4×10^{11} cm^{-2}. No quantum devices have yet been fabricated using SiGe nanomembranes 2DEGs. From electron mobility measurements of nanomembrane devices, it has been deduced that the main scattering source can be still related to the charge impurities accumulated at the Si-dielectric surface, as in many conventional SiGe devices.

These experiments put the strained Si QW built in Si/SiGe IGFET structures into a promising perspective for spin qubits application.

In the following 2 sections we will review the main aspects of crystal growth for Si/SiGe heterostructures.

[5] According to their suggestions, the main improvements come from using an ultra-high-vacuum chemical-vapor-deposition (UHVCVD) and by employing 300 nm thermally evaporated SiO, instead of Al_2O_3 (ALD deposited), as an insulator (notice also that the Hall bar used for the mobility-density measurements are not mesa etched but rather top-gate defined, for accumulation) and that the system, once accumulated, needs a long (several hours) stabilization time.

[6] The energy value obtained by this measurement can set a lower bound for the E_{VS} of a QD realized in the same heterostructure.

[7] Here, strained Si-relaxed SiGe layers are grown on an unstrained single-crystalline sheet of SiGe.

4.1.1. STRAIN ENGINEERING

Silicon and Germanium are the only two elements of the IV group of the periodic table that are completely miscible in a random $Si_{(1-x)}Ge_x$ alloy in which each atom is covalently bonded to four atoms with arbitrary composition [8] [14]. Both Si and Ge crystallize in the same diamond lattice structures[9] with lattice constants 5.431 $A°$ for Si and 5.464 $A°$ for Ge (4.2 % larger than Si) [14].
The physical properties of $Si_{(1-x)}Ge_x$ alloys change gradually from those of Si to those of Ge for most of the composition interval $x < 0.5$, which is a typical upper bound for Germanium content used in all the devices created for electron confinement. In this regime (more Si-like) all the relevant physical parameters (effective mass, electron g-factor, dielectric constant, ...) are close to those of relaxed bulk Si.

The lattice constant of the relaxed $Si_{1-x}Ge_x$ alloy, $a_{SiGe}(x)$, can be predicted accurately by the linear interpolation (Vergand's law [14] in nm) $a_{Si} + (a_{Ge} - a_{Si})x$. However, a better fit can be obtained using the relation

$$a_{Si_{1-x}Ge_x}(nm) = a_{Si}(1-x) + a_{Ge}x + 0.0273(x^2 - 10x),$$

where the last term represents an empirical correction [32]. Here, the important point to notice is that already for a $Si_{0.7}Ge_{0.3}$/Si heterostructure the lattice mismatch is ~1.2% (almost 10 times higher than that of the typical GaAs/AlAs heterostructures ~0.1-0.2%). For this reason, growing a thick layer of $Si_{1-x}Ge_x$ directly on top of Si, would result in a high density of misfit and threading dislocations due to the large lattice constant mismatch. These types of dislocations are, in general, very efficient carrier generation-recombination sites (see Fig. 4.1(c) and (e)) [33, 34].

For thin $Si_{1-x}Ge_x$ films (thickness<critical thickness) grown on top of a $Si_{1-y}Ge_y$ relaxed substrate, the relaxation process is forbidden because the elastic energy stored in this strained but still homogeneous layer is lower than the elastic energy associated to the onset of local distortions around dislocations. Therefore, the atoms in this layer stretch in order to line up with the buffer layer below (see Fig. 4.1(b)-orange arrows representing the changing in lattice parameters). Then for $x > y$ the top layer is compressively strained, while for $x < y$ this layer is tensile strained (Fig. 4.1(b)).

In this context, one of the most relevant parameters is the critical thickness t_c [14, 17, 35]. This is defined as the specific thickness above which the generation of a misfit dislocation is energetically allowed[10]. As the thickness of the epitaxial layer is increased, it approaches a maximum thickness (t_c) above which would cost too much energy to elastically strain additional heterolayers to adapt to the underlying substrate. Hence, for film thickness exceeding t_c, the strain accumulated in the film is partially relaxed by the creation of structural defects (see Fig. 4.1(c)), mainly misfit and threading dislocations (see Fig. 4.1 (e)). Their density is a function of the Ge content mismatch between two consecutive layers. For a typical Ge content of 30% used in our relaxed substrates, the

[8] Each lattice site is occupied by a Ge atom with probability x and by a Si atom with probability (1-x).
[9] The diamond structure unit cell consists of two interpenetrating face centered cubic cells, one of which is displaced along the main diagonal by a quarter of unit cell lattice constant.
[10] It is more correct to look at those dislocations not as real physical objects, but instead as a boundary between layers of crystalline material that are displaced relative to each other.

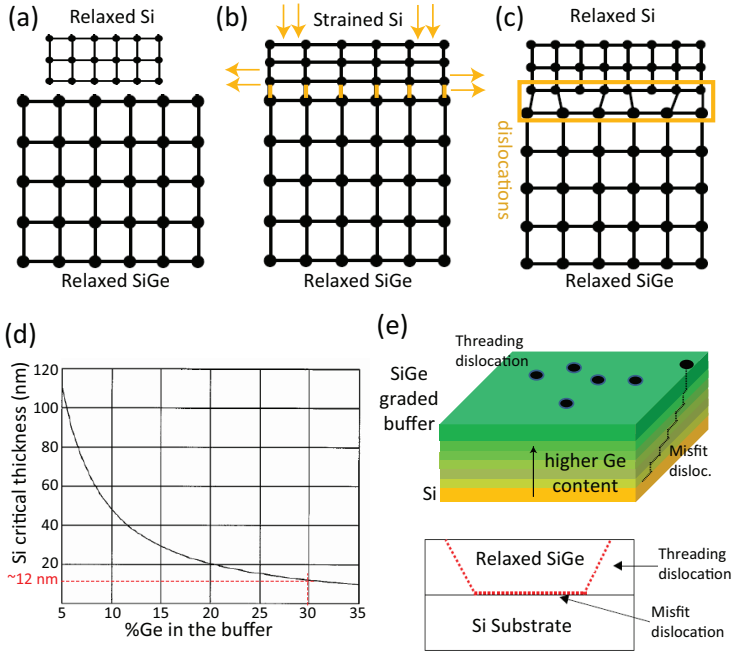

Figure 4.1: (a) Schematic representation of the difference in lattice constant between a fully relaxed SiGe alloy and Si. (b) The initial thin Si epilayer is tensile strained to adapt to the SiGe substrate, with higher lattice constant (no defects for Si thickness lower than t_c ('critical thickness'). (c) If the total thickness of the Si layer increases more than t_c, the strained Si begins to relax, by accumulating misfit dislocations (defects inside the orange rectangle). (d) Critical thickness of a strained silicon epilayer, grown on top of a fully relaxed $SiGe_x$ substrate, as a function of Ge composition (x). Adapted from [17]. (e) Schematic representation of misfit and threading dislocations.

critical thickness for a strained Si QW is around 12 nm (see Fig. 4.1(d)) [17, 36, 37]. These dislocation defects contribute strongly to the final electrical quality of the Si QW because they constitute very efficient recombination-generation sites for carriers [16, 17].

4.1.2. BANDGAP ENGINEERING

Si-SiGe heterostructures allow both strain engineering (previous section) and band-gap engineering [14]. In designing the final device it is very important to understand how modifying the Ge content in the SiGe random alloy affects the conduction and valence band profile which defines the physical properties of the free or confined charge carriers, such as effective mass, valley degeneracy and spin-orbit interaction.

The bulk (relaxed) bandstructure of Si and Ge presents an indirect band gap with the valence band edge at k=0, but in the conduction band they show quite different properties. In fact, the minima of the Ge conduction band are at the L-points of the Brillouin zone along the [111] momentum directions; so there are 8 equivalent half-valleys or 4 equivalent full valleys (Fig. 4.2(a)). For relaxed silicon, instead, the minima of the conduction band are in correspondence of a point in the Brillouin zone at about 0.85 along

the Δ direction (of the [100]), toward the zone boundary at the X-points (Fig. 4.2(b)), which, for bulk silicon, presents a 6-fold symmetry; so there are 6 equivalent valleys [38]. For the unstrained (relaxed) SiGe alloy the size of the bandgap is shown in Fig. 4.2(d), as a function of the Ge content (x). There is a smooth transition to the Ge-like gap till x=0.85, where the band gap nature changes between the Si-like Δ_6-valley minima to L-valleys. Moreover, in relaxed SiGe layers the degeneracy of the 6 valleys is preserved [14]. The band structure is affected by two main components of strain that are presented in Fig. 4.2 (e) [14, 39]:
- hydrostatic strain: it comes from the volume change of the material and results in a shift of the conduction and valence band energy without breaking the valley degeneracy (keeping the symmetry);
- uniaxial strain: it splits the valley degeneracy of both conduction and the valence bands. Because of the anisotropic nature of this strain, the four x, y minima are shifted toward higher energy with respect to the two z minima ($\Delta E \sim 200$ meV for 1% of accumulated strain), resulting in the effective splitting of the Δ-conduction band (see Fig. 4.2 (c) and (e))[40].

Another key parameter that plays an important role in the electron transport, and particularly for the electron confinement, is the electron effective mass [14, 39]. The curvature of the conduction band minima of the Si QW along the transverse and longitudinal directions provides the transverse and longitudinal effective mass, 0.196 and 0.918 m_0 respectively, with m_0 the bare electron mass in vacuum.
To obtain a strong confinement of electron in a QW with a sufficient band gap discontinuity, a tensile strained Si or $Si_{1-x}Ge_x$ layer must be grown on a relaxed $Si_{1-y}Ge_y$ virtual substrate (where $x < y$). When Si is grown on top of a (100)-oriented relaxed SiGe virtual substrate, the final band alignment results to be of type II (see Fig. 4.2(f)), allowing the confinement of a 2DEG. The degree of the vertical (out-of-plane) 2DEG confinement depends on the magnitude of the conduction band offset, ΔE_c, which can be approximated with 65 meV per each 10% Ge content [39]; so, for a silicon layer on top of a relaxed 30% Ge content layer we have $\Delta E_c \sim 0.2eV$[11] (see Fig. 4.2(f)).

4.2. FABRICATION PROCESS

During the past 5 years several important experiments with confined electrons have been realized by using P-doped modulation doped heterostructures (single shot spin readout [3], T_1 relaxation time measurement [3, 5], Pauli spin blockade [5])[12].
In order to realize a depletion gate device, robust barriers between the metallic gates on the surface of the heterostructure are required. Usually, in doped GaAs heterostructures, a good Schottky barrier is naturally created between the GaAs heterostructure and the gold depletion gates deposited on its surface. This prevents the current flow between the top gates and the 2DEG. On the contrary, as noticed by different groups, the deposition of metallic gates on top of a P-doped SiGe heterostructure is not a trivial task. In

[11] Notice that this typical value is ~ 5 times lower than the typical band offset in Si/SiO_2 structures (~ 1 eV); as a result the maximum $E_\perp$ we can safely apply by a top-accumulation gate in the latter is usually higher.
[12] Those systems have the advantage of a simpler (i.e. fewer lithographic steps) fabrication process than the one necessary for an undoped device. Conversely, doped SiGe devices have shown the tendency to be quite unstable (due to diffusion-segregation of the P dopants from the delta-doping layer).

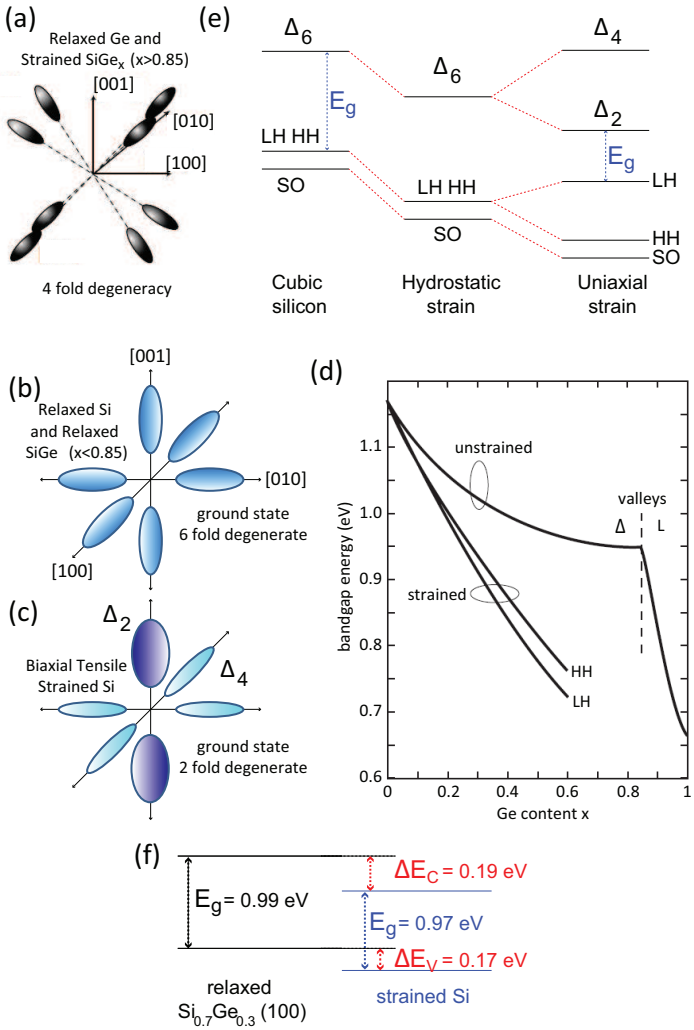

Figure 4.2: (a) Constant energy surface near the conduction band minima for a relaxed $Si_{(1-x)}Ge_x$ alloy for $0.85 < x \leq 1$; there is a 4-fold Ge-like valley degeneracy. (b) Constant energy surface near the conduction band minima for a relaxed $Si_{(1-x)}Ge_x$ alloy for $0 \leq x < 0.85$; there is a 6-fold Si-like valley degeneracy. (c) Constant energy surface near the conduction band minima for a tensile strained Si; the 6-fold valley degeneracy is split in Δ_4 (valleys in plane) higher in energy and Δ_2 (valleys along z-[001] growth direction). (d) Bandgap energies as a function of Ge content for strained SiGe grown on bulk-silicon substrates and for unstrained SiGe. Adapted from [14]. (e) Schematic representation of the effect of the hydrostatic and uniaxial strain on the Si valence band edge (energy level and degeneracy). Hydrostatic strain shifts the band edge either to higher or lower energy, while uniaxial strain splits the degeneracy of the bands. Adapted by [14, 39]. (f) Schematic representation of the conduction and valence band energy discontinuities between the strained Si and relaxed $Si_{0.7}Ge_{0.3}$.

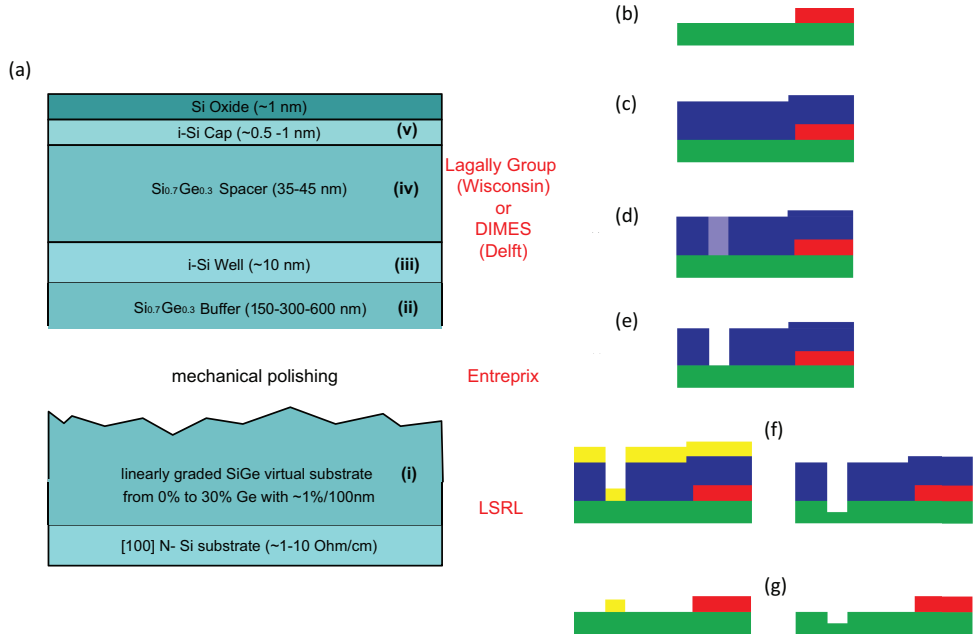

Figure 4.3: (a) Schematic representation of a typical SiGe heterostructure, described in the text in more details. (b-g) Different steps of the fabrication process, based on electron-beam (ebeam) lithography, imply the creation of a resist masks to use in a subsequent step. (b) shows a substrate (green) with some previously fabricated features (red). In (c) the sample is spin-coated with an e-beam resist (purple) that is subsequently patterned (d). The patterning changes the molecular structure of the resist and these altered regions can be removed in a development step (e). (f) shows two possible following steps: a metal is deposited on the sample (left) or the resist can be used as an etch mask (right). In the lift-off step (g), the resist is dissolved, leaving behind the designed structure. Adapted from [41].

fact, the metallic gates result to be quite hysteretic and often their leakage current is not negligible [33, 42, 43]. This problem turns out to be likely related to the P-ions migration through the SiGe buffer, till the surface of the Si cap layer[13].

After the experiment on the S-T_0 coherent control performed by HRL group (in the 2012) [44], which demonstrated a S-T_0 T_2^* ~ 350 ns (single axis control), the Si-spin qubits community started a more systematic study and use of the undoped heterostructures, which turns out to provide superior results with respect to doped heterostructures in terms of charge stability, 2DEG mobility and charge noise (the device is more stable and quiet). This is also the system of choice for the Si/SiGe work presented in the Chapters 5, 6 and 7 of this thesis.

The process reported in the next two sections was developed in collaboration with Ferdy Walvoort (Master thesis project) [41], following the indications of our collaborators at University of Wisconsin (M. Eriksson group).

4.2.1. HETEROSTRUCTURE SCHEMATIC

The starting point of the fabrication process of depletion QDs is a high quality undoped Si/SiGe heterostructure with a ~10 nm silicon quantum well (Si QW) embedded 30-50 nm below the surface. The Si/SiGe experiments reported in the rest of the thesis are realized in devices fabricated by our collaborators at University of Wisconsin (M. Eriksson group), starting from heterostructures grown by Chemical Vapor Deposition (CVD) systems, by the M. Lagally group (University of Wisconsin). The electronic measurements presented in this Chapter, instead, are performed on devices fabricated starting from undoped heterostructures grown at DIMES[14] (TU Delft) by Tom Scholtes and Wiebe De Boer. We use CVD growth procedure for the strained Si QW, starting from a relaxed graded buffer SiGe substrate purchased from Lawrence Semiconductor Research Laboratories (LSRL). The typical mobility of these DIMES heterostructures, characterized by Hall measurements, is limited to around 1-3 $\times 10^4$ cm^{-2}/(Vs) for 3-6$\times 10^{11}$ cm^{-2} 2DEG densities, still a factor ~10 lower than recently reported in similar structures by [28], for similar charge densities.

In order to guarantee a good quality of the epitaxial process for the final Si QW it is fundamental to ensure that the exposed surface of the SiGe substrate will be as clean as possible, reducing the density of possible impurities which, if incorporated in the heterostructure, can constitute extra sources of defects, degrading the electron mobility [45]. Therefore, the LSRS SiGe substrate undergoes a careful cleaning procedure outside and inside the CVD reactor.

A typical schematic of the layer structure of a SiGe-Si-SiGe heterostructure used in our experiments is shown in Fig.4.3(a).
From the Si (N-doped) substrate to the surface, there are several epitaxial layers:
(i) $Si_{1-x}Ge_x$ graded buffer ($0 < x < 0.3$ for this work),
(ii) $Si_{0.7}Ge_{0.3}$ relaxed buffer,
(iii) strained Si quantum well (2DEG),
(iv) relaxed $Si_{0.7}Ge_{0.3}$ spacer,

[13] Possible current paths between the gates and the 2DEG can follow lattice dislocations always present due to the strain relaxation growing technique of Si/SiGe heterostructures [33, 34].
[14] Delft Institute of Microelectronics and Submicrontechnology

(v) strained Si cap.
All of these layers play an important role in the creation of the final high quality Si QW, with various functions, described as follows.
(i) The $Si_{1-x}Ge_x$ graded layer (usually $0 < x < 0.3$) reduces the number of the introduced plastic relaxation defects by controlling the grading rate (<10% Ge/μm) in the Ge content [48]. Due to the large lattice mismatch between Si and SiGe, the misfit dislocations nucleate at the growth interface and the threading dislocations can extend through the entire structure and reach the 2DEG area [46, 47] (see Fig. 4.1(c) and (e)).
Next (ii), a thick relaxed SiGe layer of constant Ge concentration, equal to the final virtual layer Ge content (30 %Ge in our case), is grown on top of the graded buffer. A chemical-mechanical polishing (CMP) step is implemented to reduce the effect of these accumulated epitaxy defects [49]. Then, another fully relaxed SiGe buffer layer of constant Ge composition is regrown, to separate the Si QW, grown in the next step, far from the re-grown interface, which may contain a high impurity concentration. This extra layer, in fact, further reduces the effect of the electron scattering induced by the buried dislocation in the 2DEG [45].
The layer (iii) consists of a strained intrinsic Si layer on top of the relaxed $Si_{0.7}Ge_{0.3}$ layer. This layer is where the quantum well is formed. The thickness of this layer determines the electron confinement along the growth direction and it is limited by the critical thickness of a strained Si layer on a relaxed SiGe substrate [17, 36, 37] (see Fig. 4.1(d)), to prevent any further relaxation defects which will limit the 2DEG mobility[15].
The Si layer is followed by a constant Ge composition $Si_{0.7}Ge_{0.3}$ spacing layer (iv), which effectively creates the QW and sets the distance from the QW and the heterostructure surface [16], determining the depth of the 2DEG. In principle, increasing the thickness of this layer can contribute in improving the mobility of the 2DEG as it increases the distance between the 2DEG and surface of the heterostructure [25]. However, it cannot be made arbitrarily high for quantum electronic application, as it also makes harder to control the QD electrostatic confinement (number of electrons, tunnel barriers, ...).
Finally, a Si cap layer (v) terminates the heterostructure with a more stable and inert surface (after the creation of the natural SiO) than a SiGe layer. In fact, it has been found that a Si-dielectric interface is electrically quieter than a SiGe-dielectric interface. Furthermore, particular care needs to be taken to keep the silicon cap layer thin enough (<1 nm), to prevent the accumulation of a second parasitic conduction channel in it, which will hinder the control of the electron density in the Si QW [50].

4.2.2. OVERVIEW OF FABRICATION PROCESS

Test structures to characterize the density and mobility of the electron accumulated in the Si QW are reported in Fig. 4.7.
The realization of a QD device by using undoped Si-SiGe heterostructure is a quite complex process due to several electron-beam (ebeam) lithography steps for defining the control elements needed for the lateral gates QD structure (geometry). Many of those steps involve the creation of a protection layer or lift-off mask, which is schematically

[15] the typical thickness for the Si QW on top of a $Si_{0.7}Ge_{0.3}$ is around 10 nm.
[16] usually one of the major sources of disorder are the ionized impurities at the interface between Si cap and dielectric

depicted in Fig. 4.3(b-g). It consists of covering the device with a polymer mask (usually PMMA) which is selectively patterned by an electron beam and subsequently developed and used for lifting off a new evaporated metal layer or to protect some areas of the device from the etching action. Except for ion implantation, which is done in DIMES, all the fabrication steps have been realized in the Kavli Nanolab Delft, the ISO class 5 cleanroom facility of the Faculty of Applied Sciences of Delft University of Technology.

A cross-section schematic of the final device with all the different layers involved is reproduced in Fig. 4.4. The entire process can be schematically divided in 11 steps, summarized below and illustrated in Fig. 4.5 and Fig. 4.6 (lateral and top view respectively).

1) Deposition of a thin layer of **dielectric** (Fig. 4.5(1)). This layer will protect the heterostructure during the rest of the fabrication (together with applied resist) and will provide the necessary isolation between the metallic depletion gates, evaporated on top of the heterostructure, and the semiconductor material itself, reducing gate leakage [51]. Among the different dielectrics available in our clean room, aluminium oxide (Al_2O_3) has been preferred because it can be deposited with very high quality (stability, uniformity and high breakdown voltage) [52], by Atomic Layer Deposition process (ALD).

2) Deposition of alignment **markers** (Fig. 4.6(1)). Reference markers play a fundamental role for all future ebeam steps, because they will ensure a good alignment (up to ~10 nm) between consecutive steps [17].

3) Etching of the **mesa structure** (Fig. 4.5(3) and Fig. 4.6(2)). Most of the heterostructure that is not intended to be used for the dot itself or for metallic gates support, will be removed (i.e. by etching away deeper than the depth of the quantum well), in order to prevent accumulating charges. The actual region of the final quantum dot (and some of its surroundings) device will be isolated from the larger contact pads. This central part of the heterostructure is called the *micro-mesa* and in our structures it has typical size of $\sim 150 \times 150\ \mu m^2$. The creation of the micro-mesa structure can significantly reduce gate leakage and makes the electrostatic environment, where the QDs will be realized, overall more stable and quieter.

3b) The fabrication recipe proceeds, at this stage, with another step of Al_2O_3 ALD deposition (~ 5 nm), in order to ensure that the subsequent metal layers deposition in the etched area will not short the Si QW laterally.

4) **Ion implantation** to make ohmic contacts to the 2DEG (Fig. 4.5(4) and Fig. 4.6(4)). In GaAs/AlGaAs heterostructures it is a common practice to use diffusion of metal alloy annealed in order to contact the 2DEG. Even though it is possible to use the same fabrication principle also in Si/SiGe heterostructures, it leaves the surface very rough. We realized ohmic contacts by phosphorous ion implantation followed by rapid thermal annealing. This is a well established fabrication technique in the modern Si semiconductor industry, so it gives a very high yield for the Ohmic contacts. A typical shape of the ion implantation windows is shown in Fig. 4.7(c), with the green area representing the resist mask.

5) In the regions where the aluminium oxide has been removed for ion implantation, the silicon cap layer will grow a native oxide, forming an insulating layer, thereby ham-

[17] The marker dimensions and positions play a crucial role for the final alignment precision; we usually use 16 square markers (20x20 μm) placed at the border of each of the 16 cells; but if we place these markers close to the central 'micro-mesa', where all the fine features will be realized, we can further improve the alignment.

pering the realization of a good ohmic contact. After removing the native oxide with a HF dip, a thin layer of metal is deposited on top of the implanted regions. **Metallization** of the surface of the implanted region will prevent a further Si-cap oxidation. This will ensure a good electrical connection, realized in the next step, between the implanted regions and the leads (Fig. 4.5(5) and Fig. 4.6(5)).

6) In order to get a higher yield during the gates lift-off process, we split this step. First we define **fine gates** on top of the first dielectric layer (~5 nm of Ti and ~25 nm of Au). These are the depletion gates, mentioned above, to which we will apply, usually, negative electric voltage, in order to define the quantum dot and charge sensor confinement potential. Each of them presents an extension that runs until the edge of the micro-mesa, where they will be contacted by a second thicker metal layer during the next step, defining also the metallic leads and bond pads (Fig. 4.5(6) and Fig. 4.6(6)).

7) Step (6) is followed by a second e-beam step to define and deposit metallic **leads and bond pads**. The former connect the extensions of the fine gates, at the edge of the micro-mesa, to the latter. The contact pads are large enough (100x100 μm^2) to be connected with the macroscopic world (usually through a PCB) by a micro-soldering machine. This metallic layer needs to be thick enough, to fully fill the etched mesa 'moat', providing in this way a non-interrupted electrical path from the contact pads to the fine gates on top of the 'micro-mesa' (Fig. 4.5(7) and Fig. 4.6(7)).

8) At this stage, another layer of **dielectric**, usually thicker than the first, is deposited always by ALD. The higher thickness of this dielectric is needed to support the electric field across it without leaking[18]. Its main purpose is to insulate all underlying gates and structures from the accumulation gate that is to be fabricated on top (Fig. 4.5(8) and Fig. 4.6(8)).

9) At this stage we deposit the **fine accumulation gates** (Fig. 4.5(9) and Fig. 4.6(9)). Also for the accumulation gates we split the fabrication in two steps, as done in (6) and (7) for the depletion gates. But in this case the leads and bond pads for the accumulation gates have already been deposited during step (7). So they are buried below the second layer of oxide [19].

10) Etching **vias**. A via is a hole etched on specific locations of the dielectric in order to expose part of the metallic leads buried underneath that we need to contact. The via allows an electrical connection from designated leads to the top gates (Fig. 4.5(10) and Fig. 4.6(10)).

11) Deposition of **interconnects**. The interconnects connect the designated leads to the accumulation gates by making an electrical connection through the vias created in the previous step (Fig. 4.5(11) and Fig. 4.6(11)).

4.3. QD FABRICATION

All the fabrication steps, reported above, were tested and optimized individually. The entire fabrication process has been initially realized on two different Si/SiGe heterostructures grown by DIMES starting from a linearly graded SiGe LSRL substrate. The 4 inch

[18] The voltage applied to the accumulation gate can be up to +10 V; whereas the voltage applied to the depletion gates is usually never lower than -2 V.

[19] It has been noticed that realizing the accumulation gates entirely on top of the dielectric layer can induce some adhesion problems.

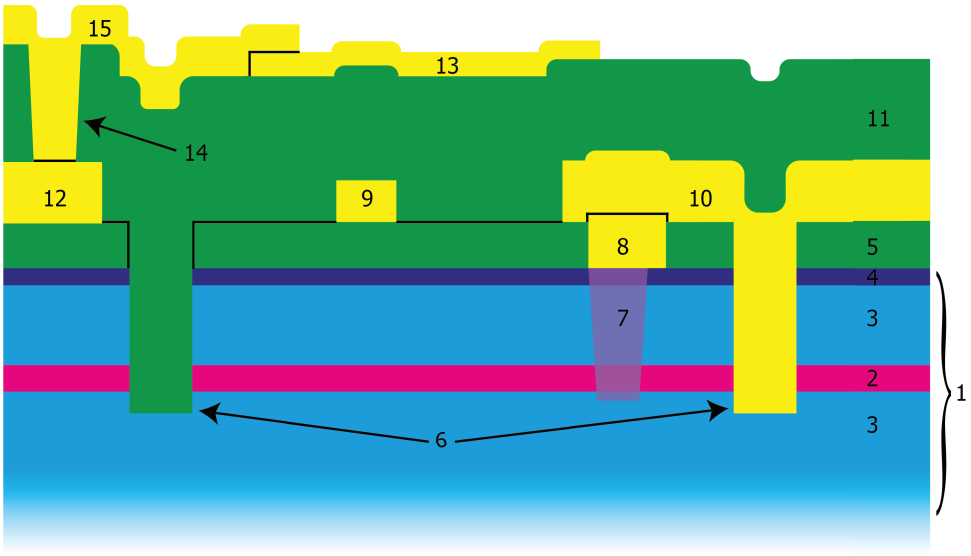

Figure 4.4: Schematic cross-cut of the device. Fabrication starts with a heterostructure (1) composed of a silicon quantum well (2) between two layers of silicon germanium (3) and a silicon cap layer on top (4). After the heterostructure is covered with aluminum oxide (5), the mesa (6) is etched into the heterostructure, at least to the depth of the quantum well (2), creating the micro-mesa (region between the etched trenches). After selective removal of aluminum oxide, ion implantation (7) creates an ohmic path between the subsequent metallization (8) and the quantum well (2). Fine gates (9) are deposited on the aluminum oxide. Leads (10) connect the ohmic metallization (8) and fine gates (9) (not shown) to big contact pads outside of the micro-mesa. A thick layer of aluminum oxide (11) covers everything, including the leads (12) for the accumulation gates. Fine accumulation gates (13) are deposited on top of the aluminum oxide. Holes (14) are etched in the aluminum oxide and used to connect (15) the fine accumulation gates (13) to the now exposed leads (12). Black lines are added for clarity. Figure is not on scale. Adapted from [41].

4

wafer heterostructure was diced in squares of 10×10 mm^2 that were processed one at a time. Because the entire double dot structure (including contact pads) is only 1.5×1.7 mm^2 (see the device in Fig. 4.8(a)), we can realize 16 devices on a 1 cm^2 piece with sufficient margin for future dicing.

In order to test the quality of the heterostructure and the reproducibility of the fabrications process, some cells are usually patterned with Hall and Van der Pauw structures and ion-implantation test lines (see Figs. 4.7(a) and Appendix A.3). Figs. 4.7(d-e) report respectively an intermediate step and the final device of a Van der Pauw testing structure; the panel (d) shows the device almost finished after mesa etching, P-ions implantation and metallization steps, excluding the accumulation gate, which is clearly visible in panel (e).

Hall and Van der Pauw structures have been realized on an undoped Si/SiGe heterostructure, nominally consisting of 1.5 nm Si / 32 nm SiGe(29%) / 12 nm Si / 150 nm SiGe(29%), grown at DIMES on top of a very thick LSRL $SiGe_{0.29}$ linearly graded buffer. For this structure we got a 4 K mobility of $\sim 3 \times 10^4$ cm^2/(Vs) for a saturated electron density of $\sim 6.25 \times 10^{11}$ (saturation voltage of ~+2 V).

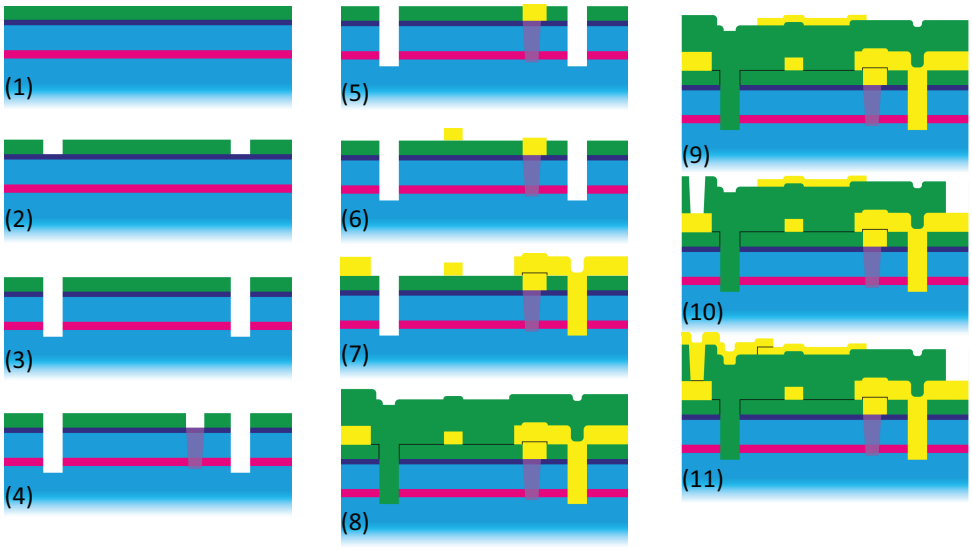

Figure 4.5: Schematic cross-cuts of the device during the different fabrication steps. (1) Fabrication starts with a SiGe/Si/SiGe QW covered with a few nm Al_2O_3 layer and a resist layer. (2) After writing into the resist the desired geometry the Al_2O_3 is removed locally with HF and later selectively (3) the heterostructure below is etched away, deep enough to make the QW confinement ineffective, creating a well isolated micro-mesa. After selective removal of aluminum oxide, ion implantation (4) is performed in order to create ohmics contacts; after an HF dip meant to remove the native oxide layer, the surface of the implanted regions are metallized (5). Fine gates (6) are deposited on top of the aluminum oxide and subsequently connected with leads (7) connected to big contact pads, outside of the micro-mesa region. A second thick layer of aluminum oxide (8) is now deposited on top of the device, covering everything, including the leads. Fine accumulation gates (9) are deposited on top of this new aluminum oxide layer. Holes (10) are etched in the aluminum oxide and used to connect (11) the fine accumulation gates with the rest of the leads embedded below the Al_2O_3. Adapted from [41].

4

4.3.1. QD DEVICES

Despite the relatively low mobility[20], we proceeded further with the manufacturing of a QD device starting from the DIMES SiGe heterostructure.
After completing the fabrication, we dice each heterostructure piece into individual samples. These are glued on top of a printed circuit board and subsequently bonded with a microbonder (see section 2.4). Preliminary measurements were realized in a dip stick (4 - 1.2 K) in order to test the possibility to accumulate a 2DEG by the top gate and deplete it by fine gates. QDs transport measurements have been realized in a Oxford Instruments Triton system (14 mK base temperature).

Fig. 4.8 shows optical (left) and SEM (right) microscope images of a completed sample. All metallic gates are made of Ti/Au, and the different colors come from different thickness of the gates and depend on whether or not they are covered by aluminium oxide. On panel (b) we can easily distinguish the edges of the central micromesa region. Looking at the shape of the metallic gates we can discern 4 different sets of gates (the

[20] For comparison, usually heterostructures used by Wisconsin group present mobility ranging ~40-100×10^3 $cm^2/(Vs)$ for comparable electron densities and QW depth.

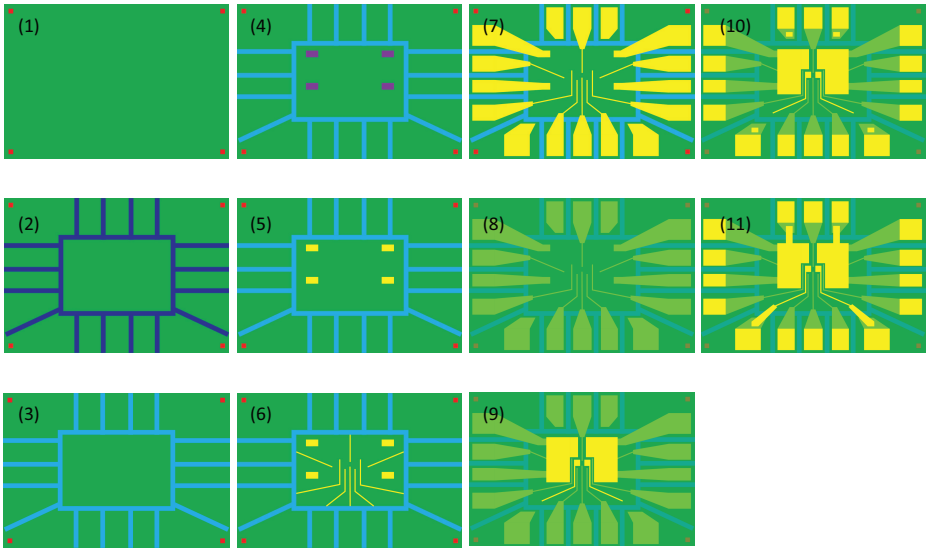

Figure 4.6: Schematic top view of the device during the different fabrication steps. (1) Fabrication starts with markers deposition on top of a SiGe/Si/SiGe QW covered with a few nm Al_2O_3 layer and a resist layer. (2) After patterning the resist into the desired geometry, exposing the Al_2O_3 below just in specific windows, the dielectric is removed locally with HF and later selectively (3) the heterostructure below etched away, deep enough in order to make the QW confinement ineffective, creating a well isolated micro-mesa. After selective removal of aluminum oxide, ion implantation (4) is realized in order to create ohmics contacts; after an HF dip meant to remove the native oxide layer, the surface of the implanted regions are metallized (5). Fine gates (6) are deposited on top of the aluminum oxide and subsequently connected with leads (7) connected to big contact pads, outside of the micro-mesa region. A second thick layer of aluminum oxide (8) is now deposited on top of the device, covering everything, including the leads. Fine accumulation gates (9) are deposited on top of this new aluminum oxide layer. Holes (10) are etched in the aluminum oxide and used to connect (11) the fine accumulation gates with the rest of the leads embedded below the Al_2O_3. Adapted from [41].

numbers refer to the labels in the Fig. 4.8(b)):
(1) The depletion gates, which will be used to shape the 2DEG accumulated in the Si QW by applying a negative voltage. The geometry defined by these gates will determine the size (orbital spectrum) of the QD and charge sensors and the capacitive coupling between them.
(2) The leads for the Ohmic contacts of the device are defined on the same layer of the depletion gates but they end on top of the ion implanted windows, without reaching the center of the micromesa. Notice how they do not cover completely the whole implanted region (the meander fingers stay out, see Fig. 4.7(c,d)).
(3) Accumulation gates, deposited on a second layer and separated from the previous one by a dielectric layer, used to create the electron reservoirs (by applying a positive voltage to these gates we will induce a 2DEG below). They partially overlap with the meander region of the ion implanted windows and they extend till the center of the micromesa, as clearly shown in panel (b).
(4) Accumulation gates for the QD regions. In the device represented in Fig. 4.8 they are realized on the same layer as the reservoir accumulation gates, but recently we also

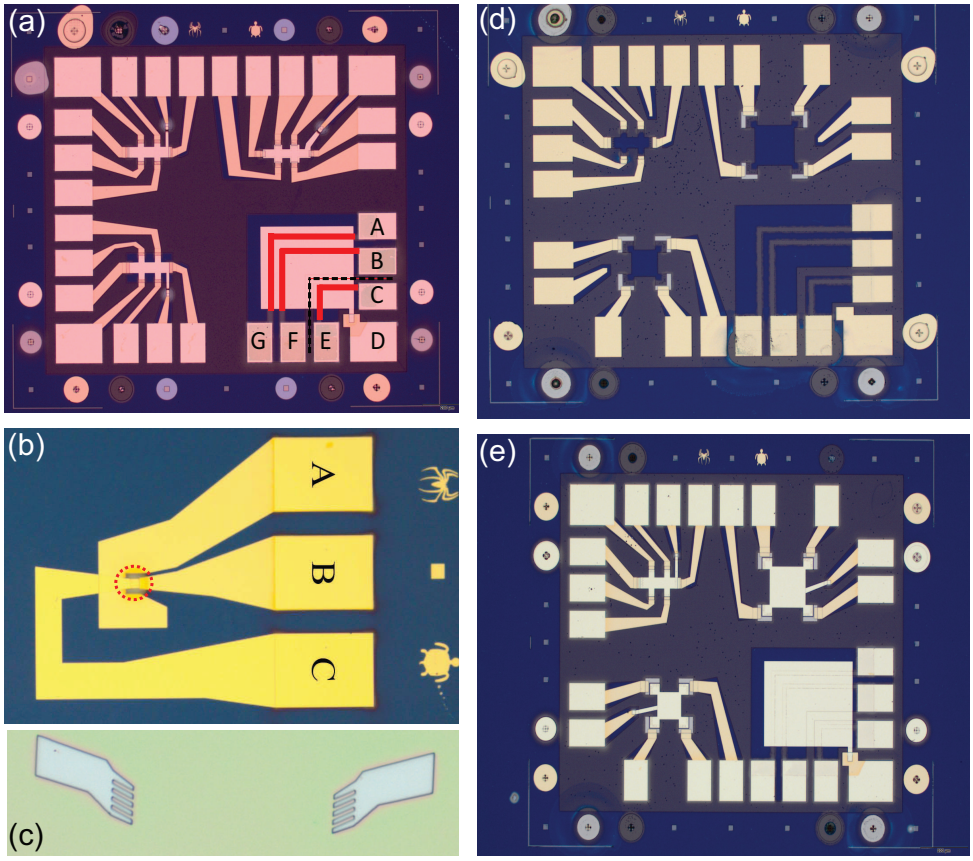

Figure 4.7: (a) Optical microscope image of the structure used to test ion implantation and electron accumulation in the Si QW. Three implanted regions, shaped as lines with metallized contact pads (labeled A through C and E through G), of increasing length, are depicted in red. The shortest line is separated by a mesa etch from the other two implanted lines. An accumulation gate (contact pad D) is partially superimposing with all the implanted lines. Results of the test are shown in Tab. A.1. (b) Optical microscope image of the set of metallic gates used to electrically test the via etching process. Left (A) and middle (B) gates (separation 8 μm) are covered with Al_2O_3. After the vias are opened (red circle), the C gate is deposited. When etching occurred successfully, the C gate will connect to the B gate, while remaining electrically insulated from the A gate. Note the halo-like coloring around the etched via, indicative of over-etching. Results of the test are shown in Appendix A.5. (c) Optical picture of the ion implantation windows defined in the resist mask. (d-e) Optical microscope images of Hall and Van der Pauw structures before (d) and after (e) the deposition the accumulation gates.

explored devices where they are realized on the same level of the fine gates. The latter solution allows for a bigger capacitive coupling between the QD and the accumulation gate but it can be realized only by sacrificing some of the control gates (LP and RP defined below)[21].

[21] Devices with a single global accumulation gate have been realized in the past [44]. By separating the accumulation gates for the reservoirs and for the QD regions, we increase the complexity of the structure but we can gain in terms of tunability.

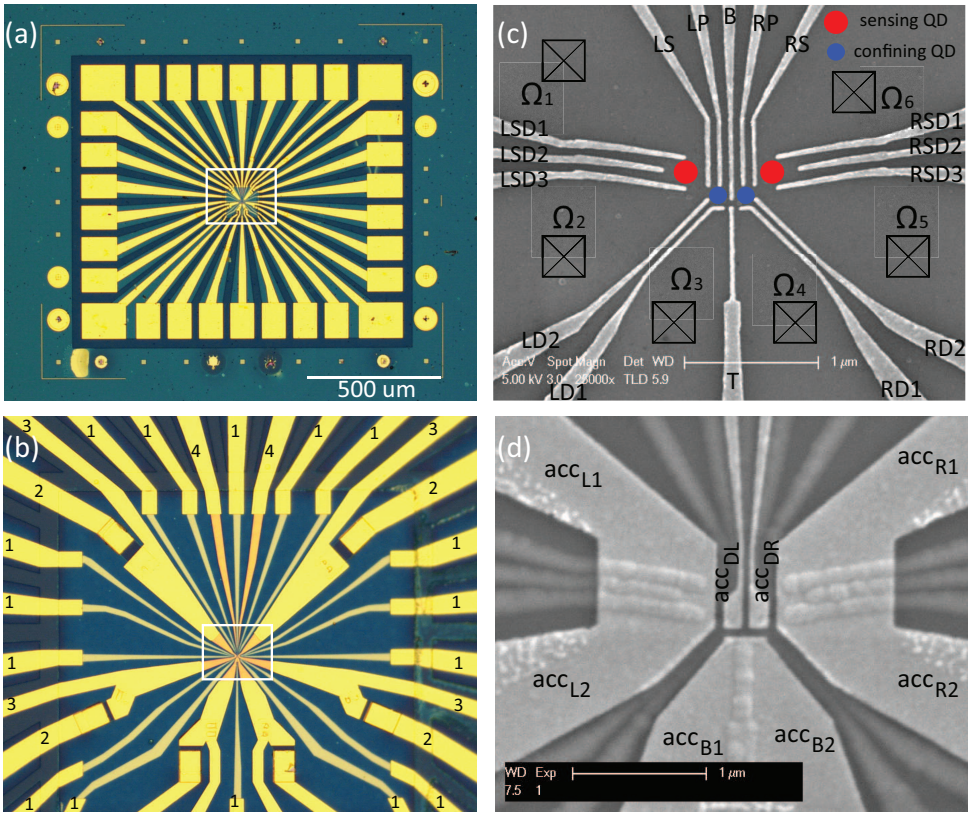

Figure 4.8: (a-b) Optical images of a typical DQD device on a Si/SiGe undoped heterostructure. We can distinguish metallic structures representing depletion gates (1), Ohmic leads (2), accumulation gates for the electron reservoirs (3) and for the QDs (4). (c) SEM image of fine gates defining a DQD on a silicon dummy sample. The fine gates are made of 5 nm Ti and 25 nm Au, deposited by evaporation. (d) SEM image of fine accumulation gates on top of fine depletion gates. The accumulation gates (5 nm Ti and 30 nm Au) are separated by 80 nm Al_2O_3 from the fine depletion gates. The fine depletion gates are visible in the background and through the relieved accumulation gates.

Panel (c) of Fig. 4.8 reports a SEM picture of a fine gate geometry used to realize a DQD (indicated by blue dots) and two sensing dots (indicated by red dots). This geometry has been proposed by our collaborator at University of Wisconsin, to achieve with each metallic gate a more independent control of one specific characteristic parameter of the final QD device, such as tunneling rate of each tunnel barrier and local dot electrochemical potentials:
- the gates T-B control the inter-dot tunnel barrier;
- the gates LS (RS) and LD2 (RD2) control the second tunnel barrier of each QD with the left (right) electron reservoir;
- the gates LP and RP are used to tune the local electrochemical potential of the left and right QD respectively;
- the three gates LSD1-2-3 (RSD1-2-3) are used to define and tune the left (right) read-

out dot sensor;
The six black squares Fig. 4.8(c) schematically represent the ohmic contacts of the device, realized by ion implantation.

4.3.2. PRELIMINARY QD MEASUREMENTS

The first step towards the realization of a working QD device consists of testing the 2DEG accumulation capability.
Panel (a) of Fig. 4.9 reports a typical accumulation curve for a device similar to the one reported in Fig. 4.8(c), realized recording the current flowing from Ω_1 to Ω_2 (see inset) by applying a constant bias voltage (~250 μeV). For an initial low positive voltage applied on gate acc$_{L1}$ (see Fig. 4.8(d)), the Si QW portion between the ion implanted regions (below the gate acc$_{L1}$) is in the insulating phase, so the measured current is almost zero. The threshold voltage (V_{thr}) of this device is around +200 mV (see Fig. 4.9(a))[22]. Above V_{thr} the Si QW starts to be conductive and then, we can measure a finite current running between the ion implanted regions, below the accumulation gate. By keeping on increasing the voltage we induce a higher electron density that will better screen the electrostatic disorder. As a result, the electron mobility of the channel increases. Above a certain maximum voltage applied to the accumulation gate (V_{sat}) the electron density accumulated in the Si QW saturates and any further enhancement of the accumulation gate voltage cannot produce any further increment of the electron density. This is believed to be related to the formation, for accumulation voltage around V_{sat}, of a second conductive layer, parallel to the main 2DEG and with much lower mobility. This extra conduction channel can be positioned at the interface between the oxide and the Si cap layer or inside the Si cap itself, if it is quite thick [50]. Any increment of the accumulation gate voltage contributes to increase the population of this second 2DEG that will electrostatically screen the Si QW region. We also observed that usually the first accumulation curve is quite hysteretic and unstable. By repeating it several times the device tends to stabilize.

After accumulating the left and right electron reservoirs, the next step of a standard device tuning procedure consists of activating the accumulation gates of the QDs region. When these gates are biased very positively we can create a continuum for the 2DEG connecting this region with the respective reservoir. By properly tuning the negative voltage applied on the fine gates we can create two tunnel barriers that define a QD. This is usually done by pinching off, for example, the 2DEG between gates T-B and between LS-LD1 in Fig. 4.8(c). By symmetrically increasing the negative voltage applied to the two gates defining a point contact (PC), it is possible to define a constriction in the 2DEG below (Chapter 2) that represents a tunnel barrier between the electron reservoirs at the two sides of the PC. By increasing the negative voltage on the PC gates we can make this tunnel barrier more opaque, till completely close it. A typical pinch-off trace between two gates of a SiGe device is reported in Fig. 4.9(b). Due to the low mobility of this kind of structure, the electron mean free path is comparable to the PC channel size. As a result, an unintentional QD confinement potential can be naturally created during the pinch-off process, causing Coulomb blockade-like features on the pinch-off trace of a

[22] V_{thr} depends from the quality and from the specifics of each heterostructure and from the capacitive coupling between the accumulation gate and the QW region.

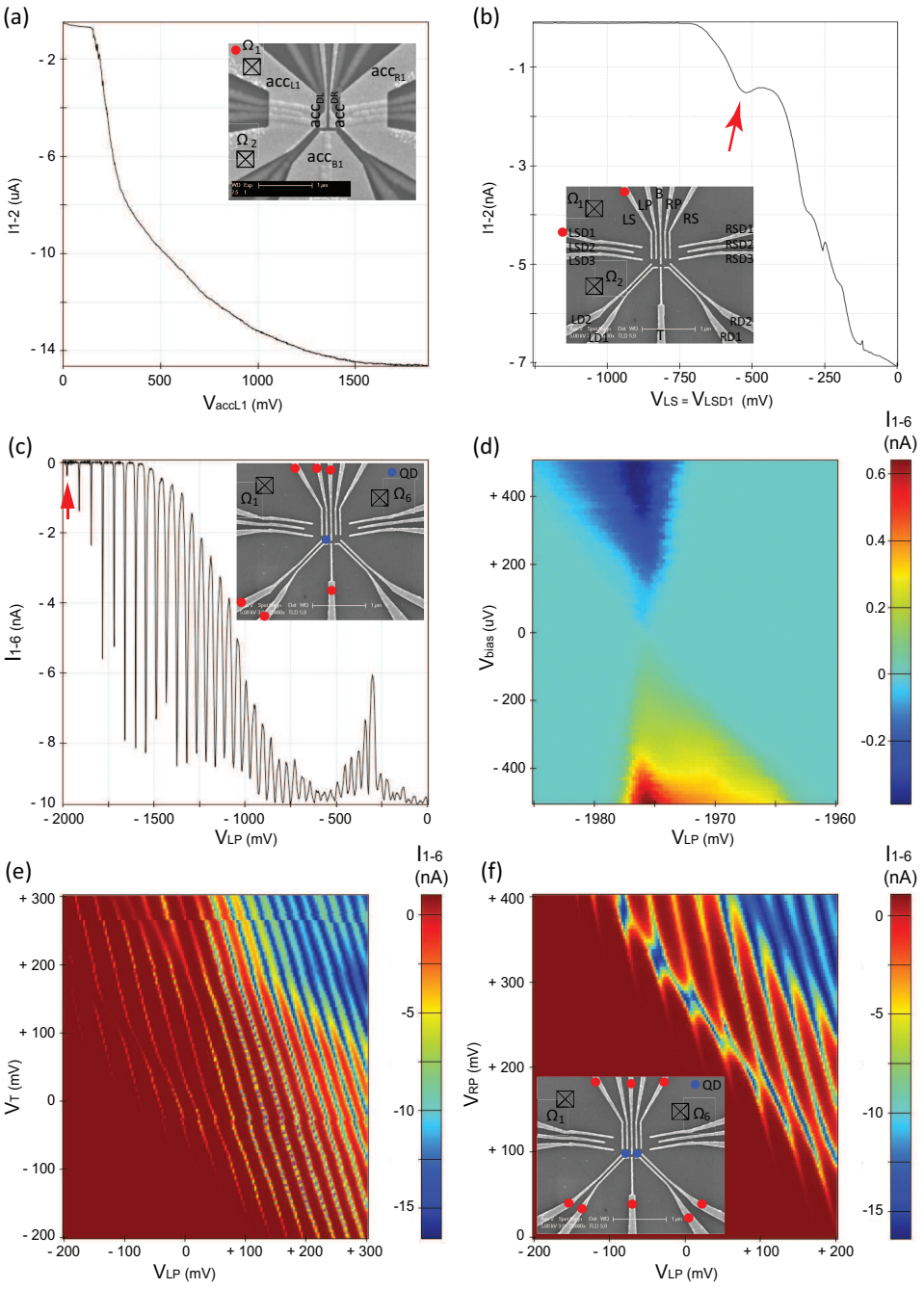

Figure 4.9: Preliminary test of a QD/DQD device. The red dot and the crossed-square, in each inset, indicate respectively the gates and Ohmic contacts used in the measurement (realized at ~15 mK). (a) Accumulation trace (negative voltage bias). (b) Pinch of trace; the red arrow indicates a Coulomb Blockade feature. (c) Coulomb oscillations, measured in transport through the left QD (indicated by the blue dot in the inset). (d) Coulomb diamond recorded for the last visible Coulomb peak, indicated by the red arrow in panel (c). (e) Coulomb oscillations recorded by sweeping the voltage on both gates LP and T. (e) Transport current through a DQD (blue dots in the inset).

single PC, as clearly visible in panel (b), indicated by the red arrow.

A typical Coulomb Blockade measurement for electrons confined in a QD is reported in Fig. 4.9(c). Panel (d) of the same figure shows, instead, the peculiar Coulomb diamond structure, obtained by changing the bias across the single QD (y-axis) for the last Coulomb peak indicated by the red arrow in the panel (c). From this figure it is possible to estimate the electron temperature of the electron reservoirs, the orbital energy of the QD, and the capacitive coupling ratio between the dot and the leads and the gate used to shift the QD electrochemical potential (see Fig. 2.2(f) of Chapter 2) [53, 54].
It is also possible to keep track of the Coulomb oscillations as a function of the voltage applied to two of the lateral fine gates, defining the QD (see Fig. 4.9(e)). As explained in Chapter 2, the capacitive coupling between each gate and the electrons confined into the QD determines the shift of the QD electrochemical potential. From the slopes of the Coulomb peaks in panel (e) it is possible to estimate the ratio between the capacitive coupling of the two gates, representing the two axes, with the dot.
Furthermore, by reducing the positive voltage applied previously on the accQD1 and properly tuning the voltages on the rest of the fine gates, we can also reach a DQD configuration. Panel (e) in Fig. 4.9 reports a typical transport measurement for a DQD system, with clear features of the 'honeycomb' charge stability diagram[23] (see Fig. 2.3(c) of Chapter 2).

REFERENCES

[1] T. Ando, A. B. Fowler and F. Stern, Rev. Mod. Phys. **54**, 437 (1982).

[2] T. Ihn, 'Semiconductor Nanostructures: Quantum states and electronic transport', Oxford Scholarship Online (2010).

[3] C. B. Simmons, J. R. Prance, B. J. Van Bael, T. S. Koh, Z. Shi, D. E. Savage, M. G. Lagally, R. Joynt, Mark Friesen, S. N. Coppersmith, and M. A. Eriksson, Phys. Rev. Lett. **106**, 156804 (2011).

[4] C. B. Simmons, M. Thalakulam, B. M. Rosemeyer, B. J. V. Bael, E. K. Sackmann, D. E. Savage, M. G. Lagally, R. Joynt, Mark Friesen, S. N. Coppersmith, and M. A. Eriksson, Nano Lett. **9**, 3234 (2009).

[5] J. R. Prance, Z. Shi, C. B. Simmons, D. E. Savage, M. G. Lagally, L. R. Schreiber, L. M. K. Vandersypen, Mark Friesen, R. Joynt, S. N. Coppersmith, and M. A. Eriksson, Phys. Rev. Lett. **108**, 046808 (2012).

[6] D. Kim, Z. Shi, C. B. Simmons, D. R. Ward, J. R. Prance, T. S. Koh, J. K. Gamble, D. E. Savage, M. G. Lagally, Mark Friesen, S. N. Coppersmith, and M. A. Eriksson, Nature **511**, 70 (2014).

[7] Z. Shi, C. B. Simmons, D. R. Ward, J. R. Prance, X. Wu, T. S. Koh, J. K. Gamble, D. E. Savage, M. G. Lagally, Mark Friesen, S. N. Coppersmith, and M. A. Eriksson, Nat. Commum. **5**, 3020 (2014).

[23] We are investigating the DQD system in transport; therefore the 'honeycomb' stability diagram results to be visible due to cotunneling processes [54], which usually take place for very transparent tunnel barriers.

[8] V. Umansky, M. Heiblum, Y. Levinson, J. Smet, J. Nübler, and M. Dolev, Journal of Crystal Growth **311**, 1658 (2009).

[9] A. B. Fowler, F. F. Fang, W. E. Howard, and P. J. Stiles, Phys. Rev. Lett. **16**, 901 (1966).

[10] K. v. Klitzing, G. Dorda, and M. Pepper Phys. Rev. Lett. **45**, 494 (1980).

[11] K. Eng, R. N. McFarland, and B. E. Kane, Appl. Phys. Lett. **87**, 052106 (2005).

[12] S. V. Kravchenko and M. P. Sarachik, Reports on Progress in Physics **67**, 1 (2004).

[13] B. Hu, M. M. Yazdanpanah, B. E. Kane, E. H. Hwang, and S. Das Sarma, Phys. Rev. Lett. **115**, 036801 (2015).

[14] F. Schäffler, Semicond. Sci. Technol. **12**, 1515 (1997).

[15] G. Abstreiter, H. Brugger, T. Wolf, H. Jorke, and H. J. Herzog, Phys. Rev. Lett. **54**, 2441 (1985).

[16] J. G. Fiorenza et al., Semicond. Sci. Technol. **19**, L4 (2004).

[17] K. Ismail, F. K. LeGoues, K. L. Saenger, M. Arafa, J. O. Chu, P. M. Mooney, and B. S. Meyerson, Phys. Rev. Lett. **73**, 3447 (1994).

[18] D. Monroe, Y. H. Xie, E. A. Fitzgerald, P. J. Silverman, and G. P. Watson, Journal of Vacuum Science and Technology B **11**, 1731 (1993).

[19] E. A. Fitzgerald, Y. H. Xie, M. L. Green, D. Brasen, A. R. Kortan, J. Michel, Y. J. Mii and B. E. Weir, Appl. Phys. Lett. **59**, 811 (1991).

[20] K. Ismail, M. Arafa, K. L. Saenger, J. O. Chu, and B. S. Meyerson, Appl. Phys. Lett. **66**, 1077 (1995).

[21] N. Sugii, K. Nakagawa, Y. Kimura, S. Yamaguchi, and M. Miyao, Semiconductor Science and Technology **13**, A140 (1998).

[22] T. M. Lu, D. C. Tsui, C. H. Lee, and C. W. Liu, Appl. Phys. Lett. **94**, 182102 (2009).

[23] S. H. Huang, T. M. Lu, S. C. Lu, C. H. Lee, C. W. Liu, and D. C. Tsui, Appl. Phys. Lett. **101**, 042111 (2012).

[24] J. Y. Li, C. T. Huang, L. P. Rokhinson, and J. C. Sturm, Appl. Phys. Lett. **103**, 162105 (2013).

[25] D. Laroche, S. H. Huang, E. Nielsen, Y. Chuang, J. Y. Li, C. W. Liu and T. M. Lu, AIP Advances **5**, 107106 (2015).

[26] M. Yu. Melnikov, A. A. Shashkin, V. T. Dolgopolov, S. H. Huang, C. W. Liu and S. V. Kravchenko, JETP Letters **100**, 114 (2014).

[27] M. Yu. Melnikov, A. A. Shashkin, V. T. Dolgopolov, S. H. Huang, C. W. Liu and S. V. Kravchenko, Appl. Phys. Lett. **106**, 092102 (2015).

[28] X. Mi, T. M. Hazard, C. Payette, K. Wang, D. M. Zajac, J. V. Cady, and J. R. Petta, Phys. Rev. B **92**, 035304 (2015).

[29] D. M. Paskiewicz, B. Tanto, D. E. Savage, M. G. Lagally, ACS Nano **5**, 5814 (2011).

[30] D. M. Paskiewicz, D. E. Savage, M. V. Holt, P. G. Evans, M. G. Lagally, Sci. Rep. **4**, 4218 (2014).

[31] Y. S. Li, P. Sookchoo, X. Cui, R. T. Mohr, D. E. Savage, R. H. Foote, R. B. Jacobson, J. R. Sanchez-Perez, D. M. Paskiewicz, X. Wu, D. R. Ward, S. N. Coppersmith, M. A. Eriksson, and M. G. Lagally, ACS Nano **9**, 4891 (2015).

[32] E. Kasper, A. Schuh, G. Bauer, B. Holländer, H. Kibbel, J. Cryst. Growth **157**, 68 (1995).

[33] T. Berer, D. Pachinger, G. Pillwein, M. Mühlberger, H. Lichtenberger, G. Brunthaler and F. Schäffler, Appl. Phys. Lett. **88**, 162112 (2006).

[34] L. M. Giovane, H. C. Luan, A. M. Agarwal, and L. C. Kimerling, Appl. Phys. Lett. **78**, 541 (2001).

[35] R. People and J. C. Bean, Appl. Phys. Lett. **47**, 322 (1985).

[36] S. B. Samavedam, W. J. Taylor, J. M. Grant, J. A. Smith, P. J. Tobin, A. Dip, A. M. Phillips and R. Liu, J. Vac. Sci. Technol. B **17**, 1424 (1999).

[37] J. W. Matthews and A. E. Blakeslee, J. Cryst. Growth **27**, 118 (1974).

[38] F. A. Zwanenburg, A. S. Dzurak, A. Morello, M. Y. Simmons, L. C. L. Hollenberg, G. Klimeck, S. Rogge, S. N. Coppersmith, and M. A. Eriksson, Rev. Mod. Phys. **85**, 961 (2012).

[39] D. J. Paul, Semiconductor Science and Technology **19**, R75 (2004).

[40] C. Euaruksakul, Z. W. Li, F. Zheng, F. J. Himpsel, C. S. Ritz, B. Tanto, D. E. Savage, X. S. Liu, and M. G. Lagally, Phys. Rev. Lett. **101**, 147403 (2008).

[41] F. Walvoort, 'Fabrication and characterization of double quantum dots in an undoped Si-SiGe heterostructure', Master thesis, Delft University of Technology (2014).

[42] P. M. Mooney and J. O. Chu, Annu. Rev. Mater. Sci **30**, 335 (2000).

[43] M. A. Eriksson, Mark Friesen, S. N. Coppersmith, R. Joynt, L. J. Klein, K. A. Slinker, C. Tahan, P. M. Mooney, J. O. Chu, and S. J. Koester, Quant. Inf. Proc. **3**, 133 (2004).

[44] B. M. Maune et al., Nature **481**, 344 (2012).

[45] J. Liu, T. M. Lu, J. Kim, K. Lai, D. C. Tsui, and Y. H. Xie, Appl. Phys. Lett. **92**, 112113 (2008).

[46] R. People and J. C. Bean, Appl. Phys. Lett. **47**, 322 (1985).

[47] R. People and J. C. Bean, Appl. Phys. Lett. **49**, 229 (1985).

[48] M. L. Lee, E. A. Fitzgerald, M. T. Bulsara, M. T. Currie, and A. Lochtefeld, Jour. of Appl. Phys. **97**, 011101 (2005).

[49] K. Sawano, K. Kawaguchi, T. Ueno, S. Koh, K. Nakagawa, Y. Shiraki, Materials Science and Engineering: B **89**, 406 (2002).

[50] A. Sareen, Y. Wang, U. Sodervall, P. Lundgren, and S. Bengtsson, Journ. of Appl. Phys. **93**, 3545 (2003).

[51] H. C. Lin, P. D. Ye and G. D. Wilk, Appl. Phys. Lett. **87**, 182904 (2005).

[52] K. Lai, P. D. Ye, W. Pan, D. C. Tsui, S. A. Lyon, M. Muhlberger, and F. Schäffler, Appl. Phys. Lett. **87**, 142103 (2005).

[53] R. Hanson, L. P. Kouwenhoven, J. R. Petta, S. Tarucha, and L. M. K. Vandersypen, Rev. Mod. Phys. **79**, 1217 (2007).

[54] W. G. van der Wiel, S. De Franceschi, J. M. Elzerman, T. Fujisawa, S. Tarucha, and L. P. Kouwenhoven, Rev. Mod. Phys. **75**, 1 (2002).

5

ELECTRICAL CONTROL OF A LONG-LIVED SPIN QUBIT IN A SI/SIGE QUANTUM DOT

Nanofabricated quantum bits permit large-scale integration but usually suffer from short coherence times due to interactions with their solid-state environment [1]. The outstanding challenge is to engineer the environment so that it minimally affects the qubit, but still allows qubit control and scalability. Here we demonstrate a long-lived single-electron spin qubit in a Si/SiGe quantum dot with all-electrical two-axis control. The spin is driven by resonant microwave electric fields in a transverse magnetic field gradient from a local micromagnet [2], and the spin state is read out in single-shot mode [3]. Electron spin resonance occurs at two closely spaced frequencies, which we attribute to two valley states. Thanks to the weak hyperfine coupling in silicon, a Ramsey decay timescale of 900 ns is observed, almost two orders of magnitude longer than the intrinsic timescales in GaAs quantum dots [4, 5], while gate operation times are comparable to those reported in GaAs [6–8]. The spin echo decay time is around 40 μs both with one and with four echo pulses, possibly limited by intervalley scattering. These advances strongly improve the prospects for quantum information processing based on quantum dots.

The work in this chapter has been published as: E. Kawakami*, P. Scarlino*, D. R. Ward, F. R. Braakman, D. E. Savage, M. G. Lagally, Mark Friesen, S. N. Coppersmith, M. A. Eriksson and L. M. K. Vandersypen, Nature Nanotech. **9**, 666 (2014).

5.1. INTRODUCTION

The proposal by Loss and DiVincenzo [9] to define quantum bits by the state of a single electron spin in a gate-defined semiconductor quantum dot has guided research for the past 15 years [7]. Most progress was made in well-controlled III-V quantum dots, where spin manipulation with two [5, 10], three [11] and four [12] dots has been realized, but gate fidelities and spin coherence times are limited by the unavoidable interaction with the fluctuating nuclear spins in the host substrate [4, 5]. While the randomness of the nuclear spin bath could be mitigated to some extent by feedback techniques [13], eliminating the nuclear spins by using group IV host materials offers the potential for extremely long electron spin coherence times. For instance, a dynamical decoupling decay time of half a second was observed for an electron bound to a P impurity in 28Si [14].

Much effort has been made to develop stable spin qubits in quantum dots defined in carbon nanotubes [15, 16], Ge/Si core/shell nanowires [17], Si MOSFETs [18, 19] and Si/SiGe 2D electron gases [20–22]. However, coherent control in these group IV quantum dots is so far limited to a Si/SiGe singlet-triplet qubit with a spin dephasing time of 360 ns but single-axis control only [22] and a carbon nanotube single-electron spin qubit, with two-axis control but a Hahn echo decay time of only 65 ns [15].

5.2. DEVICE AND MEASUREMENT SETUP

Our device is based on an undoped Si/SiGe heterostructure with two layers of electrostatic gates (Fig. 5.1(a)). Compared to conventional, doped heterostructures, this technology strongly improves charge stability [22]. First, accumulation gates ($V_a \sim +150$ mV) are used to induce a two-dimensional electron gas (2DEG) in a 12 nm wide Si quantum well 37 nm below the surface. Second, a set of depletion gates, labelled 1-12 in Fig. 5.1(a), is used to form a single or double quantum dot in the 2DEG, flanked by a quantum point contact and another dot intended as charge sensors. Two 1 μm-wide, 200 nm-thick, and 1.5 μm-long Co magnets are placed on top of the accumulation gates (Fig. 5.1(a)), providing a stray magnetic field with components $B_{\parallel}$ and $B_{\perp}$, parallel and perpendicular to the external magnetic field, respectively. The sample is attached to the mixing chamber of a dilution refrigerator with base temperature ~25 mK and the electron temperature estimated from transport measurements is ~150 mK (not applying microwaves). We tune the right dot to the few-electron regime (Supplementary Fig. 5.5(c)) and adjust the tunnel rate between the dot and the reservoir to ~1 kHz, so that dot-reservoir tunnel events can be monitored in real time using the sensing dot (Fig. 5.1(a)). The left dot is not used in the experiment and the constrictions between gates 4 and 8 and between 3 and 10 are pinched off. Gates 3, 8, 9 and 11 are connected to high-frequency lines via bias-tees. Microwave excitation applied to one of these gates oscillates the electron wave function back and forth in the dot. Because of the gradient $dB_{\perp}/dx \sim 0.3$ mT/nm (Fig. 5.1(b)), the electron is then subject to an oscillating magnetic field. Electric dipole spin resonance (EDSR) occurs when the microwave frequency matches the electron spin precession frequency in the magnetic field at the dot position [2, 6].

All measurements shown here use 4-stage voltage pulses applied to gate 3 (Fig. 5.1(c)): (1) initialization to spin-down [4 ms, fidelity ~ 0.95 (Supplementary Section 5.6.10)], (2) spin manipulation through microwave excitation of gate 8 (1 ms), (3) single-shot spin

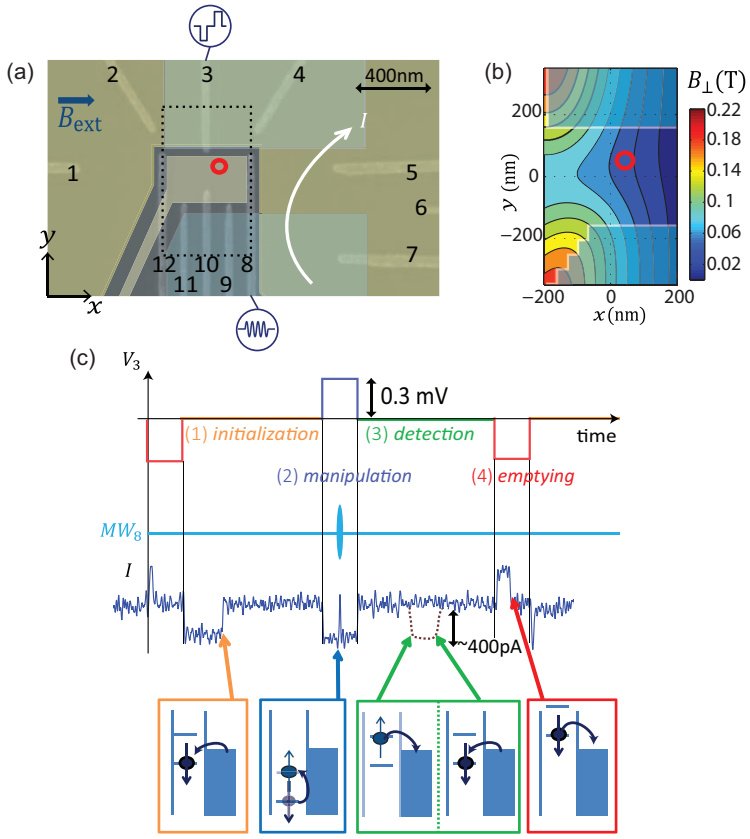

Figure 5.1: Device schematic and measurement cycle. (a) False color device image showing a fabricated pattern of split gates, labeled 1-12. For this experiment we create a single quantum dot (QD), estimated location at the red circle) and a sensing dot (SD). The current I is measured as a function of time for a fixed voltage bias of -600 μeV. The voltage pulses are applied to gate 3 and the microwaves are applied to gate 8. The blue semi-transparent rectangles show the position of two Co 200 nm thick micromagnets. The yellow shaded pieces show the location of two accumulation gates, one for the reservoirs and another for the double quantum dot region. (b) Numerically computed magnetic field component perpendicular to the external field, induced by the micromagnet in the plane of the Si quantum well, for fully magnetized micromagnets. The straight solid lines indicate the edges of the micromagnet as simulated. The region shown is outlined with dotted lines in panel (a). (c) Microwave (MW) and gate voltage pulse scheme (see main text) along with an example trace of recorded during the pulse cycle and cartoons illustrating the dot alignment and tunnel events. During stages (1) and (3), the Fermi level in the reservoir is set in between the spin-down and spin-up energy levels so that only a spin-down electron can tunnel into the dot and only a spin up electron can tunnel out 3. During stage (2), the dot is pulsed deep into Coulomb blockade, in order to minimize photon-assisted tunneling. The MW burst of duration t_p ends about 100 ns-500 ns before the detection stage. When a step is observed during stage (3), see the dotted line, we count the electron as spin-up. Stage (4) serves to keep the DC component of the pulse zero and to symmetrize pulse distortions from the bias tee. In the process, the QD is emptied. The spike during the manipulation stage is due to the influence of the microwave burst (here 700 μs) on the detector.

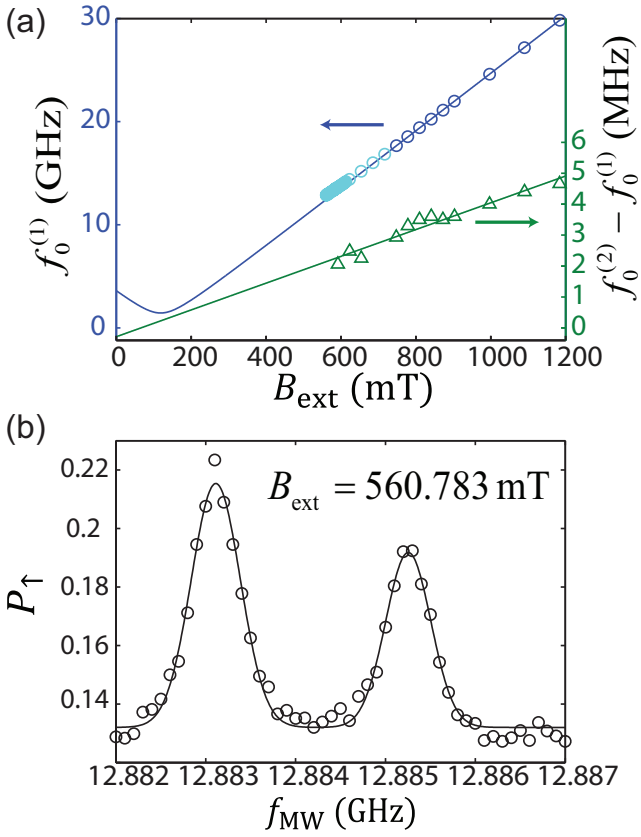

Figure 5.2: Qubit spectroscopy. (a) Measured microwave frequency that matches the electric dipole spin resonance (EDSR) condition $f_0^{(1)}$ (dark blue and light blue circles) and the difference between the two resonance frequencies $f_0^{(2)} - f_0^{(1)}$ (green triangles) as a function of externally applied magnetic field. The 6 points where f_{MW} > 6GHz are measured by two-photon transitions [25]. The microwave burst time $t_p = 700\mu s \gg T_2^*$, effectively corresponding to continuous wave (CW) excitation (here we used low power excitation, P = -33 dBm to -10 dBm at the source, decreasing with lower microwave frequency). The upper of the two resonances in panel (b) is shown. The blue solid curve is a fit to the dark blue circles using eq. 5.1. The light blue circles are excluded from the fit; presumably the micromagnet begins to demagnetize here. The green line is a linear fit to the green triangles. (b) Measured spin-up probability $P_\uparrow$ as a function of applied microwave frequency f_{MW} for B_{ext} = 560.782 mT (P = -33 dBm), averaged over 200 minutes, i.e. 1200000 single-shot measurements.

read-out [4 ms, fidelity ~ 0.95 (Supplementary Section 5.6.10)], and (4) a compensation/empty stage (1 ms). By repeating this cycle, typically 150-1000 times, we obtain statistics of how often an electron leaves the dot during the detection stage, giving the spin-up probability at the end of the manipulation stage.

5.3. ELECTRON SPIN RESONANCE SPECTROSCOPY

The measured spin resonance frequency as a function of applied magnetic field is shown in Fig. 5.2(a). We can extract the electron g-factor using the relation:

$$hf_0 = g\mu_B B_{local}, \tag{5.1}$$

where $B_{local} = \sqrt{(B_{ext} + B_\parallel)^2 + B_\perp^2}$, h is Planck's constant and μ_B is the Bohr magneton. From fits to eq. 5.1 (blue curve in Fig. 5.2(a)), we find $g = 1.998 \pm 0.002$, where we used $B_\parallel$= 120 mT and $B_\perp$= 50 mT, based on numerical simulation of the stray magnetic field from the micromagnet at the estimated dot location (Supplementary Section 5.6.5).

Surprisingly, when measuring the EDSR peak at a sufficiently low power to avoid power broadening, we resolve two lines, separated by 2-4 MHz in the range B_{ext} =0.55-1.2 T (Fig. 5.2(b)). We return to the origin of this splitting later.
Fitting each resonance peak with a Gaussian function yields $\delta f^{(2)}_{FWHM} = 0.63 \pm 0.06$ MHz for the higher-energy transition at frequency $f_0^{(2)}$ and $\delta f^{(1)}_{FWHM} = 0.59 \pm 0.56$ for the lower-energy transition at frequency $f_0^{(1)}$. From this line width, we extract a dephasing time

$$T_2^* = \frac{\sqrt{2}\hbar}{g\mu_B\sigma_B} = \frac{2ln(2)}{\pi\delta f_{FWHM}} = 840 \pm 70ns \tag{5.2}$$

[7], 30-100 times longer than T_2^* in III-V dots [4, 5, 7, 8]. This dephasing timescale can be attributed to the random nuclear field from the 0.05 29Si atoms in the substrate with standard deviation $\sigma_B = 9.6$ μT, consistent with theory [23]. Previous T_2^* measurements in Si/SiGe dots [22, 24] gave somewhat shorter values of 220 ns to 360 ns. T_2^* is expected to scale with the square root of the number of nuclear spins the electron wavefunction overlaps with. Considering these other measurements were done on double dots, this would imply variations in the volume per dot up to a factor of 7, if nuclear spins were dominating the decay. Given the presence of a magnetic field gradient $dB_\parallel/dx \sim 0.2$ mT/nm, the line width also gives an upper bound on the electron micromotion induced by low-frequency charge noise of ~50 pm (rms).

5.4. COHERENT CONTROL OF ELECTRON SPIN AND SPIN ECHO

Coherent control of the electron spin is achieved by applying short high-power microwave bursts of duration t_p. Figure 5.3(a) shows the measured spin-up probability, $P_\uparrow$, as a function of f_{MW} and burst time t_p, which exhibits the chevron pattern that is characteristic of high-quality oscillations (here two partly overlapping patterns). On resonance, the spin rotates at the bare Rabi frequency, f_1. When detuned away from resonance by $\Delta f = f_{MW} - f_0$, the spin rotates about a tilted axis, the oscillation frequency increases as $\sqrt{\Delta f^2 + f_1^2}$, and the visibility is reduced. The fast Fourier transform over the microwave

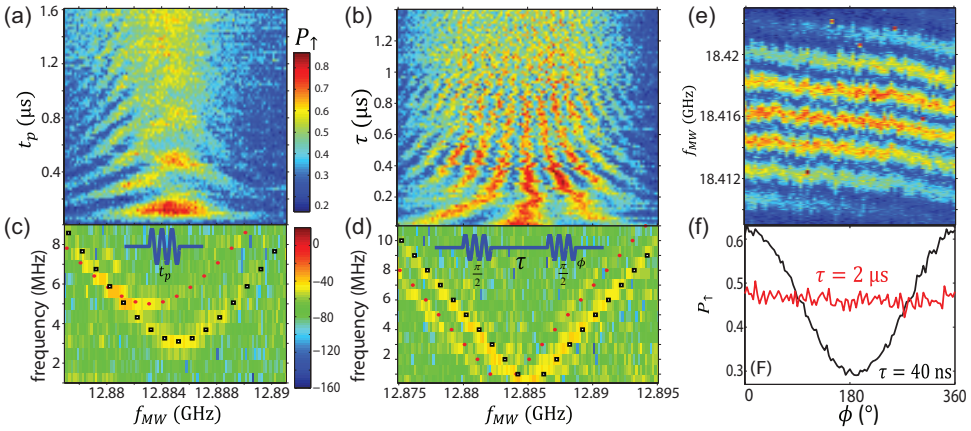

Figure 5.3: Universal qubit control. (a) Measured spin-up probability, $P_\uparrow$, as a function of f_{MW} and burst time t_p (B_{ext} = 560.782 mT, P=16.4 dBm). (b) Measured spin-up probability, $P_\uparrow$, as a function of f_{MW} and waiting time τ (B_{ext} = 560.782 mT, P=16.4 dBm) between two $\pi/2$ (75 ns) pulses with equal phase, showing Ramsey interference (Color map as in (a)). (c) Fourier transform over the microwave burst time t_p of Fig. 5.3(a) showing a hyperbolic dependence (black rectangles and red circles) as a function of f_{MW} for each transition, $f_0^{(1)}$ and $f_0^{(2)}$. Inset: microwave pulse scheme used in (a). (d) Fourier transform over the waiting time τ of Fig. 5.3(b) showing two linear patterns superimposed, with vertices at $f_0^{(1)}$ and $f_0^{(2)}$. Inset: microwave pulse scheme used in (b,d,e,f). (Color map as in (c)) (e) Measured spin-up probability, $P_\uparrow$, as a function of f_{MW} and the relative phase ϕ between two microwave pulses for τ = 400 ns (B_{ext} = 763.287 mT, P=18.8 dBm). (Color map as in (a)) (f) Ramsey signal as a function of the relative phase ϕ between the two microwave pulses for τ = 400 ns (black curves) and $\tau = 2$ μs (red curves) (B_{ext} = 763.287 mT, P=18.8 dBm, $f_{MW} = f_0^{(2)}$ = 18.41608 GHz).

burst time of the data in Fig. 5.3(a) is shown in Fig. 5.3(c) and exhibits the expected hyperbolic dependence as a function of Δf for both transitions, $f_0^{(1)}$ and $f_0^{(2)}$. We fit both hyperbolae with one free parameter f_1 each (black rectangles and red circles), giving $f_1^{(1)} = 5.0 \pm 0.6$ MHz ($B_1 \sim 0.18$ mT) and $f_1^{(2)} = 3.1 \pm 0.6$ MHz (errors arise from the finite number of points in the FFT) for the respective transitions. These single-spin Rabi frequencies are comparable to those observed in GaAs [6, 8]. The relative amplitude of the oscillations at $f_0^{(1)}$ and $f_0^{(2)}$ is about 30/70; note that despite its lower weight, the peak at $f_0^{(1)}$ is tallest in Fig. 5.2(b), since its Rabi frequency is a factor of 1.5 ± 0.2 higher than that of the other peak (Supplementary Section 5.6.8). The extracted Rabi frequencies of both transitions are proportional to the microwave amplitude, as expected (Supplementary Fig. 5.9).

The observed decay of the Rabi oscillations cannot be explained only by the spread in the Larmor frequency, σ_B. Numerical simulations of the Rabi oscillations give good agreement with the measurements of Fig. 5.3(a) when including a variation in the Rabi frequency, $\sigma_{Rabi} \sim 0.25$ MHz (Supplementary Section 5.6.7). The fluctuations in the transverse nuclear field [25] are too small to explain this spread. Instead, instrumentation noise could be responsible. Modeling the gate operation taking into account f_1, σ_B, and σ_{Rabi}, we estimate that the fidelity for flipping a spin from down to up is 0.99 (0.97) for an electron spin resonant at $f_1^{(1)}$ ($f_1^{(2)}$). For an electron in a 30/70 statistical mixture of the two resonance conditions, the fidelity is ~0.80 (Supplementary Section

5.6.10).

Two-axis control of the spin is demonstrated by varying the relative phase ϕ of two $\pi/2$ microwave bursts resonant with $f_1^{(2)}$ separated by a fixed waiting time $\tau = 40\text{ns} \ll T_2^*$ (Fig. 5.3(f), black trace). As expected, the signal oscillates sinusoidally in ϕ with period 2π. For $\tau = 2\ \mu\text{s} \gg T_2^*$, the contrast has vanished, indicating that all phase information is lost during the waiting time (Fig. 5.3(f), red trace). Similar measurements with the pulses applied off-resonance by an amount Δf with $\phi = 0$, are expected to show an oscillation with frequency Δf and an envelope that decays on the timescale T_2^*. Because of the presence of two resonance lines just 2.1 MHz apart, the measurement of $P_\uparrow$ versus f_{MW} and τ (Fig. 5.3(b)) shows a superposition of two such patterns. This becomes clear from taking the Fourier transform over the waiting time τ (Fig. 5.3(d)) which shows 2 linear patterns superimposed, with vertices at $f_0^{(1)}$ and $f_0^{(2)}$. The stability of the measurement can be appreciated from Fig. 5.3(e), which shows $P_\uparrow$ versus f_{MW} and the relative phase between the two bursts at $\tau = 400$ ns.

Spin coherence can be extended by spin echo techniques, provided the source of dephasing fluctuates slowly on the timescale of the electron spin dynamics. We perform a Hahn echo experiment, consisting of $\pi/2$, π and $\pi/2$ pulses separated by waiting times $\tau/2$ [7, 20], and record $P_\uparrow$ as a function of the total free evolution time τ (Fig. 5.4(a)). A fit to a single exponential yields a time constant $T_2 = 37 \pm 3\ \mu$s, almost 50 times longer than T_2^*. While this is encouraging, we had expected an even longer T_2 based on the 200 μs Hahn echo decay observed for an electron spin bound to a P-impurity in natural Si [26]. Furthermore, contrary to our expectations for an echo decay dominated by slowly fluctuating nuclear spins, the decay is well-described by a single exponential, with no signatures of a flat top. One possible explanation is that the fluctuations that dominate the echo decay are fast compared to the few μs timescale of the first few data points [27]. Another possible explanation is that the observed decoherence rate reflects the valley switching rate; as soon as the valley switches, the spin resonance frequency jumps by about 2 MHz, and the phase of the spin is randomized (cannot be recovered anymore). Both explanations are consistent with the fact that a four-pulse decoupling pulse sequence does not further extend the decay time (Fig. 5.4(b)). Either way, this implies that the slowly fluctuating nuclear field does not yet limit T_2 [28]. Finally, when we shift the position of the third pulse, the time intervals before and after the echo pulse are no longer equal and coherence is lost, as expected (Fig. 5.4(c)). A fit of this decay with a Gaussian function, gives measured in the time domain, consistent with extracted from the line width.

We now return to the origin of the two resonance lines that are visible in all the measurements. From the individual measurements, we deduce that the higher (lower) frequency resonance contributes to the signal 0.7 (0.3) of the time, indicating that the system does not simply exhibit two resonances but instead switches between two conditions. The splitting between the two lines varies linearly with B_{ext}, corresponding to a difference in g-factors of about 0.015 percent, and an offset in B_{local} between the two resonances of 65 ± 138 mT (Fig. 5.2(a), green triangles). Finally, as mentioned before, the higher-frequency resonance exhibits $\sim$ 1.5 times slower Rabi oscillations than the lower-frequency resonance.

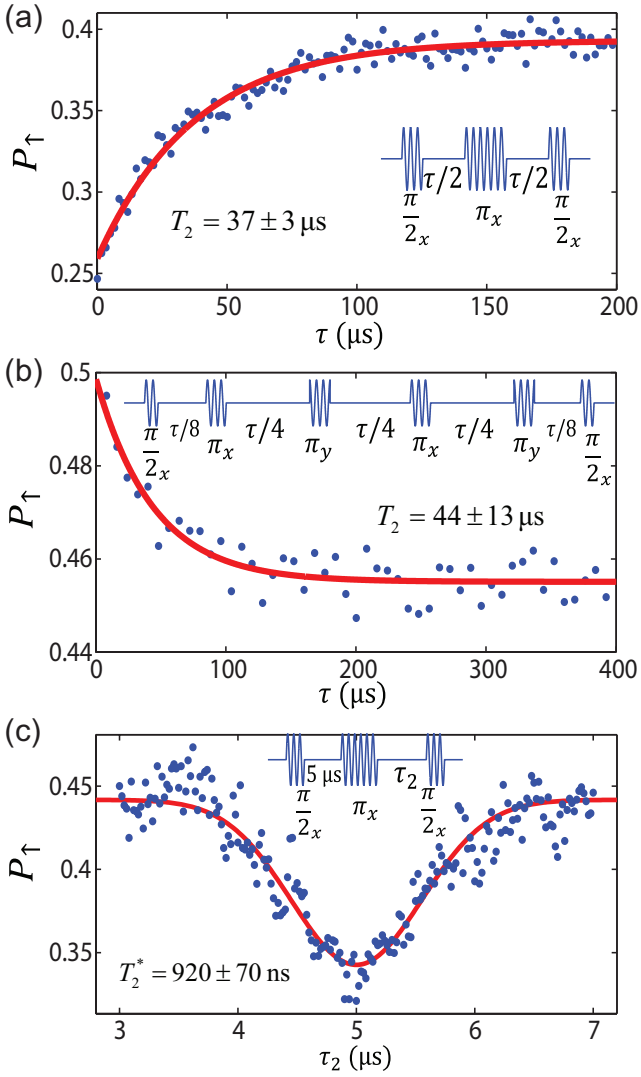

Figure 5.4: Qubit coherence (Here, B_{ext} = 747.710 mT, P=18.4 dBm, $f_{MW} = f_0^{(2)} = 17.695$ GHz, $f_1^{(2)} = 2.7$ MHz). (a) Measured spin-up probability, $P_\uparrow$, as a function of the total free evolution time τ in a Hahn echo experiment (pulse scheme in inset). We did not see a significant difference in the decay when changing the relative phase between the first pulse (77 ns) and the π pulse (150 ns) from $\phi = 0$ to $\phi = 90$. The decay curve is fit well to a single exponential decay. (b) Measured spin-up probability, $P_\uparrow$, as a function of the total free evolution time τ when using four decoupling pulses. (c) Measured spin-up probability, $P_\uparrow$, as a function of the position of the third pulse in the Hahn echo experiment. The free evolution time between the first and second pulse is fixed at 5 μs and that between the second and third pulse is varied from 3 to 7 μs.

5.5. ELECTRON SPIN RESONANCE AND VALLEY STATES IN SI

We propose that the two lines correspond to EDSR with the electron in one or the other of the two lowest valley states, with a 30/70 occupation ratio. This ratio is set either by the injection probabilities into the respective valley states, or by thermal equilibration, depending on whether the valley lifetime is shorter than the few ms delay between injection and manipulation. We note that either way, initialization to a single valley can be achieved when the valley splitting is several times larger than the electron temperature. Initial reports of electric-field controlled valley splittings in Si dots may point to a way of achieving such control [18]. A valley-dependent spin splitting can arise from several sources. Intrinsic spin-orbit coupling is weak in silicon, but the field gradient from the micromagnet admixes spin and orbitals, leading to a renormalization of the g-factor by an amount that depends on the orbital level spacing [2]. Due to valley-orbit coupling, the orbital level spacing in turn depends on the valley. We estimate that this can result in observed valley-dependent g-factor shifts of 0.015 percent (Supplementary Section 5.6.13). The difference in Rabi frequencies can be understood from a valley-dependent orbital level spacing as well. Another mechanism that can account for the observed g-factor shifts is valley-dependent penetration of the Bloch wave function into the SiGe barrier region (Supplementary Section 5.6.13). Other explanations we considered include switching between two separate dot locations, a double dot, and transitions in a two-electron manifold, but these are not consistent with the above observations; see also the supplementary information.

The demonstration of all-electrical single-spin control with coherence times orders of magnitude longer than intrinsic coherence timescales in III-V hosts greatly enhances the promise of quantum dot based quantum computation. The presence of two closely spaced resonances that we attribute to occupation of two different valleys shows the necessity for valley splitting control [18] not only for exchange-based quantum gates [20] but also for single-spin manipulation. The use of a micromagnet facilitates selective addressing of neighboring spins and provides a coupling mechanism of quantum dot spins to stripline resonators that can form the basis for two-qubit gates and a scalable architecture [29].

5.6. SUPPLEMENTARY INFORMATION

5.6.1. SAMPLE FABRICATION

A SEM image of the sample used in this experiment is shown in Fig. 5.5(a). While Fig. 5.1(a) shows only the SEM image of the depletion gates, Fig. 5.5(a) shows also the two accumulation gates and the two micro-magnets. The epitaxial structure, shown in Fig. 5.5(b), is grown by chemical vapor deposition. An 800 nm $Si_{0.7}Ge_{0.3}$ buffer is deposited on a substrate, followed by a 12 nm thick strained Si well. A 32 nm $Si_{0.7}Ge_{0.3}$ layer is then deposited, followed by a 1 nm thick Si cap layer. The sample is undoped; charge carriers are induced in the Si quantum well by application of positive voltages to the accumulation gates, forming a 2DEG [30, 31]. To minimize unwanted accumulation and charge leakage, most of the substrate is etched to below the Si quantum well using reactive ion etching, leaving active material for the dot structures only in small 100 μm × 100 μm mesas. All exposed surfaces are then uniformly coated with 10 nm of Al_2O_3 via atomic

layer deposition (ALD). Ohmic contacts to the 2DEG are created by 20 kV phosphorus implantation activated with a 15 s, 700° C anneal. Two layers of gates, separated by an isolating layer of 80 nm of Al_2O_3 deposited by ALD, are defined by a combination of photo- and electron-beam lithography and deposited by electron-beam evaporation of 1.7 nm Ti/40 nm Au. Two Co micro magnets are defined on top of the upper layer of gates by electron-beam lithography and deposited by electron-beam evaporation of 5 nm Ti/200 nm Co/20 nm Au. The top Au layer minimizes oxidation of the Co material. The sample is glued on a printed circuit board (PCB) with 4 high-frequency lines connected to gates 3, 8, 9 and 11. Those lines are fitted with homemade resistive bias tees on the PCB (R = 10 MΩ, C = 47 nF; 1/RC ~2 Hz) to allow fast pulsing of the gate voltages while also maintaining a DC bias on the gates. The presence of the bias tee is the reason why we use four stage pulses while we could have used two stage pulse [26]. The extra two stages make the voltage level during the initialization and detection stages much less variable. The high-frequency lines contain a 20 dB attenuator at 1 K and a 10 dB attenuator at the mixing chamber.

5.6.2. QUANTUM DOT CHARACTERIZATION AND CHARGE DETECTION

The right dot is tuned to the few-electron regime by adjusting the voltages on gates 3, 4, 5, 8, 9 and 10. Fig. 5.5(c) shows the differential transconductance $\frac{dI}{dV_{gate3}}$ as a function of the voltages on gates 3 and 5. No other charge transitions are observed when pushing the voltage of gate 3 down to -375 mV with the other gate voltages kept at the same values as used in Fig. 5.5(c), which permits us to assign tentative absolute electron numbers as shown in Fig. 5.5(c). The experiment is done at the 0-1 charge transition. This QD presents an addition energy of 9 meV and an orbital level spacing of 450 μeV, estimated by pulse spectroscopy measurements. From the addition energies we extract a dot radius of 21 nm (in the approximation of a circular QD); from the orbital level spacing we deduce 28 nm assuming a harmonic confining potential and again a circular dot. Pulse spectroscopy measurements (not reported here) also show the linear dependence of the Zeeman splitting of the lowest orbital state as a function of external magnetic field, allowing us to calibrate the conversion factor between pulse amplitude and energy.
Thanks to the capacitive coupling between the dot and the sensing QD, the current level of the sensing QD is decreased (increased) by ~400 pA when an electron jumps from the dot to the reservoir (from the reservoir to the dot). We use a room temperature IV converter to record the sensing dot current, I, using a low-pass filter with ~20 kHz cut-off to obtain a sufficient signal-to-noise ratio.

5.6.3. HEATING EFFECTS FROM THE MICROWAVE BURSTS

The application of high power microwave bursts affects the response of the sensing dot, presumably due to heating, and this effect increases with burst time. In order to keep the response constant and get better uniformity in the visibility of the spin oscillations as we vary the burst time during the manipulation stage, we include a second microwave burst at the end of the readout stage such that the total microwave burst duration over a full cycle is kept constant at 2 μs.

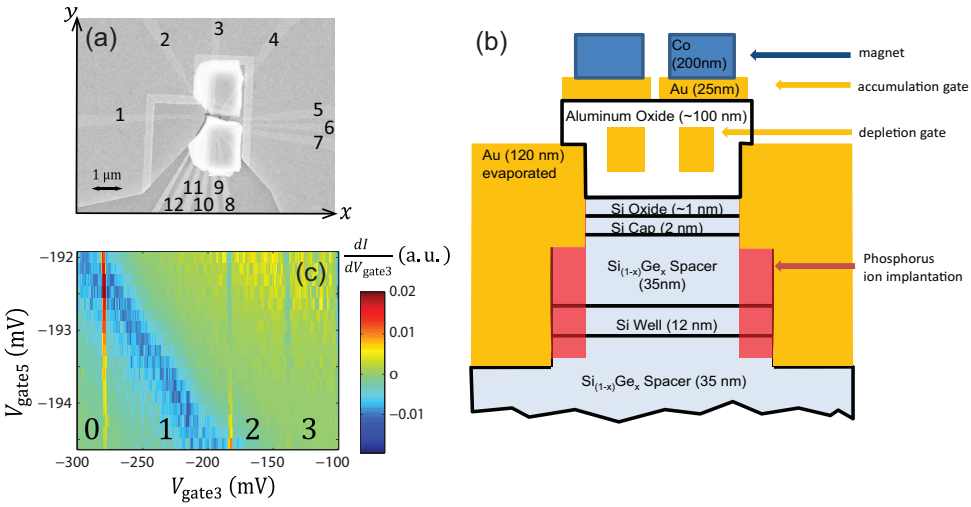

Figure 5.5: Device schematic and charge stability diagram (a) Scanning electron micrograph of the sample. The white regions around the area of the micro magnets are thin pieces of metal that were bent upwards during lift-off. (b) Schematic cross-section of the device. (c) Charge stability diagram of the single dot system, measured via the sensing quantum dot differential transconductance as a function of V_{gate3} and V_{gate5}. The sharp nearly vertical lines correspond to changes in the dot occupation. The broad diagonal blue line corresponds to a Coulomb peak in the sensing dot. The tentative absolute electron numbers 0-3 are shown.

5.6.4. FINDING THE SPIN RESONANCE CONDITION

Before performing the experiment, the electron spin g-factor is not precisely known. The presence of the micromagnet creates further uncertainty in the spin resonance condition. The continuous wave low power EDSR response exhibits very narrow lines, making it easy to miss the resonance when scanning the magnetic field or frequency for the first time. At higher power, the line is power broadened, so larger steps in field or frequency can be taken, accelerating the scan. We used an even more efficient technique, adiabatic rapid passage. This technique was successfully used in quantum dots before 4 and allows one to step the frequency in increments corresponding to the frequency chirp range used for the adiabatic inversion (40-60 MHz in our experiments).

5.6.5. MAGNETIC FIELD GRADIENT INDUCED BY MICROMAGNETS

Figure 5.6 shows the result of a numerical calculation of the magnetic field created by the two micro magnets, along the x, y and z directions, where z is perpendicular to the quantum well and x and y are marked in Fig. 5.5 [33, 34]. The external magnetic field is applied along x. From this simulation, we obtain the magnitudes of the magnetic field and the magnetic field gradient at the position of the dot: $B_{\parallel} = B_x = 120$ mT, $B_{\perp} = \sqrt{B_y^2 + B_z^2} = 50$ mT, $dB_{\perp}/dx \sim 0.3$ mT/nm, $dB_{\perp}/dy \sim 0.04$ mT/nm, $dB_{\parallel}/dx \sim 0.2$ mT/nm and $dB_{\parallel}/dy \sim 0.05$ mT/nm.

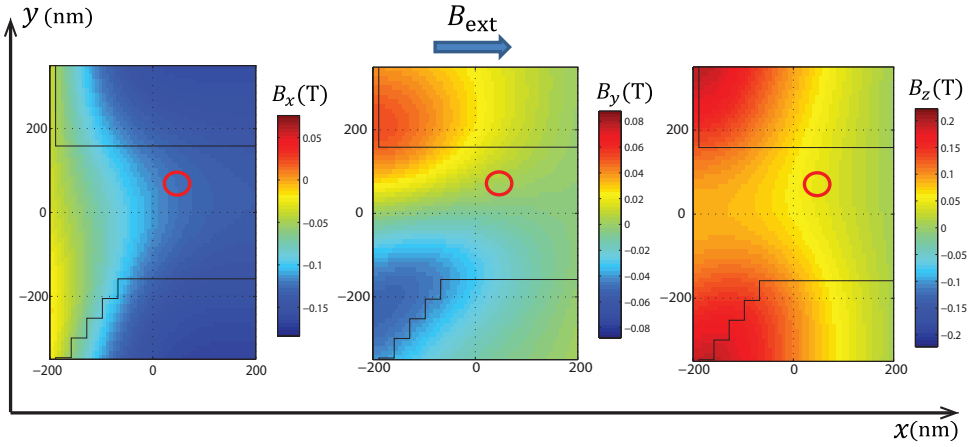

Figure 5.6: Numerically computed x, y and z components of the magnetic field induced by the micromagnets in the plane of the Si quantum well, for fully magnetized micromagnets. The black solid lines indicate the edges of the micromagnet as simulated. The region shown is the same as that in Fig. 5.1(b), and is outlined with dotted lines in Fig. 5.1(a). The red circle shows the estimated position of the dot.

5.6.6. SPIN RELAXATION TIME T1

We did not observe any change in the measured spin-up probability when changing the timing of the microwave burst during the manipulation stage by up to 2 ms. Thus we conclude that the spin relaxation time T_1 is much longer than the ms timescale of our pulse cycle and that the measurements shown here are not affected by T_1 decay, consistent with the long T_1 times seen in earlier measurements on Si or Si/SiGe dots and donor [18, 35, 36]. We note that due to the very long spin relaxation time, we cannot initialize by equilibration, as was commonly done in previous work [3, 10], since this would take 100 ms or more. Therefore, instead of pulsing both the spin up and spin down levels below the reservoir Fermi energy, thereby pulling an electron of unknown spin state inside the QD, we pulse so that only the lowest energy spin level (spin down) is below the Fermi level of the reservoir during the initialization stage (stage (1) in Fig. 5.1(c) of the main text).

5.6.7. RABI OSCILLATION

The probability that a single spin with Larmor frequency f flips when it is subject to microwave excitation at frequency f_{MW} with an amplitude that gives a Rabi frequency f_1 for a duration t_p [32] is

$$p_{\uparrow\downarrow}(f_1, f, f_{MW}, t_p) = sin^2\theta sin^2\left(\pi t_p \sqrt{(f_{MW}-f)^2 + f_1^2}\right), \tag{5.3}$$

with $sin\theta = \frac{f_1}{\sqrt{(f_{MW}-f)^2+f_1^2}}$. There are two resonance frequencies, $f_0^{(1)}$ and $f_0^{(2)}$, as discussed in the main text. Here we assume that the populations in resonances (1) and (2) are $\varepsilon^{(1)}$, and $\varepsilon^{(2)}$, respectively. If in addition we assume that both the Larmor frequency and the Rabi frequency follow a Gaussian distribution, the spin flip probability is given

by

$$P_{\uparrow\downarrow}(f_{MW},t_p)=\sum_{n=1,2}\varepsilon^{(n)}P^{(n)}_{\uparrow\downarrow}(f_{MW},t_p), \tag{5.4}$$

with $P^{(n)}_{\uparrow\downarrow}(f_{MW},t_p)=\int df_1\int df G^{(n)}(f)g^{(n)}(f_1)p^{(n)}_{\uparrow\downarrow}(f_1,f,f_{MW},t_p)$,
where $G^{(n)}(f)=\frac{1}{2\sigma_f\sqrt{2\pi}}exp\left(-\frac{(f-f_0^{(n)})^2}{2\sigma_f^2}\right)$ and $g^{(n)}(f_1)=\frac{1}{2\sigma_f\sqrt{2\pi}}exp\left(-\frac{(f_1-f_1^{(n)})^2}{2\sigma_{f_1}^2}\right)$.

The standard deviation of the Larmor frequency σ_f=0.268 MHz is extracted directly from the line width (Fig. 5.2(b)). In order to estimate the standard deviation of the Rabi frequency, σ_{f_1}, and the ratio of the two populations $\varepsilon^{(1)}/\varepsilon^{(2)}$ that applies in the experiment, we compare the measurement results of Fig. 5.3(a) with results from numerical simulations for $P_{\uparrow\downarrow}(f_{MW},t_p)$ shown in Fig. 5.7(a) for a range of values for both the ratio $\varepsilon^{(1)}/\varepsilon^{(2)}$ and σ_{f_1}. Based on this rough comparison, we consider the agreement the best for $\varepsilon^{(1)}/\varepsilon^{(2)}\sim 0.3\pm0.1/0.7\pm0.1$ and $\sigma_{f_1}\sim 0.25\pm0.05$ MHz. As a further consistency check, we plot the same simulation results again in Fig. 5.7(b), but now rescaled to account for the read-out and initialization fidelities estimated in supplementary section 5.6.10 below. The same values $\varepsilon^{(1)}/\varepsilon^{(2)}\sim 0.3\pm0.1/0.7\pm0.1$ and $\sigma_{f_1}\sim 0.25\pm0.05$ MHz give good agreement with the data of Fig. 5.3(a).

Figure 5.8(a) shows the measured spin-up probability, $P_\uparrow$, as a function of f_{MW} and burst time t_p, for B_{ext} = 763.287 mT. At this magnetic field, the two resonances are separated by $f_0^{(2)}-f_0^{(1)}=2.838$ MHz. Thus the individual chevron patterns produced by two resonances are more easily distinguished than in Fig. 5.3(a). The numerical simulations for $P_{\uparrow\downarrow}(f_{MW},t_p)$ for $f_0^{(2)}-f_0^{(1)}=2.838$ MHz, taking into account the read-out and initialization fidelities estimated in supplementary section 5.6.10, are shown in Fig. 5.8(b).

5.6.8. POPULATION AND TIME DEPENDENCE OF THE TWO RESONANCES

Fig. 5.2(b) shows the average of the 86 traces shown in Fig. 5.9. We see from Fig. 5.9 that the center of the resonance frequency f_0 fluctuates over time and the fluctuation behaviour is the same for the two resonances. For the measurement of Fig. 5.2(b), the applied microwave power is very low ($f_1\ll\sigma_f$) and the burst time is very long ($t_p\gg T_2^*$). Assuming that the ratio of the Rabi frequencies between two resonances is κ ($f_1^{(1)}=\kappa\eta$, $f_1^{(2)}=\eta$) and we can neglect the unknown spread in f_1 for low microwave power, the ratio of the steady state spin flip probability at the two Larmor frequencies is

$$\begin{aligned} r(\eta)&=\frac{P^{(1)}_{\uparrow\downarrow}\left(f_{MW}=f_0^{(1)},t_p\gg T_2^*\right)}{P^{(2)}_{\uparrow\downarrow}\left(f_{MW}=f_0^{(2)},t_p\gg T_2^*\right)}= \\ &=\frac{\int df G(f)p^{(1)}_{\uparrow\downarrow}\left(f_1^{(1)}=\kappa\eta,f,f_{MW}=f_0^{(1)},t_p\gg T_2^*\right)}{\int df G(f)p^{(2)}_{\uparrow\downarrow}\left(f_1^{(2)}=\eta,f,f_{MW}=f_0^{(2)},t_p\gg T_2^*\right)}, \end{aligned} \tag{5.5}$$

where $p_{\uparrow\downarrow}$ and $G(f)$ are defined as in Eq. 5.3 and Eq. 5.4. In the limit of low microwave power, the ratio $r(\eta)$ converges to:

$$r_0\equiv r(\eta\longrightarrow 0)=\lim_{\eta\longrightarrow 0}r(\eta)=\kappa^2. \tag{5.6}$$

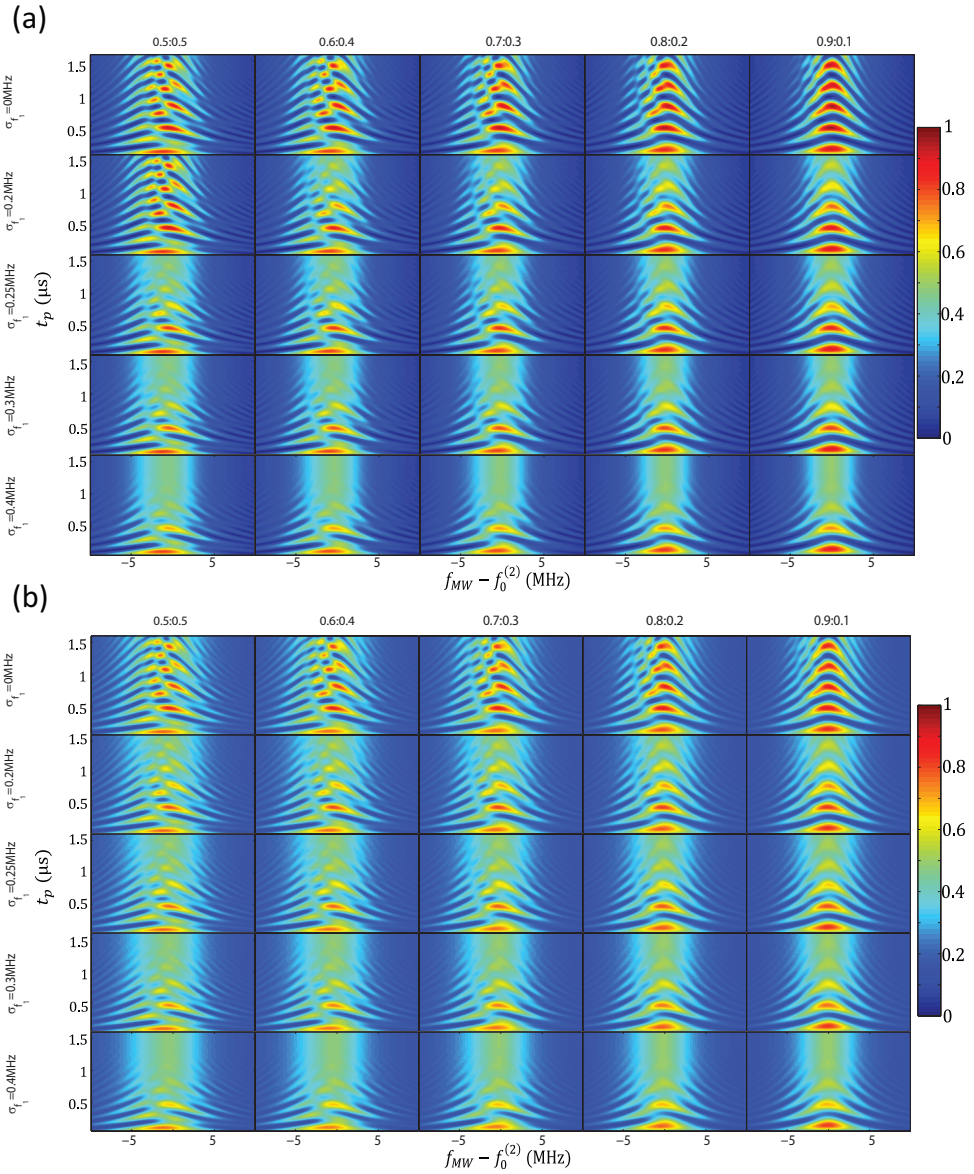

Figure 5.7: Simulation for Rabi oscillations. (a) Numerically simulated spin flip probability $P_{\uparrow\downarrow}(f_{MW}, t_p)$ for population ratios $\varepsilon^{(1)}/\varepsilon^{(2)}$ =0.5:0.5, 0.4:0.6, 0.3:0.7, 0.2:0.8, 0.1:0.9 and spread in Rabi frequencies σ_{f_1} =0, 0.2 MHz, 0.25 MHz, 0.3 MHz, 0.4 MHz, as a function of driving duration t_p and frequency detuning $f_{MW} - f_0^{(2)}$. From comparison with the data of Fig. 5.3(a), we conclude that $\varepsilon^{(1)}/\varepsilon^{(2)} \sim 0.3\pm0.1/0.7\pm0.1$ and $\sigma_{f_1} \sim 0.25\pm0.05$ MHz are reasonable. (b) The same simulation results as in panel (a), but taking into account the initialization and read-out fidelities estimated in section 5.6.10 below. Again $\varepsilon^{(1)}/\varepsilon^{(2)} \sim 0.3\pm0.1/0.7\pm0.1$ and $\sigma_{f_1} \sim 0.25\pm0.05$ MHz match well to the data.

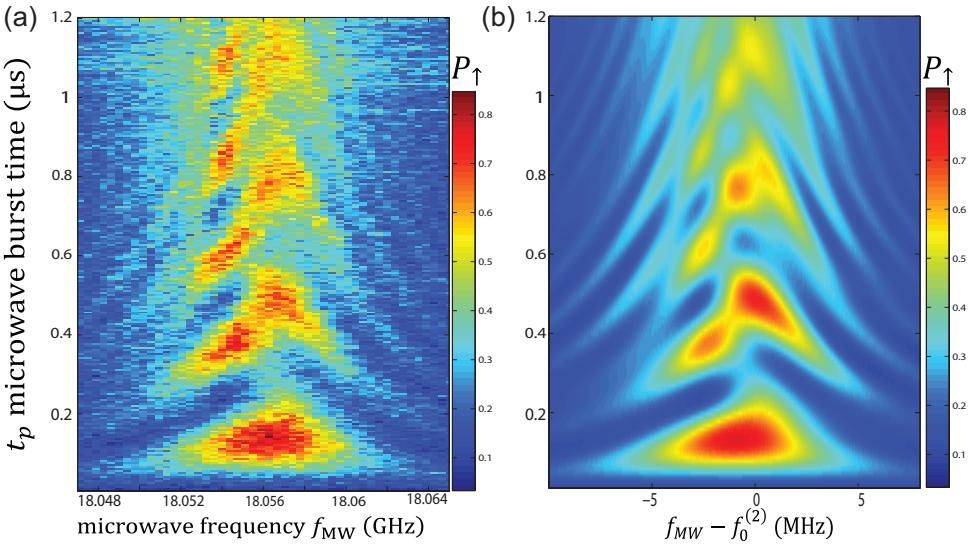

Figure 5.8: Comparison of the data to a simulation for Rabi oscillations at B_{ext} = 763.287 mT. (a) The measured spin-up probability $P_\uparrow$ for a Rabi experiment. (b) The simulated spin-up probability $P_\uparrow$ using population fractions $\varepsilon^{(1)}/\varepsilon^{(2)} = 0.3 : 0.7$, spread in Rabi frequencies $\sigma_{f_1} \sim 0.25$ MHz, readout fidelity parameters $\alpha = 0.06$, $\beta = 0.05$, $\gamma = 0.04$, and the two Rabi frequencies $f_1^{(2)} = 3.1$ MHz and $f_1^{(1)} = 4.1$ MHz.

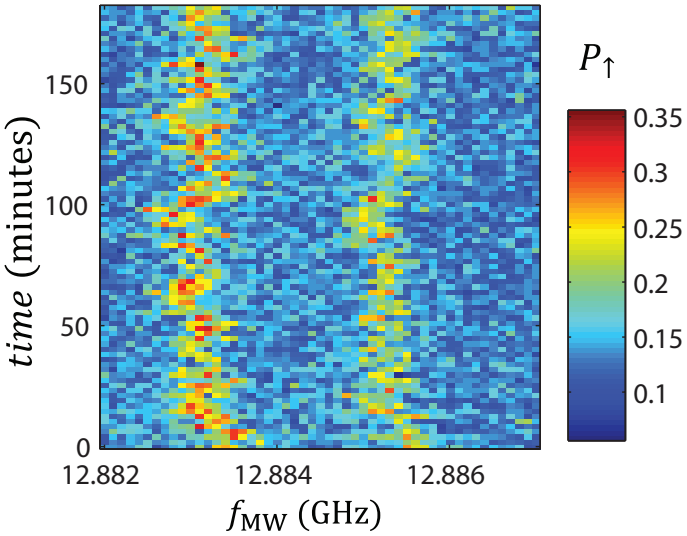

Figure 5.9: The raw data on which Fig. 5.2(b) is based. Measured spin-up probability $P_\uparrow$ as a function of applied microwave drive frequency f_{MW} and time (power P = -33 dBm, microwave pulse duration t_p=700 μs). Each horizontal scan in the figure takes ~2 minutes (200 cycles, which takes 2s, per datapoint), and the scan is repeated 86 times. Fig. 5.2(b) shows the average of the 86 horizontal scans.

If we assume that the ratio of the Rabi frequencies between two resonances at low MW power is the same as the ratio at high MW power determined in Section 5.6.11 of the supplementary material, then $\kappa = 1.53 \pm 0.19$. The ratio of the measured peak amplitudes in Fig. 5.2(b) is 1.4 ± 0.3 and it is the product of the ratio of the spin flip probabilities and the ratio of the populations:

$$r_0 \times \frac{\varepsilon^{(1)}}{\varepsilon^{(2)}} = 1.4 \pm 0.3. \tag{5.7}$$

From Eq. 5.5 and Eq. 5.7, we get

$$\frac{\varepsilon^{(1)}}{\varepsilon^{(2)}} = \frac{1.4 \pm 0.3}{\kappa^2} = \frac{1.4 \pm 0.3}{2.34 \pm 0.58} = 0.60 \pm 0.28. \tag{5.8}$$

From this relation, we get $\varepsilon^{(1)}/\varepsilon^{(2)} \sim 0.37/0.63$, consistent with the rough estimate of 0.3/0.7 based on the Rabi oscillations (see Section 5.6.7 of the supplementary information).

5.6.9. π PULSE FIDELITY

The probability that a spin down is flipped to spin up when applying a π pulse is given in Eq. 5.4. This probability corresponds to the state fidelity of the output state relative to the ideally expected spin up state. This fidelity is here estimated based on a numerical model with input from the experiment. Quantum process tomography or randomized benchmarking can be used to estimate the gate fidelity directly from the experiment. For the lower transition, using the values $f_1^{(1)} = 5$ MHz, $\sigma_f = 0.268$ MHz and $\sigma_{f_1} = 0.25$ MHz, we find a spin flip probability

$$\begin{aligned} &P_{\uparrow\downarrow}^{(1)}\left(f_{MW} = f_0^{(1)}, t_p = \frac{1}{2f_1^{(1)}} = 100ns\right) = \\ &= \int df_1 \int df G^{(1)}(f) g^{(1)}(f_1) p_{\uparrow\downarrow}^{(1)}(f_1, f, f_{MW}, t_p) = 0.99. \end{aligned} \tag{5.9}$$

For the higher transition, using $f_1^{(2)} = 3.1$ MHz, $\sigma_f = 0.268$ MHz and $\sigma_{f_1} = 0.25$ MHz, we find

$$\begin{aligned} &P_{\uparrow\downarrow}^{(2)}\left(f_{MW} = f_0^{(2)}, t_p = \frac{1}{2f_1^{(2)}} = 160ns\right) = \\ &= \int df_1 \int df G^{(2)}(f) g^{(2)}(f_1) p_{\uparrow\downarrow}^{(2)}(f_1, f, f_{MW}, t_p) = 0.97. \end{aligned} \tag{5.10}$$

When we have a $\varepsilon^{(1)}/\varepsilon^{(2)} = 0.3/0.7$ contribution of the two resonances, $P_{\uparrow\downarrow}(= 0.3 \times P_{\uparrow\downarrow}^{(1)} + 0.7P_{\uparrow\downarrow}^{(2)})$ reaches its maximum 0.79 when $P_{\uparrow\downarrow}^{(1)} = 0.53$ and $P_{\uparrow\downarrow}^{(2)} = 0.90$ at $t_p = 130$ ns and for $f_{MW} = f_0^{(2)}$.

5.6.10. INITIALIZATION FIDELITY AND READOUT FIDELITY

For applications in quantum information processing it is important to know the read-out and initialization fidelities. These fidelities are usually characterized by three parameters

α, β and γ. The parameter α corresponds to the probability that the sensing dot current exceeds the threshold even though the electron was actually spin-down, for instance due to thermally activated tunnelling or electrical noise. The parameter β corresponds to the probability that the sensing dot current does not cross the threshold even though the electron was actually spin-up at the end of the microwave burst time. The measurement time (< 4 ms) we used is much shorter than T_1 and so β is not affected by T_1 decay (see supplementary section 5.6.6). It is limited by the bandwidth of the sensing dot current measurement (~20 kHz). $(1-\beta)$ can be directly measured as the probability that the step from the charge sensor in correspondence of the electron jumping in during the initialization stage is missed using the same threshold value as is used for detection of the electron jumping out during the read-out stage. We find $\beta \sim 0.05$ (Fig. 5.10).

The parameter γ corresponds to the probability that the electron is in spin-up instead of spin-down at the end of the initialization stage. The measured spin-up probability $P_\uparrow$ can be written as follows using the parameters α, β and γ and the probability for flipping the spin during manipulation, $P_{\uparrow\downarrow}$:

$$P_\uparrow = P_{\uparrow\downarrow}(1-\gamma)(1-\beta) + (1-P_{\uparrow\downarrow})\gamma(1-\beta) + (1-P_{\uparrow\downarrow})(1-\gamma)\alpha + P_{\uparrow\downarrow}\gamma\alpha. \tag{5.11}$$

When $P_{\uparrow\downarrow} = 0$ (i.e. the microwaves are applied far off-resonance or not at all), the measured spin-up probability can be expressed as follows:

$$P_\uparrow(P_{\uparrow\downarrow}=0) = (1-\gamma)\alpha + \gamma(1-\beta) \tag{5.12}$$

$$= \alpha + \gamma(1-(\alpha+\beta)). \tag{5.13}$$

$P_\uparrow(P_{\uparrow\downarrow}=0) \sim 0.1$ is measured. From this and Eq. 5.12, we get an upper bound on α.

$$P_\uparrow(P_{\uparrow\downarrow}=0) > \alpha,\ 0.1 > \alpha. \tag{5.14}$$

As discussed above, $(1-\beta) \sim 0.95$ is measured (Fig. 5.10(b)). From this and Eq. 5.12, we get an upper bound on γ.

$$P_\uparrow(P_{\uparrow\downarrow}=0) > \gamma(1-\beta) \Rightarrow \frac{P_\uparrow(P_{\uparrow\downarrow}=0)}{(1-\beta)} > \gamma \Rightarrow 0.11 > \gamma. \tag{5.15}$$

By looking at Fig. 5.3(a), $P_\uparrow(f_{MW} = f_0^{(2)})$ reaches its maximum ~0.72 when t_p ~130 ns. Here, since $P_{\uparrow\downarrow}$ is expected to be large, the 2^{nd}, 3^{rd} and 4^{th} terms of Eq. 5.11 are much smaller than the 1^{st} term (each of them contains two factors much smaller than 1, whereas the 1^{st} term contains no such small factors). So $P_\uparrow$ can be well approximated as follows:

$$P_\uparrow \sim P_{\uparrow\downarrow}(1-\gamma)(1-\beta) = 0.72 \Rightarrow P_{\uparrow\downarrow}(1-\gamma) = 0.72/(1-\beta) = 0.76. \tag{5.16}$$

Using the upper bound of γ (Eq. 5.15), we can put bounds on $P_{\uparrow\downarrow}(f_{MW} = f_0^{(2)}, t_p \sim 130\,ns)$:

$$0.76 < P_{\uparrow\downarrow}(f_{MW} = f_0^{(2)}, t_p \sim 130\,ns) < 0.85. \tag{5.17}$$

Numerical simulation for $\sigma_{f_1} = 0.25$ MHz gives $P_{\uparrow\downarrow}^{(2)}(f_{MW} = f_0^{(2)}, t_p = 130\,ns) = 0.9$ and $P_{\uparrow\downarrow}^{(1)}(f_{MW} = f_0^{(2)}, t_p = 130\,ns) = 0.53$, where we note that the 130 ns burst time is

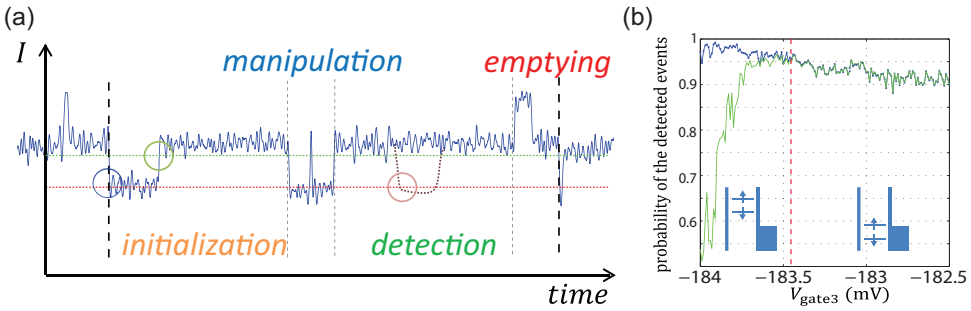

Figure 5.10: Measurement of fidelity parameter $(1-\beta)$. (a) An example real time trace of the sensing dot current. The black dashed lines indicate the start and end of one cycle. When the recorded current dips below the threshold level indicated by the dotted red line during the detection stage, we conclude an electron tunnelled out from the dot to the reservoir. In this case, we infer the electron was spin up. When the signal remains above the threshold, we conclude the electron was spin down (the lowest energy spin state). (b) Blue trace: Measured probability that the sensing dot current passes below the threshold indicated by the red dotted line in panel (a) during the initialization stage, as a function of V_{gate3} (averaged over 1000 cycles). Since the dot is always emptied during the previous stage, ideally we would always see the signal dip below the red threshold at the start of the initialization stage (blue circle in (a)). However, because of the finite bandwidth of the measurement, the dip will be missed if it is too fast. This occurs with the same probability as the probability for missing dips in the detection stage, and is thus a good measure of $(1-\beta)$. Green trace: Measured probability that the current subsequently passes the green threshold from below during the initialization stage, as a function of V_{gate3} (green circle in (a)). When the green and blue traces coincide, the dot is filled during the initialization stage. When the dot level is high (V_{gate3} is low, see also the schematic in the inset), the time it takes for an electron to tunnel in is long, and so $(1-\beta)$ is high, but the dot is not always filled (the green line is low here). As the dot level is lowered ($(1-\beta)$ is raised, see also inset), the tunnel rate increases, and the dot is always initialized, at the cost of a slightly lower value of $(1-\beta)$, due to the finite measurement bandwidth. The vertical red dashed line indicates the operating point used in the experiments.

longer respectively shorter than the burst time for a π pulse for the lower and higher energy resonance. Then, using $\varepsilon^{(1)}/\varepsilon^{(2)} = 0.3/0.7$, we obtain $P_{\uparrow\downarrow}(f_{MW} = f_0^{(2)}, t_p = 130\,ns) = 0.53\times 0.3 + 0.9\times 0.7 = 0.79$, which is consistent with Eq. 5.17. Now, using $P_{\uparrow\downarrow}(f_{MW} = f_0^{(2)}, t_p = 130\,ns) = 0.79$ and Eq. 5.17 we can estimate $\gamma = 0.04$.
Then, from Eq. 5.12, we can also extract α:

$$P_\uparrow(P_{\uparrow\downarrow}=0) = (1-\gamma)\alpha + \gamma(1-\beta) = 0.10 \Rightarrow 0.96\alpha + 0.04\times 0.95 = 0.10 \Rightarrow \alpha = 0.06. \quad (5.18)$$

We use $\alpha = 0.06$, $\beta = 0.05$ and $\gamma = 0.04$ in Eq. 5.11 to compute the spin-up probability $P_\uparrow$ that can be expected in the measurement, which is shown in Fig. 5.7(b), Fig. 5.8(b) and Fig. 5.12(b).

5.6.11. POWER DEPENDENCE OF THE RABI FREQUENCY

Fig. 5.11(a) shows the measured Rabi frequencies for the two resonance conditions, $f_1^{(1)}$ and $f_1^{(2)}$, as a function of the microwave amplitude emitted from the source. $f_1^{(1)}$ and $f_1^{(1)}$ are determined by the fast Fourier transform (FFT) of Rabi oscillations, as in Fig. 5.3(b). The error bars arise from the finite number of points in the FFT. The linear fits shows that the ratio of the Rabi frequencies of two resonance transitions is $f_1^{(1)}/f_1^{(2)} = 1.53\pm 0.19$.
Fig. 5.11(b) shows Rabi oscillations for a range of microwave amplitudes emitted from

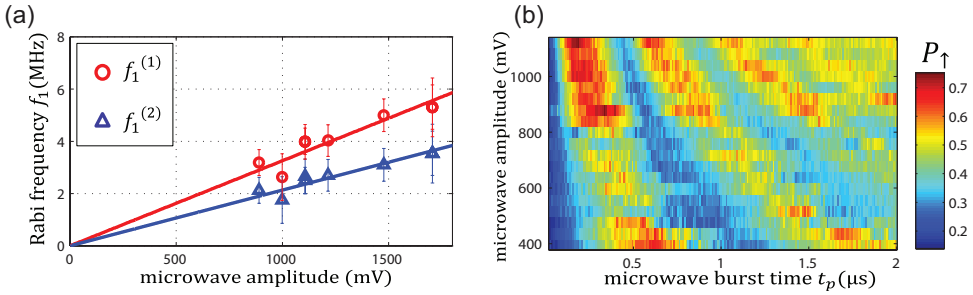

Figure 5.11: Rabi oscillations versus microwave amplitude. (a) Rabi frequencies $f_1^{(1)}$ (red circles) and $f_1^{(2)}$ (blue triangles) at B_{ext} = 763.287 mT as a function of the microwave amplitude emitted from the source, as verified with a spectrum analyzer. The solid lines are linear fits to the data. As expected, the Rabi frequency is linear in the driving amplitude. (b) The measured spin-up probability $P_\uparrow$ as a function of the microwave burst time t_p and the microwave amplitude emitted from the source by applying microwave excitation at $f_{MW} = f_0^{(2)}$ = 12.885 GHz (B_{ext} = 763.287 mT). We see the pattern expected for Rabi oscillations.

the source. The scattering and the low spin-up probability around microwave amplitude 500 mV ~ 800mV may be due to a background charge switch that caused the dot to move away from the electrochemical potential alignment that is best for read-out. The measurement of Fig. 5.11(b) took 20 hours.

5.6.12. MEASUREMENTS OF RAMSEY FRINGES

Here we give results of numerical simulations corresponding to the two-pulse Ramsey interference measurements of Fig. 5.3(c). The overall procedure is analogous to that used for the simulations of the Rabi oscillations. Instead of a single microwave burst, we now have two bursts of duration $t_p = 1/(4f_1^{(1)})$ separated by a wait time τ. The expression that the spin is flipped at the end of this sequence is as follows (same symbols as in the Rabi simulations, see Eq. 5.3 [37]:

$$\begin{aligned} & p_{\uparrow\downarrow}(f_1, f, f_{MW}, \tau) = \\ & 4sin^2\theta sin^2\left(\pi t_p\sqrt{(f_{MW}-f)^2+f_1^2}\right)\times \\ & \times\left[cos(\pi(f_{MW}-f)\tau)cos\left(\pi t_p\sqrt{(f_{MW}-f)^2+f_1^2}\right)-\right. \\ & \left. cos\theta sin(\pi(f_{MW}-f)\tau)sin\left(\pi t_p\sqrt{(f_{MW}-f)^2+f_1^2}\right)\right]^2, \end{aligned} \tag{5.19}$$

with $sin\theta = f_1/\sqrt{(f_{MW}-f)^2+f_1^2}$.

Here we can neglect the spread in f_1 because t_p is short and its effect is small. Then the spin flip probability averaged over the Larmor frequency distribution is expressed as

$$P_{\uparrow\downarrow}(f_{MW}, t_p) = \int df\left(G^{(1)}(f)\varepsilon^{(1)}p_\uparrow^{(1)} + G^{(2)}(f)\varepsilon^{(2)}p_\uparrow^{(2)}\right). \tag{5.20}$$

Using Eq. 5.20, $\alpha = 0.06$, $\beta = 0.05$, and $\gamma = 0.04$ in Eq. 5.11, we compute the expected spin-up probability $P_\uparrow$ at the end of the Ramsey sequence, see Fig. 5.12(b). The corresponding

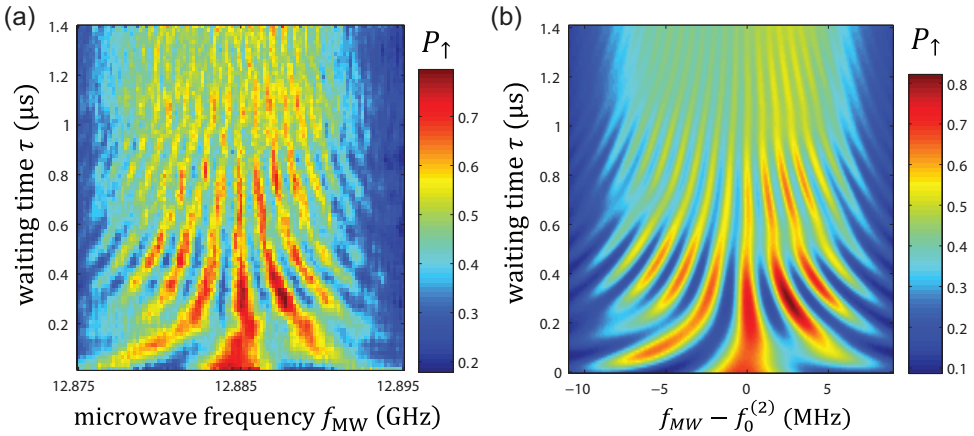

Figure 5.12: Comparison of the data to a simulation for Ramsey fringes. (a) The measured spin-up probability $P_\uparrow$ for a two-pulse Ramsey style experiment. The data are those shown in Fig. 5.3(b) but taking a moving average along t_p over 5 points (79 ns). (b) The simulated spin-up probability $P_\uparrow$ using $\varepsilon^{(1)} : \varepsilon^{(2)} = 0.3 : 0.7$, $\sigma_f = 0.268$ MHz, $\alpha = 0.06$, $\beta = 0.05$, and $\gamma = 0.04$ as a function of τ and $f_{MW} - f_0^{(2)}$, also taking a moving average over 79 ns. There is good agreement between the data and simulation.

data is shown in Fig. 5.12(a).

5.6.13. DIFFERENCE IN G-FACTORS AND RABI FREQUENCIES BETWEEN THE TWO RESONANCES

Here we discuss several possible explanations for the existence of two closely spaced electron spin resonance conditions, characterized by g-factors that differ by 0.015% and Rabi frequencies that differ by 50%.

As stated in the main text, we attribute the presence of two spin resonance signals to a partial occupation of the two lowest valley states. We can estimate the valley splitting E_V from the 30/70 relative contributions of the two resonances (see main text), assuming it results from thermal equilibration between the two valley states. This gives $E_V \sim 0.85\ k_B T_e$, which for $T_e = 150$ mK yields $E_V = 11\ \mu$eV. We note that the electron temperature may be somewhat larger since we apply microwave excitation to the sample, so the valley splitting may be larger as well.

We have identified two mechanisms that can explain a 0.015% relative difference in the electron g-factors between the two valleys, defined as $2(g^{(2)} - g^{(1)})/(g^{(2)} + g^{(1)})$. The first is valley-dependent g-factor renormalization due to the transverse gradient magnetic field; the other is valley-dependent penetration of the electron wavefunction into the SiGe barrier region. We first discuss these two mechanisms. We then mention other potential mechanisms that cannot explain the observed g-factor shift.

(1) Tokura et al. [2] find that the unperturbed Zeeman splitting E_{0z} is renormalized in the presence of a magnetic field gradient to a value E_Z given by $E_z = E_{0z}\left[1 - \frac{1}{2}\frac{M}{\Delta^2 - E_{0z}^2}\right]$. Here $M \sim 0.5(g\mu_B max(b_{SL})2L)^2$ is the perturbation matrix element between the ground orbital state with spin up and the first excited orbital state with spin down, $max(b_{SL}) \sim$

($dB_\perp/dx$) and L is the dot radius. We see that E_z depends on the orbital energy splitting Δ (energy level spacing to the first excited state). At lowest order in the valley-orbit coupling, Δ depends only on the orbital energy splitting, which can differ for the two valley states due to valley-orbit coupling [38]. Contributions to the renormalization of the g-factor from differences in the lateral positions of the different valley states can also occur, but are higher order in the valley-orbit coupling.

The difference in g-factors between the two valleys could then be explained if the two valley states exhibit sufficiently different orbital splittings Δ. Valley-dependent orbital splitting arises from the valley-orbit interaction due to disorder at the interface, and can have important effects. In J. K. Gamble et al., [39], it is estimated that the centers of the charge distributions of the two valley states can be separated by as much as the dot diameter, and differences in orbital splitting between the two valleys can be 20% or more. Taking $dB_\perp/dx = 1$ mT/nm, $E_{0z} \sim 60$ μeV, $\Delta^{(1)} \sim 400$ μeV and $\Delta^{(1)} \sim 320$ μeV (where the superscripts refer to the two resonances as in the main text), we obtain corrections to E_{0z} of 0.013% and 0.010%. The difference between the two corresponds to a difference in g-factors of 0.003%, within a factor of 5 of the observed value.

A valley-dependent orbital splitting can also account for the observed difference in Rabi frequencies for the two resonances. From Tokura et al., and M. Pioro-Ladri et al., [2, 40], neglecting the contribution from spin-orbit interaction as it is small in Si/SiGe, we roughly have $f_{Rabi} = \frac{g\mu_B}{2h} eE_{a.c.} \left|\frac{dB_\perp}{dx}\right| \frac{L^2}{\Delta}$, where $E_{a.c.}$ is the a.c. electric field generated by the nearby gate. Given that $L \propto 1/\sqrt{\Delta}$, it follows that $f_{Rabi} \propto 1/\Delta^2$. Then, we have that $f^{(1)}_{Rabi}/f^{(2)}_{Rabi} = \left(\Delta^{(2)}/\Delta^{(1)}\right)^2$. Assuming that $E_{a.c.}$ is equal for the two valley states, the factor 1.5 between the Rabi frequencies of the two resonances can be explained by a $\sim 20\%$ difference in orbital level spacing, $2\left(\Delta^{(1)} - \Delta^{(2)}\right)/\left(\Delta^{(1)} + \Delta^{(2)}\right)$. This is consistent with the difference in orbital splitting needed to explain the g-factor shifts.

(2) A second explanation for the g-factor shifts could be that the two valley states penetrate differently into the SiGe barrier. This effect also gives rise to valley splitting. For g-factors, the state with the largest probability in the barrier should have the g-factor closest to SiGe. It is difficult to estimate the resulting g-factor shift because the g-factors in SiGe alloys are not well known. Our rough estimate yields a g-factor shift of 0.0025%, which is 6 times smaller than the experiment, but is still comparable. We view this mechanism as less likely than mechanism (1) above because observing the difference in Rabi frequencies would require that the different valley states have significantly different direction of wavefunction motion. In principle, further experiments have the potential to distinguish these two mechanisms for g-factor shifts. Valley-dependent penetration should be similar in similar devices, and its dependence on extrinsic parameters (e.g., accumulation gate voltages) should be systematic. On the other hand, valley-orbit renormalization should vary significantly from device to device.

We now briefly consider explanations for the g-factor shifts that yield less successful agreement with experiment.

(3) In principle, the combination of valley-orbit coupling and spin-orbit coupling could give rise to valley-dependent g-factor shifts. The renormalization in the g-factor from this mechanism is proportional to the inverse square of the spin-orbit length [41]. According to Z. Wilamowski et al., [42] the spin-orbit coupling strength in quantum well structures is three orders of magnitude smaller in Si than in III-V semiconductors. Since

such g-factor renormalization effects are small already in GaAs, we can conclude that the change in g-factor mediated by this mechanism in Si will be much smaller than the 0.015% that is observed experimentally.

(4) As mentioned above, valley-orbit coupling may cause a lateral separation of the centers of the charge distributions for the two valley state [39]. When this effect is combined with local fluctuations of the Ge concentration in the SiGe alloy, it yields slightly different g-factor shifts for the two states. In general, the g-factor shift described in (2) (above) would be expected to dominate over such a disorder effect. However, because valley-orbit coupling depends on the interference between valley state [38], destructive interference could suppress the dominant g-factor shift in (2). Our simulations (not reported here) indicate that it is possible for the disorder-induced effect to dominate, though still smaller than the estimate given in (2) above.

(5) Finally, we consider explanations for the two closely spaced spin resonance conditions that do not invoke valley physics. A natural thought is that we may be driving spin transitions in a two- or three-electron manifold, either in a single dot or in a double dot. Under appropriate conditions, this could give rise to closely spaced spin resonance frequencies with g-factors around 2. However, in this scenario, whenever microwave excitation is applied at either one of the two resonance frequencies, spin transitions would be induced 100% of the time. In the experiment, in contrast, when applying microwave excitations resonant with the lower (upper) resonance frequency, there is a contribution to the signal only ~ 30% (70%) of the time. If the dot location jumped between two positions, for instance due to a background charge that is hopping back and forth, a 30/70 occupation would be possible. Due to the magnetic field gradient, we can also expect different spin splittings for different dot locations. However, the difference in spin splittings would be a fixed value set by the stray field from the micromagnet (as soon as it is fully polarized). In contrast, in the measurements, the difference between the resonance frequencies varies linearly with magnetic field (Fig. 5.2(a)).

We have not been able to come up with other plausible explanations except those related to valley physics presented above.

5

5.6.14. SOURCES OF RABI DECAY

Here we estimate how much random nuclear fields, instrumentation and charge noise can contribute to the spread in the Rabi frequency. The Rabi frequency in the present EDSR measurements can be expressed as $f_{Rabi} = \frac{g\mu_B}{2h} eE_{a.c.} \left|\frac{dB_\perp}{dx}\right| \frac{L^2}{\Delta}$ (See also section 5.6.13). We consider here only fluctuations in the electric field $E_{a.c.}$ and in the tranverse gradient $dB_\perp/dx$, as we expect fluctuations in L and Δ to give smaller contributions. For each noise source, we estimate whether it can account for the 5% spread in the Rabi frequency (rms) observed in the experiment.

First, the transverse component of the nuclear field exhibits a gradient that adds to the gradient from the micromagnet by a random amount that slowly fluctuates in time over the course of the measurement. The lateral displacement of the electron induced by the microwave excitation is estimated to be $\Delta x_{rms} = 0.707 \frac{B_1}{dB_\perp/dx} = 0.707 \frac{0.18\,mT}{0.27\,mT/nm} = 0.47$ nm. An approximate upper bound on the transverse nuclear field gradient is $\Delta B_{nucl}/2L =$ 7.6 kHz/nm. To estimate this bound, we assume that the nuclear field is uncorrelated between two positions that are separated by the dot diameter, $2L \sim 50$ nm. The measured

spread in Larmor frequency is $\sigma_f = 0.268$ MHz so the rms difference in nuclear fields ΔB_{nucl} between these two positions becomes $\Delta B_{nucl} = \sqrt{2}\sigma_f = 0.38$ MHz. Then the spread in the nuclear field gradient is $(\Delta B_{nucl}/2L) \times \Delta x_{rms} = 3.6$ kHz, which is about 70 times smaller than σ_{Rabi} we measured.
An additional contribution of the random transverse nuclear field arise from a modulation in the phase ϕ of the atomic scale oscillations of the electron wave function that is present in Si/SiGe quantum dots [20]. If an electric field changes ϕ by 90 degrees, the electron wave function is in contact with a different ensemble of nuclei. An AC electric field excitation at frequency f_0 then leads to a (random) contribution to the Rabi frequency. The effect of an out-of-plane electric field is small as ϕ does not depend on this component to leading order in the ratio of the valley coupling to the quantum well depth (for example, see Eqs. 10, 13 and 14 in M. Friesen et al., [43]). The effect of an in-plane electric field is mediated by disorder at the quantum well interface. We have found (see section 5.6.15 below) that ϕ varies over length scales of order $d = 10 \sim 100$ nm, which implies that the nuclear field would be uncorrelated for two positions $10 \sim 100$ nm. Taking $d = 10$ nm and following an analogous reasoning as above, the estimated dot displacement $\Delta x_{rms} = 0.47$ nm produces a random contribution to the Rabi frequency of order $\frac{\Delta x_{rms}}{d} \Delta B_{nucl} \sim 0.02$ MHz, 13 times smaller than σ_{Rabi} we measured.

Second, low-frequency charge noise or gate voltage noise can cause random shifts in the average dot position. If the transverse field gradient from the micromagnet itself changes with position, low-frequency charge noise leads to a low-frequency fluctuation in the gradient strength, and thus to a spread in the Rabi frequency. As discussed in the main text, the EDSR line width puts an upper bound on the electron micromotion induced by low-frequency charge or voltage noise of $\delta x = 50$ pm (rms). Based on simulations, the variation of the transverse gradient from the micromagnet with position is $\frac{d}{dx}\left(\frac{dB_\perp}{dx}\right) \sim 2\ \mu\text{T}/(\text{nm})^2$ and so the spread in transverse field gradient due to low-frequency noise is $\frac{d}{dx}\left(\frac{dB_\perp}{dx}\right)\delta x = 0.1\ \mu\text{T}/(\text{nm})$. This spread is 3000 times smaller than the average transverse gradient of 0.3 mT/nm, and can thus not explain the 5% spread in the Rabi frequency we observe.

Third, charge noise/instrumental noise that is resonant with the Larmor frequency adds to $E_{a.c.}$ and can thus cause a spread in the Rabi frequency. The output amplitude of the microwave source (Agilent Vector Signal Generator E8267D) could fluctuate, either rapidly or in the form of a slow drift. We measured the drift in the output amplitude of the vector source operating in vector modulation mode over twenty hours. We found a variation in output amplitude, which correlates with the temperature in the room, of about 0.2%. Thermal noise (and other broadband noise sources) also has some spectral content at the resonance frequency, which is independent of the microwave power. However, if this spectral content amounted to 5% in amplitude of the driving from the vector source during Rabi experiments, it would overwhelm the driving amplitude of the source during the CW measurements, where we applied about 50 dB less power than during the Rabi experiments, corresponding to 300 times smaller amplitudes. In this case, spin transitions would have been observed also when the applied microwave frequency is applied off-resonance, which is clearly not the case.

Fourth, fluctuations in $E_{a.c.}$ are also introduced by the vector modulation whereby the microwave signal is multiplied by a 250 mV rectangular pulse generated by a Tektronix Arbitrary Wave function Generator (AWG 5014C) and applied to the I and Q inputs of the vector source. Fluctuations in the AWG pulse amplitude then translate to fluctuations in $E_{a.c.}$. The twenty hour measurement of the output amplitude of the vector source was done with the same 250 mV pulse amplitude from the AWG applied to the I and Q inputs, so this contribution is already included in the 0.2% variation in output amplitude discussed above.

Finally, high frequency phase noise of the microwave source causes fluctuations in the applied frequency. The specifications for the frequency stability of the source are many orders of magnitude below the measured line width of 0.6 MHz. Finally, noise in the amplitude of the AWG channels going into the I and Q inputs causes not only amplitude fluctuations (discussed above) but also phase fluctuations. The noise of the AWG is dominated by low-frequency noise, which thus translates to low-frequency phase noise of the vector source output. When measuring Rabi oscillations, low-frequency phase noise does not contribute to damping.

5.6.15. VALLEY PHASE RELAXATION LENGTH SCALE

Here we estimate the length scale over which the valley phase relaxes by considering a quantum well interface that is not perfectly flat, but contains a single-atom step. Far enough away from the step, a single-electron wavefunction does not feel the presence of the step, and we wish to estimate the width d of the region near the step over which the wavefunction is perturbed. We will estimate the perturbation to the energy of the electron ground state due to this step, taking d as a variational parameter. Minimizing this energy then provides an expression for the valley relaxation length scale d. A characteristic length scale emerges because of the competition between the energy cost of deforming the phase and the possible energy gain that deformation yields because of the decrease of the valley splitting in the vicinity of the step.
The shift in the kinetic energy of the electron ground state is of order
$\hbar^2/(2m_t)(d\phi/dx)^2(d/L)$. Here, $m_t = 0.19\ m_e$ is the transverse electronic effective mass in silicon, d is the lateral extent of the disturbance, and L is a normalization constant that is essentially the lateral extent of the wavefunction[1]. The quantity $(d\phi/dx)$ is the spatial rate of change of the valley phase, which is given approximately by $(\Delta\phi/d)$, where $\Delta\phi = k_0 a_0/4$ is the change in the asymptotic values of the valley phase arising from a single step, $k_0 = 0.85\,2\pi/a_0$ is the position of the center of the valley in the Brillouin zone, and $a_0 = 0.54$ nm is the length of the Si cubic unit cell. If E_V is the valley splitting for a flat quantum well, then the presence of a step suppresses the total valley splitting by an amount $E_V(d/L)$, and therefore increases the ground state energy by $E_V(d/L)$. Minimizing the total energy shift of the ground state with respect to d yields $d = (\hbar^2/m_t E_V)^{1/2}(0.85\pi/2)$. For typical valley splittings in the range 0.1-1 meV [44, 45] this yields valley relaxation lengths on the order of 10s of nm. A 2D tight binding calculation using the model described in A. L. Saraiva et al., [46] corroborates these results.

[1] Note that L plays no role in our calculation if it is much larger than the other length scales in the problem.

5.6.16. VALLEY SCATTERING AS A SOURCE OF SPIN ECHO DECAY

We assume that the switching between valley (2) and valley (1) happens in a Poisson process and the switching rate from valley (2) to valley (1) is Γ. When the first MW pulse is applied (in the beginning of the manipulation stage), the electron is in valley (2) with probability 70% and in valley (1) with probability 30%.
We consider the following 4 cases.
(I) The electron is in valley (2) when the first pulse is applied. It stays in valley (2) until the third pulse is applied.
(II) The electron is in valley (2) when the first pulse is applied. It switches to valley (1) before the third pulse is applied.
(III) The electron is in valley (1) when the first pulse is applied. It stays in valley (1) until the third pulse is applied.
(IV) The electron is in valley (1) when the first pulse is applied. It switches to valley (2) before the third pulse is applied.
The point is that Hahn echo works only for the case (I).
In the cases (II) and (IV), the phase information is lost as soon (~500 ns knowing that the difference in resonance frequency of two valleys is ~2 MHz) as the valley switches. The Hahn echo cannot recover the phase information, even if the valley switches back again to the original valley later.
In case (III), the Hahn echo doesn't work because the second pulse acts as $\sim 2\pi$ pulse instead of π pulse. We set the microwave burst time so that the second pulse acts as π pulse for valley (2). The Rabi frequency of valleys (2) and (1) are $f_1^{(2)} = 2.7$ MHz and $f_1^{(1)} = 4.3$ MHz respectively. Since the microwave excitation is applied here $\Delta f = 2.9$ MHz away from the resonance frequency for valley (1), the effective Rabi frequency for valley (1) is $f_1^{(1)}{}_{eff} = \sqrt{\Delta f^2 + f_1^{(1)2}} = 5.2$ MHz. Then the second pulse acts as a $\frac{f_1^{(1)}{}_{eff}}{f_1^{(2)}} \times \pi = 96\% \times 2\pi$ pulse for valley (1). Thus we expect that the echo signal is very small in this case.
In case (I), the Hahn echo works. The probability that the electron stays in valley (2) until the third pulse is applied is $exp(-\Gamma\tau)$. Thus if Γ is faster than the other decoherence mechanisms, we observe $exp(-\Gamma\tau)$ as the spin echo decay.
The same reasoning applies to the four-pulse decoupling sequence (CPMG). As soon as the valley switches, spin coherence is irreversibly lost. The probability that the valley has not yet switched (and spin coherence is not yet lost) after a time τ goes as $exp(-\Gamma\tau)$.
Finally, we note that valley switching on a 40 μs timescale cannot explain the decay of the Rabi oscillations which occurs on a few μs timescale.

REFERENCES

[1] J. N. Eckstein, J. Levy, MRS Bulletin **38**, 783 (2013).

[2] Y. Tokura, W. van der Wiel, T. Obata, and S. Tarucha, Phys. Rev. Lett. **96**, 047202 (2006).

[3] J. M. Elzerman, R. Hanson, L. H. Willems van Beveren, B. Witkamp, L. M. K. Vandersypen and L. P. Kouwenhoven, Nature **430**, 431 (2004).

[4] E. A. Chekhovich, M. N. Makhonin, A. I. Tartakovskii, A. Yacoby, H. Bluhm, K. C. Nowack, and L. M. K. Vandersypen, Nature Mater. **12**, 494 (2013).

[5] J. R. Petta, A. C. Johnson, J. M. Taylor, E. A. Laird, A. Yacoby, M. D. Lukin, C. M. Marcus, M. P. Hanson, and A. C. Gossard, Science **309**, 2180 (2005).

[6] T. Obata, M. Pioro-Ladri, Y. Tokura, Y. Shin, T. Kubo, K. Yoshida, T. Taniyama, and S. Tarucha, Phys. Rev. B **81**, 085317 (2010).

[7] R. Hanson, L. P. Kouwenhoven, J. R. Petta, S. Tarucha, L. M. K. Vandersypen, Rev. Mod. Phys. **79**, 1217 (2007).

[8] F. H. L. Koppens, C. Buizert, K. J. Tielrooij, I. T. Vink, K. C. Nowack, T. Meunier, L. P. Kouwenhoven, and L. M. K. Vandersypen, Nature **442**, 766 (2006).

[9] D. Loss, D. P. DiVincenzo, Phys. Rev. A **57**, 120 (1998).

[10] K. C. Nowack, M. Shafiei, M. Laforest, G. E. D. K. Prawiroatmodjo, L. R. Schreiber, C. Reich, W. Wegscheider, L. M. K. Vandersypen, Science **333**, 1269 (2011).

[11] J. Medford, J. Beil, J. M. Taylor, S. D. Bartlett, A. C. Doherty, E. I. Rashba, D. P. DiVincenzo, H. Lu, A. C. Gossard, and C. M. Marcus, Nature Nanotech. **8**, 654 (2013).

[12] M. D. Shulman, O. E. Dial, S. P. Harvey, H. Bluhm, V. Umansky, A. Yacoby, Science **336**, 202 (2012).

[13] H. Bluhm, S. Foletti, D. Mahalu, V. Umansky, and A. Yacoby, Phys. Rev. Lett. **105**, 216803 (2010).

[14] J. T. Muhonen, J. P. Dehollain, A. Laucht, F. E. Hudson, T. Sekiguchi, K. M. Itoh, D. N. Jamieson, J. C. McCallum, A. S. Dzurak, A. Morello, Nature Nanotech. **9**, 986991 (2014).

[15] E. A. Laird, F. Pei, L. P. Kouwenhoven, Nature Nanotech. **8**, 565 (2013).

[16] H. O. H. Churchill, A. J. Bestwick, J. W. Harlow, F. Kuemmeth, D. Marcos, C. H. Stwertka, S. K. Watson and C. M. Marcus, Nature Phys. **5**, 321 (2009).

[17] A. P. Higginbotham, T. W. Larsen, J. Yao, H. Yan, C. M. Lieber, C. M. Marcus, F. Kuemmeth, Nano Lett. **14**, 35823586 (2014).

[18] C. H. Yang, A. Rossi, R. Ruskov, N. S. Lai, F. A. Mohiyaddin, S. Lee, C. Tahan, G. Klimeck, A. Morello and A. S. Dzurak, Nat. Commun. **4**, 2069 (2013).

[19] X. Hao, R. Ruskov, M. Xiao, C. Tahan, H. Jiang, Nat. Commun. **5**, 3860 (2013).

[20] F. A. Zwanenburg, A. S. Dzurak, A. Morello, M. Y. Simmons, L. C. L. Hollenberg, G. Klimeck, S. Rogge, S. N. Coppersmith, and M. A. Eriksson, Rev. Mod. Phys. **85**, 961 (2012).

[21] J. R. Prance, Z. Shi, C. B. Simmons, D. E. Savage, M. G. Lagally, L. R. Schreiber, L. M. K. Vandersypen, M. Friesen, R. Joynt, S. N. Coppersmith, and M. A. Eriksson, Phys. Rev. Lett. **108**, 046808 (2012).

[22] B. M. Maune et al., Nature **481**, 344 (2012).

[23] L. V. C. Assali, H. M. Petrilli, R. B. Capaz, B. Koiller, X. Hu, and S. Das Sarma, Phys. Rev. B **83**, 165301 (2011).

[24] X. Wu, D. R. Ward, J. R. Prance, D. Kim, J. K. Gamble, R. T. Mohr, Z. Shi, D. E. Savage, M. G. Lagally, Mark Friesen, S. N. Coppersmith, M. A. Eriksson, PNAS **111** (33), 11938 (2014).

[25] E. A. Laird, C. Barthel, E. I. Rashba, C. M. Marcus, M. P. Hanson, and A. C. Gossard, Semicond. Sci. Technol. **24**, 064004 (2009).

[26] J. J. Pla, K. Y. Tan, J. P. Dehollain, W. H. Lim, J. J. L. Morton, D. N. Jamieson, A. S. Dzurak, and A. Morello, Nature **489**, 541 (2012).

[27] L. Cywiski, R. M. Lutchyn, C. P. Nave, S. Das Sarma, Phys. Rev. B **77**, 174509 (2008).

[28] W. M. Witzel, S. Das Sarma, Phys. Rev. B **74**, 035322 (2006).

[29] Z. L. Xiang, S. Ashhab, J. Q. You, F. Nori, Rev. Mod. Phys. **85**, 623 (2013).

[30] D. R. Ward, D. E. Savage, M. G. Lagally, S. N. Coppersmith, M. A. Eriksson, Appl. Phys. Lett. **102**, 213107 (2013).

[31] M. G. Borselli et al., Appl. Phys. Lett. **99**, 063109 (2011).

[32] M. Shafiei, K. C. Nowack, C. Reichl, W. Wegscheider, L. M. K. Vandersypen, Phys. Rev. Lett. **110**, 107601 (2013).

[33] J. R. Goldman, T. D. Ladd, F. Yamaguchi, Y. Yamamoto, Appl. Phys. A **71**, 11 (2000).

[34] M. Pioro-Ladri, Y. Tokura, T. Obata, T. Kubo, S. Tarucha, Appl. Phys. Lett. **90**, 024105 (2007).

[35] C. B. Simmons, J. R. Prance, B. J. Van Bael, T. S. Koh, Z. Shi, D. E. Savage, M. G. Lagally, R. Joynt, Mark Friesen, S. N. Coppersmith, and M. A. Eriksson, Phys. Rev. Lett. **106**, 156804 (2011).

[36] A. Morello et al., Nature **467**, 687 (2010).

[37] J. Lu, F. Hoehne, A. R. Stegner, L. Dreher, M. Stutzmann, M. S. Brandt, and H. Huebl, Phys. Rev. B **83**, 235201 (2011).

[38] M. Friesen, S. N. Coppersmith, Phys. Rev. B **81**, 115324 (2010).

[39] J. K. Gamble, M. A. Eriksson, S. N. Coppersmith, M. Friesen, Phys. Rev. B **88**, 035310 (2013).

[40] M. Pioro-Ladri, T. Obata, Y. Tokura, Y. S. Shin, T. Kubo, K. Yoshida, T. Taniyama, and S. Tarucha, Nature Phys. **4**, 776 (2008).

[41] M. Borhani, X. Hu, Phys. Rev. B **85**, 125132 (2012).

[42] Z. Wilamowski, W. Jantsch, H. Malissa, and U. Rssler, Phys. Rev. B **66**, 195315 (2002).

[43] M. Friesen, S. Chutia, C. Tahan, and S. N. Coppersmith, Phys. Rev. B **75**, 115318 (2007).

[44] T. B. Boykin, G. Klimeck, M. A. Eriksson, Mark Friesen, S. N. Coppersmith, P. von Allmen, F. Oyafuso and S. Lee, Appl. Phys. Lett. **84**, 115 (2004).

[45] S. Goswami, K. A. Slinker, Mark Friesen, L. M. McGuire, J. L. Truitt, C. Tahan, L. J. Klein, J. O. Chu, P. M. Mooney, D. W. van der Weide, R. Joynt, S. N. Coppersmith and M. A. Eriksson, Nature Phys. **3**, 41 (2007).

[46] A. L. Saraiva, B. Koiller, and M. Friesen, Phys. Rev. B **82**, 245314 (2010).

6

SECOND HARMONIC COHERENT DRIVING OF A SINGLE ELECTRON SPIN IN SI-GE SINGLE QD

We demonstrate coherent driving of a single electron spin using second harmonic excitation in a Si/SiGe quantum dot. Our estimates suggest that the anharmonic dot confining potential combined with a gradient in the transverse magnetic field dominates the second harmonic response. As expected, the Rabi frequency depends quadratically on the driving amplitude and the periodicity with respect to the phase of the drive is twice that of the fundamental harmonic. The maximum Rabi frequency observed for the second harmonic is just a factor of two lower than that achieved for the first harmonic when driving at the same power. Combined with the lower demands on microwave circuitry when operating at half the qubit frequency, these observations indicate that second harmonic driving can be a useful technique for future quantum computation architectures.

The work in this chapter has been published as: P. Scarlino, E. Kawakami, D. R. Ward, D. E. Savage, M. G. Lagally, Mark Friesen, S. N. Coppersmith, M. A. Eriksson, and L. M. K. Vandersypen, Phys. Rev. Lett. **115**, 106802 (2015).

6.1. INTRODUCTION

Controlled two-level quantum systems are essential elements for quantum information processing. A natural and archetypical controlled two-level system is the electron spin doublet in the presence of an external static magnetic field [1, 2]. The common method for driving transitions between the two spin states is magnetic resonance, whereby an a.c. magnetic field ($B_{a.c.}$) is applied transverse to the static magnetic field (B_{ext}), with a frequency, f_{MW}, matching the spin Larmor precession frequency $f_L = g\mu_B B_{tot}/h$ (h is Planck's constant, μ_B is the Bohr magneton and B_{tot} the total magnetic field acting on the spin). When the driving rate is sufficiently strong compared to the dephasing rates, coherent Rabi oscillations between the ground and excited state are observed.

Both spin transitions and Rabi oscillations can be driven not just at the fundamental harmonic but also at higher harmonics; i.e., where the frequency of the transverse a.c. field is an integer fraction of the Larmor frequency, $f_{MW} = f_L/n$, with n an integer. Second or higher harmonic generation involves non-linear phenomena. Such processes are well known and explored in quantum optics using non-linear crystals [3] and their selectivity for specific transitions is exploited in spectroscopy and microscopy [4–8]. Two-photon coherent transitions have been extensively explored also for biexcitons in (In,Ga)As quantum dots [9] and in superconducting qubit systems [10–13]. In cavity QED systems, a two-photon process has the advantage that it allows the direct transition from the ground state to the second excited state, which is forbidden in the dipole transition by the selection rules [14].

For electron spin qubits, it has been predicted that the non-linear dependence of the g-tensor on applied electric fields should allow electric-dipole spin resonance (EDSR) at subharmonics of the Larmor frequency for hydrogenic donors in a semiconductor [15, 16]. For electrically driven spin qubits confined in a (double) quantum dot, higher-harmonic driving has been proposed that takes advantage of an anharmonic dot confining potential [17–21] or a spatially inhomogeneous magnetic field [22]. In order to use higher harmonic generation for coherent control of a system, the corresponding driving rate must exceed the decoherence rate. This requires a non-linearity that is sufficiently strong. Although weak non-linearities are easily obtained and have allowed higher harmonics to be used in continuous wave (CW) spectroscopy for quantum dots hosted in GaAs, InAs, InSb and carbon nanotubes [23–28], coherent spin manipulation using higher harmonics has not been demonstrated previously.

In this Chapter we present experimental evidence of coherent second harmonic manipulation of an electron spin confined in a single quantum dot (QD) hosted in Si/SiGe quantum well. We show that this second-harmonic driving can be used for universal spin control, and we use it to measure the free-induction and Hahn-echo decay of the electron spin. Furthermore, we study how the second harmonic response varies with the microwave amplitude and phase, and comment on the nature of the non-linearity that mediates the second harmonic driving process in this system.

6.2. DEVICE AND MEASUREMENT TECHNIQUE

The quantum dot is electrostatically induced in an undoped Si/SiGe quantum well structure, through a combination of accumulation and depletion gates (see Sec. 6.9.1 for full

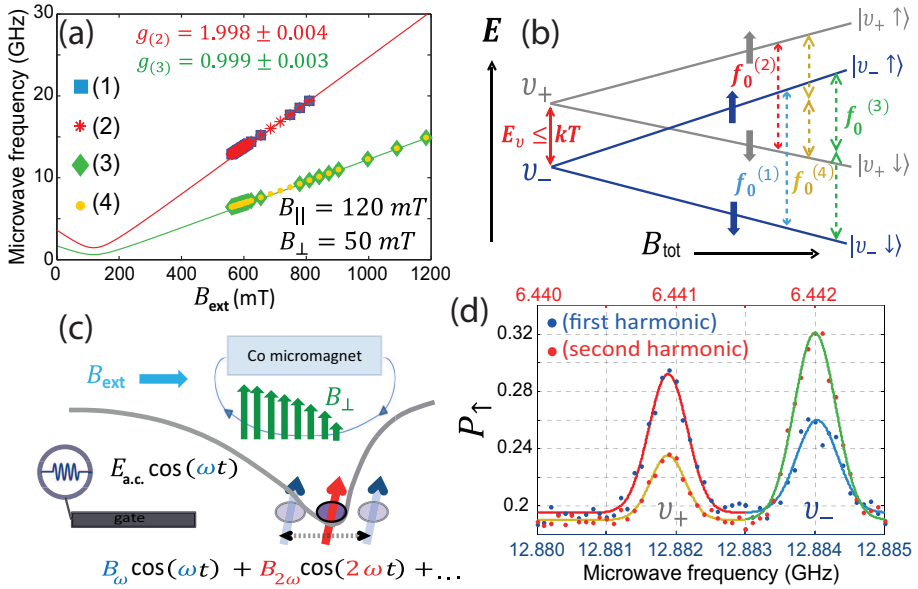

Figure 6.1: (a) Measured resonance frequencies as a function of externally applied magnetic field B_{ext}. The long microwave burst time t_p =700 μs $\gg T_2^*$ means that the applied excitation is effectively continuous wave (CW). The microwave source output power was $P = -33$ dBm to -10 dBm (-20 dBm to -5 dBm) for the case of fundamental (second) harmonic excitation, decreasing for lower microwave frequency in order to avoid power broadening. The red and green lines represent fits with the relation $hf = g\mu_B\sqrt{(B_{ext} - B_{||})^2 + B_\perp^2}$ respectively to the resonance data labeled (2) and (3) (we excluded points with $B_{ext} < 700$ mT from the fit because the micromagnet apparently begins to demagnetize there) [29]. (b) Schematic of the energy levels involved in the excitation process, as a function of the total magnetic field at the electron location. The dashed arrows correspond to the four transitions in panel (a), using the same color code. (c) Schematic of an anharmonic confinement potential, leading to higher harmonics in the electron oscillatory motion in response to a sinusoidally varying excitation. (d) Measured spin-up probability, $P_\uparrow$, as a function of applied microwave frequency, f_{MW}, for B_{ext}= 560.783 mT ($P = -30$ dBm for the fundamental response, $P = -12$ dBm for the second harmonics), averaged over 150 repetitions per point times 80 repeated frequency sweeps (160 mins in total). The frequency axis (in red on top) has been stretched by a factor of two for the second harmonic spin response (red datapoints). From the linewidths, we extract a lower bound for the dephasing time $T_2^{*(1)} = 760 \pm 100$ ns, $T_2^{*(2)} = 810 \pm 50$ ns, $T_2^{*(3)} = 750 \pm 40$ ns and $T_2^{*(4)} = 910 \pm 80$ ns. The Gaussian fits through the four peaks use the same color code as in panels (a) and (b).

details). The sample and the settings are the same as those used in Ref. [29]. A cobalt micromagnet next to the QD creates a local magnetic field gradient, enabling spin transitions to be driven by electric fields [29, 30].

All measurements shown here are performed using single-shot readout via a QD charge sensor [31]. They make use of four-stage gate voltage pulses implementing (1) initialization to spin-down, (2) spin manipulation through all-electrical microwave excitation, (3) single-shot spin readout, and (4) a compensation/empty stage [29]. The results of many single-shot cycles are used to determine the spin-up probability, $P_\uparrow$, at the end of the manipulation stage.

First we apply long, low-power microwave excitation to perform quasi-CW spectroscopy. Fig. 6.1(a) shows four observed spin resonance frequencies, $f_0^{(1)}$ through $f_0^{(4)}$, as a function of the external magnetic field. The resonances labeled (1) and (2) represent the response at the fundamental frequency. As in [29], these two closely spaced resonances correspond to the electron occupying either of the two lowest valley states, both of which are thermally populated here. The other two resonances occur at exactly half the frequency of the first two, $f_0^{(1)} = 2f_0^{(3)}$, $f_0^{(2)} = 2f_0^{(4)}$, and represent the second harmonic response.

The effective g-factors extracted from the slopes for the second harmonic response are half those for the first harmonic response [see Fig. 6.1(a) inset]. The relevant energy levels and transitions as a function of the total magnetic field, B_{tot}, are visualized in Fig. 6.1(b), where the color scheme used for the resonances is the same as in Fig. 6.1(a). We see two sets of Zeeman split doublets, separated by the splitting between the two lowest-energy valleys, E_v. The transition between the Zeeman sublevels within each doublet can be driven by absorbing a single photon or two photons, as indicated by the single and double arrows.

6.3. ORIGIN OF THE NON LINEARITY

To drive a transition using the second harmonic, a non-linearity is required. In principle, several mechanisms can introduce such a non-linearity in this system (see Sec. 6.9.6). First, as schematically shown in Fig. 6.1(c), if the confining potential is anharmonic, an oscillating electric field of amplitude $E_{a.c.}$ and angular frequency $\omega = 2\pi f_{MW}$ induces effective displacements of the electron wavefunction with spectral components at angular frequencies $n\omega$, with n an integer. In analogy with non-linear optical elements, we can look at this process as generated by an effective non-linear susceptibility of the electron bounded to the anharmonic QD confinement potential.

The gradient in the transverse magnetic field in the dot region ($B_\perp$ in green) converts the electron motion into an oscillating transverse magnetic field of the form

$$B_\perp^{a.c.}(t) = B_\omega \cos(\omega t) + B_{2\omega} \cos(2\omega t) + \dots \tag{6.1}$$

that can drive the electron spin for $\hbar\omega = E_z$, $2\hbar\omega = E_z$ and so forth [17]. A possible source of anharmonicity arises from the nonlinear dependence of the dipole moment between the valley (or valley-orbit) ground (v_-) and excited states (v_+) [32], as a function of $E_{a.c.}$.

A second possible source of nonlinearity is a variation of the transverse field gradient, $\frac{dB_\perp}{dx,dy}$, with position [see Fig. 6.1(c)]. Even if the confining potential were harmonic, this

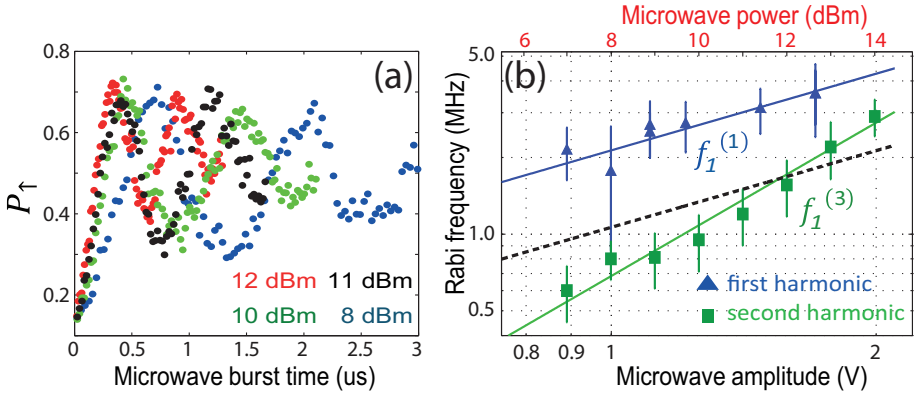

Figure 6.2: Rabi oscillations. (a) Measured spin-up probability, $P_\uparrow$, as a function of microwave burst time (B_{ext} = 560.783 mT, f_{MW} = 6.4455 GHz) at four different microwave powers, corresponding to a rms voltage at the source of 998.8 mV, 1257.4 mV, 1410.9 mV, 1583.0 mV. (b) Rabi frequencies recorded at the fundamental harmonic, $f_0^{(1)}$ (blue triangles, adapted from [29]), and at the second harmonic, $f_0^{(3)}$ (green squares), as a function of the microwave amplitude emitted from the source (top axis shows the corresponding power). For the second harmonic, the amplitude shown corresponds to a 5 dB higher power than the actual output power, to compensate for the 5 dB lower attenuation of the transmission line at 6 GHz versus 12 GHz (estimated by measuring the coax transmission at room temperature). The green solid (dashed black) line is a fit of the second harmonic data with the relation $\log(f^R) \propto 2\log(E_{a.c.})$ [$\log(f^R) \propto \log(E_{a.c.})$]. The large error bars in the FFT of the data in Fig. 6.2(a) arise because we perform the FFT on only a few oscillations. B_{ext}= 560.783 mT.

would still lead to an effective transverse magnetic field containing higher harmonics, of the same form as Eq. 6.1.

A third possibility is that not only the transverse magnetic field but also the longitudinal magnetic field varies with position. This leads to an a.c. magnetic field which is not strictly perpendicular to the static field, which is in itself sufficient to allow second harmonic driving [21, 33, 34], even when the confining potential is harmonic and the field gradients are constant over the entire range of the electron motion.

However, simple estimates indicate that the second and third mechanisms are not sufficiently strong in the present sample to allow the coherent spin manipulation we report below (see Sec. 6.9.6). We propose that the first mechanism is dominant in this sample, supported by our observation that the strength of the second harmonic response is sensitive to the gate voltages defining the dot.

6.4. CW ANALYSIS

In Fig. 6.1(d) we zoom in on the four CW spin resonance peaks, recorded at low enough power to avoid power broadening (see Sec. 6.9.1). Fitting those resonances with Gaussians, we extract the dephasing times $T_2^{*,(1,2)} = \frac{\sqrt{2}\hbar}{\pi\delta f_{FWHM}^{(1,2)}}$, $T_2^{*,(3,4)} = \frac{\sqrt{2}\hbar}{2\pi\delta f_{FWHM}^{(3,4)}}$, giving values in the range of 750 to 910ns for all four resonances [see caption of Fig. 6.1(d)]. This directly shows that the linewidth (FWHM) extracted for the two-photon process is half that for the one-photon process, as expected [15, 22, 34].

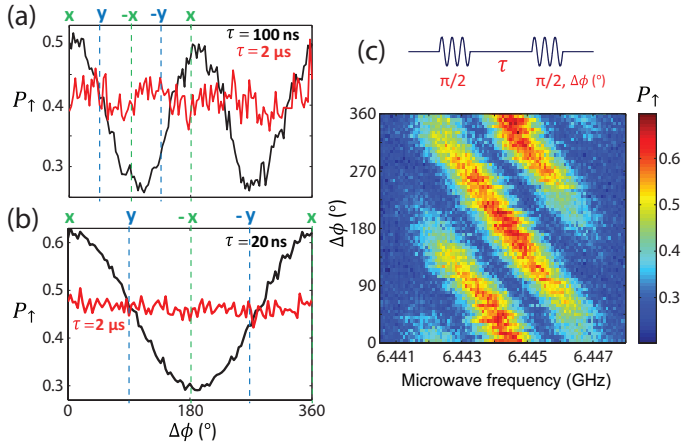

Figure 6.3: Phase control of oscillations. (a) Probability $P_\uparrow$ measured after applying two $\pi/2$ rotations via second harmonic excitation, as a function of the relative phase between the two microwave bursts, $\Delta\phi$. The two rotations are separated by $\tau = 100$ ns (black) and $\tau = 2$ μs (red). ($P = 16.0$ dBm, $B_{ext} = 560.783$ mT, $f_{MW} = f_0^{(3)} = 6.44289$ GHz). (b) Similar to panel (a), but now driving the fundamental harmonic for $\tau = 20$ ns (black) and $\tau = 2$ μs (red). ($P = 12.0$ dBm, $B_{ext} = 560.783$ mT, $f_{MW} = f_0^{(2)} = 12.88577$ GHz). Inset: Microwave pulse scheme used for this measurement. (c) Measured spin-up probability, $P_\uparrow$ (1000 repetitions for each point), as a function of f_{MW} and the relative phase $\Delta\phi$ between two $\pi/2$ microwave bursts (130 ns, $P = 16.0$ dBm) for second harmonic excitation, with $\tau = 50$ ns. The measurement extends over more than 15 hours.

From the relative peak heights in Fig. 6.1(d), we can estimate the ratio of the Rabi frequencies between the two peaks in each pair (see Sec. 6.9.2). In [29], we found that the relative thermal populations of the two valleys ($\epsilon^{(4)}/\epsilon^{(3)}$) were about 0.3 ± 0.1 to 0.7 ± 0.1. Given this, the ratio between the Rabi frequencies, f_1, extracted from the peak heights is $r_R(2ph) = f_1^{(4)}/f_1^{(3)} = 0.9 \pm 0.2$ for the second harmonics. This is different from the ratio observed in [29] for the fundamental harmonic, $r_R(1ph) = f_1^{(2)}/f_1^{(1)} = 1.70 \pm 0.05$[1].

Such a difference is to be expected. The ratio $r_R(2ph)$ is affected by how the degree of anharmonicity in the confining potential differs between the two valleys. In contrast, $r_R(1ph)$ depends on how the electrical susceptibility differs between the two valleys [35]. In addition, since the valleys have different charge distributions [32], the microwave electric field couples differently to the two valley states, and this difference can be frequency dependent [36, 37]. Because the second harmonic Rabi oscillations are driven at half the frequency of the Rabi oscillations driven at the fundamental, this frequency dependence also contributes to a difference between $r_R(1ph)$ and $r_R(2ph)$. We note that the difference in Rabi frequency ratio between the 1-photon and 2-photon case demonstrates that the second harmonic response is not just the result of a classical up-conversion of the microwave frequency taking place before the microwave radiation impinges on the dot, but takes place at the dot itself.

[1] Note that the ratio between the two Rabi frequencies is independent of the microwave amplitude in both cases, as we have $r_R(1ph) = f_1^{(2)}/f_1^{(1)} = m_2 E_{a.c.}/m_1 E_{a.c.} = m_2/m_1$ and $r_R(2ph) = f_1^{(4)}/f_1^{(3)} = q_4 E_{a.c.}^2/q_3 E_{a.c.}^2 = q_4/q_3$, respectively.

6.5. COHERENT SPIN OSCILLATIONS

The second harmonic response also permits coherent driving, for which a characteristic power dependence is expected [22, 34, 38]. Fig. 6.2(a) shows Rabi oscillations, where the microwave burst time is varied keeping $f_{MW} = f_0^{(3)}$ for different microwave powers. We note that the contribution to the measured spin-up oscillations coming from the other resonance, (4), is negligible because the respective spin Larmor frequencies are off-resonance by 2 MHz, $f_1^{(3)}/f_1^{(4)} \approx 1$ and its population is ~ three times smaller.

To analyze the dependence of the Rabi frequency on microwave power, we perform a FFT of various sets of Rabi oscillations similar to those in Fig. 6.2(a). Fig. 6.2(b) shows the Rabi frequency thus obtained versus microwave power for driving both at the second harmonic (green) and at the fundamental (blue), taken for identical dot settings [29]. We see that for driving at the frequency of the second harmonic, the Rabi frequency is quadratic in the applied electric field amplitude (linear in power), as expected from theory [22, 34, 38]. When driving at the fundamental resonance, the Rabi frequency is linear in the driving amplitude, as usual. It is worth noting that at the highest power used in this experiment the Rabi frequency obtained from driving the fundamental valley-orbit ground state spin resonance is just a factor of two higher than the one from driving at the second harmonic. This ratio indicates that the use of second harmonic driving is quite efficient in our device. This result is consistent with Ref. [22], which shows that Rabi frequencies at subharmonic resonances can be comparable to the Rabi frequency at the fundamental resonance, and also with the theory and experiments in Refs. [20] and [26], which report resonant response at a second harmonic that can exceed that at the fundamental.

6.6. UNIVERSAL PHASE CONTROL

A further peculiarity in coherent driving using second harmonics is seen when we vary the phase of two consecutive microwave bursts. Fig. 6.3(a) shows the spin-up probability following two $\pi/2$ microwave bursts with relative phase $\Delta\phi$, resonant with $f_0^{(3)}$ and separated by a fixed waiting time τ. For short τ, the signal oscillates sinusoidally in $\Delta\phi$ with a period that is half that for the single-photon case [compare the black traces in Figs. 6.3(a,b)].

Therefore, in order to rotate the electron spin around an axis in the rotating frame rotated by 90 degrees with respect to a prior spin rotation axis (e.g. a Y rotation following an X rotation in the rotating frame), we need to set $\Delta\phi$ to 45 degrees, instead of 90 degrees, when driving via the second harmonic. Of course, for $\tau \gg T_2^*$, the contrast has vanished, indicating that all phase information is lost during the waiting time [Fig. 6.3(a,b) red traces]. Fig. 6.3(c) shows two-pulse measurements as in Fig. 6.3(a) as a function of frequency detuning and phase difference, where we can appreciate the extraordinary stability of the undoped device.

6.7. RAMSEY MEASUREMENT AND ECHO

To probe further the coherence properties of the spin, we perform a free induction (Ramsey) decay measurement, see Fig. 6.4(a), as a function of frequency detuning and delay time, τ, between the two bursts. The absence of a central frequency symmetry axis is

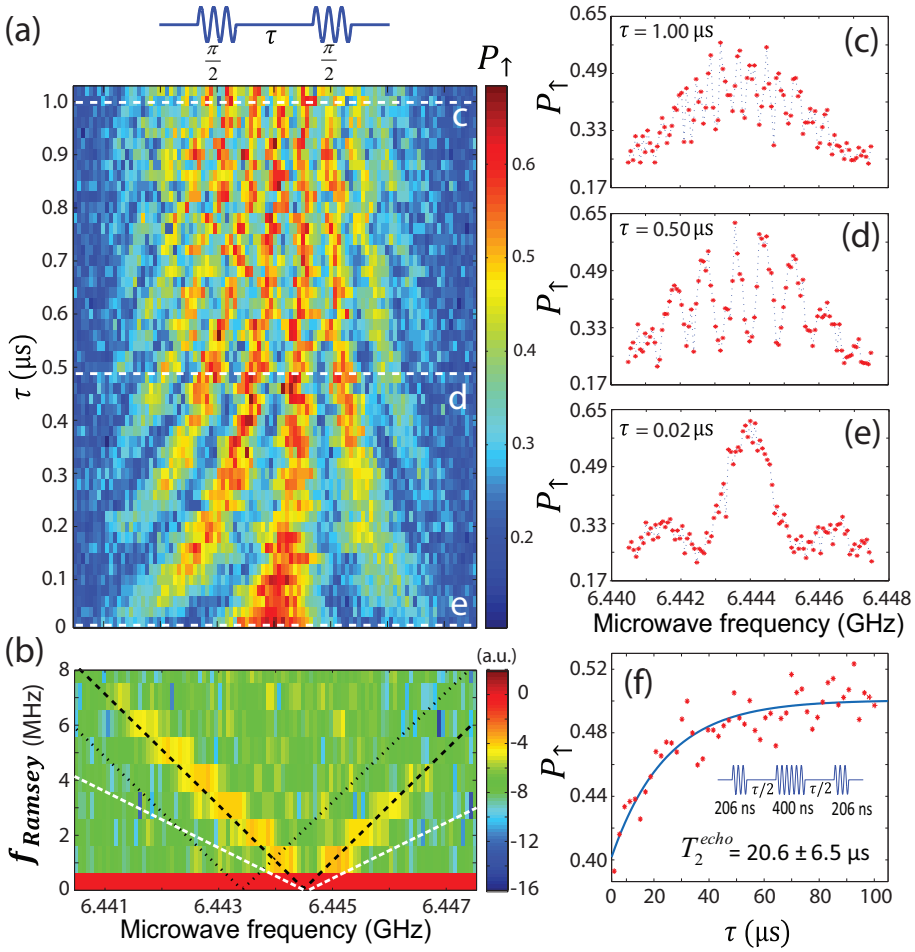

Figure 6.4: Ramsey fringes. (a) Measured spin-up probability, $P_\uparrow$, as a function of f_{MW} and waiting time τ (B_{ext} = 560.783 mT, P = 13.0 dBm) between two $\pi/2$ pulses (130 ns) with equal phase, showing Ramsey interference. Each data point is averaged over 300 cycles. Inset: Microwave pulse scheme used for this measurement. (b) Fourier transform over the waiting time, τ, of the data in panel (a), showing a linear dependence on the microwave frequency, with vertex at $f_{MW} = f_0^{(3)}$ and slope $f_{Ramsey} = 2\Delta f_{MW}$ (black dashed lines). The expected position of the FFT of the signal arising from resonance $f_0^{(4)}$ is indicated by the dotted black line. For comparison, the white dashed line represents the relation $f_{Ramsey} = \Delta f_{MW}$. (c-d-e) Sections of the Ramsey interference pattern in (a) along the three white dashed lines; the respective waiting times are indicated also in the inset of each panel. (f) Measured spin-up probability as a function of the total free evolution time, τ, in a Hahn echo experiment (pulse scheme shown in inset). The decay curve is fit well to a single exponential (blue). Here, $f_{MW} = f_0^{(3)}$, B_{ext}= 560.783 mT.

due to the presence of two superimposed oscillating patterns, originating from the resonances at $f_0^{(3)}$ and $f_0^{(4)}$. Figs. 6.4(c-e) show sections of the Ramsey measurement in Fig. 6.4(a), corresponding to different waiting times τ (see the white dashed lines). The visibility of the Ramsey fringes clearly decreases for longer waiting times between the two $\pi/2$ pulses. Fitting the decay of the visibility of the fringes as a function of τ with a Gaussian ($\propto \exp[-(t/T_2^*)^2]$, see Sec. 6.9.4) we find $T_2^* = 780 \pm 110$ ns, in agreement with the value extracted from the linewidth.

Furthermore, and analogously to the observations of Fig. 6.3(a), we report a doubling effect in the frequency of the Ramsey oscillations, f_{Ramsey}, as a function of the detuning $\Delta f_{MW} = f_{MW} - f_0^{(3)}$. Fig. 6.4(b) shows $f_{Ramsey}(\Delta f_{MW})$, extracted from the data in Fig. 6.4(a) via a FFT over the waiting time τ. The black dashed line indicates the condition $f_{Ramsey} = 2\Delta f_{MW}$, closely overlapping with the position of the yellow peaks in the FFT. The black dotted line indicates the condition $f_{Ramsey} = 2(f_{MW} - f_0^{(4)})$; this second resonance is not very visible in the data, due to the lower population of the corresponding valley. For comparison, the white dashed line indicates the condition $f_{Ramsey} = \Delta f_{MW}$, which is the expected response when driving at the fundamental.

Finally, we perform a spin echo experiment via second harmonic driving. Fig. 6.4(f) shows $P_\uparrow$ as a function of the total free evolution time τ, for a typical Hahn echo pulse sequence (illustrated in the inset) consisting of $\pi/2$, π and $\pi/2$ pulses applied along the same axis, separated by waiting times $\tau/2$ [39]. A fit to a single exponential yields $T_2^{echo} = 20.6 \pm 6.5\mu$s at B_{ext}= 560.783 mT, compatible with the T_2^{echo} of 23.0 $\pm$1.2 μs we observed at the same magnetic field when driving via the fundamental harmonic (see Sec. 6.9.5).

6.8. CONCLUSION

To summarize, we report coherent second harmonic driving of an electron spin qubit defined in a Si/SiGe quantum dot, including universal single-spin rotations. The nonlinearity that permits second harmonic driving is likely related to the anharmonic confining potential for the electron. This means that routine use of second harmonics for spin control would be possible provided there is sufficient control over the degree of anharmonicity of the confining potential. This could be very useful since driving a spin qubit at half its Larmor frequency would substantially simplify the microwave engineering required for high fidelity qubit control.

6.9. SUPPLEMENTARY INFORMATION

6.9.1. DEVICE AND MEASUREMENT TECHNIQUE

The device used for all the measurements shown in the main text, is based on a 12 nm wide Si quantum well 37 nm below the surface in an undoped Si/SiGe heterostructure, with two layers of electrostatic gates [see Fig. 6.5(a)]. Two accumulation gates (in yellow) are used to induce a two-dimensional electron gas (2DEG) and a set of depletion gates (in gray), labeled 1-10 in Fig. 6.5(a), is used to form a single quantum dot in the 2DEG (on the right side) with a charge sensor next to it (made by gates 4, 5 and 6). Two 1 μm-wide, 200 nm-thick, and 1.5 μm-long Co magnets (in green), placed on top of accumulation gates (separated by an Al_2O_3 layer), provide a stray magnetic field [see Fig. 6.5(b)]. The

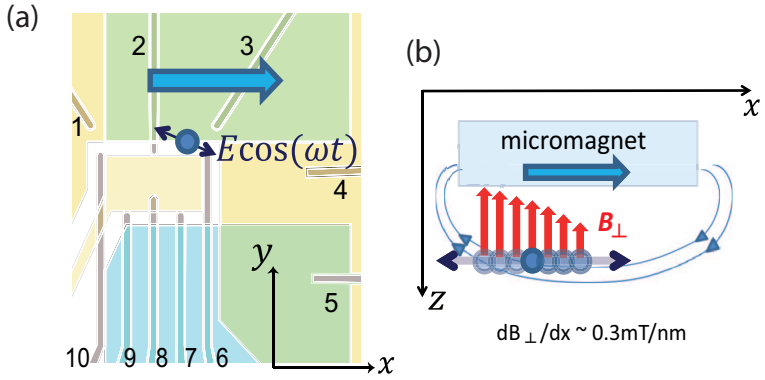

Figure 6.5: (a) False-color device image showing a fabricated pattern of split gates, labeled 1-10. For this experiment we create a single quantum dot (estimated location indicated by a blue circle) and a sensing dot (gates 4 and 5). The current through the charge sensor is recorded in real time for a fixed voltage bias of 500 μeV. The voltage pulses and microwave excitation are applied to gate 2 and 6 respectively. Green semitransparent rectangles show the position of two 200-nm-thick Co micromagnets. The yellow-shaded areas show the location of two accumulation gates, one for the reservoirs and the other for the double quantum dot region. (b) Schematic side view of the stray magnetic field generated by a single micromagnet, completely magnetized along the x-axis; $B_\perp$ represents the component of the stray magnetic field perpendicular to the static field. The external magnetic field B_{ext} is applied along the x-axis [blue arrow in both (a) and (b) panels].

sample is thermally anchored to the mixing chamber of a dilution refrigerator with base temperature 25 mK and the electron temperature estimated from transport measurements is 150 mK.

Microwave excitation, generated by a Agilent E8267D Vector Source, is applied to gate 6 through the following attenuation chain: DC block/ULT-05 Keycom coax/20 dB attenuator (1.7 K)/ NbTi coax /10 dB attenuator (50 mK)/flexible coax/SMA connector on the printed circuit board (PCB). The high frequency signal is combined on the PCB with a DC voltage line by a homemade resistive bias tee (R = 10 MΩ, C= 47 nF). We tested the transmission of the whole microwave line with a network analyzer at room temperature and we found an attenuation of ~45 dB and ~40 dB for a 12 GHz and 6 GHz signal respectively.

The microwave excitation generates an a.c. electric field, $E_{a.c.}$, which makes the electron oscillate back and forth in the dot. Due to the gradient in the transverse magnetic field, $dB_\perp/dx$, estimated to be ≈0.3 mT/nm [Fig. 6.5(b)], the electron is then subject to an oscillating magnetic field $B_{a.c.} = \frac{eE_{a.c.}l_{orb}^2|dB_\perp/dx|}{\Delta_{orb}} \propto \frac{eE_{a.c.}|dB_\perp/dx|}{\Delta_{orb}^2}$, perpendicular to the external static magnetic field. Here $\Delta_{orb} \propto 1/l_{orb}^2$ is the orbital level spacing, with l_{orb} the typical QD dimension. We notice that the amplitude of $B_{a.c.}$ is proportional to the magnitude of the magnetic field gradient, to $1/\Delta_{orb}^2$ and to the amplitude of $E_{a.c.}$.

We tune the right dot to the few-electron regime (with the left dot empty) and adjust the tunnel rate between the dot and the reservoir to be around ~1 kHz, so that dot-reservoir tunnel events can be monitored in real time by collecting the charge sensor current, read through a room temperature I-V converter, after a low-pass-filter with corner frequency of 30 kHz. The single-shot data [29, 31] are processed on the fly by using an

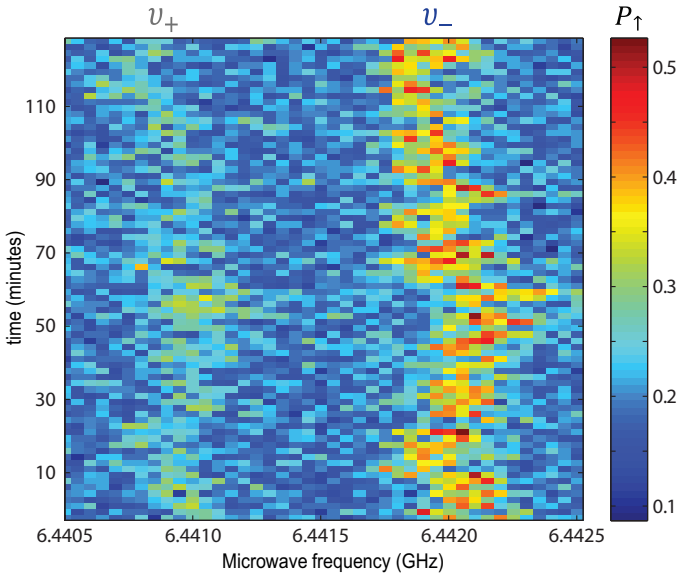

Figure 6.6: The raw data on which Fig. 6.1(d) is based. Measured spin-up probability, $P_\uparrow$, as a function of applied microwave drive frequency f_{MW} and time (external field B_{ext}= 560.783 mT, power P = -12 dBm, microwave pulse duration 700 μs). Each horizontal scan in the figure takes ~2 minutes (200 cycles, in which each data point takes 2s), and the scan is repeated ~60 times. The time reported on the y-axis is counted from the start of the measurement.

FPGA which directly counts the number of spin excited state events by using a threshold detection scheme.

6.9.2. ESTIMATION OF THE RATIO OF RABI FREQUENCIES FROM CW MEASUREMENTS

A typical CW spin resonance measurement is reported in Fig. 6.6, which shows the spin excited state probability as a function of the applied microwave frequency, f_{MW}, and time. We note that the fluctuations of the two spin resonance frequencies, $f^{(3)}$ and $f^{(4)}$, are highly correlated; this suggest that the two resonances are affected by the same low-frequency source of noise (very likely hyperfine fluctuations) on the ~minute timescale. The trace for the second harmonic in Fig. 6.1(d) in the main text is obtained by averaging the data in Fig. 6.6 over the time axis.

As reported in the supplementary information of Ref. [29] (Chapter 5), the ratio of the steady-state spin-flip probability measured for the two valley states converges at low driving power to $r_R^2(2ph)$, with $r_R(2ph) = f_1^{(4)}/f_1^{(3)}$ the ratio of the Rabi frequencies between two valleys.

The ratio of the measured peak amplitudes in Fig. 6.1(d), which we write as $A(v_+)/A(v_-)$, is the product of $r_R^2(2ph)$ and the ratio of the respective populations at the end of the initialization stage, $\epsilon^{(4)}/\epsilon^{(3)}$:

$$\frac{A(v_+)}{A(v_-)} = r_R^2(2ph) \times \frac{\epsilon^{(4)}}{\epsilon^{(3)}} \tag{6.2}$$

From a Gaussian fit to the spin resonance response for the two valleys in Fig. 6.1(d), we extract $A(v_+)/A(v_-) \sim 0.35$. Furthermore, it is reasonable to assume that the ratio between the valley ground and excited state populations after the initialization stage, is the same when driving via the second harmonic as when driving via the fundamental. Therefore, we can use the ratio extracted for the fundamental in [29] (Chapter 5):

$$\frac{\epsilon^{(4)}}{\epsilon^{(3)}} \equiv \frac{\epsilon^{(2)}}{\epsilon^{(1)}} = \frac{0.3 \pm 0.1}{0.7 \pm 0.1} = 0.42 \pm 0.20. \tag{6.3}$$

From eq. 6.2 and eq. 6.3 we obtain

$$r_R(2ph) = f_1^{(4)}/f_1^{(3)} = 0.90 \pm 0.21. \tag{6.4}$$

We remark that we also assume that the ratio of the Rabi frequencies between two valleys is the same at high microwave power as it is at low microwave power, which seems reasonable.

6.9.3. CHEVRON PATTERN USING SECOND HARMONIC DRIVING

In Fig. 6.7(a) we report the spin excited state probability oscillations as a function of the microwave burst time and detuning frequency (driving with P_{MW}= 11.0 dBm at the source). The quality of the data (stability of the measurement) is not high enough to extract independently the Rabi frequencies for the two valley states directly from the superimposed Chevron patterns (as was done in [29] (Chapter 5) for driving via the fundamental harmonic). However, using the Rabi frequency ratio $r_R(2ph) \approx 1$ extracted above, the ratio of initial populations of the two valleys of $\epsilon^{(4)}/\epsilon^{(3)}$ ~0.3/0.7 discussed above as well, and a Rabi frequency of 1.05 MHz for the valley ground state [estimated from a FFT along the MW burst time of Fig. 6.7(a)], we can simulate the two superimposed Chevron patterns, see Fig. 6.7(b). This simulation agrees qualitatively with the data of Fig. 6.7(a), in particular it captures the slight asymmetry along the detuning axis, and the fact that mostly one Chevron pattern is visible.

6.9.4. T_2^* ESTIMATION FROM RAMSEY ENVELOPE DECAY AND RAMSEY SIMULATION

In order to get an alternative estimation of the dephasing time T_2^*, we can perform a Ramsey measurement [see Fig. 6.4(a)] and record the amplitude of the Ramsey oscillations as a function of the waiting time τ between the two $\pi/2$ pulses, keeping $f_{MW} \approx f_0^{(1)}$. We show this data in Fig. 6.8, with the blue dotted curve representing the fitting relation $P_\uparrow = a\exp[-(t/T_2^*)^2] + c$. From this fit we get a T_2^* of 780 ± 110 ns, compatible with what we estimated from the CW spin resonance linewidth in Fig. 6.1(d). On the same figure we report in black for comparison a fit with the exponential relation $P_\uparrow = a\exp(-t/T_2^*) + c$.

6.9.5. ECHO DECAY OF A QUBIT DRIVEN FUNDAMENTAL HARMONIC AND COMPARISON TO RESULTS FOR DRIVING AT SECOND HARMONIC

In Fig. 6.9 we show a Hahn echo measurement realized driving spin resonance at the fundamental harmonic, recorded at the same magnetic field B_{ext} as the measurement reported in Fig. 6.4(e) (driven by second harmonic). The $T_2^{echo}(1ph)$ extracted from a fit

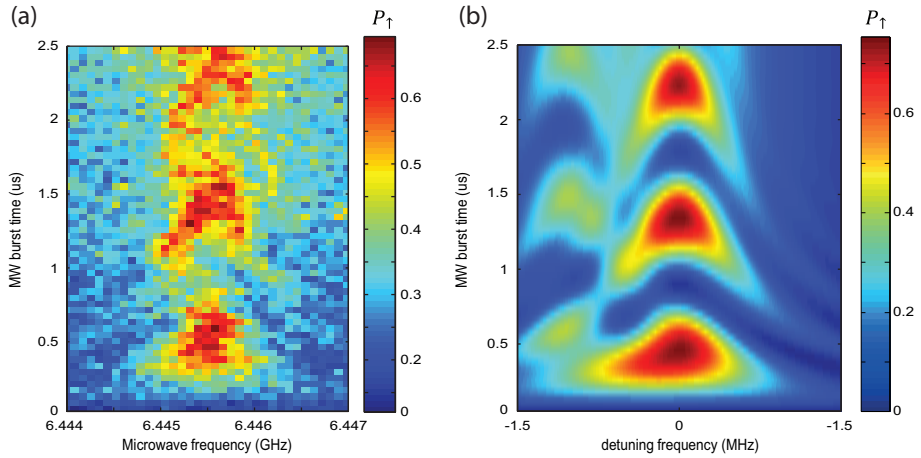

Figure 6.7: (a) Measured spin-up probability, $P_\uparrow$, as a function of drive frequency f_{MW} and microwave burst time (B_{ext} = 560.783 mT, P = 11.0 dBm). (b) Simulated spin-up probability using population fractions 0.3:0.7, Rabi frequencies 1.0 MHz and 1.1 MHz for the v_+ and v_- valley states respectively, and the Larmor frequencies separated by ~1.04 MHz, extracted from low-power CW measurements in Fig. 6.1(d).

with a single exponential decay is similar to the $T_2^{echo}(2ph)$ extracted from Fig. 6.4(e). The decay obeys a single exponential similar to that observed in Ref. [29] (Chapter 5), indicating the presence of a high-frequency decoherence process.

6.9.6. MECHANISMS MEDIATING SECOND HARMONIC GENERATION

Here we elaborate on the three mechanisms discussed in the main text that can lead to second harmonic generation.

Position dependent magnetic field gradient.

From a simulation of the stray magnetic field of the micromagnet, see also the supplementary information of Ref. [29] (Chapter 5), we can put an upper bound on the second derivative of the stray magnetic field with respect to the dot coordinates of $d^2B_\perp/dx^2 < 1\ \mu\text{T}/(\text{nm})^2$. This is far too small to produce second harmonic Rabi frequencies that are comparable to the fundamental harmonic Rabi frequencies (which is what we observed experimentally).

Tilted drive field.

If the a.c. magnetic field that is driving spin resonance is not strictly perpendicular to the static magnetic field, second harmonic driving becomes possible [21, 34]. Eq. 18 of Ref. [34] expresses the two-photon Rabi frequency, $\omega_{eff}^{(2ph)}$, as a function of the drive strength $\omega_1 \propto B_{a.c.}$ and the drive frequency $\omega \propto B_{tot}$, for the case of an angle ϑ between static and oscillating field of 45 degrees. They found $\omega_{eff}^{(2ph)} = 2\omega_1^2/\omega$. In our system the magnetic field gradient (which will provide $B_{a.c.}(t)$ in combination with the microwave

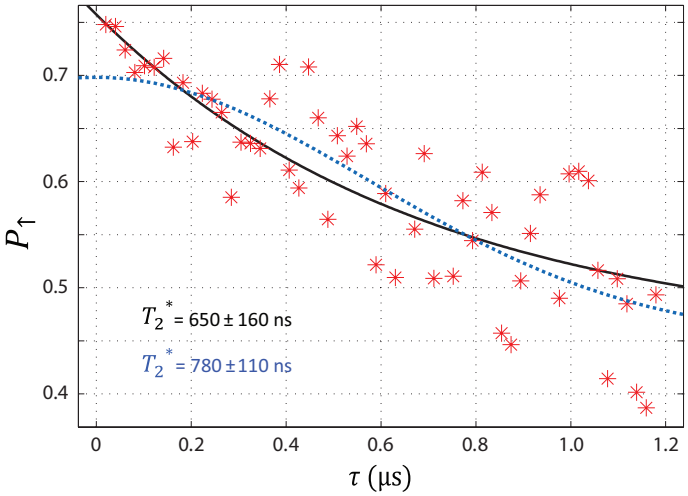

Figure 6.8: Decay of Ramsey envelope as a function of the waiting time between the two Ramsey pulses. The blue dotted line is a fit of the data with the relation $P_\uparrow = a\exp[-(t/T_2^*)^2]+c$, with T_2^* as a free parameter and c = 0.46, the average value for $\tau \gg T_2^*$ (see Fig. 6.4), which we also obtain keeping c a free parameter (c =0.46±0.09; T_2^* = 790±330 ns). The fact that the center of the $P_\uparrow$ oscillations is not 0.5 is attributed to initialization and measurement errors.

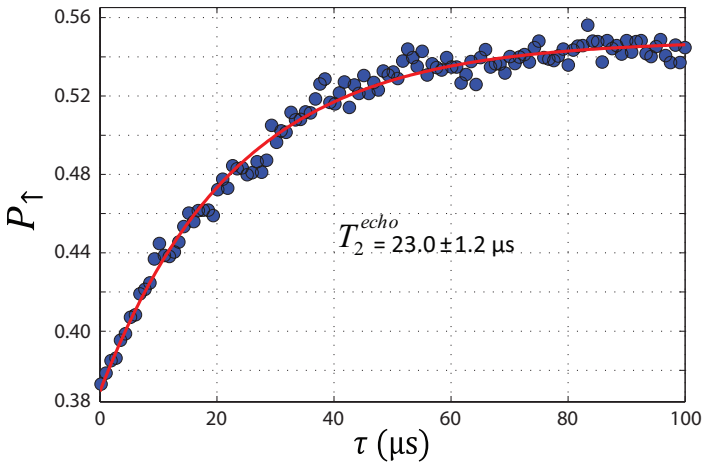

Figure 6.9: Spin echo measurement for the ground valley-orbit state driven at the fundamental harmonic for B_{ext}= 560.783 mT and $f_{MW} = f_0^{(1)} = 2f_0^{(3)}$. The observed T_2^{echo} times are similar for driving at the fundamental and second harmonic.

electric field) has components in all three directions of space. More specifically, from [29] (Chapter 5) we have $dB_{//}/dx \approx 0.2$ mT/nm and $dB_{\perp}/dx \approx 0.3$ mT/nm, from which we can estimate that $\vartheta \sim 56$ degrees. Furthermore, from [29] we also get $\omega_1 \approx 3$ MHz and $\omega \approx 13$ GHz from which $\omega_{eff}^{(2ph)}/\omega^{(1ph)} = 2\omega_1/\omega << 10^{-3}$, too small to explain the measured $f_1^{(3)}/f_1^{(1)} \sim 0.5$ for the highest microwave driving field used in the experiment [see Fig. 6.2(b)].

Anharmonic confining potential.

Another possible mechanism which can give rice to the two-photon process in the Si/SiGe micromagnet-EDSR experiments can be related to the presence of an intermediate level (valley excited state spin down) lying between the initial and final states (valley ground spin down and up) which can mediate the resonance process [private communication A. Pályi and M. Rudner]. If this is the case, by measuring the B-field dependence of the two-photon Rabi frequency, one should observe a non-monotonic $f_{Rabi}^{2ph}(B_{ext})$ dependence: the Rabi frequency should grow as half of the Larmor frequency approaches the valley splitting either from above or from below. Even if we did not perform a systematic study of the f_{Rabi}^{2ph} vs B_{ext}, from the measurement we recorded we can exclude this striking dependence.

In the absence of detailed knowledge of the shape of the confining potential, it is difficult to quantitatively estimate the magnitude of this effect. However, what we can say is that the details of the confining potential strongly influence the efficiency of second harmonic driving: after tuning the device into a new gate voltage configuration (for which the valley splitting is higher than it is here), it has not been possible to observe again clear signatures of second harmonic driving. The new settings will likely also shift the average dot position in the micro magnet stray field, thereby altering the tilt of the effective driving field as well as the position dependent field gradient. However, as discussed in the preceding sections, these two effects are several orders of magnitude too small to explain the observed second harmonic driving. If the degree of anharmonicity of the confining potential dominates second harmonic driving, control of the anharmonicity will be required to make routine use of second harmonic driving in future spin qubit experiments.

REFERENCES

[1] D. Loss and D. P. DiVincenzo, Phys. Rev. A **57**, 120 (1998).

[2] R. Hanson, L. P. Kouwenhoven, J. R. Petta, S. Tarucha, and L. M. K. Vandersypen, Rev. Mod. Phys. **79**, 1217 (2007).

[3] P. Franken, A. Hill, C. Peters, and G. Weinreich, Phys. Rev. Lett. **7**, 118 (1961).

[4] T. F. Heinz, C. K. Chen, D. Ricard, and Y. R. Shen, Phys. Rev. Lett. **48**, 478 (1982).

[5] Y. R. Shen, Nature **337**, 519 (1989).

[6] W. Denk, J. H. Strickler, and W. W. Webb, Science **248**, 73 (1990).

[7] C. Xu, W. Zipfel, J. B. Shear, R. M. Williams, W. W. Webb, Proceedings of the National Academy of Sciences **93**, 10763 (1996).

[8] K. Konig, Journal of Microscopy **200**, 83 (2000).

[9] S. Stufler, P. Machnikowski, P. Ester, M. Bichler, V. M. Axt, T. Kuhn, and A. Zrenner, Phys. Rev. B **73**, 125304 (2006).

[10] Y. Nakamura, Y. A. Pashkin, and J. S. Tsai, Phys. Rev. Lett. **87**, 246601 (2001).

[11] A. Wallraff, T. Duty, A. Lukashenko, and A. V. Ustinov, Phys. Rev. Lett. **90**, 037003 (2003).

[12] W. D. Oliver, Y. Yu, J. C. Lee, K. K. Berggren, L. S. Levitov, and T. P. Orlando, Science **310**, 1653 (2005).

[13] S. N. Shevchenko, A. N. Omelyanchouk, and E. Ilichev, Low Temperature Physics **38**, 283 (2012).

[14] S. Poletto, J. M. Gambetta, S. T. Merkel, J. A. Smolin, J. M. Chow, A. D. Córcoles, G. A. Keefe, M. B. Rothwell, J. R. Rozen, D. W. Abraham, et al., Phys. Rev. Lett. **109**, 240505 (2012).

[15] A. De, C. E. Pryor, and M. E. Flatté, Phys. Rev. Lett. **102**, 017603 (2009).

[16] J. Pingenot, C. E. Pryor, and M. E. Flatté, Phys. Rev. B **84**, 195403 (2012).

[17] E. I. Rashba, Phys. Rev. B **84**, 241305 (2011).

[18] M. P. Nowak, B. Szafran, and F. M. Peeters, Phys. Rev. B **86**, 125428 (2012).

[19] E. N. Osika, A. Mrenca, and B. Szafran, Phys. Rev. B **90**, 125302 (2014).

[20] J. Danon and M. S. Rudner, Phys. Rev. Lett. **113**, 247002 (2014).

[21] J. Romhányi, G. Burkard, and A. Pályi, Phys. Rev. B **92**, 054422 (2015).

[22] G. Széchenyi and A. Pályi, Phys. Rev. B **89**, 115409 (2014).

[23] E. A. Laird, C. Barthel, E. I. Rashba, C. M. Marcus, M. P. Hanson, and A. C. Gossard, Semicond. Sci. Technol. **24**, 064004 (2009).

[24] F. Pei, E. A. Laird, G. A.Steele, L. P. Kouwenhoven, Nature Nanotech. **7**, 630 (2012).

[25] E. A. Laird, F. Pei, and L. P. Kouwenhoven, Nature Nanotech. **8**, 565 (2013).

[26] J. Stehlik, M. D. Schroer, M. Z. Maialle, M. H. Degani, and J. R. Petta, Phys. Rev. Lett. **112**, 227601 (2014).

[27] S. Nadj-Perge, V. S. Pribiag, J. W. G. van den Berg, K. Zuo, S. R. Plissard, E. P. A. M. Bakkers, S. M. Frolov, and L. P. Kouwenhoven, Phys. Rev. Lett. **108**, 166801 (2012).

[28] F. Forster, M. Mühlbacher, D. Schuh, W. Wegscheider, and S. Ludwig (2015), arXiv:cond-mat/1503.01938.

[29] E. Kawakami, P. Scarlino, D. R. Ward, F. R. Braakman, D. E. Savage, M. G. Lagally, Mark Friesen, S. N. Coppersmith, M. A. Eriksson, and L. M. K. Vandersypen, Nature Nanotech. **9**, 666 (2014).

[30] T. Obata, M. Pioro-Ladrière, Y. Tokura, Y. S. Shin, T. Kubo, K. Yoshida, T. Taniyama, and S. Tarucha, Phys. Rev. B **81**, 085317 (2010).

[31] J. M. Elzerman, R. Hanson, L. H. Willems Van Beveren, B. Witkamp, L. M. K. Vandersypen, and L. P. Kouwenhoven, Nature (London) **430**, 431 (2004).

[32] J. K. Gamble, M. A. Eriksson, S. N. Coppersmith, and Mark Friesen, Phys. Rev. B **88**, 035310 (2013).

[33] R. Boscaino, I. Ciccarello, C. Cusumano, and M. Strandberg, Phys. Rev. B **3**, 2675 (1971).

[34] I. Gromov and A. Schweiger, Journal of Magnetic Resonance **146**, 110 (2000).

[35] R. Rahman, G. P. Lansbergen, S. H. Park, J. Verduijn, G. Klimeck, S. Rogge, and L. C. L. Hollenberg, Phys. Rev. B **80**, 165314 (2009).

[36] T. H. Oosterkamp, L. P. Kouwenhoven, A. E. A. Koolen, N. C. van der Vaart, and C. J. P. M. Harmans, Phys. Scr. **T69**, 98 (1997).

[37] E. Kawakami, P. Scarlino, L. R. Schreiber, J. R. Prance, D. E. Savage, M. G. Lagally, M. A. Eriksson, and L. M. K. Vandersypen, Appl. Phys. Lett. **103**, 132410 (2013).

[38] F. W. Strauch, S. K. Dutta, H. Paik, T. A. Palomaki, K. Mitra, B. K. Cooper, R. M. Lewis, J. R. Anderson, A. J. Dragt, C. J. Lobb, et al., IEEE Transactions on Applied Superconductivity **17**, 105 (2007).

[39] E. Hahn, Phys. Rev. **80**, 580 (1950).

7

ADIABATIC AND NONADIABATIC NONLINEAR DRIVING OF A TWO-LEVEL SYSTEM

The symmetry of the crystalline structure in silicon forces us to consider effects coming from the valley degree of freedom in the quantum technology context [1]. The introduction of this further degree of freedom doubles the original Hilbert space (spin 1/2) and can introduce unwanted complications in the realization of single and two qubits gates [2]. In Si/SiGe QW, due to the omnipresence of interface disorder, the valleys strongly hybridize with the orbitals [3, 4]. This usually reduces the ground state valley energy splitting [3, 5]. As we will show in this Chapter for a single electron confined in a Si/SiGe single quantum dot, the coupling between the two valley-orbit states makes the system non trivial and highly non-linear. This allows the observation of different kinds of resonances, in addition to the usual fundamental harmonic intra-valley spin resonance [2, 6]. The response generates subharmonics in EDSR, which occur even in the weak driving regime and can also give rise to an inter-valley Landau-Zener process [7, 8]. We foresee our results to benefit the field spin and valley control for quantum technology in silicon systems.

The work in this Chapter is in preparation for submission for publication. The results are due to P. Scarlino, E. Kawakami, D. R. Ward, D. E. Savage, M. G. Lagally, Mark Friesen, S. N. Coppersmith, M. A. Eriksson, and L. M. K. Vandersypen.

7.1. INTRODUCTION

A spin-1/2 particle is the canonical two-level quantum system. Its energy level structure is extremely simple, consisting of just the spin-up and spin-down levels. Therefore, when performing spectroscopy on an electron spin, an elementary spin-1/2 particle, only a single resonance is expected corresponding to the energy separation between the two levels.

Recent measurements have shown that the spectroscopic response of a single electron spin in a quantum dot can be much more complex than this simple picture suggests. This is particularly true when using electric-dipole spin resonance, where an oscillating electric field couples to the spin via spin-orbit coupling. First, due to non-linearities in the response to oscillating driving fields, subharmonics can be observed, and the nonlinear response can even be exploited for driving coherent spin rotations. Second, due to spin-orbit coupling, the exact electron spin resonance frequency in given magnetic field depends on the orbital the electron occupies. In silicon or germanium quantum dots, the conduction band valley is an additional degree of freedom, and the electron spin resonance frequency should depend on the valley state as well. As a result, when valley or orbital energy splittings are comparable to or smaller than the thermal energy, thermal occupation of the respective levels leads to the observation of multiple closely spaced spin resonance frequencies (see Chapter 5).
The picture becomes even richer when considering transitions when not only the spin state but also the orbital or valley quantum number changes. Such phenomena abundantly take place in optically active dots, but have been observed also in electrostatically defined (double) quantum dots in the form of spin-flip photon-assisted tunneling [9]. However, transitions involving the valley state have so far remained unexplored.

Here we study a quantum dot with a valley splitting of the same order as the electron thermal energy. As we have shown in [2], this implies that both valley states participate in the spin resonance process, doubling the usual spin resonance spectrum. Furthermore, in [6] it has been demonstrated the possibility to excite and coherently drive both intra-valley spin resonances also by second harmonic driving. Here, we report transitions whereby both the spin and valley-orbit state are flipped in a Si/SiGe quantum dot and demonstrate that we can sensitively Stark shift the transition. We show that a theory incorporating a driven four-level system comprising of two valley-orbit and two spin states subject to strong ac driving provides a consistent description of these transitions, including the observation of a dynamic level repulsion, as well as all the previously reported transitions for this system.

7.2. DEVICE AND MEASUREMENT TECHNIQUE

The device used for this experiment has been extensively described in [2] (see Fig. 7.6). It is based on an undoped Si/SiGe heterostructure with two layers of electrostatic gates. Two accumulation gates are used to induce a two-dimensional electron gas (2DEG) in a 12 nm wide Si quantum well 37 nm below the surface and a set of depletion gates is used to form a single quantum dot in the 2DEG, and a charge sensor next to this dot. The dot is tuned so it is occupied by just one electron. Two micromagnets placed on top of the accumulation gates produce a local magnetic field gradient. The sample is

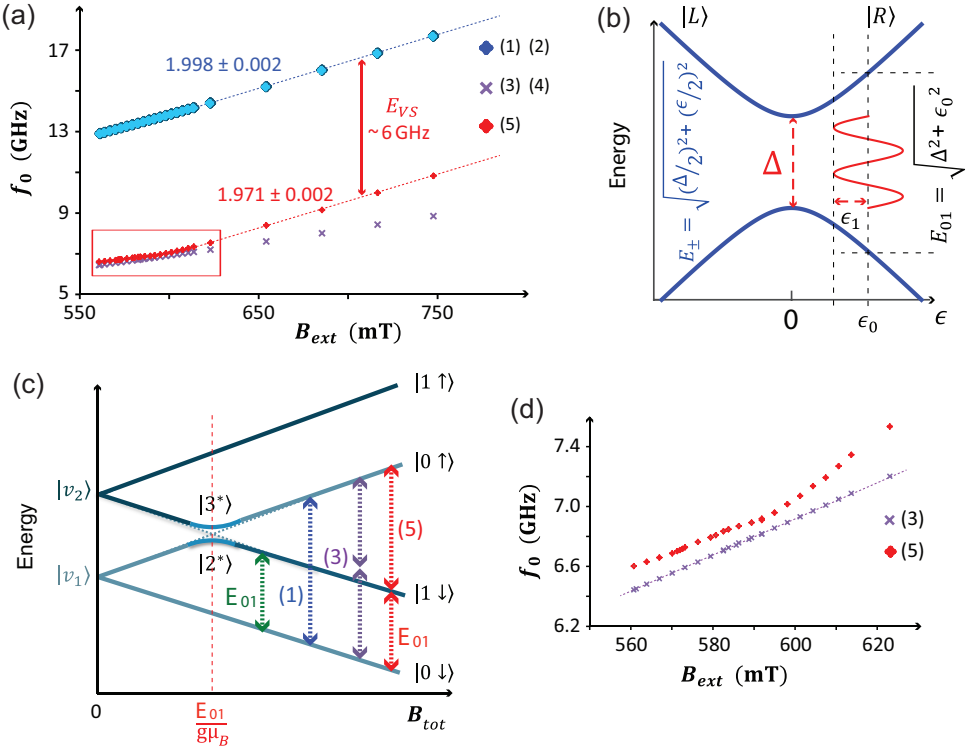

Figure 7.1: (a) Measurements of the electron spin resonances for a single electron confined in a single QD defined in Si/SiGe QW; the g-factor of the resonance (5) is 1% different from the g-factor of the fundamental harmonic resonance (1). Reducing the magnitude of B_{ext} and following the frequency evolution of the resonance (5), we notice that around 600 mT it starts to deviate from a straight line (for this measurement we keep the microwave power as low as possible). A magnification of the region inside the red rectangle is reported in panel (d). We notice that the frequency difference between the spin resonance (5) and the second harmonic (3) reaches a minimum at $B_{ext} \sim 590$ mT and then it increases again. (b) Schematic representing the energy of the simple two-level system of the model (eq. 7.1) as a function of the detuning ϵ and with an harmonic driving around ϵ_0. (c) The four energy levels considered in this work, comprised of two valley-orbit and two spin states. Vertical arrows indicate the four types of spin-flip processes observed in our simulations. From left to right: (i) an orbital state excitation, (ii) the fundamental (one-photon) ESR resonance, (iii) its first harmonic, and (iv) an orbital-state excitation followed by a spin flip. We note that process (i) is not observed in the experiments, and process (iv) is responsible for the resonance (5). Here, E_{01} is the energy for a valley-orbital-state excitation.

attached to the mixing chamber of a dilution refrigerator with base temperature ~25 mK and an electron temperature estimated from transport measurements of ~150 mK. For the present gate voltage configuration, the valley splitting, E_{01}, is comparable to the thermal energy, $k_B T_{el}$.

Microwave excitation applied to one of the gates oscillates the electron wave function back and forth in the dot (see Fig. 7.6). Because of the local magnetic field gradient ~0.3 mT/nm (see Fig. 7.6), the electron is then subject to an oscillating magnetic field [11, 12] and electron spin transitions can be induced when the excitation is resonant with the spin splitting. The spin-up probability $P_\uparrow$ in response to the microwave

excitation is measured by repeated single-shot cycles (see section 7.6.1 for details). We cannot reduce B_{ext} further than what is reported in Fig. 7.1(a) because the energy selective spin initialization and readout procedures are effective only when $E_z > k_B T_{el}$, where $E_Z = g_B \mu_B B_{tot}$ is the Zeeman splitting (with g_B is the Landé g-factor in silicon, μ_B is the Bohr magneton, and B_{tot} is the total magnetic field acting on the electron).

When varying the applied microwave frequency, we observe five distinct resonance peaks (Fig. 7.1(a)). The two resonances labeled (1) and (2), not resolved on this scale, are two intra-valley spin resonances, one for each of the two lowest-lying valley states that are thermally occupied [2]. They exhibit a $T_2^* \sim 1$ μs and Rabi frequencies of order MHz. The two resonances labeled (3) and (4), similarly not resolved between them, arise from second harmonic driving of the two intra-valley spin flip transitions. These transitions too can be driven coherently, with Rabi frequencies comparable to those for the fundamental harmonic [6].

The resonance labeled (5) has not been discussed before. Its frequency is ~6 GHz lower than the fundamental intra-valley spin resonance frequency (1,2), and from its magnetic field dependence measured above 650 mT, we extract a g-factor of about 1.97 ± 0.03. This is close to but different (~ 1%) from the g-factors for resonances (1) and (2). Its line width is extracted from Fig. 7.7 to be ~ 6 MHz ($T_2^* \sim 100$ ns, reported in inset of Fig. 7.3(a)), almost ten times wider than the intra-valley resonances. Around 600 mT, the slope of resonance (5) changes, in a way typical of level repulsions (see Fig. 7.1(d)). Without the change in slope, resonance (5) would have crossed resonances (3,4), however the latter do not show any sign of level repulsion and continue their linear dependence on magnetic field.

We interpret this puzzling observation starting from Fig. 7.1(c). Two sets of Zeeman split levels are seen, separated by the energy of the first excited valley-orbit state E_{01}. The blue and purple double arrows show driving of spin transitions via the fundamental and second harmonic respectively. The red double arrows indicate a transition whereby both spin and valley(-orbit) are flipped. We identify resonance (5) with this transition. It has the same field dependence as resonance (1), but (above 600 mT) it is offset by a fixed amount of about 6 GHz. From Fig. 7.1(c), we see that this offset is a measure of the valley-orbit splitting, E_{01}. As we will discuss further below, the partly valley-nature of transition (5) makes it more sensitive to electric fields [10, 13, 14], as compared to the pure spin transitions (1-4). This may also contribute the almost ten times larger line width of resonance (5).

In order to understand the origin of the apparent level repulsion, we introduce a simple model Hamiltonian that captures the essential physics, and reproduces all the observed transitions (and more).

7.3. MODELING THE QUANTUM DOT

Here we want to derive a model that will explain the presence of both the first and second harmonic driven spin resonance and that also predicts the observed inter-valley spin resonance[1]. We show that resonances such as those reported in Fig. 7.1 are generic

[1] This model has been developed by M. Friesen and S. N. Coppersmith (University of Wisconsin)

features of a strongly driven four-level system composed of two orbital levels and two spin levels in which there is a nonlinear coupling between the orbital levels, such as a tunnel coupling.

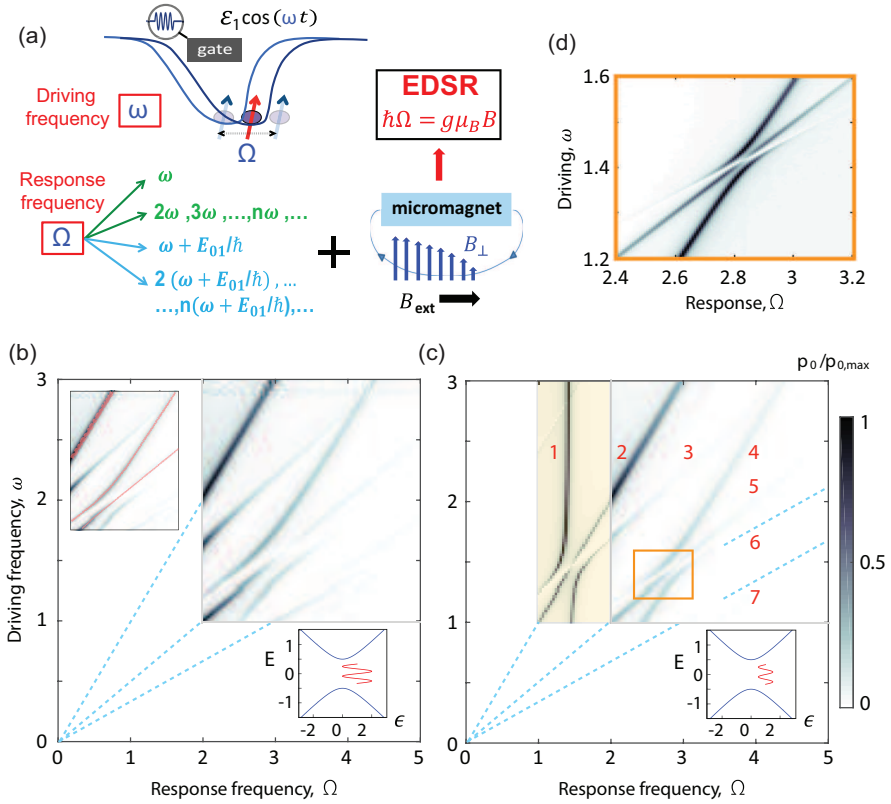

Figure 7.2: Resonances in an ac-driven qubit induced by adiabatic and non-adiabatic processes. (a) Schematic representing the idea behind the model. In green (light blue) are reported the adiabatic (non-adiabatic) response frequencies of the electron dipole moment $p_0(\Omega) = FFT[p_0(t)]$. (b-d) Simulations of the a.c.-driven qubit model according to Eqs. (7.1) and (7.4), setting $\hbar = 1$. The dynamics of the dipole moment p_0, defined in Eq. (7.5), are solved in the time domain for the driving frequency ω, then Fourier transformed to obtain the response frequency Ω. (b) Resonance spectrum corresponding to the parameters $\epsilon_0 = \epsilon_1 = \Delta = 1$. The lower inset shows the relation between the energy levels and the driving term. The upper inset shows the same results as the main panel, with the experimentally relevant resonances highlighted. (Compare to Fig. 7.1.) (c) Resonance spectrum corresponding to the parameters $\epsilon_0 = \Delta = 1$ and $\epsilon_1 = 0.5$. Here, the shaded region was normalized separately from the rest of the figure. The resonance features labeled 1-7 are discussed in the main text. (d) A blowup of the region shown in the center box of panel (c), using the parameters $\Delta = \epsilon_0 = 1$ and $\epsilon_1 = 0.11$, which give a good match to the level repulsion observed in the EDSR experiments in Figs. 7.1(a) and 7.1(d).

As summarized in the schematic of Fig. 7.2(a), when a spin qubit is driven at a frequency ω, it responds at one or more frequencies Ω, which may be the same as ω, but may also be different. Spin resonance is observed if (i) the spin is flipped, and (ii) $\hbar\Omega = E_Z$. The spin flip requires a physical mechanism, such as spin-orbit coupling in EDSR [11]. Indeed, this is the mechanism responsible for spin flips in our experiment,

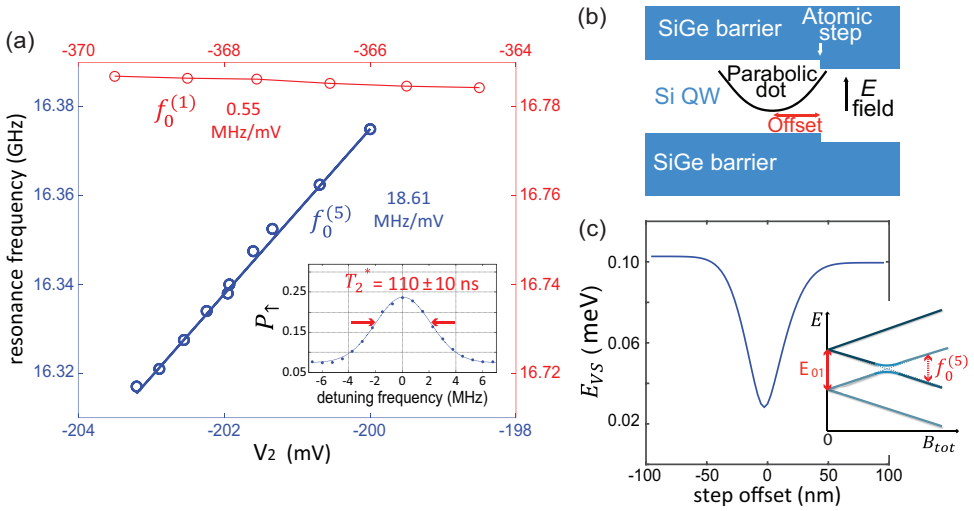

Figure 7.3: (a) The figure reports the tunability of the Larmor frequency for both the inter-valley ($f_0^{(5)}$ at B_{ext} =792 mT, blue data and axes) and intra-valley ($f_0^{(1)}$ at B_{ext} =550 mT, red data and axes) spin resonances, as a function of V_2 (the voltage applied on the gate 2). The figure clearly shows that we can systematically shift the $f_0^{(5)}$ ($f_0^{(1)}$) resonance frequency towards higher (lower) frequency by making the voltage on the gate 2 less negative. The frequency shifting rate ($\Delta f/\Delta V_2$) of the inter-valley spin resonance is ~35 times more pronounced compared to the intra-valley spin resonance, suggesting a clear different physical origin. Inset: CW measurement of the inter-valley spin resonance with the estimated T_2^* ~ 100 ns. (b) Schematic representation of the atomic step disorder and of the QD parabolic confinement potential. (c) 2D tight binding calculation of the valley-orbit energy splitting using the geometry shown in panel (b), using the parameters extracted for our device in [2]. We included a single-atom step at the quantum well interface, displaced from the dot by a variable distance, laterally (step offset) [14]. In the plots, this quantity is positive when the step is on the right-hand side of the dot.

which takes place in the strong magnetic field gradient of the micromagnet [2]. Rashba has suggested that the mapping $\omega \to \Omega$ occurs entirely within the orbital sector, and that EDSR simply provides a tool for observing this mapping [15]. In this paper, we adopt Rashba's orbital-based model as our starting point. Whenever possible, we will simply ignore the spin physics in favor of the orbital physics.

Several theoretical explanations have been put forth to explain strong-driving phenomena in EDSR, such as the generation of higher harmonics [15, 18, 20], and an even-odd harmonic structure [19, 21]. For silicon dots, the exact orbital Hamiltonian is difficult to write down from first principles, since it involves both orbital and valley components [2], and depends on the atomistic details of the quantum well interface [3–5]. However, a minimal model for investigating the physics of the orbital sector is given by the two-level system

$$H = \frac{1}{2}(\epsilon\sigma_z + \Delta\sigma_x), \tag{7.1}$$

where σ_x and σ_z are Pauli matrices. The basis states in this model may correspond to excited orbitals in a single quantum dot [11], valley states in a single dot [3], localized orbital states in a double dot [15], or a hybridized combination of these systems [4]. In

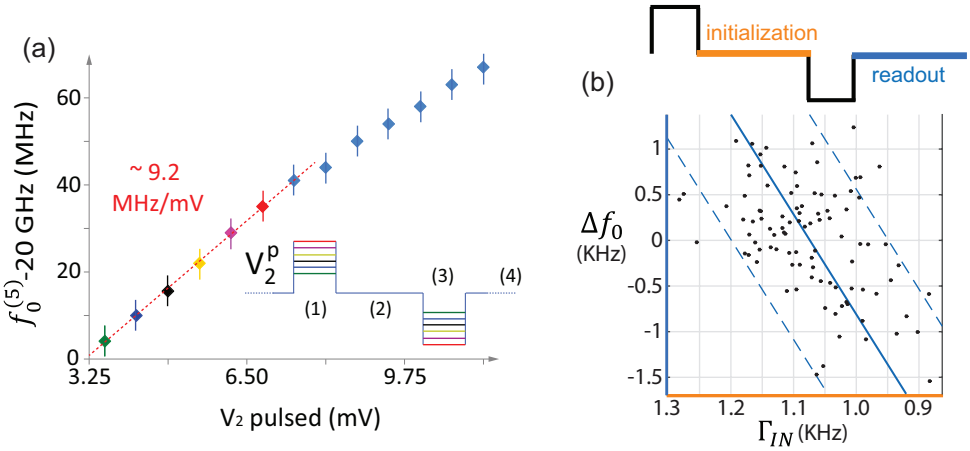

Figure 7.4: (a) It is possible to systematically shift the resonance frequency also by changing the voltage amplitude during the manipulation stage (the color code of the 6 voltage pulse levels is in correspondence of the first 6 resonances reported in Fig. 7.8(c)). Notice that we keep the pulse shape symmetric, compensating by using the same voltage pulse amplitude, but with opposite sign, during the initialization stage. Pulsing deeper in the Coulomb Blockade configuration (see red point respect to green) $f_0^{(5)}$ increases. (b) Measurement of the correlation between the fluctuations of the tunnel-IN rate, $\Delta\Gamma_{IN}$, (due to electric-charge noise in the electrostatic environment) and the Larmor frequency fluctuations, Δf_0, for the inter-valley spin resonance. We make use of the initialization and the readout stage of the pulse scheme (reported in the inset) in order to get respectively information about the electric noise (Fig. 7.9(b) in orange) and Larmor frequency fluctuation (Fig. 7.9(b) in blue). The x and y axes colors are in correspondence of the colors attributed at the initialization and readout stages respectively (see also square frames in Fig. 7.9(b-d)). From the distribution of the $(\Gamma_{IN}, \Delta f_0)$ points in the main panel we can deduce a clear correlation between the fluctuations due to electric-charge noise and of the Larmor frequency of the inter-valley spin resonance. The dashed lines represent the 95% confidence interval.

each case, the two basis states have distinct charge distributions that can support EDSR through the mechanism described by Tokura et al. [11]

Equation (7.1) is, in fact, the most general theoretical model of a two-level system. Mapping the theoretical model onto a real, experimental system requires specifying the dependence of the effective detuning parameter ϵ and the effective tunnel coupling Δ on the voltages applied to the top gates for a given device.

To take a simple example that is relevant for silicon quantum dots, we consider such a mapping for the basis comprised of valley states. In this case, ϵ represents a valley splitting, which can be tuned with a vertical electric field, while Δ represents a valley coupling, which can depend on the interfacial roughness of the quantum well and other materials parameters [14]. The centers of mass of the charge distributions of the basis states in this example differ by about a lattice spacing in the vertical direction. It is likely that the silicon dot in our experiment experiences an additional valley-orbit coupling, which induces a lateral variation of the charge distributions. In this case, the gate voltage dependence of ϵ and Δ is very complicated; however Eq. (7.1) should still provide a useful theoretical description.

For convenience in the following analysis, we adopt the picture of a charge qubit, for which the basis states correspond to “left" ($|L\rangle$) and “right" ($|R\rangle$). The eigenstates of H

are then given by

$$|0\rangle = \frac{\Delta}{\sqrt{\Delta^2+(\epsilon+E_{01})^2}}|L\rangle - \frac{\epsilon+E_{01}}{\sqrt{\Delta^2+(\epsilon+E_{01})^2}}|R\rangle, \tag{7.2}$$

$$|1\rangle = \frac{\Delta}{\sqrt{\Delta^2+(\epsilon-E_{01})^2}}|L\rangle - \frac{\epsilon-E_{01}}{\sqrt{\Delta^2+(\epsilon-E_{01})^2}}|R\rangle, \tag{7.3}$$

and the energy splitting is given by $E_{01} = \sqrt{\Delta^2+\epsilon^2}$.

To begin with, we consider a classical a.c. driving field, applied to the detuning parameter:

$$\epsilon(t) = \epsilon_0 + \epsilon_1 \sin(\omega t). \tag{7.4}$$

Our goal is to determine the response of the two-level system to this $\epsilon(t)$. In contrast with Rashba, we will not limit our analysis to the driving regime, $\epsilon_1, E_{01} \ll \hbar\omega$. To proceed, we note that the basis states couple differently to the applied electric field because they have different spatial charge distributions. We specifically consider the time evolution of the dipole moment of the ground state $|0\rangle$, defined as

$$p_0 = \frac{eL}{2}\langle 0|\sigma_z|0\rangle = \frac{eL}{2}\left[|\langle 0|L\rangle|^2 - |\langle 0|R\rangle|^2\right], \tag{7.5}$$

where L is the distance between the center of mass of the charge in states $|L\rangle$ and $|R\rangle$[2].

Two fundamentally different types of response to the driving are observed in $p_0(t)$: adiabatic vs. nonadiabatic.

7.3.1. ADIABATIC EFFECTS

We first consider adiabatic processes, which are determined by the adiabatic eigenstates of the Hamiltonian, given in Eqs. (7.2) and (7.3). The corresponding dipole moment, computed from Eq. (7.5), is

$$p_0 = \frac{eL}{2}\left[\frac{\Delta^2-(\epsilon+E_{01})^2}{\Delta^2+(\epsilon+E_{01})^2}\right] = -\frac{eL\epsilon}{2E_{01}}. \tag{7.6}$$

Substituting Eq. (7.4) into Eq. (7.6), we see that the adiabatic response of $p_0(t)$ is a nonlinear function of $\sin(\omega t)$. For example, in the weak driving limit, we can expand Eq. (7.6) to second order in the small parameter ϵ_1/E_{01}, giving

$$\begin{aligned} p_0(t) \quad &\simeq \quad (\text{const.}) - \left(\frac{eL\Delta^2}{2\bar{E}_{01}^3}\right)\epsilon_1 \sin(\omega t) \\ &\quad - \left(\frac{3eL\Delta^2\epsilon_0}{8\bar{E}_{01}^5}\right)\epsilon_1^2 \cos(2\omega t) + \ldots. \end{aligned} \tag{7.7}$$

[2] For a charge qubit, L is the lateral separation between the two sides of the double quantum dot. For an orbital qubit, L is the lateral separation of the center of mass of the two orbital states. For a pure valley qubit, L is the vertical separation of the even and odd states (~0.16 nm). For a complicated system like a valley-orbit qubit with interface disorder, L will have lateral and vertical components, with the lateral component being usually much larger than the vertical one. In this last case the exact length L will depend on the specifics of the interface disorder; a reasonable guess would be L ~0.5-5 nm.

Here, $\tilde{E}_{01}$ denotes the energy splitting when $\epsilon = \epsilon_0$. We see that the nonlinear dependence of the dipole moment on ϵ_1 translates into a series of response terms at frequencies $\Omega = \omega, 2\omega, 3\omega, \ldots$. Since spin resonances only occur when $\hbar\Omega = E_Z$, these should be observed as subharmonics of the fundamental Zeeman frequency: $\omega = E_Z/\hbar, E_Z/2\hbar, E_Z/3\hbar, \ldots$. For the two-level system defined by Eq. (7.1), we note that all resonances depend on the presence of a coupling between the basis states, Δ. In Fig. 7.1(c), the fundamental resonance condition and its first harmonic are sketched as the second and third sets of vertical arrows. We note that adiabatic resonances can be observed in both the strong and weak driving regimes, although the higher harmonics may be suppressed for weak driving, as consistent with Eq. (7.7).

7.3.2. NONADIABATIC EFFECTS

We next consider nonadiabatic, or Landau-Zener (LZ) processes [7, 8], which always involve an excitation (or deexcitation) of an orbital state. For the two-state Hamiltonian of Eq. (7.1), LZ excitations can arise in two ways: (i) a sudden pulse of a control parameter (e.g., ϵ), or (ii) strong periodic driving of the control parameter [e.g., Eq. (7.4)]. In the first case, the qubit is suddenly projected onto a new adiabatic eigenbasis, which induces a Larmor response at the frequency $\Omega = \pm E_{01}/\hbar$. In the second case, fast periodic excursions of $\epsilon(t)$ at driving frequencies different than $E_{01}/\hbar$ can achieve a similar response. Such "conventional" LZ excitation processes are indicated by the first vertical arrow in Fig. 7.1(c)[3].

In our experiment, simple LZ orbital excitations are undetectable, because the excitation energy E_{01} is smaller than the Fermi level broadening. However, the EDSR spin-flip mechanism allows us to generate and detect more complex processes at higher energies. The resonance condition indicated by the fourth set of vertical arrows in Fig. 7.1(c) is particularly important for our experiment; when combined with a spin flip, it describes one portion of the resonance (5) detailed in Figs. 7.1(a) and 7.1(d). Resonances of this type occur when $\hbar\Omega = m\hbar\omega \pm E_{01}$, corresponding to the driving frequencies $\omega = (E_Z \pm E_{01})/\hbar, (E_Z \pm E_{01})/2\hbar, (E_Z \pm E_{01})/3\hbar, \ldots$ [4].

7.3.3. SIMULATION RESULTS

We first perform numerical simulations of Eq. (7.1), which do not require any theoretical interpretation. The results are shown in Figs. 7.2(b-d). Setting $\hbar = 1$, the dynamical simulations proceed by solving the Schrödinger equation $i\partial|\psi\rangle/\partial t = H|\psi\rangle$ for Eqs. (7.1) and (7.4) and computing $p_0(t)$ as defined in Eq. (7.5) for a fixed driving frequency ω. The Hamiltonian parameters used in the simulations are indicated in the caption (we employ time steps in the range 0.061-0.073). The resulting $p_0(t)$ is Fourier transformed, yielding a $p_0(\Omega)$ whose peaks reflect the resonant response. Finally, we smooth $p_0(\Omega)$ by convolving it with a Gaussian of width 0.025. As described in previous sections, spin physics is not explicitly included in the simulations. To make contact with the EDSR

[3] In typical resonant driving experiments, the LZ process is actually more general than what is shown in the figure, because it can occur at any B-field. The process indicated in the figure implies an orbital excitation combined with a spin flip, which we discuss below.

[4] Since these resonance lines are parallel to the conventional spin resonances, Rashba has called them "satellites" [15].

experiments, we therefore assume that the magnetic field gradient in the experimental device transforms the electrical response at frequency Ω into an a.c. magnetic field at the same frequency. Spin flips then occur via the EDSR mechanism at an appropriate Zeeman resonance, given by $E_Z/\hbar = \Omega$ (Fig. 7.2(a)).

Figure 7.2 shows the results of our simulations for $p_0(\Omega)$ as a function of both driving frequency ω and response frequency Ω over a range of parameters analogous to those in Fig. 7.1(a). Figures 7.2(b)-7.2(d) correspond to three different driving amplitudes, with panel (c) chosen to match the experimental results in Fig. 7.1(a). The dashed blue lines correspond to the conventional ESR signals (the fundamental resonance, and the first two harmonics, top to bottom), which are all visible in the simulations. In Fig. 7.2(c), these are labeled 2, 5, and 7. The inset on the left-hand side of Fig. 7.2(b) highlights the particular resonances that should be compared to the experimental data in Fig. 7.1(a).

In addition to conventional ESR resonances, several LZ resonances can be seen in the simulations. Two LZ resonances, labeled 3 and 4 in Fig. 7.2(b), are observed between the fundamental resonance and the first harmonic. At high frequencies, we note that resonance 3 has the same slope as the first harmonic 5, while resonance 4 has the same slope as the fundamental 2. More explicitly, these lines correspond to the resonance conditions given by $\omega = (E_Z + E_{01})/2\hbar$ and $\omega = (E_Z - E_{01})/\hbar$, respectively. The latter resonance is clearly visible in Fig. 7.1, and corresponds to the resonance (5) at high frequencies.

An interesting feature of the LZ resonances, which is also observed in the experiments, is the apparent level repulsion between the resonance peaks. Several of these anticrossings are seen in Fig. 7.2. The effect is purely dynamical, as demonstrated by the fact that the anticrossing is suppressed in going from panels (b) to (d), as consistent with the smaller driving amplitudes.

Several excitations are observed in the simulations of Fig. 7.2 that are not also observed in the experiments. For example, the vertical line labeled 1 in Fig. 7.2(c) corresponds to the nonresonant (Larmor) LZ excitation discussed in Sec. 7.3.2. This excitation occurs at an energy $\hbar\Omega$ that is too small to be detected experimentally. Resonance 3 is suppressed in the simulations, compared to resonance 4, and it is not observed at all in the experiments. A level anticrossing is observed between resonances 1 and 3 in the simulations, which also occurs outside the experimental measurement window. Resonance 6 (highlighted with a dashed line) is somewhat faint in Fig. 7.2(c), but more prominent in Fig. 7.2(b). The slope of this resonance is the same as the 2nd conventional harmonic (7), with a frequency given by $\omega = (E_Z + E_{01})/3\hbar$. The anticrossing comprising the resonance (5) occurs between the two LZ resonance peaks labeled 4 and 6 in Fig. 7.2(c). Several other features can be observed in the lower-right corner of Fig. 7.2(a), which are very faint, and can also be classified according to the resonance scheme discussed above.

Hints of the origin of the level repulsion are found by expanding $E_{01}(t)$ for the two-state Hamiltonian in the limit of weak driving, $\epsilon_1 \ll \Delta$. Taking the time average of this quantity, we obtain

$$\langle E_{01} \rangle \simeq \bar{E}_{01} + \frac{\Delta^2}{4\bar{E}_{01}^3}\epsilon_1^2. \tag{7.8}$$

This is the leading order a.c. correction to the Larmor frequency $f_0^{(5)}$ for the two-level system defined by Eq. (7.1), with the classical driving field given in Eq. (7.4). Since $\langle E_{01} \rangle$ determines the LZ resonance frequency ($(\omega = E_z \pm E_{01})/h$), Eq. (7.8) shows that ϵ_1 can

indeed affect the position of the LZ resonance. In the strong driving regime, level repulsion has a very strong effect on the position of the resonance, as observed in experimental Fig. 7.1, Figs. 7.5(a-b) and 7.10(c). Because we do not know the magnitudes of the couplings and non-linearities in the experiment, precise prediction of the shape of the curve in the experimental Fig. 7.10(c) is not predictable. Nonetheless, the qualitative agreement of the simple model with experimental Fig. 7.1(a), reported in the inset of Fig. 7.2(b), is striking. In Fig. 7.11(b) we report a simulation realized to follow the evolution of the response frequency of the system, for a fixed value of the response frequency, as a function of the driving amplitude. From it we can clearly notice that the LZ resonances shifts to higher frequencies for stronger driving strengths and that the harmonic resonance seems to fade when it crosses the LZ resonance.

There are two main theoretical approaches for describing such nonadiabatic phenomena. In either description, the orbital excitation is followed by a spin-flip caused by the orbital dynamics. Since the orbital excitation involves an LZ process, it must be described quantum mechanically. However, the a.c. driving field can be described with a semiclassical, adiabatic theory like the one described in the previous section. In this approach, the qubit gains a “Stückelberg phase" each time it passes through an energy level anticrossing, resulting in interference effects that can be described using standard LZS theory [16][5]. An alternative theoretical approach (not reported in this Thesis) developed by M. Friesen and S. N. Coppersmith (University of Wisconsin), uses a dressed state formalism that encompasses all of the same interference effects, and plays a key role in understanding the detailed behavior of resonance (5). In this case, the process can be described fully quantum mechanically as an orbital excitation combined with a photon absorption.

7.4. COHERENCE PROPERTIES OF THE INTER-VALLEY SPIN RESONANCE

If resonance (5) involves both a spin and a valley-orbit transition, one would expect its frequency to be much more sensitive to electric fields than the valley-conserving spin transition. The sensitivity to electric fields of resonance (1) has been studied in ref. [2]. It results from a combination of spin-orbit coupling induced by the micromagnet and valley-orbit coupling. In this way, the gate voltage, which couples directly to the orbitals, also has a small effect on the spin states and their splitting. In contrast, the sensitivity to electric fields of resonance (5) only requires valley-orbit coupling.

Fig. 7.3(a) shows that we can continuously shift the transition frequencies of both resonances (1) and (5) by varying the voltage applied to one of the gates that defines the dots, V_2. As expected, resonance (5) exhibits a much greater sensitivity to the gate voltage than resonance (1): the measured frequency shift is ~18.5 MHz/mV for resonance (5), versus ~0.5 MHz/mV for resonance (1). We also notice that the two resonance shifts as a function of V_2 have an opposite sign, which indicates that different mechanisms are responsible. For resonance (1), we believe that the dominant effect of electric field shifts

[5] Note that the standard theory assumes the qubit is driven all the way through the energy level anticrossing in Eq. (7.1); however, the interference effects observed in our simulations occur even without passing through the anticrossing.

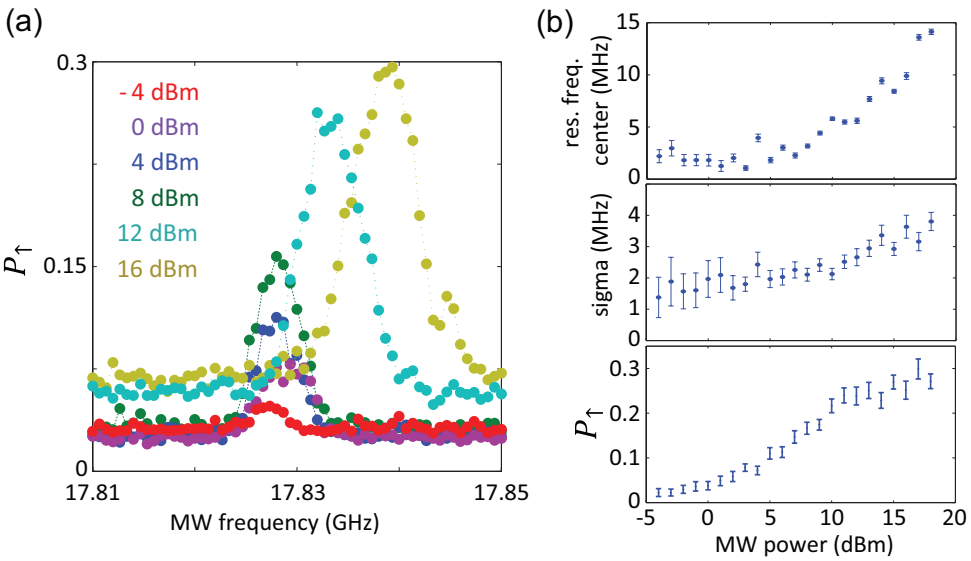

Figure 7.5: (a) Spin resonance as a function of MW power, for a fixed MW burst time of 1 μs. By increasing the MW driving field, the center of the resonance $f_0^{(5)}$ moves towards higher frequency, and the resonance becomes broadened and higher (notice that the off-resonance counting increases as well) as summarized in panel (b) top, medium and bottom respectively.

is the displacement of the electron wave function in the magnetic field gradient from the micromagnets [2]. This effect also contributes to the frequency shift of resonance (5), but here it is masked by the change in valley splitting (E_{01}) resulting from the displacement of the electron wave function in the presence of interface disorder [4, 22]. For instance, as reported by Fig. 7.3(b,c), moving the electron towards or away from a simple atomic step at the Si-SiGe interface leads to a change of the valley-orbit energy splitting (see section 7.6.4 for more details on the simulation). As expected, we see that the valley splitting exhibits a minimum when the wave function is centered around the atomic step, but interestingly it does not vanish, i.e. the opposite signs for the valley splitting left and right of the atomic step to not lead to complete cancellation (see section 7.6.4).

As a further check, we record the slope of the energy splitting versus magnetic field (Fig. 7.8(a)), finding that the g-factors extracted for various gate voltages are the same with the error bars (Fig. 7.8(b)). This further indicates that the Stark shift of resonance (5) works primarily via the valley-orbit contribution to its energy splitting.

An equivalent way to explore this effect is reported in Fig. 7.4(a) (see also Fig. 7.8(c)), where keeping a constant static d.c. voltage configuration, we change the amplitude of the voltage pulse applied on gate 2 to bring the system in Coulomb Blockade during the manipulation stage. As summarized in Fig. 7.4(a), by increasing the pulse amplitude V_2^p, the resonance peak systematically moves toward lower frequencies. The lever-arm of this process ($\Delta f/\Delta V_2^p$) is around 9 MHz/mV. This measurement demonstrates the dynamic Stark shifting of resonance (5) and creates opportunities for site-selective addressing (voltage pulse induced addressability). The difference in $\Delta f/\Delta V_2$ between the

d.c. and pulsed case can be ascribed to the fact that for the measurement reported in Fig. 7.3 we have to compensate the change in V_2 by changing the voltage on another gate, in order to keep a good initialization-readout fidelity. Instead, for the pulsed case we just modify the voltage pulse amplitude on the gate 2 in the manipulation stage (and the empty stage, to keep the symmetry of the pulse), without any further compensation.

The ~ 35 times greater sensitivity of the spin-valley transition frequency to electric fields may also contribute to its ten times larger line width compared to the intra-valley spin transition. The line width of the intra-valley spin transition is believed to be dominated by the 4.7% ^{29}Si nuclear spins in the host material [2]. The nuclear field also contributes to the width of the spin-valley transition, but obviously only accounts for a small contribution. We propose that the dominant contribution is low-frequency charge noise. Although not definitive, some evidence for this interpretation is found in Fig. 7.4(b), which shows a scatter plot of $f_0^{(5)}$ and one of the dot-reservoir tunnel rates, simultaneously recorded over many hours. The dot-reservoir tunnel rate serves as a sensitive probe of the local electrostatic environment, including charges that randomly hop around in the vicinity of the quantum dot (see section 7.6.3 for a more detailed explanation of the measurement procedure). The plot shows a modest correlation between the measured tunnel rate and $f_0^{(5)}$, suggesting that the shifts in time of both quantities may have a common origin, namely low-frequency charge noise.

We can also place an upper bound on $[T_2^*]_{(1)}$ for the intra-valley spin transition imposed by charge noise, inside the actual given magnetic field gradient, assuming the inter-valley spin transition is indeed charge-noise limited. Given that $[T_2^*]_{(5)} \sim 110$ ns and the ratio of ~ 35 in sensitivity to electric fields, we find that charge noise, in combination with the magnetic field gradient which makes the spin resonance frequency position dependent, would limit $[T_2^*]_{(1)}$ to ~ 3.8 μs in this sample. The gain in $[T_2^*]_{(1)}$ that can be obtained from isotopic purification thus appears limited. However, this is by no means an intrinsic limitation, since the micro magnet can be redesigned so that the gradient in the longitudinal component is minimized while maintaining a strong gradient of the transverse component, necessary for driving spin transitions.

7.5. RABI DRIVING AND MW POWER DEPENDENCE

In order to try to perform coherent spin oscillations using this resonance, we increase the MW power and we record the spin excited state probability as a function of the MW burst time. The results are reported in Figs. 7.10(a) and (b). Oscillations are barely or not visible, indicating that the highest Rabi frequency we can obtain for resonance (5) is far smaller than $1/T_2^* \sim 10$ MHz. From the dressed state analysis (not reported here), we can estimated a Rabi frequency of 10-100 kHz for the inter-valley spin resonance.

We also recorded a very peculiar evolution of the resonance peak as a function of the MW driving power, reported in Fig. 7.5(a). Increasing the driving MW power the resonance not only broadens (central panel of Fig. 7.5(b)) but also shifts in frequency (upper panel of Fig. 7.5(b)). This dynamical evolution is very different if compared to the intra-valley spin resonance (which is power broadened but stays at fixed frequency).
A possible explanation of this frequency shift, at least for a limited MW power range, can be found in Eq. 7.8, which gives an expression for $\langle E_{01} \rangle$ that determines the Larmor frequency of resonance (5) ($f_0^{(5)} = (\Delta E_z - \langle E_{01} \rangle)/h$). In this respect, experimental Fig. 7.5(b)

shows a variation of the inter-valley spin resonance frequency with respect to driving power, compatible with what indicated by Eq. (7.8). The simple relation in Eq. (7.8) is similar to an a.c. Stark shift [24] and can explain the monotonous resonance shift for moderate power, reported in Fig. 7.5(b).

However, for strong driving power the resonance shift is not anymore monotonous and appears quite unpredictable, as reported in Fig. 7.10(c). Moreover, the observations are completely reproducible. Quite remarkably, for driving power around 12.5 dBm (output of the MW source), for the magnetic field specified in the figure, the resonance peak apparently splits into 3 distinct peaks (red dashed line in Fig. 7.10(c) and inset). This pattern is different for different B_{ext}, in other words, it is specific for the frequency range explored. The origin of the monotonic shift in Eq. (7.8) lies in the purely positive curvature of E_{01} with respect to ϵ. The a.c. Stark shift described by Eq. (7.8) is purely repulsive, therefore it clearly cannot explain the non-monotonic behavior reported in Fig. 7.10(c). A non-monotonic frequency shift could be obtained from a more complicated model Hamiltonian.

Recently we realized (not reported in this Chapter) that the observation of a nontrivial dependence of the resonance frequency on applied MW power, including the observation of multiple resonance frequencies at one power, are consistent with frequency-dependent attenuation in the high-frequency lines. This can be seen by considering a generic system in which (i) the resonance frequency depends on the power that reaches the sample, and (ii) the attenuation in the coaxial lines depends strongly on the frequency (both conditions are satisfied in our case).

7.6. SUPPLEMENTARY INFORMATION

7.6.1. EXPERIMENTAL DETAILS

All the measurements shown here make use of 4-stage voltage pulses (see inset of Fig. 7.4(a)) applied to gate 3 [2] (see Fig. 7.6): (1) initialization to spin-down (4 ms), (2) spin manipulation through microwave excitation of gate 8 (1 ms), (3) single-shot spin read-out (4 ms), and (4) a compensation/empty stage (1 ms). By repeating this cycle, typically 150-1000 times, we collect statistics of how often an electron leaves the dot during the detection stage, giving the spin-excited state probability, $P_\uparrow$, at the end of the manipulation stage.

Microwave excitation, generated by a Agilent E8267D Vector Source, is applied to gate 6 through the following attenuation chain: DC block/ULT-05 Keycom coax/20 dB attenuator (1.7 K)/ NbTi coax /10 dB attenuator (50 mK)/flexible coax/SMA connector on the printed circuit board (PCB). The high frequency signal is combined on the PCB with a DC voltage line by a homemade resistive bias tee (R = 10 MΩ, C= 47 nF).

In Fig. 7.7 we report repeated measurements of resonance (5) recorded over time, in order to investigate the low frequency noise fluctuations. In the main central panel we report, in blue, the spin resonance peak obtained by averaging directly, over time, the data of panel (a), inside the blue square frame. From its full width at half maximum (FWHM) we can get a lower bound for T_2^*, in this case of 100 ns. Alternatively we can also perform a Gaussian fit for each of the time traces in panel (a) and then shift the center of each dataset in order to align the centers of each resonance peak on top of each

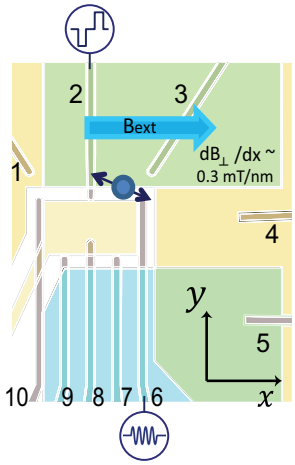

Figure 7.6: False-color device image showing a fabricated pattern of split gates, labeled 1-10. For this experiment we create a single quantum dot (estimated location indicated by a blue circle) and a sensing dot (gates 4 and 5). The current through the charge sensor is recorded in real time for a fixed voltage bias of 500 μeV. The voltage pulses and microwave excitation are applied to gate 2 and 6 respectively. Green semitransparent rectangles show the position of two 200-nm-thick Co micromagnets. The yellow-shaded areas show the location of two accumulation gates, one for the reservoirs and the other for the double quantum dot region.

other, as reported in panel (b). If we now perform the averaging we get the red Gaussian, reported in the main central panel(a), from which we can extract a T_2^* of 150 ns. This last averaging strategy is equivalent to filtering out the very low frequency component of the noise (~mHz), clearly visible in panel (a)[6].

In what follows we report 3 different measurements realized in order to confirm the high sensitivity of the resonance (5) to the electrostatic environment and to electrical noise.

7.6.2. INFLUENCE OF THE STATIC ELECTRIC FIELD

Controlling the electrostatic potential by the voltage applied to the gates defining the QD confinement potential, we can systematically shift in frequency resonance (5) (Fig. 7.3). The inset of Fig. 7.8(a) shows the peak of resonance (5) for five different voltage configurations of the gate 2 (V_2, represented by different colors). The main panel reports a measurement of the g-factor in each of the gate voltage configurations reported in the lower inset of Fig. 7.8(a). The extracted g-factors are compatible with each other, considering their associated errors, as reported in Fig. 7.8(b). This implies that, by changing the gate voltage we can modify the Larmor frequency of the 2-level system involved in the resonance process, without appreciably modifying the Zeeman energy[7]. This suggests that, in this case, we are directly modifying the valley splitting (modelled by moving the

[6] the charge noise has a 1/f dependence, therefore it is a relevant noise contribution.

[7] Changing the gate voltage also will result in a changing of QD position in the micromagnet magnetic field gradient but the derivative of the gradient with respect to the position is quite small as we can estimate from simulation and measure from the red data in Fig. 7.8.

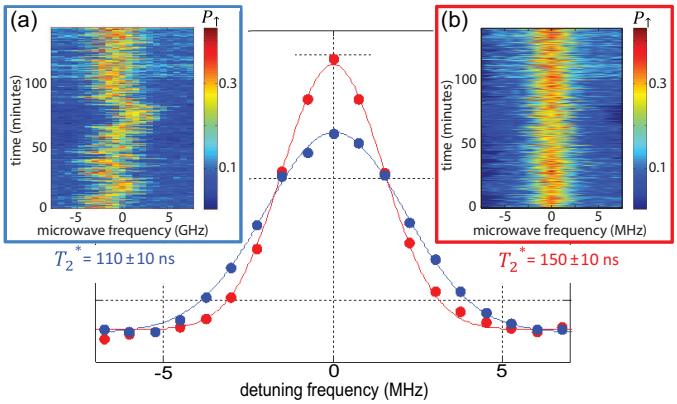

Figure 7.7: The main panel represents a CW (low MW power) measurement of the inter-valley spin resonance. The blue and red traces are obtained averaging over time the data reported respectively in panels (a) and (b). Both panels report the CW resonance recorded over time (y-axis). Each point is averaged over ~100 ms and there are 150 points per trace. We observe that over time the resonance shifts in frequency. Averaging the bare data in panel (a) we get the blue trace. Fitting with a Gaussian we can get a lower bound for the T_2^* of ~110 ns. Furthermore, we can operate a different kind of averaging procedure: we can fit each trace to a Gaussian, get the center of each fit, shift each set of data to center all of the resonance traces (see panel (b)) and average all of them. In this way we get the red trace in the main panel, that gives us a T_2^* of ~150 ns. The difference in the 2 average procedures is the different cutoff frequency imposed at the effective noise spectrum affecting the intra-valley spin resonance: in the first case we are sensitive also to the noise on the timescale between different traces (minutes); in the second case the timescale is set by the time it takes to get a single resonance trace (seconds).

QD towards a step defect in the QW, as schematically represented in Fig. 7.3(b)).

We can estimate the effective wave function 'shift' in space (mainly in the QW plane) generated by modifying the voltage applied to the gate 2 by 1 mV, by using the shift of the Larmor frequency of the intra-valley spin resonance (red trace in Fig.7.3(a)) due to the magnetic field gradient. From the simulation of the magnetic field gradient we can estimate an upper bound for the magnetic field gradient of ~0.2 mT/nm (in the y-direction ~gate 2), equivalent to ~56 MHz/nm in silicon. This energy gradient gives a position lever-arm of ~0.01 nm/mV, considering the slope of 0.55 MHz/mV of the red curve. Furthermore, by making use of the measured value 18.5 MHz/mV for $f_0^{(5)}$ (see blue trace in Fig. 7.3(a)) and of the estimation above ~ 0.01 nm/mV, we can conclude that $\Delta E_{01}/\Delta|\mathbf{r}|$ ~ 1.8 GHz/nm (where $\mathbf{r}$ is the vector representing the motion of the electron generated in the Si QW by the changing of the voltage on gate 2).

7

7.6.3. INFLUENCE OF THE ELECTRIC FIELD NOISE

The measurements reported above reveal that the electrostatic configuration considerably affects the inter-valley resonance frequency. Next we consider the effect of the electrical noise on the coherence of the inter-valley spin resonance.
We already have a clear evidence of the importance of the electric noise from the upper bond of T_2^* of the resonance (5), estimated from the FWHM measurement reported in in Fig. 7.7, which is 10 times shorter than what it should be if just hyperfine fluctuations

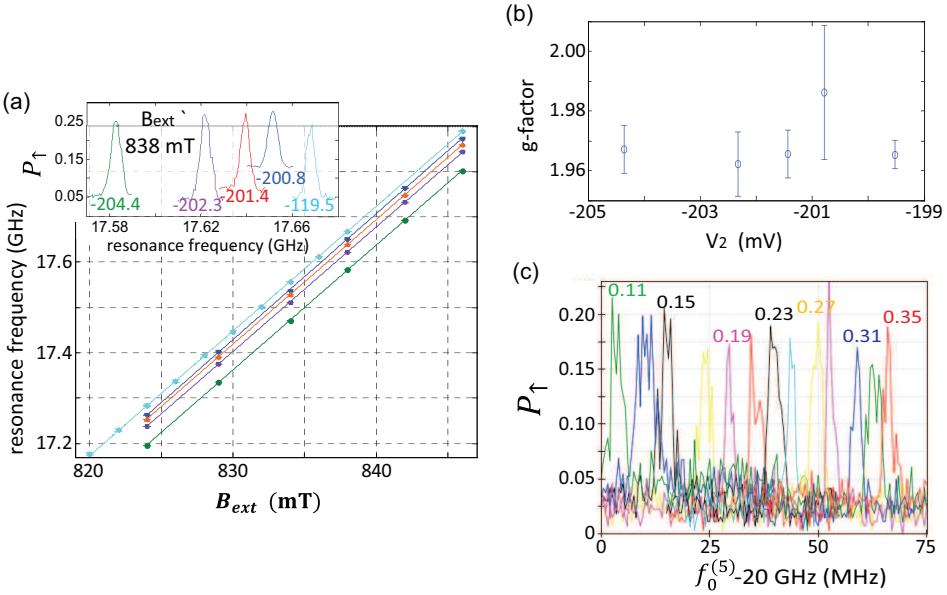

Figure 7.8: (a) g-factor measurements for different voltage values on gate 2 (V_2), reported in mV with different colors in the inset; the extracted g-factors for each V_2 are reported in panel (b). The fact that the g-factor stays constant suggests that the mechanism responsible for the gate dependence of the Larmor frequency $f_0^{(5)}$ is not related to the shift of the electron wave function in the micromagnet stray field (see main text). In panel (c) we show that it is possible to systematically shift the resonance frequency also by changing the voltage amplitude during the manipulation stage (see inset of Fig. 7.4(a) for the color code in correspondence of the first 6 resonances). Notice that we always keep the pulse shape symmetric, compensating by using the same voltage pulse amplitude during the initialization stage-1. $f_0^{(5)}$ increases by pulsing deeper in the Coulomb Blockade configuration. The number reported on each resonance represents the voltage pulse amplitude (in mV) on gate 2.

dominated [2]. This results from the higher sensitivity of resonance (5) to the electrical environment, so also to the electrical noise. In the hypothesis that the hyperfine (HF) and the electric noise (en) are independent, we can write the total noise affecting this resonance as $\delta S_{tot} = \sqrt{(\delta S_{HF})^2 + (\delta S_{en})^2}$, from which $[T_2^*]_{en} \sim 1/\sqrt{([T_2^*]_{tot})^{-2} - ([T_2^*]_{HF})^{-2}} \sim 100$ ns. Therefore, we can deduce that the coherence properties of the inter-valley spin resonance are almost completely dominated by the electric noise (here for $[T_2^*]_{HF}$ we use the value 950 ns extracted for the inter-valley spin resonance in [2]).

Now, we want to perform a measurement to study the correlation between the low frequency fluctuations of resonance (5) and low frequency electric noise (low respect to the electron tunnel rate during the readout stage).
In this respect we made use of the following measurement technique (see Fig. 7.9):
i) the tunnel rate for an electron jumping inside (or outside) a QD from (into) an electron reservoir is a sensitive function of the relative energy alignment between the Fermi level of the electron reservoir and the electrochemical potential of the single electron

inside the QD [23]. Fig. 7.9(a) reports a schematic representation of Γ_{IN} (the single electron tunnel rate IN), as a function of the voltage on gate 2 (V_2) that controls the relative alignment of the two levels (measured data represented in Fig. 7.9(c)). Making V_2 more positive the tunnel rate will increase, also due to the participation of the excited state in the tunneling process. Each tunnel rate is extracted recording, on fly (by FPGA), the tunneling events during the initialization stage (~5 ms) and fitting the histogram of the number of events ($N°$) v.s. the time τ, with an exponential relation (see schematic in Fig. 7.9(a)). τ is the time interval between the tunneling event and the voltage pulse that brings the system into the initialization stage. For the experiment we used V_2 around -196 mV (red points in Fig. 7.9(c)), which has been optimized for a good readout and initialization process. As schematically represented inside the orange frame of Fig. 7.9(b), if we model the electric noise from the environment as a relative fluctuations of V_2 (δV_2), we can write $\delta\Gamma_{IN} \sim \frac{\partial\Gamma_{IN}}{\partial V_2}\delta V_2$. In this way we use $\delta\Gamma_{IN}$, the tunnel rate fluctuations during the initialization stage (of the 4-stages pulse sequence), as a probe of electric noise.
ii) The same 4-stage voltage pulse scheme allows us to perform rotation of the electron spin and to read it out in the last stage (see inset of Fig. 7.4(b)). Due to the coupling with the environment noise, the spin Larmor frequency, $f_0^{(5)}$, fluctuates (see blue frame of Fig. 7.9(b)) over time, as reported in the CW measurement in Fig. 7.9(d). We fit each resonance trace to a Gaussian in order to extract the center of it (Larmor frequency). The evolution over time (on the time scale between two measured traces) of this parameter is determined by an effective magnetic noise. We want to prove that the noise affecting the spin resonance (5) is dominated by charge-electrical noise.
iii) We repeat this measurement over time (each trace takes tens of seconds), in order to get enough statistics, and plot, as reported in Fig. 7.4(b), the extracted Γ_{IN} (x-axis) and Larmor frequency fluctuation Δf_0 (y-axis) traces, for each measurement cycle.

7.6.4. SIMULATION OF E_{01} V.S. QD SHIFT IN FIG.7.3(C)

The simulation reported in Fig. 7.3(c) represents the result of a 2D tight binding calculation[8]. The fact that the simulation is 2D rather than 3D affects just the magnitude of E_{01}, but not its qualitative dependence from the step offset. The quantum well barrier has been chosen to be 160 meV, corresponding to 30% Ge. We assumed a parabolic confinement potential for the dot (for simplicity) of size $< x^2 >= 21.1$ nm, corresponding to an orbital energy splitting of $\hbar\omega = 0.45$ meV [2]. The electric field and the quantum well width have been chosen to be 1.5×10^6 V/m and 13 nm, respectively. The experimental quantum well is nominally 12 nm and the experimental electric field is not well known.

There are 3 competing effects that determine the energy splitting between the two lowest eigenstates, which we usually refer as 'valley splitting', for simplicity. (i) The first is the actual valley splitting, which is maximized when the electron sees no step. However, the ground and excited states move to the left or right differently as a function of the step offset. (ii) The second effect is related to the electrostatic energy. When the electron sits to the left of the step, it gains a little energy because the energy is given by eEz, where z is the vertical position. For a single atom step with $E = 1.5 \times 10^6$ V/m, this energy scale is 0.20 meV, so it competes with the valley splitting, whose characteristic value in the plots is about 0.22 meV. This competition is always present, for any value

[8] Realized by M. Friesen (University of Wisconsin)

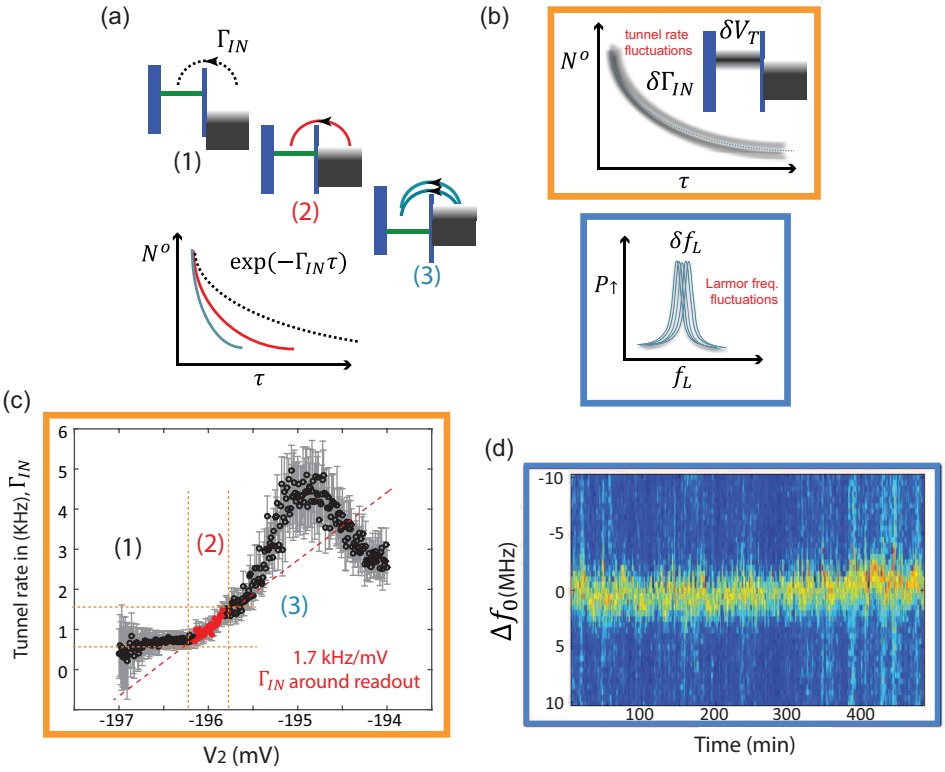

Figure 7.9: (a) Schematic representing the variation of the tunnel-IN rate Γ_{IN}, as a function of V_2; we are operating around the readout position indicated by the red points in panel (c), for which we can get a sensitivity of 1.7 kHz/mV. (b) Schematic of the effect of the magnetic noise and electrical noise, causing respectively the Larmor frequency fluctuation (lower panel) and tunnel rate fluctuations (upper panel). (c) Tunnel-IN rate, Γ_{IN}, recorded during the initialization stage as a function of V_2. (d) CW measurement of the inter-valley resonance at low MW power (as in Fig 7.7) over time, in order to study the low frequency (tens of mHz) noise spectrum affecting the inter-valley spin resonance. It has been recorded during the readout stage of the same pulse sequence.

of the electric field, because the electrostatic energy and the valley splitting both have a linear dependence on E. (iii) The third competing effect is the confinement energy of the parabolic dot: when the electron center of mass moves to the left or right, this increases the average energy of the electron in the parabola. For the maximum shift of ~20 nm shown in Fig. 7.11(a), this confinement energy scale is ~0.1 meV, so all the energy scales are comparable. The competition between these different effects causes the left-right symmetry of the plots to be broken. The competition also makes it difficult to gain much intuition about the final results. Without the competing effects, we would expect the valley splitting to go to zero as the ground state changes from 'even' to 'odd' in the valley parameter. But the electron always wants to maximize the energy splitting between the two eigenstates, and the competing effects (in particular, the shifting of the electrons to the left and right) allow it to keep a nonzero energy splitting at all times. It

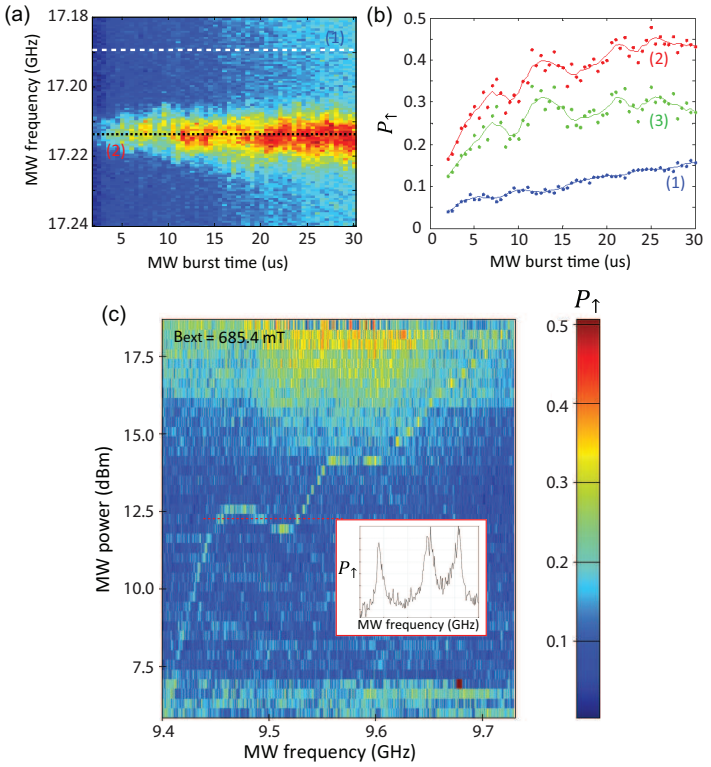

Figure 7.10: This figure reports a study of $P_\uparrow$ for the spin resonance (5) as a function of MW burst time. In (a) $P_\uparrow$ is recorded as a function of the MW burst time and MW frequency, for a fixed MW source output of 12 dBm. Increasing the MW burst time, the off resonance counting (dashed-white line (1)) increases as well and the resonance becomes broadened. (b) Sections of (a) along the dashed lines (1) and (2) and their difference (3). (c) As reported in Figs. 7.5(a-b), the Larmor frequency $f_0^{(5)}$ is a function of the MW power applied during the manipulation stage. Increasing the MW power, $f_0^{(5)}$ increases as well. This effect is quite remarkable: 10 dB changing in MW power results into a shift of 300 MHz of Larmor frequency, equivalent to a relative shift of roughly 3%. The functional relation between the MW power and $f_0^{(5)}$ is not trivial. In the beginning, for small MW power, the Larmor frequency of the inter-valley resonance stays constant; by increasing the MW power, it increases linearly (according to Eq. (7.8)) piecewise, spaced by anomalous evolutions, as for instance around 12.5 dBm. For a specific power range the spin resonance splits into 3 resonance peaks or it evolves into a very broaden resonance.

is interesting that this minimum valley splitting (~25 μeV) is very close to the one we observed in our experiments.

From Fig. 7.2(b-c) we can notice as the first harmonic resonance seems to fade for high response frequencies. In the simulations reported in Fig. 7.11(b) we study the visibility of the spin resonances as a function of the driving amplitude (for a fixed value of the response frequency Ω). We notice that the harmonic resonance (red arrow, $\Omega/2$) seems to fade when it crosses the Landau-Zener resonance (black arrow). This can simply indicate entering the strong driving regime, where the Landau-Zener process (which is a dynamical effect) dominates the regular harmonics (which are simply due to the

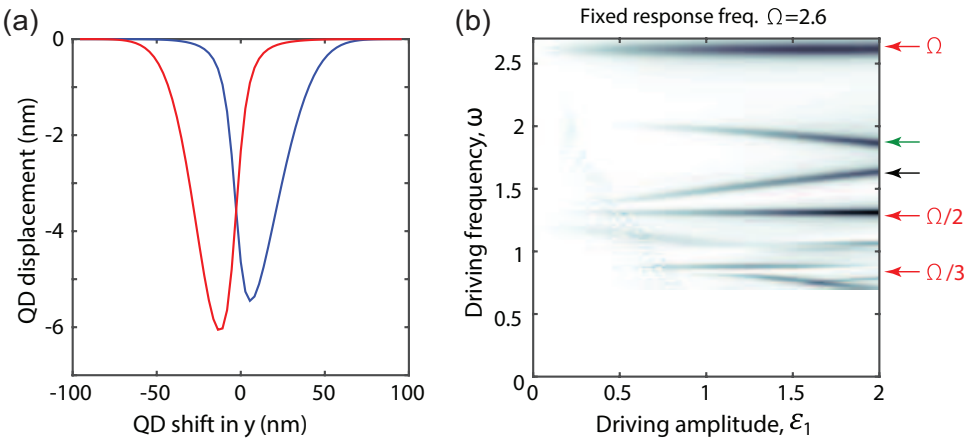

Figure 7.11: (a) The displacement of the electron center of mass for the ground state (blue), and the first excited valley state (red). (b) A resonance spectrum for driving frequency vs. microwave amplitude, obtained for a fixed value of the response frequency. The red arrows indicate the fundamental resonance and its first two harmonics, whose values are largely unaffected by the microwave power. The green and black arrows indicate Landau-Zener-mediated, dynamical processes, which are highly sensitive to the driving strength. The resonance at the green arrow evolves into $\hbar\omega = (E_Z + E_{01})/2$ at larger response frequencies. The resonance at the black arrow corresponds to the intra-valley spin resonance and evolves into $\hbar\omega = (E_Z - E_{01})$.

non-linearities in the Hamiltonian).

REFERENCES

[1] F. A. Zwanenburg, A.S. Dzurak, A. Morello, M. Y. Simmons, L. C. L. Hollenberg, G. Klimeck, S. Rogge, S. N. Coppersmith, and M. A. Eriksson, Rev. Mod. Phys. **85**, 961 (2012).

[2] E. Kawakami, P. Scarlino, D. R. Ward, F. R. Braakman, D. E. Savage, M. G. Lagally, Mark Friesen, S. N. Coppersmith, M. A. Eriksson and L. M. K. Vandersypen, Nature Nanotech. **9**, 666 (2014).

[3] M. Friesen, M. A. Eriksson, and S. N. Coppersmith, Appl. Phys. Lett. **89**, 202106 (2006).

[4] M. Friesen and S. N. Coppersmith, Phys. Rev. B **81**, 115324 (2010).

[5] S. Goswami, K. A. Slinker, Mark Friesen, L. M. McGuire, J. L. Truitt, C. Tahan, L. J. Klein, J. O. Chu, P. M. Mooney, D. W. van der Weide, R. Joynt, S. N. Coppersmith and M. A. Eriksson, Nature Phys. **3**, 41 (2007).

[6] P. Scarlino, E. Kawakami, D. R. Ward, D. E. Savage, M. G. Lagally, Mark Friesen, S. N. Coppersmith, M. A. Eriksson, and L. M. K. Vandersypen, Phys. Rev. Lett. **115**, 106802 (2015).

[7] L. Landau, Phys. Z. Sowjetunion **32**, 46 (1932).

[8] C. Zener, Proc. R. Soc. Lond. A **137**, 696 (1932).

[9] L. R. Schreiber, F. R. Braakman, T. Meunier, V. Calado, J. Danon, J. M. Taylor, W. Wegscheider, and L. M. K. Vandersypen, Nat. Commum. **2**, 566 (2011).

[10] C. H. Yang, A. Rossi, R. Ruskov, N. S. Lai, F. A. Mohiyaddin, S. Lee, C. Tahan, G. Klimeck, A. Morello, and A. S. Dzurak, Nat. Commun. **4**, 2069 (2013).

[11] Y. Tokura, W. van der Wiel, T. Obata, and S. Tarucha, Phys. Rev. Lett. **96**, 047202 (2006).

[12] M. Pioro-Ladriere, T. Obata, Y. Tokura, Y. S. Shin, T. Kubo, K. Yoshida, T. Taniyama, and S. Tarucha, Nature Phys. **4**, 776 (2008).

[13] X. Hao, R. Ruskov, M. Xiao, C. Tahan, and H. W. Jian, Nat. Commun. **5**, 3860 (2014).

[14] J. K. Gamble, M. A. Eriksson, S. N. Coppersmith, and M. Friesen, Phys. Rev. B **88**, 035310 (2013).

[15] E. I. Rashba, Phys. Rev. B **84**, 241305 (2011).

[16] S. N. Shevchenko, S. Ashhab, and F. Nori, Phys. Rep. **492**, 1 (2010).

[17] E. C. G. Stückelberg, Helv. Phys. Acta **5**, 369 (1932).

[18] J. Stehlik, Y. Dovzhenko, J. R. Petta, J. R. Johansson, F. Nori, H. Lu, and A. C. Gossard, Phys. Rev. B **86**, 121303(R) (2012).

[19] J. Stehlik, M. D. Schroer, M. Z. Maialle, M. H. Degani, and J. R. Petta, Phys. Rev. Lett. **112**, 227601 (2014).

[20] G. Széchenyi and A. Pályi, Phys. Rev. B **89**, 115409 (2014).

[21] J. Danon and M. S. Rudner, Phys. Rev. Lett. **113**, 247002 (2014).

[22] Z. Shi, C. B. Simmons, J. R. Prance, J. K. Gamble, T. S. Koh, Y. P. Shim, X. Hu, D. E. Savage, M. G. Lagally, M. A. Eriksson, Mark Friesen, and S. N. Coppersmith, Phys. Rev. Lett. **108**, 140503 (2012).

[23] L. M. K. Vandersypen, J. M. Elzerman, R. N. Schouten, L. H. Willems van Beveren, R. Hanson, and L. P. Kouwenhoven, Appl. Phys. Lett. **85**, 4394 (2004).

[24] M. Brune, P. Nussenzveig, F. Schmidt-Kaler, F. Bernardot, A. Maali, J. M. Raimond, and S. Haroche, Phys. Rev. Lett. **72**, 3339 (1994).

8

SPIN RELAXATION ANISOTROPY IN A GAAS QUANTUM DOT

We report that the electron spin relaxation time, T_1, in a GaAs quantum dot with a spin-1/2 ground state has a 180 degree periodicity in the orientation of the in-plane magnetic field. This periodicity has been predicted for circular dots as being due to the interplay of Rashba and Dresselhaus spin orbit contributions. Different from this prediction, we find that the extrema in the T_1 do not occur when the magnetic field is along the [110] and [1$\bar{1}$0] crystallographic directions. This deviation is attributed to an elliptical dot confining potential. The T_1 varies by more than an order of magnitude when rotating a 3 Tesla field, reaching about 80 ms for the optimal angle. We infer from the data that in our device the signs of the Rashba and Dresselhaus constants are opposite.

The work in this chapter has been published as: P. Scarlino, E. Kawakami, P. Stano, M. Shafiei, C. Reichl, W. Wegscheider, and L. M. K. Vandersypen, Phys. Rev. Lett. **113**, 256802 (2014).

8.1. INTRODUCTION

The high control reached in the manipulation of a single electron spin in a semiconductor environment [1] is encouraging for future application of this natural two-level system for quantum computation technology. In GaAs, InAs and other III-V quantum dots it has been shown that this manipulation can be realized using exclusively electrical fields [2, 3]. Coupling of the electric field to the spins is mediated by the spin-orbit (SO) interaction naturally provided by the semiconductor host environment. The semiconductor environment also implies that the electron is intimately in contact with phonons, charge fluctuations and nuclear spins, and these interactions are responsible for the relaxation and dephasing process of the electron spin.

During the last ten years, a significant experimental [4–10] and theoretical [11–15] effort has been devoted to understanding the effect of electron spin relaxation in lateral quantum dots (QDs). At magnetic fields of the order of Tesla, spin relaxation in GaAs dots was found to be dominated by the SO interaction in combination with piezoelectric phonons. Two contributions to the SO interaction usually dominate. The local electric field due to a crystal with bulk inversion asymmetry generates a Dresselhaus (D) SO contribution [16] which, for electrons confined in the plane (xy, with x and y along the [100] and [010] crystallographic directions, respectively) of the quantum well, can be written as $H_D = \beta(-\sigma_x P_x + \sigma_y P_y)/\hbar$, with $\hbar$ the Planck constant, β the Dresselhaus SO coupling strength, $\mathbf{P}$ the electron kinematic momentum and $\boldsymbol{\sigma}$ the vector of Pauli matrices. In addition, the electric field associated with the asymmetric confining potential along the heterostructure growth direction (z along [001]) gives rise to the Rashba (R) SO contribution [17], $H_R = \alpha(\sigma_y P_x - \sigma_x P_y)/\hbar$, with α the Rashba SO coupling strength. The effect of the SO interaction can be viewed as an effective magnetic field $\mathbf{B}_{SO}$ acting on the conduction electron spin, with an amplitude and direction that depend on the electron momentum [see Fig. 8.1(b)]. The interplay of R and D coupling gives rise to an anisotropy in the direction and magnitude of $\mathbf{B}_{SO}$ in the plane of the quantum well. As a result, spin relaxation in a quantum dot is anisotropic in the direction of the in-plane magnetic field [13, 14].

The anisotropy of electron spin relaxation originating from SO interaction has not been studied experimentally so far, even though it is highly relevant. Indeed, depending on the circumstances, it may be desirable to get long relaxation times or to make the relaxation process as fast as possible, for example in order to rapidly initialize the spin [18]. The SO anisotropy similarly affects the strength of the effective driving field for single-qubit rotations based on electric dipole spin resonance [19]. With a proper understanding, one can design future devices that optimally reconcile various requirements.

Here we present a measurement of T_1 as a function of the orientation of an in-plane magnetic field. We find a striking anisotropy with a 180 degree periodicity, confirming the theoretical predictions experimentally. Comparison with the predictions indicates that also the dot shape anisotropy plays an important role. We discuss in detail what information is needed to determine the ratio of the Rashba and Dresselhaus coupling strengths in this case. We also provide guidance for sample design and magnetic field orientation in future experiments.

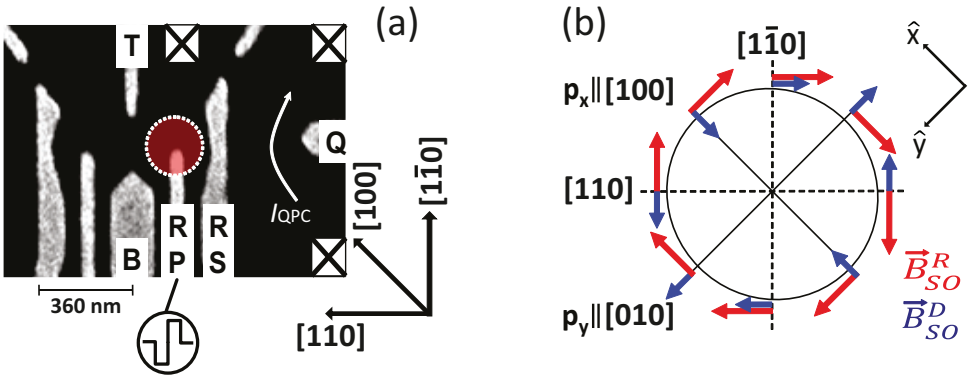

Figure 8.1: (a) Scanning electron micrograph of a device similar to the one measured. The black arrows indicate the crystallographic axes. The dotted red circle represents schematically the single QD position. (b) The spin-orbit field $\mathbf{B}_{SO}$ acting on a conduction electron is shown by red and blue arrows (for a constant magnitude of $\mathbf{P}$), arising from the Rashba and Dresselhaus contributions (chosen to be different in modulus and $\alpha < 0$, $\beta > 0$) and defined respectively as $\mathbf{B}^R_{SO} = \frac{\alpha}{g\mu_B}(-P_y, P_x)$ and $\mathbf{B}^D_{SO} = \frac{\beta}{g\mu_B}(-P_x, P_y)$, with g the electron g-factor and μ_B the Bohr magneton.

8.2. DEVICE AND MEASUREMENT TECHNIQUE

The experiment has been realized in a single depletion QD, see Fig. 8.1(a) created by applying a negative potential to surface gates on top of a GaAs/$Al_{0.33}Ga_{0.67}$As heterostructure, grown along the [001] direction. The GaAs/AlGaAs interface is 85 nm deep, with Si-delta-doping of about 1.3×10^{12}cm^{-2} atoms 40 nm away from the 2DEG, and with carrier density and mobility of 1.2×10^{11} cm^{-2} and 3.6×10^{5} cm^{2}V^{-1}s^{-1} respectively (measured at 4 K). The base temperature of the dilution refrigerator was 25 mK and we estimated the electron temperature to be 130 mK from transport measurements at zero magnetic field. From pulse spectroscopy measurements [32] we infer that the dot contains most likely three electrons (see Sec. 8.8.1). Two electrons form a closed shell, with the third electron effectively acting as a spin-1/2 system. The orientation of the quantum dot gate pattern with respect to the main crystallographic directions is shown in Fig. 8.1(a). We applied a magnetic field in the 2DEG plane (at an angle ϕ with respect to the [100] direction) of modulus 3 T, to ensure that the spin Zeeman energy ($\Delta_z \approx 76$ μeV, considering a g-factor of -0.44 [1]) is higher than the electron temperature ($k_B T_{el} \approx 11$ μeV), as required for energy selective spin read-out (see below) [5]. Real-time detection of the dot occupation is realized by monitoring the current through a quantum point contact (on the right side of the structure), amplified by a room temperature I-V converter, and low-pass filtered with a bandwidth of 30 kHz.

We measure the electron spin relaxation time by applying a three or four-stage pulse to gate RP [5] (see also Sec. 8.8.1).

The main observation is a striking variation in the relaxation time upon rotation of the in-plane magnetic field (Fig. 8.2). Fig. 8.3 shows the measured relaxation time as a function of the magnetic field orientation over the whole 360 degree range. The data show clearly the predicted 180 degree periodicity and a remarkable variation in T_1 from

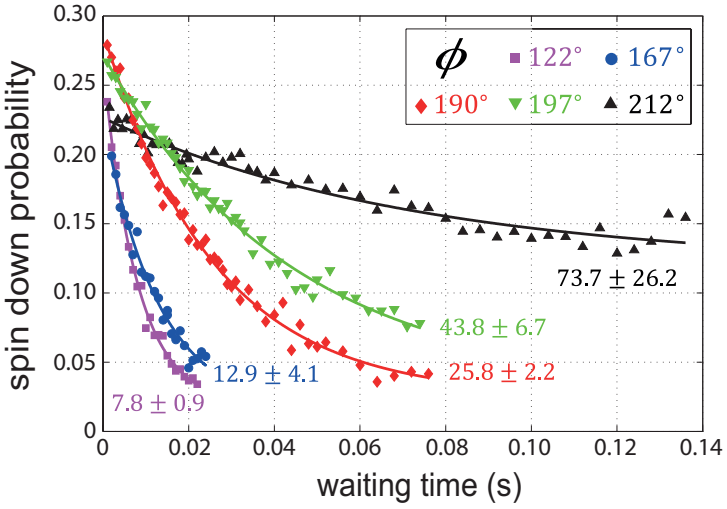

Figure 8.2: Measured spin-down probability (averaged over 5000 cycles) as a function of the waiting time between injection and read-out (see Sec. 8.8.1) for different angles ϕ of the 3 T in-plane magnetic field. The solid lines are fits to the data of the form $P_\downarrow = a\exp(-t/T_1)+b$. The fitted T_1's are indicated for each curve (in ms). Small variations in $P_\downarrow(t=0)$ can arise from variations in the read-out configuration in the course of the measurements. Measuring longer T_1's requires longer waiting times, with increased pulse distortion from the bias-tee (see Sec. 8.8.1), and therefore larger error.

7 to 85 ms [Fig. 8.3(a)]. The maxima in T_1 are sharply peaked. When plotting the same data inverted, as $\Gamma = 1/T_1$ [Fig. 8.3(b)], we see a sinusoidal variation of the relaxation rate.

8.3. MODEL: CIRCULAR DOT

To understand this sinusoidal modulation, it is useful to express the spin relaxation rate in terms of a cross-product of the external field $\mathbf{B} = B(\cos\xi\cos\phi, \cos\xi\sin\phi, \sin\xi)$, and the in-plane vector [21]

$$\mathbf{n} = x\left(l_D^{-1}, -l_R^{-1}, 0\right) + y\left(l_R^{-1}, -l_D^{-1}, 0\right), \tag{8.1}$$

which refers to crystallographic directions $\hat{x} = [100]$, and $\hat{y} = [010]$ through the operator of electron coordinates $\mathbf{r} = (x, y)$. The SO lengths, $l_{R,D} = \hbar^2/(2m^\star\alpha, \beta)$, with $m^\star$ the effective electron mass, are defined as the distance travelled by an electron over which its spin is rotated by π due to $\mathbf{B}_{SO}$ (typically 1-10 μm in GaAs). For a circular dot, the relaxation rate is (see Sec. 8.8.2)

$$\Gamma \propto |\mathbf{B}\times(l_D^{-1}, -l_R^{-1}, 0)|^2 + |\mathbf{B}\times(l_R^{-1}, -l_D^{-1}, 0)|^2, \tag{8.2}$$

since the dipole operators x and y contribute equally [14]. Parametrizing the SO lengths by $l_R^{-1} = l_{SO}^{-1}\cos\vartheta$, and $l_D^{-1} = l_{SO}^{-1}\sin\vartheta$, a straightforward evaluation of Eq. (8.2) gives the known result [13, 14]

$$\Gamma \propto l_{SO}^{-2}\left[\sin^2\xi + \cos^2\xi(1+\sin 2\phi\sin 2\vartheta)\right], \tag{8.3}$$

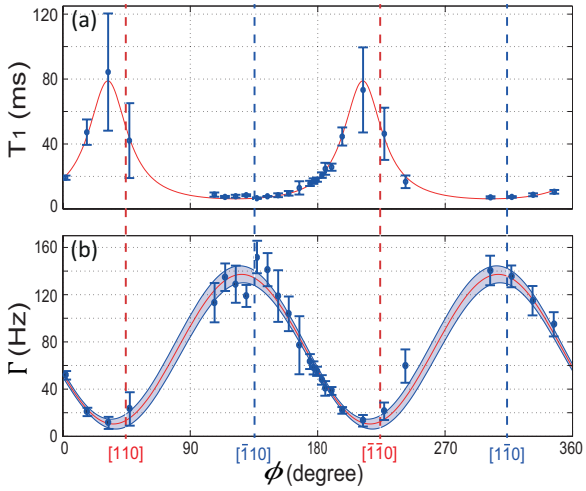

Figure 8.3: Angle dependence of the spin relaxation time (a) and rate (b), which are separately extracted from exponential fits with either the relaxation rate or time in the exponent. The magnetic field is nearly in-plane, with $|\xi| < 5°$, while the in-plane angle ϕ has a systematic error of $\pm 3°$. The red line is a fit to Eq. (8.7) with free parameters (ϕ_{min}, ξ^*, b). The shaded region between the two blue curves indicates the 95% confidence interval. The dashed vertical lines show the positions of the extrema of Γ predicted for a circular dot (at $\phi = 45°$ and $135°$, see Eq. (8.3)).

which, for an in-plane magnetic field ($\xi = 0$) reduces to

$$\Gamma \propto l_{SO}^{-2}\left(1 + \sin 2\phi \sin 2\vartheta\right). \tag{8.4}$$

For positive relative sign of the SO couplings, the rate reaches a maximum (minimum) with the external field along [110] ([1$\bar{1}$0]). If the relative sign is inverted, the positions of the minimum and maximum swap. If R and D have equal strength, the minimal rate is zero, while the sinusoidal modulation is reduced the more R and D differ in strength. Therefore, the relative strength of R and D, including the relative sign, can be extracted from the dependence of Γ on the magnetic field orientation.

8.4. MODEL: DOT SHAPE ANISOTROPY

Looking at the data in Fig. 8.3, the extrema of the rate are shifted by $\approx 10°$ from the prediction of Eqs. (8.3) and (8.4). Similar offsets were observed in the dependence of SO induced avoided level crossings on the magnetic field orientation in InAs dots [22, 23], and were explained by invoking anisotropic dot shapes [24]. The dot anisotropy influences also the spin relaxation rate, as seen experimentally in Ref. [10] and anticipated theoretically in Ref. [12] considering the Dresselhaus coupling only. In addition to the observed shift, the dot in-plane elongation is indicated also by our spectroscopy data (see Sec. 8.8.1): given the measured addition energy of about 3 meV, we would expect an orbital excitation energy of about 1 meV [1], but in this sample, for the specific electrostatic configuration used for this experiment, the first orbital excitation energy is only 120 μeV. We will therefore assume that the dot is strongly anisotropic (elongated), with

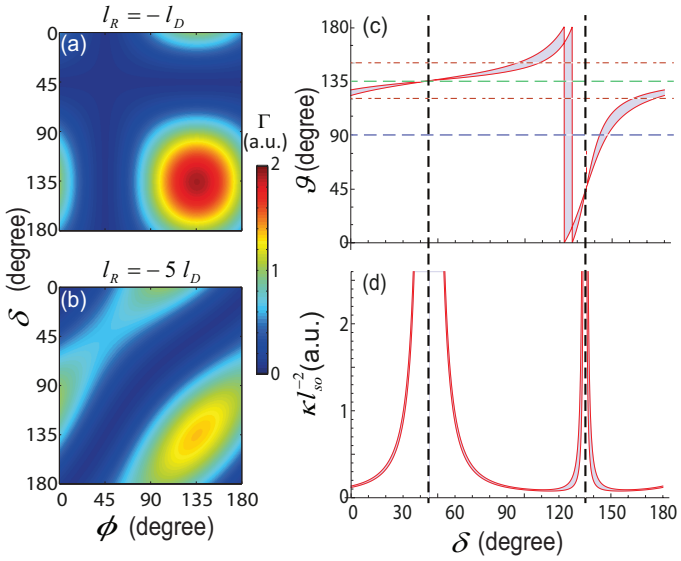

Figure 8.4: Calculated values of Γ [Eq. (8.7)] as a function of the angle of the external magnetic field ϕ and the dot major axis δ, for $\xi = 0$ and (a) $l_R/l_D = -1$ and (b) $l_R/l_D = -5$. (c-d) The result of the fit of the data of $\Gamma(\phi)$ from Fig. 8.3(b) to Eqs. (8.7) and (8.8), with ϑ and (κl_{SO}^{-2}) (the latter in arbitrary units) as fit parameters, as a function of δ. The shaded area between the two red curves indicates the 95% confidence interval (not taking into account the systematic error in ϕ). The two black vertical lines indicate $\delta = 45°, 135°$; the two red dotted lines and the green and blue horizontal lines are at $\vartheta = 120°, 150°, 135°$ and $90°$ respectively.

the confinement potential major axis rotated away from [100] by an angle δ. Neither this angle, nor the degree of anisotropy (nor any more details on the potential shape) are known.

To derive an analogue of Eq. (8.2) for an anisotropic dot, one should express Eq. (8.1) in coordinates x', y', rotated from the crystallographic axes by the angle δ,

$$\mathbf{n} = \mathbf{n}_{x'} x' + \mathbf{n}_{y'} y'. \tag{8.5}$$

For an elongated dot, the excitations along the major axis (x') dominate the transition matrix element (see Sec. 8.8.2), and the rate is [12, 14, 15]

$$\Gamma \propto |\mathbf{B} \times \mathbf{n}_{x'}|^2. \tag{8.6}$$

After some trigonometric manipulations, we are able to write the previous equation in the form

$$\Gamma = b\left[\sin^2\xi + \cos^2\xi \sin^2(\phi - \phi_{min})\right], \tag{8.7}$$

where $b \equiv \kappa l_{SO}^{-2}(1 + \sin 2\delta \sin 2\vartheta)$, with κ a proportionality constant that sets the overall scale.

This expression predicts a rate varying sinusoidally upon in-plane rotation of the magnetic field, a feature in common with Eq. (8.3). However, the details of the dependence are very different. Here, unlike in Eq. (8.3), the optimal magnetic field angle for

which the rate is minimal does depend on the ratio of Rashba and Dresselhaus coefficients (through ϑ), and on the anistropy axis of the dot (through δ):

$$\tan\phi_{min} = -\frac{\cos(\delta-\vartheta)}{\sin(\delta+\vartheta)}. \tag{8.8}$$

8.5. RESULTS AND DISCUSSION

To illustrate further the dependence of the relaxation rate on the orientation of the in-plane field and the dot major axis, we plot the prediction of Eq. (8.7) in Fig. 8.4(a-b) for different ratios of l_R and l_D. When $l_R = -l_D$, the relaxation rate is minimal for $\phi = 45°$, regardless of the dot orientation, and also for $\delta = 45°$ regardless of the in-plane magnetic field orientation [Fig. 8.4(a)]. When $l_R \neq l_D$, the field orientation that minimizes the relaxation rate depends on the dot major axis orientation [Fig. 8.4(b)], with a π periodicity.

We fit the data of Fig. 8.3(b) to Eq. (8.7) with ϕ_{min}, ξ and b as the fitting parameters. The fit is plotted in Fig. 8.3(b) as the red line. It agrees excellently with the data (fit goodness $R^2 \approx 0.99$) and gives $\phi_{min} = 35.1° \pm 1.1°$, $\xi \approx 17.4° \pm 1.1°$, and $b = (139.2 \pm 3.5)\ \mathrm{s}^{-1}$. The fitted 17° misalignment of the magnetic field out of the plane is, however, unrealistically large. We estimated it in our experimental setup via Shubnikov-de Haas oscillations, and can put an upper limit $|\xi| < 5°$ (see Sec. 8.8.1). The unexpectedly high value of ξ comes from the large value of the relaxation rate at its minimum. We note, however, that this minimum value may also be dominated by other relaxation mechanisms that do not depend on ϕ, such as the interaction with nuclear spins [12], or the contribution from the random part of the R SO coupling [25] which arises due to fluctuations in the dopant concentration in the δ-doping layer. Contributions of orbital excitations along the minor axis also lead to a finite offset, as is suggested by Eq. (8.2). Without knowing more about the dot confinement shape, we did not find it reasonable to try to separate these possible contributions by introducing more fitting parameters. Instead, we relabel $\xi \to \xi^*$, reinterpreting it as an effective angle accounting for all these possibilities together.

Using the value of ξ^* obtained from the fit and Eqs. (8.7) and (8.8), we can also perform a fit of the same data set with ϑ and κl_{SO}^{-2} as free parameters, as a function of δ. The fit results are plotted in Fig. 8.4(c-d). From there we conclude that without knowing the value of δ, we cannot establish the relative strength of the R and D couplings, as all values of δ are possible, in principle. However, we can infer that, most probably, in our sample α and β were of comparable magnitude and opposite sign [$120° \leq (\vartheta = \arctan(l_R/l_D)) \leq 150°$], as these choices cover the larger portion of (a priori equally probable) values of δ, in accordance of what is estimated in [26] for a similar heterostructure. There are two points, $\delta = 45°$ and 135°, where the rate κl_{SO}^{-2} diverges (see Sec. 8.8.3). This indicates that such values of δ cannot be reconciled with our data. Indeed, as follows from Eq. (8.8), for these values ϕ_{min} does not depend on the SO couplings and should be 45° or 135°, which is different from what we measured. We furthermore note that if δ were known, α/β could be extracted directly. In order to also determine the absolute values of α and β, more information is needed, such as the energy level spectrum of the dot.

8.6. OPTIMAL ORIENTATION OF THE GATE PATTERN AND MAGNETIC FIELD

For future experiments, we give guidance for the optimal orientation of the quantum dot gate pattern and magnetic field relative to the crystal axes. First, since spin relaxation and electron dipole spin resonance (EDSR) based spin manipulation are governed by the same matrix elements for spin transitions, it is possible to simultaneously optimize for fast EDSR driven Rabi oscillations and for fast relaxation (useful for qubit reset [18]). In contrast, slow relaxation (useful for high-fidelity read-out [5, 27]) cannot be optimized together with fast EDSR, as long as the phonon coupling is isotropic, as then both the spin relaxation rate and the EDSR rate scale with the same factor. In circular dots, this factor is given in Eq. (8.4). We see that the R and D terms maximally enhance or cancel each other when the external magnetic field is oriented along the [110] and $[1\bar{1}0]$ crystallographic axes, as can be expected also from Fig. 8.1(b). Complete cancellation of the two contributions is possible only when $|\alpha| = |\beta|$. When R and D have very different strengths, Γ does not vary with the magnetic field orientation. For anisotropic dots, the factor is given in Eq. (8.7). Here, Γ oscillates with the field orientation and can reach zero (for $\xi = 0$) regardless of the ratio of α and β. Finally, for maximizing the EDSR amplitude, in circular dots the external magnetic field has to point along [110] ($[1\bar{1}0]$), if $\alpha\beta > 0$ ($\alpha\beta < 0$), and the driving electric field should be parallel to $\mathbf{B}$. In elongated dots the magnetic field should be oriented along the in-plane angle $\phi = \phi_{min} + \pi/2$, and the driving electric field should be along the dot soft axis. If the direction of the main dot axis can be chosen, it should point along [110] ($[1\bar{1}0]$), if $\alpha\beta > 0$ ($\alpha\beta < 0$).

8.7. CONCLUSION

In conclusion, we show that the in-plane orientation of the magnetic field can strongly impact the spin relaxation time in quantum dots. We observe a variation in T_1 by more than an order of magnitude when rotating the field in the 2DEG plane. We can take advantage of this dependence in future experiments to either maximize or minimize T_1. Furthermore, the dependence of T_1 on magnetic field angle provides a sensitive probe of the ratio of the R and D SO contributions, which can be used even when SO induced avoided level crossings are too small to be measured [28], which is the case of GaAs. What is needed is either a symmetric QD confining potential or, for an elliptical dot, a good estimate of the magnitude and direction of the QD anisotropy. Similar considerations are also valid for singlet-triplet qubits [29][1], where the easy axis is given by the double dot dipole axis [28].

8.8. SUPPLEMENTARY INFORMATION

8.8.1. EXPERIMENTAL DETAILS

Here we give several experimental details, which were omitted in the main text.

[1] According to our analysis (not reported here), the dipole matrix elements between a singlet [either (1,1) and (0,2)] and a polarized triplet (1,1) in a biased two electron double dot tuned close to a singlet(1,1)-singlet(0,2) anti-crossing have the same angular dependence as the single electron matrix elements discussed here.

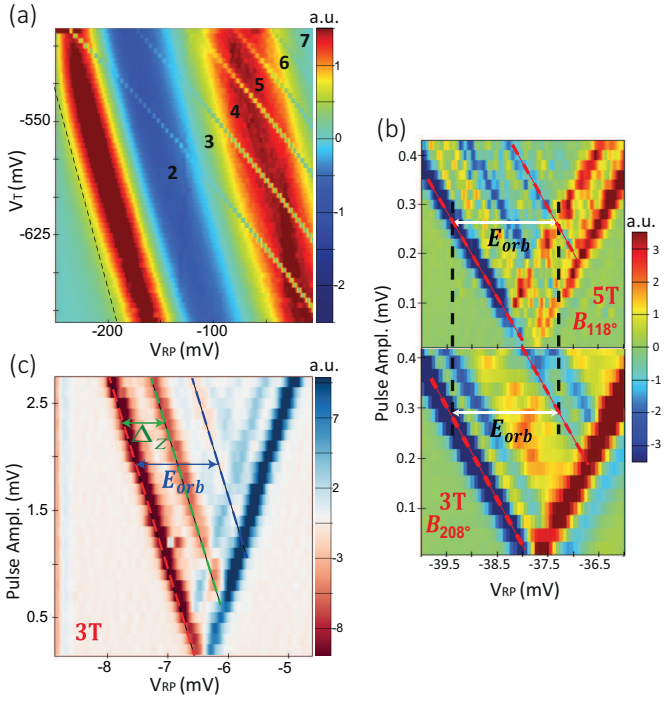

Figure 8.5: (a) Derivative of the QPC current with respect to the gate voltage on RP, as function of the gate voltages on RP and T. The wide modulations (parallel to the black dotted line) are due to resonances in the QPC transport, which affect the QPC sensitivity. The sharp lines correspond to charge transitions in the dot. Usually, the region below the last transition is inferred to have zero electrons. From pulse spectroscopy data discussed below, we find that there are still two electrons left. (b) Pulse spectroscopy data [32] for two orientations of a 3 T field, $\mathbf{B}_\phi$, 90° apart (c) Pulse spectroscopy measurement at 3 T at the gate voltage configuration used for the experiment. The green and blue dashed lines indicate the spin excited state and the first orbital excited state, respectively. The length of the blue arrow (E_{orb}) is comparable to twice of the length of the green (Δ_z) arrow.

The sample is mounted on a printed circuit board (PCB) which is attached via a coldfinger to the mixing chamber of a dilution refrigerator. The orientation of the sample with respect to the PCB is determined optically, with an estimated error of no more than ±3°. We can apply a magnetic field $\mathbf{B}_\phi$ in the 2DEG plane, at an angle ϕ with respect to the [100] crystal axis, which can be controlled via a 2D vector magnet. We tune the device to the few-electron regime [Fig. 8.5(a)] and adjust the tunnel couplings via the gate voltages. From analyzing the pulse spectroscopy data of Fig. 8.6 in detail, we conclude that the last transition seen in Fig. 8.5(a) is the transition between the two and three electron charge states.

The tunnel barrier between gate T and B is closed (tunnel rate < 1 Hz). The barrier between gate T and RS is tuned to around 5 kHz. A coax line is connected to gate RP via a homemade resistive bias tee (R = 10 MΩ, C = 47 nF, $1/RC \approx 2$ Hz) to allow fast pulsing of the dot levels while also maintaining a DC bias on RP [as indicated in Fig. 8.1(a)]. To measure the spin relaxation rate we apply a multi-stage voltage pulse to gate RP [5], us-

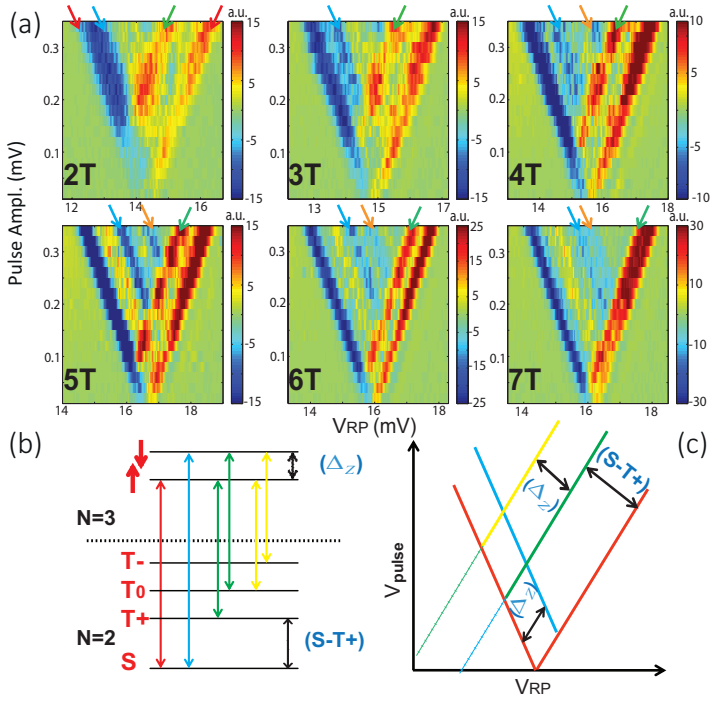

Figure 8.6: (a) Pulse spectroscopy measurements [32] for different values of $|\mathbf{B}_{118^\circ}|$ (from 2 to 7 T in 1 T steps). The red and blue arrows indicate, respectively, the position of the ↑ (ground) and ↓ (excited) states of the ground orbital state, separated by the Zeeman energy Δ_z. The green arrow denotes a two electron excited state (N=2). In particular, the distance (in mV on the x-axis) between this line and the right edge of the pulse-triangle represents the energy difference between the singlet (S) and $m = 0$ triplet (T+), which are, respectively, the ground and first excited two electron states (see panel (b)). We find that the S-T+ energy splitting gets smaller with increasing magnetic field, with the same g-factor as the (N=3) orbital ground state Zeeman splitting. For 4, 5, 6, and 7 T we can distinguish an extra light blue line in the data, indicated by the orange arrow. We attribute it to the first orbital excited state of the system, E_{orb} and we find that its distance from the left edge of the triangle is independent on $|\mathbf{B}_{118^\circ}|$. The gate voltage configuration used in this measurement is slightly different from the one used for the relaxation time measurement, giving a less elongated confining potential and a higher E_{orb} than in in Fig. 8.5(c). (b) Schematic of the energy levels involved in the energy spectrum of the 2-3 electron charge transition [1]. Arrows with the same color indicate transitions between configurations with the same energy difference, which translates in a single line in spectroscopy measurements. (c) Schematic of the typical pulse-spectroscopy picture (red lines) resulting from an application of a square gate voltage pulse with increasing amplitude (y-axis), while stepping the DC voltage on the same gate (x-axis). The case is shown for the 2-3 electron charge transition. The color of each line corresponds to the transitions shown in (b). For the pulse amplitude window we used here only the $(T+ \rightarrow \uparrow) \equiv (T0 \rightarrow \downarrow)$ transition is visible (the green line and arrows).

ing a Tektronix AWG5014. The simplest version of this pulse has three stages [blue line in Fig. 8.7(a)]. First we empty the QD by pulsing the ground state electrochemical potential above the lead Fermi level. A second pulse brings both the spin-up and spin-down levels below the lead Fermi energy, pulling one electron of unknown spin state into the QD. The last stage takes the dot to the read-out configuration, with the lead Fermi energy positioned in between the spin-up and spin-down levels. Here the electron tunnels out if and only if it is spin down. A tunnel event is reflected in the signal of the charge detector. Varying the initialization-waiting time between injection and read-out and monitoring the fraction of the time a tunnel event is seen (we typically average over 1000-5000 cycles), one can estimate the spin relaxation time, T_1, from the exponential decay of the measured spin down probability.

This three-stage pulse causes two potential artifacts when applied to the gate via the capacitor in the bias tee. First, if the pulse contains a DC component, it is blocked by the capacitor, thereby shifting the dot levels away from the desired configuration during read-out. Therefore we keep the average (DC) pulse amplitude fixed at zero, by compensating changes in the length or amplitude of the initialization-waiting stage by similar changes in the amplitude and length of the empty stage [see Fig. 8.7(a)]. Second, the high-pass filtering effect of the bias tee makes the pulse amplitude decay exponentially during every stages of the pulse, making the compensation less effective (red lines in Fig. 8.7). In order to further improve the stability of the gate voltage during read-out, we use the four-stage pulse schematically shown in Fig. 8.7(b), which introduces an extra compensation stage just after the read-out stage. This makes the alignment of the dot levels more independent from the waiting time, thereby reducing errors on the measured T_1.

A further experimental difficulty, which is most severe when applying the magnetic field along specific angles ϕ, is the coupling in of mechanical vibrations into the measurement wires, possibly by magnetic flux induced currents in ground loops. It makes the dot potential oscillate relative to the Fermi level of the reservoir at the frequency of the mechanical vibration. This hinders the spin relaxation measurement and is the reason why we lack data points in some intervals of ϕ (e.g. $50^\circ < \phi < 100^\circ$ in Fig. 8.3).

Finally, we evaluated the unintentional out-of-plane component of the applied magnetic field based on Shubnikov-de Haas oscillations, and estimate a misalignment of at most 5 degrees. We note that the out-of-plane component oscillates with the field orientation. In Fig. 8.5(b), we see no significant variation in E_{orb} extracted from pulse spectroscopy when rotating the magnetic field over 90 degrees. This means that the small perpendicular magnetic field component will not significantly affect the measured spin relaxation times through its effect on the orbital level spacing.

8.8.2. DERIVATION OF EQS. 8.2 AND 8.6

The transition rate induced by phonons between the two lowest Zeeman split states, $\Psi_\uparrow$, $\Psi_\downarrow$, is in the lowest order of the electron-phonon interactions given by Fermi's golden rule, as

$$\Gamma = \frac{2\pi}{\hbar} \sum_\alpha |D_\alpha|^2 |R_\alpha|^2 \delta(\hbar\omega_\alpha - g\mu_B B). \tag{8.9}$$

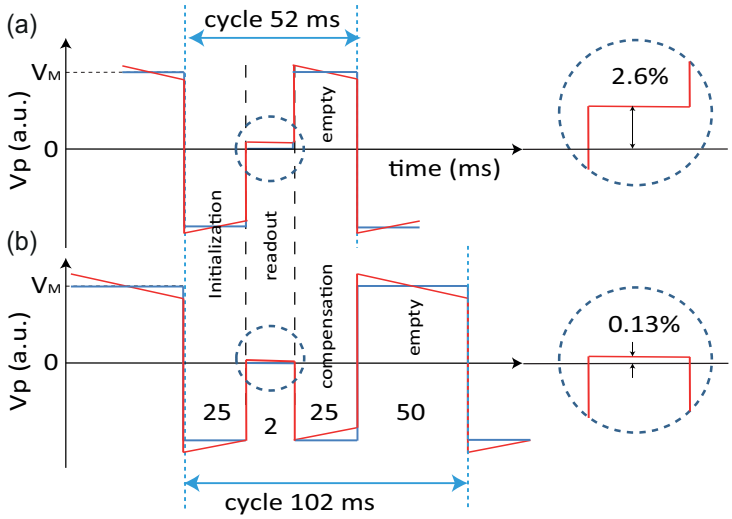

Figure 8.7: The blue curves represent schematically the gate voltage pulse produced by the waveform generator for two pulse schemes. The red curves show the signal that arrives at the sample, after being distorted in the bias tee. (a) Three-stage pulse, keeping the length of the initialization-waiting stage and empty stage the same (see text). For waiting times comparable to the RC time constant of the bias-tee, the pulse gets significantly distorted by the charging of the bias-tee capacitance (inset on the right); this affects the stability of the read-out position. The deviation from the the ideal position ($V = 0$) reaches 2.6% of the maximum pulse amplitude V_M for a 25 ms initialization-waiting time. (b) Four-stage pulse scheme used to measure $T_1 > 10$ ms. The extra compensation stage (of the same length as the waiting time) reduces appreciably the deviation of the read-out position, to about 0.13% of V_M for a 25 ms waiting time, but almost doubles the total pulse time. The voltage deviations reported here have been estimated by a simulation of the bias-tee circuit made with Micro-cap.

The sum is over acoustic phonons labeled by index α comprising phonon polarization and momentum, constrained by energy conservation requiring the phonon energy $\hbar\omega_\alpha$ to be equal to the energy splitting of the initial and final states, here the Zeeman energy $g\mu_B B$. Interested in the angular anisotropies for which an overall scale is unimportant, we do not specify the complex coefficients D_α. In the dipole approximation of the phonon displacement operator $\exp(i\mathbf{k}\cdot\mathbf{r}) \approx 1 + i\mathbf{k}\cdot\mathbf{r}$ (here $\mathbf{r}$ is the electron coordinate and $\mathbf{k}$ is the inplane phonon momentum), R is a dipole matrix element

$$R = \langle \Psi_\downarrow | \mathbf{k}\cdot\mathbf{r} | \Psi_\uparrow \rangle, \tag{8.10}$$

which is non-zero only due to the SO interactions. Treating them perturbatively, (see, e.g., Eq. (A8) in [30]) we obtain

$$R = 2 \sum_{j\neq 0,s} E_{0j}^{-1} \langle \psi_{0\uparrow} | \mu \mathbf{B}_{\text{eff}} \cdot \boldsymbol{\sigma} | \psi_{js} \rangle \langle \psi_{js} | \mathbf{k}\cdot\mathbf{r} | \psi_{0\downarrow} \rangle, \tag{8.11}$$

where the sum goes over the orbital excited states ψ_{js} offset from the ground state $j = 0$ by orbital excitation energies E_{0j} and $s = \uparrow, \downarrow$ is the spin with the quantization axis along the external magnetic field. The states ψ_{js} are those of a system without SO interactions, so that they are separable into an orbital part $|j\rangle$ and a spinor part $|\xi_s\rangle$. We denoted ψ_{0s} as the state which develops into Ψ_s appearing in Eq. (8.10) upon adiabatically turning on the SO interactions. Finally, the effective magnetic field is [31]

$$\mu \mathbf{B}_{\text{eff}} = \mu(\mathbf{n} \times \mathbf{B}) \cdot \boldsymbol{\sigma}, \tag{8.12}$$

with the SO dependent vector

$$\mathbf{n} = x\left(l_D^{-1}, -l_R^{-1}, 0\right) + y\left(l_R^{-1}, -l_D^{-1}, 0\right) = \mathbf{n}_x x + \mathbf{n}_y y, \tag{8.13}$$

where the last equality sign is a definition of $\mathbf{n}_{x,y}$, two in-plane vectors.

Before evaluating for specific cases we simplify the squared dipole element to

$$|R|^2 = 4 \sum_{jj'\neq 0} \langle 0 | \mu \mathbf{B}_{\text{eff}} | j \rangle \cdot \langle j' | \mu \mathbf{B}_{\text{eff}} | 0 \rangle \frac{\langle 0 | \mathbf{k}\cdot\mathbf{r} | j \rangle \langle j' | \mathbf{k}\cdot\mathbf{r} | 0 \rangle}{E_j E_{j'}}. \tag{8.14}$$

In going from Eq. (8.11) to Eq. (8.14) we used that the effective magnetic field is perpendicular to the external magnetic field, and that the phonon dipole operator is diagonal in the spin space.

Consider now the case of a circularly symmetric dot. The orbital states can be labeled by the orbital momentum index l. Though we allow for a possible out-of-plane magnetic field, breaking the time reversal symmetry, we assume its orbital effects are not so strong as to cause state crossings compared to the zero magnetic field case case [see also the data of Fig. 8.5(b)]. This restriction is not essential for the results and we adopt it only to simplify the notation. Under this assumption, the orbital ground state is fully symmetric, $l = 0$. The lowest two excited states are $l = \pm 1$, and are degenerate if the out-of-plane magnetic field is zero and energy split otherwise. We now approximate the sum over the whole spectrum by these two lowest excited states in Eq. (8.14). The circular symmetry

of the Hamiltonian, and consecutively its eigenstates, allows us to derive

$$\langle 0|x|+1\rangle\langle +1|y|0\rangle = -\langle 0|y|+1\rangle\langle +1|x|0\rangle, \tag{8.15a}$$
$$\langle 0|x|+1\rangle\langle -1|y|0\rangle = -\langle 0|x|-1\rangle\langle +1|y|0\rangle, \tag{8.15b}$$
$$\langle 0|x|+1\rangle\langle -1|x|0\rangle = -\langle 0|x|-1\rangle\langle +1|x|0\rangle, \tag{8.15c}$$

which follow upon inserting the identity in the form of $R_{\pi/4}R_{-\pi/4}$ into Eq (8.15a) and I_yI_y into Eqs. (8.15b) and (8.15c), with the operator of an in-plane rotation $R_\alpha|l\rangle = \exp(i\alpha l)$, and the inversion along the y axis $I_y|l\rangle = |-l\rangle$, where we adopted a phase convention $\langle \mathbf{r}|+1\rangle = \langle \mathbf{r}|-1\rangle^\dagger$. With the auxiliary results in Eq. (8.15), we see that cross terms, such as $j \neq j'$ and $\mathbf{B}\times\mathbf{n}_{x'}\cdot\mathbf{B}\times\mathbf{n}_{y'}$, cancel and Eq. (8.14), restricted to the lowest excited subspace contributions, takes the form

$$|R|^2 = \left(|\mu\mathbf{B}\times\mathbf{n}_x|^2 + |\mu\mathbf{B}\times\mathbf{n}_y|^2\right)\times \sum_{j=\pm1} 4E_j^{-2}\langle 0|x|j\rangle|^2|\langle 0|\mathbf{k}\cdot\mathbf{r}|j\rangle|^2, \tag{8.16}$$

which leads to Eq. 8.2.

The derivation for the case of an anisotropic dot is even simpler. Indeed, for such a dot there is a single lowest orbital excited state, $j = 1$, dominating the sum in Eq. (8.14). The dipole matrix element of this exited state with the ground state is an in-plane vector $\mathbf{d} = \langle 0|\mathbf{r}|1\rangle$, which by its definition fulfills $\langle 0|\mathbf{r}\cdot(\hat{z}\times\mathbf{d})|1\rangle = 0$. Defining the rotated coordinated system with axes x' along $\mathbf{d}$, and y' perpendicular to it (say along $\hat{z}\times\mathbf{d}$), we immediately get

$$|R|^2 = |\mu\mathbf{B}\times\mathbf{n}_{x'}|^2 \times 4E_1^{-2}|\mathbf{d}|^2|\mathbf{d}\cdot\mathbf{k}|^2, \tag{8.17}$$

which gives Eq. 8.6.

8.8.3. DIVERGENCES IN FITTING PARAMETER κl_{SO}^{-2}

The goal of this paragraph is to provide intuition for the presence and the shape of the two divergences, for $\delta = 45°, 135°$, in the fitting parameter κl_{SO}^{-2} reported in Fig. 8.4(d) in the main text. Fitting the data of Fig. 8.3(b) in the main text to Eq. 8.7 we get $(b, \phi_{min}, \xi^*) = (139.2 \pm 3.5\ s^{-1},\ 35.1° \pm 1.1°,\ 17.4° \pm 1.5°)$. A plot of $\phi_{min}(\delta,\vartheta)$ (from Eq. 8.8 in the main text) for $\delta, \vartheta \in [0°, 180°]$ is presented in Fig. 8.8(a), together with a plot of the angular part of the pre-factor b, $(1 + \sin 2\delta \sin 2\vartheta) = bl_{SO}^2/\kappa$, in Fig. 8.8(b). The red curve on top of those two plots represents the condition $\phi_{min}(\delta,\vartheta) = 35.1°$, the value for the optimal angle obtained from Fig. 8.3 in the main text. We notice that $(1 + \sin 2\delta \sin 2\vartheta) = 0$ for the coordinates $(\delta,\vartheta) = (45°, 135°)$ and $(135°, 45°)$, and that all the contour lines in Fig. 8.8(a) cross these points. In order to keep b fixed to $139.2 \pm 3.5\ s^{-1}$ (the value from the fit), the quantity κl_{SO}^{-2} [plotted as a function of δ in Fig. 8.4(d) in the main text] should diverge around those two points of the (δ,ϑ) plane. Furthermore, how fast κl_{SO}^{-2} diverges is determined by the derivative with respect to δ along the red curve in Fig. 8.8(b) around the singularity points. This explains why in Fig. 8.4(d) the singularity around $\delta = 135°$ looks much sharper than the one around $\delta = 45°$.

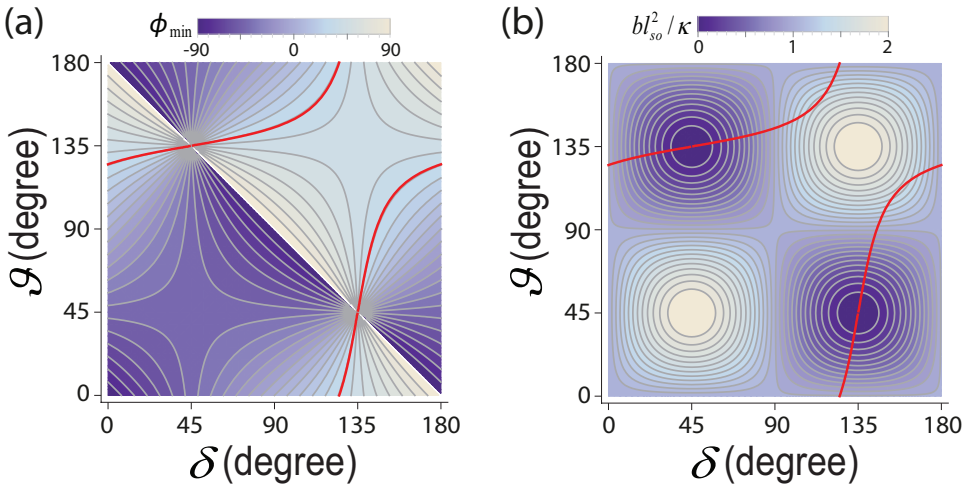

Figure 8.8: Plots of (a) $\phi_{min}(\vartheta,\delta)$ [Eq. 8.8] and (b) $(1+\sin 2\vartheta \sin 2\delta)$ [in Eq. 8.7] in the (ϑ,δ) plane. The grey contour lines show $\phi_{min}=\chi$, with $-90^\circ \le \chi \le +90^\circ$ in 25 steps. The red curve represents the relation $\phi_{min} = 35.1^\circ$ obtained from the fit to Eq. 8.7. We notice that all the contour lines in panel (a) cross in the points $(45^\circ, 135^\circ)$ and $(135^\circ, 45^\circ)$ which are zeros of the angular part of the pre-factor bl_{SO}^2/κ (panel (b)).

REFERENCES

[1] R. Hanson, L. P. Kouwenhoven, J. R. Petta, S. Tarucha, and L. M. K. Vandersypen, Rev. Mod. Phys. **79**, 1217 (2007).

[2] K. C. Nowack, F. H. L. Koppens, Y. V. Nazarov, and L. M. K. Vandersypen, Science **318**, 1430 (2007).

[3] S. Nadj-Perge, S. M. Frolov, E. P. A. M. Bakkers, and L. P. Kouwenhoven, Nature **468**, 1084 (2010).

[4] T. Fujisawa, D. G. Austing, Y. Tokura, Y. Hirayama, and S. Tarucha, Nature **419**, 278 (2002).

[5] J. M. Elzerman, R. Hanson, L. H. Willems van Beveren, B. Witkamp, L. M. K. Vandersypen, L. P. Kouwenhoven, Nature **430**, 431 (2004).

[6] M. Kroutvar, Y. Ducommun, D. Heiss, M. Bichler, D. Schuh, G. Abstreiter, and J. J. Finley, Nature **432**, 81 (2004).

[7] A. C. Johnson, J. R. Petta, J. M. Taylor, A. Yacoby, M. D. Lukin, C. M. Marcus, M. P. Hanson, A. C. Gossard, Nature **435**, 925 (2005).

[8] S. Amasha, K. MacLean, I. P. Radu, D. M. Zumbuhl, M. A. Kastner, M. P. Hanson, A. C. Gossard, arXiv:0607110 [cond-mat].

[9] T. Meunier, I. T. Vink, L. H. Willems van Beveren, K. J. Tielrooij, R. Hanson, F. H. L. Koppens, H. P. Tranitz, W. Wegscheider, L. P. Kouwenhoven, and L. M. K. Vandersypen, Phys. Rev. Lett. **98**, 126601 (2007).

[10] S. Amasha, K. MacLean, I. P. Radu, D. M. Zumbühl, M. A. Kastner, M. P. Hanson, and A. C. Gossard, Phys. Rev. Lett. **100**, 046803 (2008).

[11] A. V. Khaetskii and Y. V. Nazarov, Phys. Rev. B **61**, 12639 (2000).

[12] A. V. Khaetskii and Y. V. Nazarov, Phys. Rev. B **64**, 125316 (2001).

[13] V. N. Golovach, A. Khaetskii, and D. Loss, Phys. Rev. Lett. **93**, 016601 (2004).

[14] P. Stano and J. Fabian, Phys. Rev. B **74**, 045320 (2006).

[15] P. Stano and J. Fabian, Phys. Rev. Lett. **96**, 186602 (2006).

[16] G. Dresselhaus, Phys. Rev. **100**, 580 (1955).

[17] Y. A. Bychkov and E. I. Rashba, J. Phys. C **17**, 6039 (1984).

[18] V. Srinivasa, K. C. Nowack, M. Shafiei, L. M. K. Vandersypen, and J. M. Taylor, Phys. Rev. Lett. **110**, 196803 (2013).

[19] V. N. Golovach, M. Borhani, and D. Loss, Phys. Rev. B **74**, 165319 (2006).

[20] J. M. Elzerman, R. Hanson, L. H. Willems van Beveren, L. M. K. Vandersypen, and L. P. Kouwenhoven, Appl. Phys. Lett. **84**, 4617 (2004).

[21] L. S. Levitov and E. I. Rashba, Phys. Rev. B **67**, 115324 (2003).

[22] S. Takahashi, R. S. Deacon, K. Yoshida, A. Oiwa, K. Shibata, K. Hirakawa, Y. Tokura, and S. Tarucha, Phys. Rev. Lett. **104**, 246801 (2010).

[23] Y. Kanai, R. S. Deacon, S. Takahashi, A. Oiwa, K. Yoshida, K. Shibata, K. Hirakawa, Y. Tokura, and S. Tarucha, Nature Nanotech. **6**, 511 (2011).

[24] M. P. Nowak, B. Szafran, F. M. Peeters, B. Partoens, and W. J. Pasek, Phys. Rev. B **83**, 245324 (2011).

[25] E. Y. Sherman and D. J. Lockwood, Phys. Rev. B **72**, 125340 (2005).

[26] W. W. Yu, S. M Frolov, S. Luescher, J. A. Folk, and W. Wegscheider, arXiv:1009.5702.

[27] K. C. Nowack, M. Shafiei, M. Laforest, G. E. D. K. Prawiroatmodjo, L. R. Schreiber, C. Reichl, W. Wegscheider, and L. M. K. Vandersypen, Science **333**, 1269 (2011).

[28] V. N. Golovach, A. Khaetskii, and D. Loss, Phys. Rev. B **77**, 045328 (2008).

[29] V. Kornich, C. Kloeffel, and D. Loss, Phys. Rev. B **89**, 085410 (2014).

[30] M. Raith, P. Stano, and J. Fabian, Phys. Rev. B **86**, 205321 (2012).

[31] F. Baruffa, P. Stano, and J. Fabian, Phys. Rev. Lett. **104**, 126401 (2010).

[32] J. M. Elzerman, R. Hanson, L. H. Willems van Beveren, L. M. K. Vandersypen, and L. P. Kouwenhoven, Appl. Phys. Lett. **84**, 4617 (2004).

9

High Kinetic Inductance Superconducting Nanowire Resonators for Circuit QED in a Magnetic Field

We present superconducting microwave-frequency resonators based on NbTiN nanowires. The small cross section of the nanowires minimizes vortex generation, making the resonators resilient to magnetic fields. Measured intrinsic quality factors exceed 2×10^5 in a 6 T in-plane magnetic field, and 3×10^4 in a 350 mT perpendicular magnetic field. Due to their high characteristic impedance, these resonators are expected to develop zero-point voltage fluctuations one order of magnitude larger than in standard coplanar waveguide resonators. These properties make the nanowire resonators well suited for circuit QED experiments needing strong coupling to quantum systems with small electric dipole moments and requiring a magnetic field, such as electrons in single and double quantum dots.

The work in this chapter has been submitted for publication as: N. Samkharadze, A. Bruno, P. Scarlino, G. Zheng, D. P. DiVincenzo, L. DiCarlo, and L. M. K. Vandersypen, High Kinetic Inductance Superconducting Nanowire Resonators for Circuit QED in a Magnetic Field.

9.1. INTRODUCTION

Superconducting microwave-frequency resonators are widely considered essential building blocks of future quantum processors, providing a means for qubit readout and long-range interconnect in a circuit quantum electrodynamics (cQED) architecture [1]. They also offer a promising interface between different types of quantum systems [2]. To reap the full benefits of cQED architectures, it is crucial to reach the strong coupling regime, wherein quantum state transfer between the qubit and the resonator is possible on a time scale shorter than the coherence time of the combined system.

Several proposals have been put forward for implementing cQED using electron spin qubits in semiconducting quantum dots [3–7]. Electron spins offer very long coherence times, in some case of order a second, [8–10] but convincing mechanisms for scaling in 2D are still lacking. Therefore, exploring cQED as a means for scaling is of high importance. Pioneering experiments have demonstrated coupling of superconducting cavity modes with spin and orbital degrees of freedom of the electrons [11–14].

Achieving strong coupling in such hybrid systems has proved challenging due to the weak interaction between the zero-point fluctuations (ZPF) of conventional superconducting resonators and the quantum dot electrons. Traditionally, coplanar waveguide (CPW) resonators with characteristic impedance $Z_r \sim 50\ \Omega$ have been used as the staple cavity in cQED. However, by increasing (decreasing) Z_r, it is possible to enhance the ZPF of voltage (current), thus optimizing for electric (magnetic) dipole coupling to qubits.

Another challenge in incorporating superconducting resonators in spin- or Majorana-based systems is the typically poor performance of superconducting resonators at the magnetic fields required for the operation of such systems. Intrinsic quality factors $Q_i > 10^6$ have been measured for the highest performance resonators in magnetically-shielded cQED setups [15, 16]. However, strong magnetic fields induce vortices in the superconducting film, which move under the influence of microwave currents in the resonator, causing energy dissipation. A few methods have been employed to minimize vortex-induced dissipation in superconducting devices. These methods include creating artificial pinning sites and dams for the vortices [17–20], and steering the vortices away from the areas carrying the highest currents [17, 21–23]. To date, the most effective magnetic field resilience has been achieved in superconducting fractal resonators, with $Q_i \approx 10^5$ in parallel magnetic field $B_{||} \approx 400$ mT [22, 23], and more recently, in YBCO CPW resonators with $Q_i \approx 2 \times 10^4$ at $B_{||} = 7$ T [24].

In this Chapter, we present microwave-frequency resonators based on NbTiN nanowires, displaying magnetic field resilience and promising stronger electrical coupling. We take advantage of the high kinetic inductance of the strongly disordered superconducting nanowires to increase $Z_r = \sqrt{\mathscr{L}/\mathscr{C}}$ and thereby also the voltage ZPF, $V_{\mathrm{RMS}}^{\mathrm{ZPF}} \propto f_r \sqrt{Z_r}$. Here, f_r is the resonance frequency and $\mathscr{L}$ ($\mathscr{C}$) is the inductance (capacitance) per unit length of the nanowire. We estimate $Z_r \approx 4$ kΩ, nearly two orders of magnitude higher than that of CPW resonators used in typical cQED devices. The corresponding $V_{\mathrm{RMS}}^{\mathrm{ZPF}} \sim 20\ \mu$V (see section 9.5) makes these resonators well suited for coupling to systems with small electric dipole moments, such as electrons in single or double quantum dots. Moreover, the small nanowire cross section strongly suppresses vortex generation in a magnetic field, resulting in $Q_i > 2 \times 10^5$ at up to $B_{||} = 6$ T. We also investigate the evolution of these resonators with perpendicular magnetic field $B_\perp$, finding a clear de-

pendence of the magnetic field resilience of Q_i on the nanowire width w. The narrowest nanowires ($w \approx 100$ nm) achieve $Q_i > 3 \times 10^4$ at $B_\perp \approx 350$ mT.

9.2. METHODS

The resonators consist of NbTiN nanowire loops interrupted by a small gap (Fig. 9.1) and coupled to a common CPW feedline. To minimize $\mathscr{C}$, the ground planes are detracted by ~ 100 μm from the closest segment of the nanowire. Figure 9.1(d) shows the simulated feedline transmission for the device shown in Fig. 9.1a). The ratio between the resonance frequencies of the two lowest modes extracted from the simulation is 2.01, demonstrating that the nanowire resonators are essentially distributed resonators with a negligible direct capacitance between the nanowire ends. In the configuration of Fig. 9.1(a), the coupling between the feedline and the fundamental (half-wave) mode of the resonator is inductive, which for our high impedance resonators is extremely weak. Therefore, we here focus on the full-wave mode, leaving the discussion of the fundamental to the supplementary material section 9.5.

Device fabrication begins with the sputtering of a NbTiN film (thickness $t \sim 8$ nm) on a high-resistivity Si ⟨100⟩ substrate [16]. A CPW feedline and several (4 or 5) nanowire resonators are next defined in a single electron-beam lithography step, followed by reactive ion etching in a SF_6/He plasma. Completed devices are cooled in a ^{3}He refrigerator with 280 mK base temperature and 70 dB cold attenuation between room temperature and the feedline input. Each resonator is characterized by measuring the complex-valued feedline transmission near its resonance (Fig. 9.2). Fitting of the model from ref. [25] to the data allows extracting the resonance frequency and the coupling and intrinsic quality factors [16, 25].

The highly disordered nature of NbTiN and the extremely small cross-sectional area of the nanowires make the kinetic inductance the dominant contribution to the total inductance of the resonators. From the measured critical temperature $T_c \approx 9.3$ K and room-temperature resistivity $\rho = 200$ $\mu\Omega$cm of the film, we estimate a sheet kinetic inductance $L_S \approx 35$ pH/□ [26], close to the value 38 pH/□ needed in a Sonnet simulation to match the resonance in Fig. 9.1(d) to the measurements. For a resonator of length $l = 2.9$ mm and $w = 100$ nm (2.77 GHz full-wave mode), this corresponds to a total inline inductance $\mathscr{L} l \sim 1$ μH.

9.3. RESULTS AND DISCUSSION

Figure 9.2(c) shows Q_i of five resonators ($w = 100$ nm) as a function of input power, P_{in}. We find $Q_i > 10^5$ at $P_{in} \approx -130$ dBm corresponding to an average occupation of the resonator by $\langle n_{ph} \rangle \approx 10$ photons. The observed increase of Q_i with P_{in} indicates dominant loss by coupling to spurious two-level systems (TLS) which saturate at high power [16, 27, 28]. This conclusion is further supported by the temperature dependence of Q_i at $P_{in} \approx -110$ dBm, corresponding to $\langle n_{ph} \rangle \approx 1000$ [Figure 9.2(b)]. Thermally excited quasiparticles dominate loss only above 1 K $\sim T_c/10$, consistent with previous studies of quasiparticle-induced dissipation in highly disordered thin film resonators [29].

The resilience of the nanowire resonators to magnetic field is seen in Figure 9.3, which shows the typical dependence of intrinsic quality factors on the applied $B_{||}$. Most

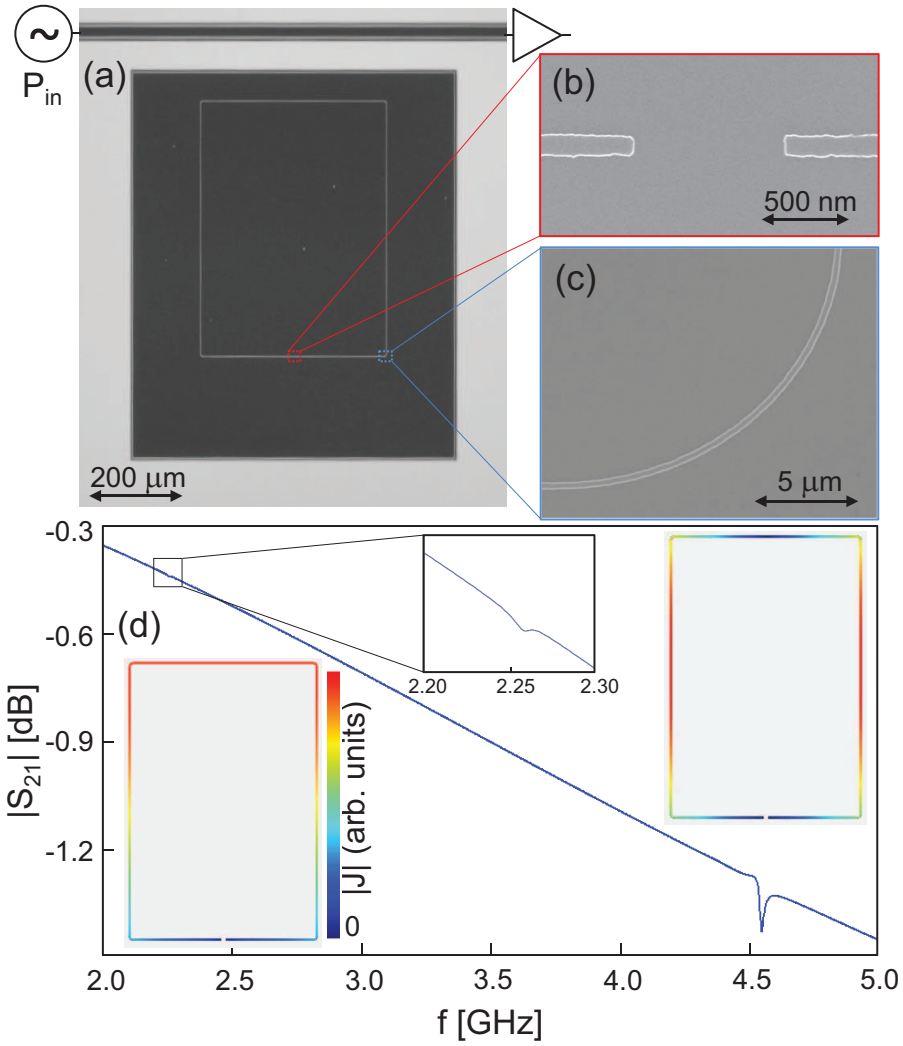

Figure 9.1: Resonator design. (a) Dark field optical image of a typical nanowire resonator. (b,c) Scanning electron microscope zoom-ins of the gap (b) and the bend (c) of a typical resonator. (d) Simulated feedline transmission for the device in (a). The insets show (absolute) current distributions along the nanowire for the fundamental and second resonance modes, as well as a zoom-in of the feedline transmission near the fundamental resonance.

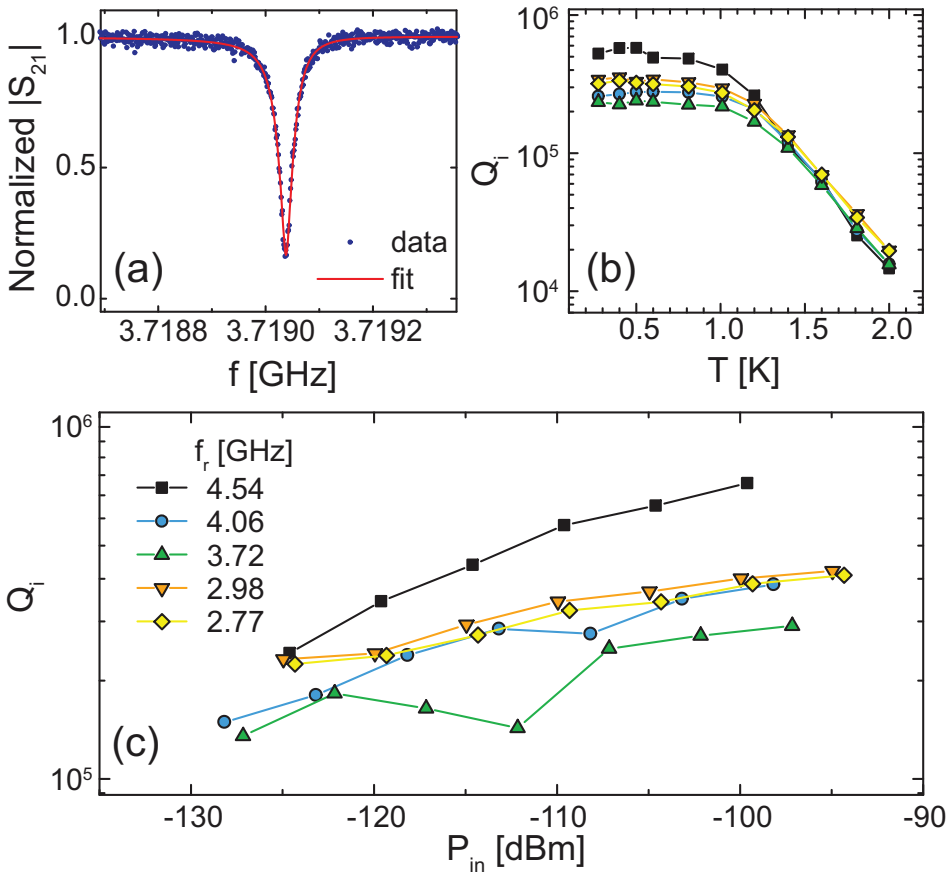

Figure 9.2: Power and temperature dependence of intrinsic quality factors of five nanowire resonators. (a) Normalized absolute transmission around a typical resonance. The curve is constructed from the best fit to the complex-valued feedline transmission data [16, 25]. (b) Temperature dependence of intrinsic quality factors measured at a fixed input power $P_{\text{in}} \approx -110$ dBm. The symbols correspond to the legend in (c). Two distinct regimes are observed for $T < 1$ K and $T > 1$ K, in which dominant loss is expected from TLS and quasiparticle dissipation, respectively. (c) Power dependence of intrinsic quality factors measured at 280 mK. The positive slope is consistent with TLS-dominated loss.

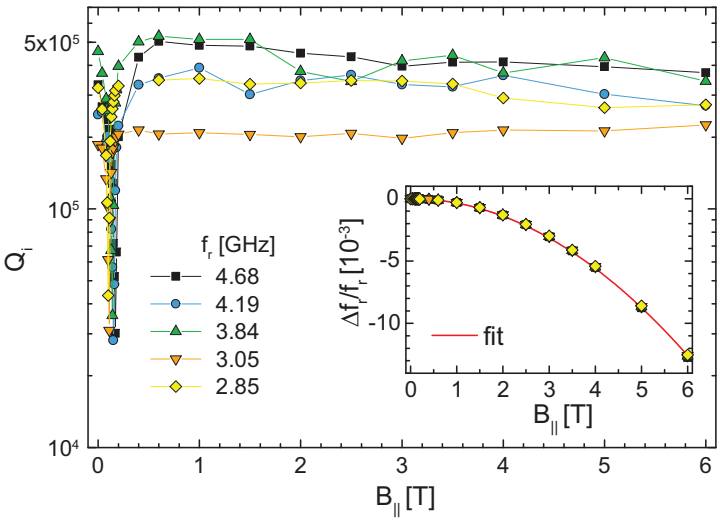

Figure 9.3: Evolution of nanowire resonator characteristics with in-plane magnetic field $B_{||}$ ($w = 100$ nm, $T = 280$ mK, $P_{in} \approx -110$ dBm). The intrinsic quality factor Q_i remains unaffected in the range 400 mT $\lesssim B_{||} \leq 6$ T. The maximum $B_{||}$ is limited by our experimental setup. We observe a sharp dip in Q_i at low $B_{||}$, which we link to loading of the resonator by spurious magnetic impurities with a Landé g-factor $g \approx 2$ (see section 9.5). (Inset) All fractional frequency shifts fit to the same simple quadratic curve.

strikingly, for $B_{||}$ between $\sim$ 400 mT and 6 T, Q_i is consistently above 10^5 without sign of degradation. This field is at least one order of magnitude higher than the highest at which such Q_i has been reported in earlier studies of planar superconducting resonators [22, 23]. Moreover, we do not observe hysteretic behavior or abrupt jumps in f_r with increasing $B_{||}$. These effects plague standard CPW resonators and are usually attributed to unstable magnetic flux vortices in the superconducting film [19, 22, 30, 31]. These findings suggest that vortex nucleation does not take place in the nanowires. Vortices may still be created in the ground plane. However, due to the large separation between the nanowires and the ground planes, we expect only minimal current densities to be induced in the ground plane, thus weakly contributing to dissipation. Finally, we observe a sharp dip in Q_i around 100 mT. We link this dissipative loading to magnetic impurities with Landé g-factor $g \approx 2$ (see section 9.5). These magnetic defects likely lie in the Si substrate or at one of the interfaces.

Further insight into the effect of magnetic field on the resonators is gained by orienting the field perpendicular to the device plane. Figure 9.4(a) shows the dependence of Q_i in seven nanowire resonators (widths ranging from $w = 100$ to 700 nm) on $B_\perp$. The magnetic field resilience depends strongly on the nanowire width, and the narrowest resonators show superior performance. We observe $Q_i > 3 \times 10^4$ for the narrowest resonator ($w = 100$ nm) for $B_\perp \leq 350$ mT [Fig. 9.4(a)]. This field range is one order of magnitude higher than the highest at which $Q_i \approx 10^4$ has been previously reported [22].

Turning our attention to the shift of resonance frequency induced by the magnetic field, we observe for both field orientations a quadratic shift of resonance frequency

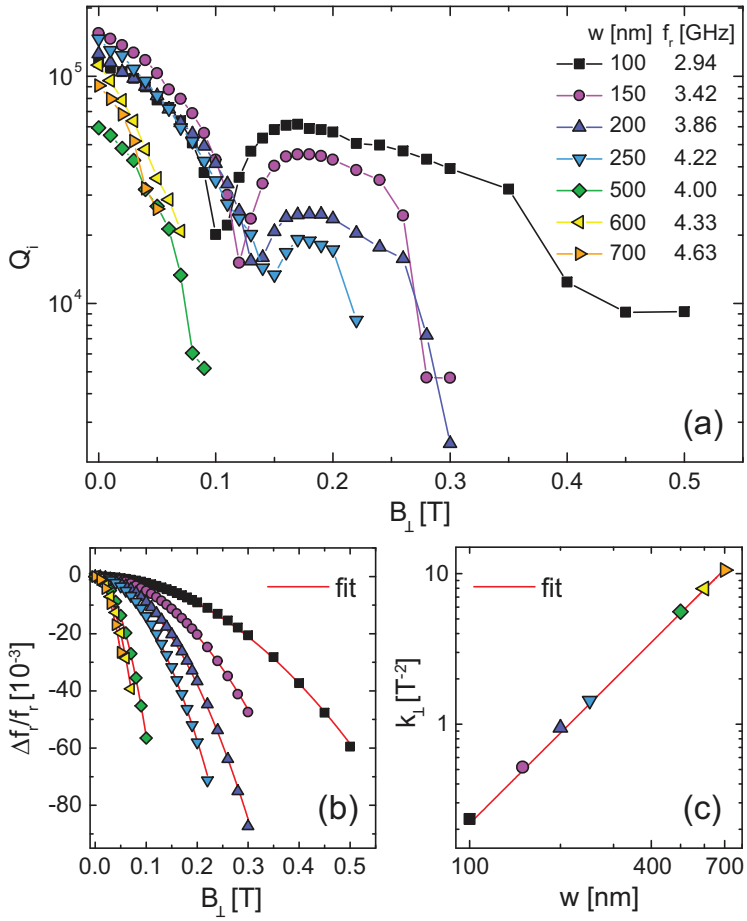

Figure 9.4: Evolution of nanowire resonator characteristics with perpendicular magnetic field, $B_\perp$. (a) Q_i as a function of $B_\perp$ for various nanowire widths w. The dips in Q_i at low field suggest coupling to magnetic impurities, similarly to the case for $B_{||}$ in Fig. 9.2. The narrowest resonator retains $Q_i > 3 \times 10^4$ up to $B_\perp$ = 350 mT. (b) Fractional shift of the resonance frequencies with $B_\perp$. Same symbols as in (a). The red curves are best fits of $\Delta f_r / f_r = -k_\perp(w) B_\perp^2$ to the data. (c) Best-fit coefficient $k_\perp$ versus w and best quadratic fit.

with applied field [Fig. 9.3 inset and Fig. 9.4(b)]. Fitting the fractional shifts with the expression $\Delta f_r/f_r = -k_{||(\perp)}B^2_{||(\perp)}$, we extract the coefficients $k_{||}$ and a width-dependent $k_\perp(w)$ [32] (see also 9.5). These coefficients reflect the increase in kinetic inductance of the superconducting nanowire due to the Cooper-pair breaking effect of the external magnetic field, and are related to the thermodynamic critical field of the superconductor: $k \propto H_C^{-2}$ [32, 33]. The penetration depth in the films $\Lambda = 2\lambda^2/t \approx 50\ \mu$m, where λ is the London penetration depth, is much greater than w. Therefore, for $B_\perp$, a Meissner state cannot be induced in the resonators and only a small fraction of the applied field is expelled. In this case, the thermodynamic critical field is modified as $H_C \propto w^{-1}$ [34], which leads to $k_\perp(w) \propto w^2$ [Fig. 9.4(c)]. Furthermore, extending this geometrical scaling to the case of a parallel field yields an effective thickness of the superconductor $t_{\text{eff}} \approx 3.5$ nm. The reduced effective thickness of the film in the context of magnetic field expulsion is likely a combined effect of surface oxidation and the suppression of shielding currents within a coherence length from the edge.

9.4. CONCLUSIONS

In summary, microwave resonators based on NbTiN nanowires with extremely small cross section are highly insensitive to parallel magnetic field, with Q_i remaining unaffected up to $B_{||} = 6$ T. Because of the high kinetic inductance of the nanowires, the resonators are expected to produce an order of magnitude higher vacuum voltage fluctuations compared to standard CPW resonators. Next experiments will focus on achieving strong coupling between these nanowire resonators and spin qubits in gate-defined quantum dots, which have small electric dipole moments and require a magnetic field.

9.5. SUPPLEMENTARY INFORMATION

This section provides calculations and additional data sets supporting the claims made in the main text. First, we show the data on the fundamental mode of the nanowire resonator, and derive the magnitude of zero-point voltage fluctuations on the ends of the resonator in the fundamental mode. Next, we provide additional data showing the coupling of the resonators to the magnetic impurities, and the performance of resonators with different widths in parallel magnetic field. Finally, we present the reasoning used to explain the scaling of frequency shifts with the applied perpendicular magnetic field and with the nanowire width.

9.5.1. STUDY OF THE FUNDAMENTAL MODE

For the fundamental mode of the nanowire resonator, the voltages at the two ends of the nanowire oscillate out of phase. In order to increase the coupling of the fundamental mode to the feedline, we rotate the resonator by 90° to enhance the capacitive coupling component [Fig. 9.5(a-c)]. Figure 9.5(d) shows the dependence of the fundamental frequencies of five nanowire resonators ($w = 100$ nm) on the inverse of their total length, l. The linear dependence of the resonance frequencies on $1/l$ is consistent with the nanowire resonators being distributed half-wave resonators with negligible direct capacitance between the nanowire ends. To further test this hypothesis, we fabricated two of the five resonators in an "open" geometry [Fig. 9.5(c), crosses in Fig. 9.5(d)] with

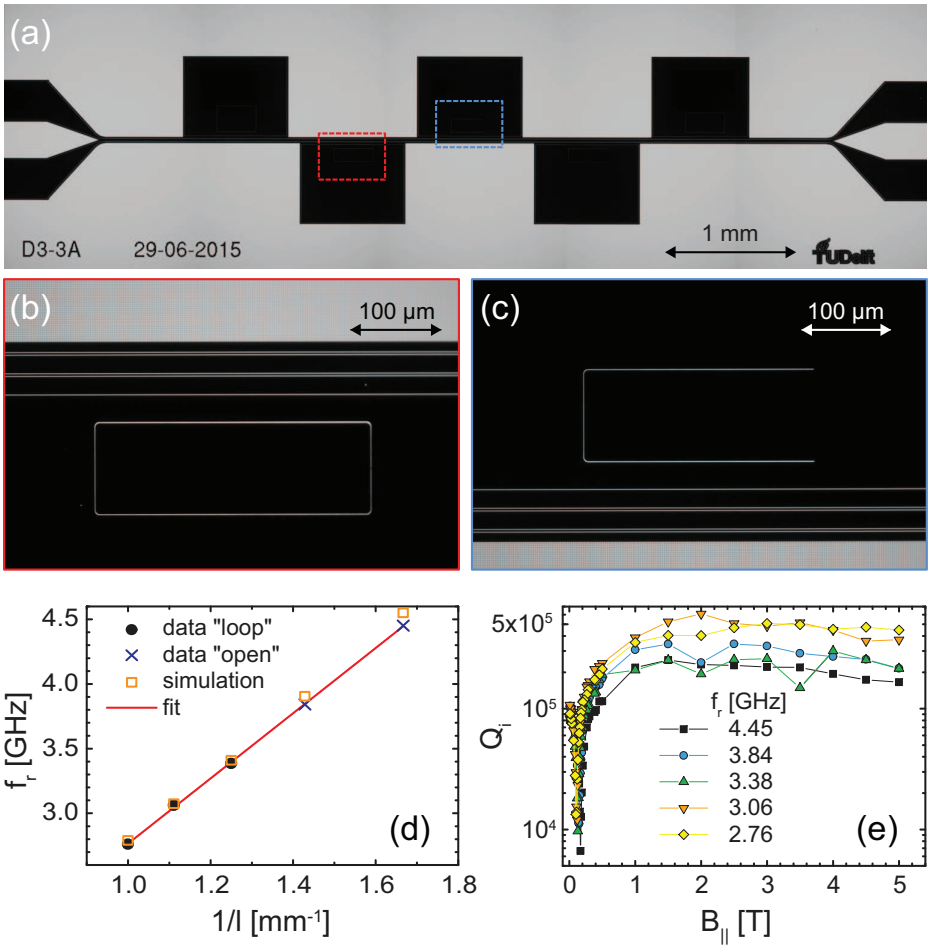

Figure 9.5: (a) Dark field micrograph of a typical device with 5 nanowire resonators. (b, c) Expanded regions from (a) showing two nanowire resonators with "loop" (b) and "open" (c) geometries, respectively. Unlike the resonators shown in the main text, the fundamental modes of these resonators couple mainly capacitively to the feedline. (d) Linear dependence of the fundamental frequency of nanowire resonators (w = 100 nm) on the inverse of their length, l. Frequencies are independent of how the nanowire winds. (e) Evolution of the intrinsic quality factor of the fundamental modes with $B_{||}$.

the ends facing outwards. We find the resonance frequencies to be independent of the nanowire winding.

The NbTiN film used in the fabrication of the new sample, was deposited a few months after the film used in the main text. Based on Sonnet simulations of the resonance frequencies [as in Fig. 9.5(d)], we estimate $L_S \approx 75$ pH/□ for the new film. This value is a factor of 2 higher than that of the film used in the main text, suggesting higher degree of disorder.

Figure 9.5(e) shows the performance of these resonators as a function of parallel

magnetic field at $P_{\text{in}} \approx -110$ dBm. At $B_{||} = 0$, the intrinsic quality factors are somewhat lower than those shown in Figs. 9.2 and 9.3. However, as the magnetic field is applied, the quality factors are enhanced and by $B_{||} \sim 2$ T become comparable to those reported in the main text.

9.5.2. ZERO-POINT VOLTAGE FLUCTUATIONS AT THE ENDS OF THE NANOWIRE RESONATOR

Figure 9.5 demonstrates that the nanowire resonator acts as a distributed half-wavelength resonator. Thus, in the lowest mode, current distribution on the resonator can be expressed as

$$I(x,t) = I_0 \sin\left(\frac{x}{l}\pi\right)\sin(\omega t), \tag{9.1}$$

where l is the length of the wire. The voltage difference over a small wire segment of length dx a distance x from the end is given by

$$dV_x = \mathscr{L}\, dx \frac{\partial I(x,t)}{\partial t}, \tag{9.2}$$

where $\mathscr{L}$ is inductance per unit length. Plugging in the expression for $I(x,t)$ from Eq. 9.1 into Eq. 9.2 gives

$$dV_x = \mathscr{L}\, dx I_0 \sin\left(\frac{x}{l}\pi\right)\omega\cos(\omega t). \tag{9.3}$$

Integrating the voltage from Eq. 9.3 over the length of the wire, we arrive at the expression for the voltage difference between the two ends of the resonator:

$$\begin{aligned}\Delta V &= \mathscr{L} I_0 \omega\cos(\omega t)\int_0^l \sin\left(\frac{x}{l}\pi\right) dx \\ &= \mathscr{L} I_0 \omega\cos(\omega t)\frac{l}{\pi}\int_0^\pi \sin\left(\frac{x}{l}\pi\right) d\left(\frac{x}{l}\pi\right) \\ &= \mathscr{L} I_0 \omega\cos(\omega t)\frac{2l}{\pi}.\end{aligned} \tag{9.4}$$

Next, we estimate the amplitude of the ZPF current I_0. The average energy stored in the inductance equals half of the zero-point energy:

$$\begin{aligned}\frac{1}{4}\hbar\omega &= 1/2\frac{1}{T}\int_0^T\int_0^l \mathscr{L} I^2\, dx\, dt \\ &= 1/2\frac{I_0^2}{T}\mathscr{L}\int_0^T \sin^2(\omega t)\, dt \int_0^l \sin^2\left(\frac{x}{l}\pi\right) = 1/8 I_0^2 \mathscr{L} l.\end{aligned}$$

Therefore,

$$I_0 = \sqrt{\frac{2\hbar\omega}{\mathscr{L} l}}. \tag{9.5}$$

Inserting the expression for I_0 from Eq. 9.5 into Eq. 9.4, we get the final expression for the voltage ZPF between two ends of the resonator:

$$\Delta V = \frac{2L}{\pi}\sqrt{\frac{2\hbar\omega}{L}}\omega\cos(\omega t).$$

Here $L = \mathscr{L} l$ is the total inductance of the resonator.

For the 4.45 GHz resonator in Fig. 9.5: $L_S = 75$ pH/□, $l = 600$ μm, and $w = 100$ nm. From these values we calculate $L \approx 450$ nH, and $\Delta V_{\mathrm{RMS}} \approx 20$ μV.

9.5.3. COUPLING TO MAGNETIC IMPURITIES

Figures 9.3 and 9.4 show sharp dips in the quality factors of the resonators around $B_{||,\perp} = 100\,\mathrm{mT}$. Upon closer inspection, it is evident that the magnetic field values, at which these dips occur, scale with the frequency of the resonators [Fig. 9.6(a,c)]. This suggests that the resonators couple with magnetic impurities in the silicon substrate or at one of the interfaces. Moreover, magnetic field dependence of the frequency shifts of the resonators shows an incipient avoided crossing [Fig. 9.6(b)]. Fitting the frequency dependence of the magnetic field positions of the quality factor minima with the condition for spin resonance $hf_r = g\mu_B B$, we extract the value for Landé g-factor: $g = 2.00 \pm 0.02$ [Fig. 9.6(c)].

9.5.4. RESONATOR WIDTH DEPENDENCE OF THE PERFORMANCE IN PARALLEL MAGNETIC FIELD

Figure 9.7 shows the $B_{||}$ evolution of Q_i and f_r for the four resonators from Fig. 9.4 with narrowest nanowires. The fractional frequency shifts for all resonators collapse onto a single curve, demonstrating that the contribution from any out-of plane component due to field misalignment is negligible.

9.5.5. FREQUENCY SHIFT IN PERPENDICULAR FIELD

Figure 9.4(b,c) demonstrated the scaling of fractional frequency shift with the square of $B_\perp$ and nanowire width w. Taking into account that the dominant contribution to the nanowire inductance is kinetic: $f_\mathrm{r} \propto L_\mathrm{k}^{-1/2}$, where L_k is the kinetic inductance of the resonator. Further, for $T \ll T_\mathrm{c}$: $L_\mathrm{k} \propto T_\mathrm{c}^{-1}$ [26], and for small changes in frequency: $\Delta f_\mathrm{r}/f_\mathrm{r} = -\frac{1}{2}\Delta L_\mathrm{k}/L_\mathrm{k} = \frac{1}{2}\Delta T_\mathrm{C}/T_\mathrm{C}$.

The applied magnetic field splits the time-reversal degeneracy of the paired electrons, giving rise to an effective depairing energy 2α [34]. In the dirty limit and for small α, the change in T_c due to this pair-breaking effect is linear in α: $k_\mathrm{B}\Delta T_\mathrm{c} = -\frac{\pi}{4}\alpha$. Keeping in mind that the effective perpendicular penetration depth is much larger than the nanowire width, we make use of the expression for α valid in the "thin film in parallel field" approximation, $\alpha = \frac{1}{6}\frac{De^2B_\perp^2 w^2}{\hbar}$, where D is the electronic diffusion constant [34]. Thus, we recover the experimentally observed scaling $\Delta f_\mathrm{r}/f_\mathrm{r} = -\frac{\pi}{48}\frac{De^2}{\hbar k_\mathrm{B} T_\mathrm{c}}B_\perp^2 w^2$, and extract the diffusion constant $D \approx 2\,\mathrm{cm^2 s^{-1}}$. This value is consistent with an earlier estimate [35] of the electronic diffusion constant in NbTiN thin films.

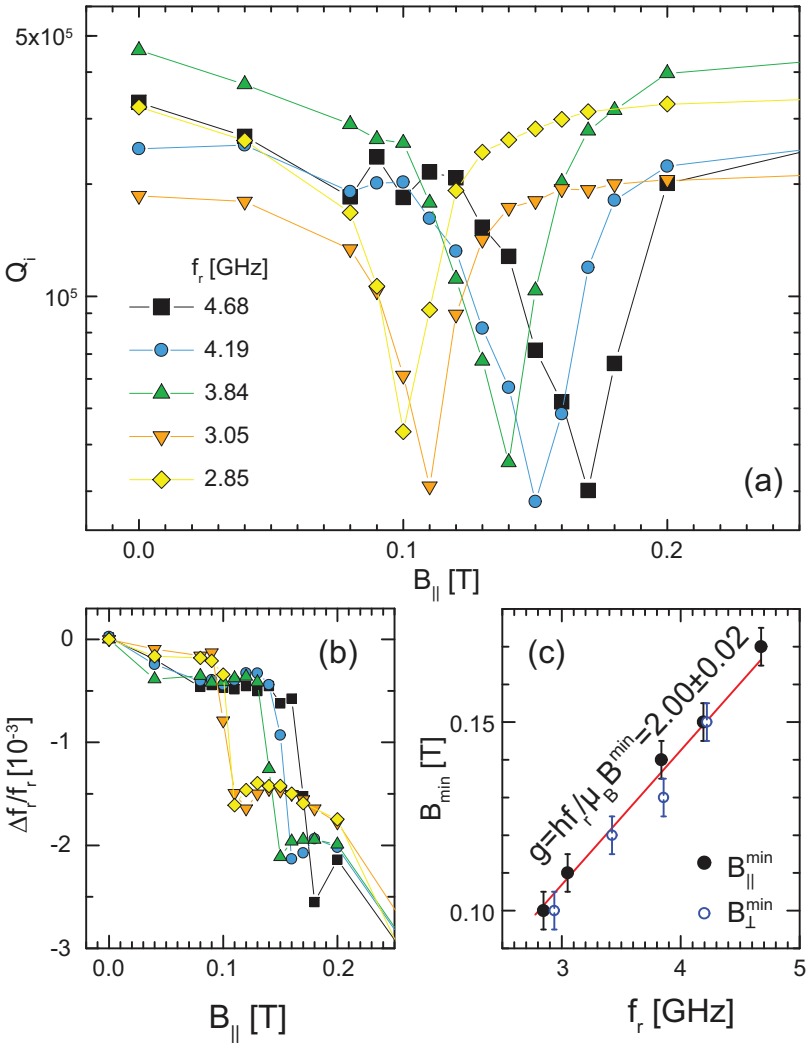

Figure 9.6: Signatures of electron spin resonance near the Zeeman field for five nanowire resonators. (a,b) Data from Fig. 9.3, expanded for clarity around 100 mT. The minima of the quality factors of the resonators occur at different values of magnetic field. (c) Dependence of the magnetic field positions of quality factor minima on the resonator frequencies. Black points correspond to $B_{||}$ measurements [Fig. 9.3], and blue points to $B_{\perp}$ measurements [Fig. 9.4(a)]. The straight line is the best fit to the data.

REFERENCES

[1] A. Blais, R. S. Huang, A. Wallraff, S. M. Girvin, and R. J. Schoelkopf, Phys. Rev. A **69**, 062320 (2004).

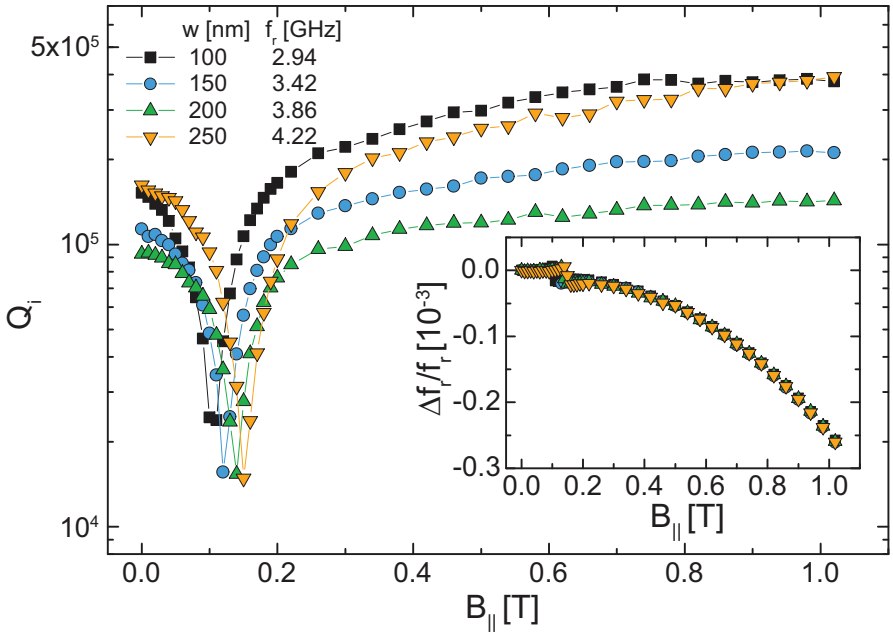

Figure 9.7: $B_{||}$ evolution of Q_i in the four narrowest nanowire resonators shown on Fig. 9.4. (Inset) Fractional shifts of the four resonance frequencies as a function of the applied field. Symbols correspond to those in Fig. 9.4.

[2] Z. L.Xiang, S. Ashhab, J. Q. You, and F. Nori, Rev. Mod. Phys. **85**, 623 (2013).

[3] X. Hu, Y. X. Liu, and F. Nori, Phys. Rev. B **86**, 035314 (2012).

[4] G. Burkard and A. Imamoglu, Phys. Rev. B **74**, 041307 (2006).

[5] L. Childress, A. S. Sørensen, and M. D. Lukin, Phys. Rev. A **69**, 042302 (2004).

[6] P. Q. Jin, M. Marthaler, A. Shnirman, and G. Schön, Phys. Rev. Lett. **108**, 190506 (2012).

[7] C. Kloeffel, M. Trif, P. Stano, and D. Loss, Phys. Rev. B **88**, 241405 (2013).

[8] D. Loss and D. DiVincenzo, Phys. Rev. A **57**, 120 (1998).

[9] R. Hanson, L. P. Kouwenhoven, J. R. Petta, S. Tarucha, and L. M. K. Vandersypen, Rev. Mod. Phys. **79**, 1217 (2007).

[10] J. T. Muhonen, J. P. Dehollain, A. Laucht, F. E. Hudson, R. Kalra, T. Sekiguchi, K. M. Itoh, D. N. Jamieson, J. C. McCallum, A. S. Dzurak and A. Morello, Nature Nanotech. **9**, 986 (2014).

[11] K. D. Petersson, L. W. McFaul, M. D. Schroer, M. Jung, J. M. Taylor, A. A. Houck, and J. R. Petta, Nature **490**, 380 (2012).

[12] T. Frey, P. J. Leek, M. Beck, A. Blais, T. Ihn, K. Ensslin, and A. Wallraff, Phys. Rev. Lett. **108**, 046807 (2012).

[13] J. J. Viennot, M. C. Dartiailh, A. Cottet, and T. Kontos, Science **349**, 408 (2015).

[14] G. W. Deng, D. Wei, J. R. Johansson, M. L. Zhang, S. X. Li, H. O. Li, G. Cao, M. Xiao, T. Tu, G. C. Guo, H. W. Jiang, F. Nori, and G. P. Guo, Phys. Rev. Lett. **115**, 126804 (2015).

[15] A. Megrant, C. Neill, R. Barends, B. Chiaro, Y. Chen, L. Feigl, J. Kelly, E. Lucero, M. Mariantoni, P. J. J. O'Malley, D. Sank, A. Vainsencher, J. Wenner, T. C. White, Y. Yin, J. Zhao, C. J. Palmstrøm, J. M. Martinis, and A. N. Cleland, Appl. Phys. Lett. **100**, 113510 (2012).

[16] A. Bruno G. de Lange, S. Asaad, K. L. van der Enden, N. K. Langford, and L. DiCarlo, Appl. Phys. Lett. **106**, 182601 (2015).

[17] R. Wördenweber, P. Dymashevski, and V. R. Misko, Phys. Rev. B **69**, 184504 (2004).

[18] C. Song, T. W. Heitmann, M. P. DeFeo, K. Yu, R. McDermott, M. Neeley, J. M. Martinis, and B. L. T. Plourde, Phys. Rev. B **79**, 174512 (2009).

[19] D. Bothner, C. Clauss, E. Koroknay, M. Kemmler, T. Gaber, M. Jetter, M. Scheffler, P. Michler, M. Dressel, D. Koelle, and R. Kleiner, Appl. Phys. Lett. **100**, 012601 (2012).

[20] D. Bothner, T. Gaber, M. Kemmler, D. Koelle, and R. Kleiner, Appl. Phys. Lett. **98**, 102504 (2011).

[21] J. I. Vestgården, V. V. Yurchenko R. Wördenweber, and T. H. Johansen, Phys. Rev. B **85**, 014516 (2012).

[22] S. E. de Graaf A. V. Danilov A. Adamyan T. Bauch, and S. E Kubatkin, J. Appl. Phys. **112** (2012).

[23] S. E. de Graaf D. Davidovikj A. Adamyan S. E. Kubatkin, and A. V. Danilov, Appl. Phys. Lett. **104**, 052601 (2014).

[24] A. Ghirri C. Bonizzoni D. Gerace S. Sanna A. Cassinese, and M. Affronte, Appl. Phys. Lett. **106**, 184101 (2015).

[25] M. S. Khalil, M. J. A. Stoutimore, F. C. Wellstood, and K. D. Osborn, J. Appl. Phys. **111**, 054510 (2012).

[26] A. J. Annunziata, D. F Santavicca, L. Frunzio, G. Catelani, M. J. Rooks, A. Frydman, and D. E. Prober, Nanotechnology **21**, 445202 (2010).

[27] J. Gao, M. Daal, A. Vayonakis, S. Kumar, J. Zmuidzinas, B. Sadoulet, B. A. Mazin, P. K. Day, and H. G. Leduc, Appl. Phys. Lett. **92**, 152505 (2008).

[28] A. D. O'Connell, M. Ansmann, R. C. Bialczak, M. Hofheinz, N. Katz, E. Lucero, C. McKenney, M. Neeley, H. Wang, E. M. Weig, A. N. Cleland, and J. M. Martinis, Appl. Phys. Lett. **92**, 112903 (2008).

[29] P. C. J. J. Coumou, M. R. Zuiddam, E. F. C. Driessen, P. J. de Visser, J. J. A. Baselmans, and T. M. Klapwijk, IEEE T. Appl. Supercon. **23**, 7500404 (2013).

[30] V. Ranjan, G. de Lange, R. Schutjens, T. Debelhoir, J. P. Groen, D. Szombati, D. J. Thoen, T. M. Klapwijk, R. Hanson, and L. DiCarlo, Phys. Rev. Lett. **110**, 067004 (2013).

[31] D. I. Schuster, A. P. Sears, E. Ginossar, L. DiCarlo, L. Frunzio, J. J. L. Morton, H. Wu, G. A. D. Briggs, B. B. Buckley, D. D. Awschalom, and R. J. Schoelkopf, Phys. Rev. Lett. **105**, 140501 (2010).

[32] J. E. Healey, T. Lindström, M. S. Colclough, C. M. Muirhead, and A. Y. Tzalenchuk, App. Phys. Lett. **93**, 043513 (2008).

[33] D. H. Wu, C. A. Shiffman, and S. Sridhar, Phys. Rev. B **38**, 9311(R) (1988).

[34] M. Tinkham, 'Introduction to Superconductivity', McGraw-Hill (New York), 1996.

[35] C. Tong, J. Stern, Megerian, H. LeDuc, T. Sridharan, H. Gibson, R. Blundell, Proc. 12th Int'l. Symp. on Space THz Techn., 253.

10

CONCLUSION AND OUTLOOK

This thesis is focused on the optimization of the performance and control of single electron spin qubits hosted in electrostatically defined quantum dots in Si/SiGe (Chapters 4, 5, 6, 7) and in GaAs (Chapter 8). In the first section of this Chapter, I summarize the main results and ideas presented in this dissertation. In the second section, I discuss some important next steps that need to be taken starting from the present work.

10.1. CONCLUSION

A spin-1/2 particle is the canonical two-level quantum system. Its energy level structure is extremely simple, consisting of just the spin-up and spin-down levels. When performing spectroscopy on an electron spin, an elementary spin-1/2 particle, only a single resonance is expected corresponding to the energy separation between the two levels. In contrast, recent measurements have shown that the spectroscopic response of a single electron spin in a quantum dot can be much more complex than this simple picture suggests. This is particularly true when using electric-dipole spin resonance, where an oscillating electric field couples to the spin via spin-orbit coupling (see Chapters 6 and 7) and when other degrees of freedom, such as the valley, start to play an important role.

Chapter 5 reports the first realization of single electron spin resonance for a SiGe/Si/SiGe device. The Si-QW is made out of natural Si, therefore with ~5% of remaining ^{29}Si nuclear spins. The HF interaction with those nuclear spins limits the dephasing time T_2^* of the electron spin to around 1 μs (already a factor of ~100 times longer than the typical dephasing time observed for a single electron spin in GaAs/AlGaAs depletion QDs [1]). Therefore, in principle, we will benefit by further reducing the contribution of the nuclear spins, hosting the electron in a ^{28}Si isotopically purified quantum well. As shown by the recent experiments of the Morello [2] and the Dzurak groups [3], at UNSW in Sydney, by making use of a single electron confined respectively in a P-atom or by an accumulation dot in an ^{28}Si epilayer, they were able to reach $T_2^* \sim 200$ μs.

In order to reap the full benefits from moving to ^{28}Si enriched material for maximal coherence times in our electrically driven Si-SiGe QD systems, also the magnetic field gradient shaping has to be carefully considered. The presence of the magnetic field gradient opens a coupling channel between the spin and the charge degrees of freedom (an artificial SO interaction). The same coupling mechanism that allows us to perform electric dipole spin resonance (EDSR) may also hinder the coherence properties of the electron spin, allowing electric noise to contribute to dephasing and relaxation processes. In Chapter 7 we use the enhanced sensitivity of the inter-valley resonance to charge noise in order to put an upper bound on the T_2^* of the intra-valley spin resonance taking place in an hypothetical device, similar to the one used, but with just ^{28}Si in the QW (no HF noise). Our estimation of ~ 4 μs clearly suggests not to underestimate the role of the magnetic field gradient. Furthermore, in [4] we report that the longest coherence time measured using dynamical decoupling is ~ 400 μs in our system. We revealed that the measured noise level in frequency range (5 kHz - 1 MHz) is higher than expected from the dynamics of the ^{29}Si nuclear spins. Instead, charge noise in combination with a local magnetic field gradient may be responsible.

In fact, in our experiment the magnetic field gradient created by the micromagnet presents not only the $dB_\perp/dx, dy$ (transversal) components (used for the spin driving), but also a not negligible $dB_{//}/dx, dy$ (longitudinal) component. This last contribution is responsible for the frequency shifting of the intra-valley spin resonance, reported in Fig. 7.3 of Chapter 7, which suggests that electric noise acting into the QW plane can directly affect the Zeeman splitting (causing dephasing). Ideally we would like to create a micromagnet stray field with high and uniform $dB_\perp/dx, dy$ (fast Rabi frequency) in the QD region, and negligible $dB_{//}/dx, dy$. The micromagnet geometry reported in [5] and reproduced in our work, has been designed with this goal in mind (respect to the QD

position, defined by depletion gates). However, in our device the QD is created outside the optimal gradient region.

Another key feature reported in Chapter 5 regards the observation of a second spin resonance, very close to the main one, and which we identify in coincidence of the spin excitation of the excited valley-orbit state. As explained in Chapters 3 and 4, in silicon, due to the symmetry of the crystal structure, it is necessary to take into account also the valley degree of freedom. In Si-Ge electrostatic QDs, the first excited state is usually an excited valley-orbit state and its excitation energy is typically a factor of 10 lower than the normal orbital energy splitting for a QD in GaAs/AlGaAs 2DEGs. In our experiment this energy splitting is of the order of 25 μeV, therefore the valley-orbit excited state is also populated; consequently, the electron spin in this excited valley-orbit configuration can be driven too. Furthermore, we noticed that, due to valley-orbit coupling, the wavefunctions of the 2 valley-orbit states present somewhat different spatial distributions [6]; therefore, the magnetic field gradient renormalizes the Zeeman splitting of the electron [7] according to the specific valley-orbit states [8], resulting in a valley dependent Larmor frequency (Chapter 5). Similarly, a difference in the Rabi frequencies between the 2 intra-valley spin resonances results (Chapter 5).

Interestingly, we observe that these two resonances can also be driven by second harmonic generation. Even coherent driving is possible, with Rabi frequencies comparable to those for the fundamental harmonic (see Chapter 6).
For electrically driven spin qubits confined in a (double) quantum dot, higher harmonic driving has been proposed that takes advantage of an anharmonic dot confining potential or a spatially inhomogeneous magnetic field. In order to use higher harmonic generation for coherent control of a system, the corresponding driving rate must exceed the decoherence rate. Obtaining an anharmonicity (in the confining potential or otherwise) that is sufficiently strong to allow coherent spin rotations is absolutely not trivial. Several previous works have reported energy spectroscopy by higher harmonics but none of these experiments reported coherent driving [9–12]. In the experiment reported in Chapter 6, the highest Rabi frequency obtained by second harmonic generation is just half the highest Rabi frequency obtained by driving at the fundamental. Furthermore, while previous works concern measurements in DQD systems, our experiment makes use of a single QD. The anharmonicity of a single QD confinement potential should be, in principle, smaller than that of a DQD.

In Chapter 7 we show that it is possible to drive not just the intra-valley sector of the spin-valley energy diagram, as reported by Fig. 7.1(c), but also the inter-valley sector. The valley-spin coupling is a second order effect mediated by valley-orbit coupling and spin-orbit (SO) coupling. The natural SO coupling should be quite small in silicon, due to its cubic lattice symmetry; however in our device, the presence of the micromagnet stray magnetic field acts as an artificial SO field. We provide a detailed study of the coherence properties of this transition whereby both the spin and valley-orbit state are flipped. We show that a driven four-level system comprising of two valley-orbit and two spin states captures, in a unified way, these transitions as well as all the previously reported transitions for this system. Furthermore, we demonstrate that we can sensitively Stark shift the spin-valley transition. The experiments reveal also a dynamical level repulsion, from which we can extract the Rabi frequency for the spin valley-orbit transition

using a dressed-state formalism (not reported in this Thesis). The observed spin-valley resonance does not show coherent oscillations (for the driving strength we are able to reach in our experiment). We estimated an upper bond of $T_2^* \sim 100$ ns.

It has been shown that a fairly small valley-orbit energy splitting can be detrimental for spin based quantum computation schemes [13–15]. But one can also look at the valley degree as a resource which can be used, if sufficiently controllable, in order to expand the Hilbert space involved in the computation protocols. In this respect, a new qubit architecture in Si quantum dots (QDs), based on the valley degree of freedom to encode and process quantum information, has been presented in [16]. The decoherence properties of a valley qubit are set by inter-valley transitions, occurring on longer time scales than intra-valley transitions, therefore permitting longer coherence times compared to a standard charge qubit.
Unfortunately, in Si/SiGe QW, due to the omnipresence of interface disorder, the valley and the orbital degrees are strongly hybridized [6, 17]. This usually reduces the valley-orbit energy splitting and, already in a single QD, leads to the development of a non-negligible dipole moment, meaning that the envelope wavefunctions for the different valley-orbit states presents quite different charge-spatial distributions. This will result in an enhanced sensitivity of this resonance to the electric fields (as reported in Chapter 7). We can conclude that the idea of a pure valley-qubit in Si-SiGe heterostructures results unfeasible and an hybrid valley-orbit qubit will present a very fast (charge-like) dephasing.

In Chapter 8, instead, we focus on the single spin relaxation time. By making use of a GaAs/AlGaAs QD device, we demonstrate how the orientation of the external magnetic field, relative to the crystallographic and QD elongation directions, can be optimized in order to increase the relaxation time (T_1). The anisotropy of the electron spin relaxation time originating from SO interaction has not been studied experimentally so far, even though it is highly relevant. Indeed, depending on the circumstances, it may be desirable to get long relaxation times or to make the relaxation process as fast as possible, for example in order to rapidly initialize the spin [18]. We show that the in-plane orientation of the magnetic field can strongly impact the spin relaxation time in quantum dots. We observe a variation in T_1 by more an order of magnitude when rotating the field in the 2DEG plane. The SO anisotropy similarly affects the strength of the effective driving field for single-qubit rotations based on electric dipole spin resonance [19]. With a proper understanding, one can design future devices that optimally reconcile various requirements. Furthermore, the dependence of T_1 on magnetic field angle provides a sensitive probe of the ratio of the Rashba and Dresselhaus SO contributions. What is needed is either a symmetric QD confining potential or, for an elliptical dot, a good estimate of the magnitude and direction of the QD anisotropy. Similar considerations are also valid for singlet-triplet qubits [20], where the DQD dipole axis replaces the role of the QD elongation direction [19].

The topic discussed in Chapter 9 need to be placed in the context of the effort of scaling to a larger number of qubits, a fundamental step for the realization of quantum computation architectures. Therefore, before commenting on its results, the topics deserves a section itself, where I will summarize the most promising scaling techniques that the spin qubits community is exploring.

10.2. OUTLOOK

Two-qubit experiments performed using electron spins confined in electrostatically defined QDs relied on the use of the exchange interaction [1, 21, 22] or of the capacitive coupling between electrons [23]; therefore, the separation between the quantum dots needs to be small (~100nm). The next fundamental step for the future of solid-state spin qubit architectures consists in building larger quantum dot systems with many more interacting qubits. Even if recent experiments have shown that it is possible to properly control linear triple and quadruple dots arrays (in the few electron regime), envisioning a scalable architecture based on the direct interaction (exchange interaction) between near neighbour QDs seems a non-trivial task. Moreover, the physical implementation of quantum dot networks requires some space between the qubits to place charge sensors and electron reservoirs. It is therefore very important to find a way to couple spins over sufficiently large distances (micrometer scale).

Even if it is easy to imagine scaling such a QDs array up to a chain of quantum dots with integrated charge sensors, defined on one side of the chain, it is not so clear what is the minimal number for electron reservoirs necessary for a given number of QDs, neither how to optimally place them with respect to the QDs. Everything becomes even more difficult to organize spatially if we consider 2D arrays, as required for a practical realization of the surface code architecture[1]. A possible solution could consist in the implementation of segments of 1D QDs-array, with dedicated charge sensors, and connecting them through some appropriate interconnecting elements (not yet investigated).

Regarding the development and study of the spin property in 1D QD-array, an important experiment has been recently realized by T. Baart et al. [24], where has been demonstrated the manipulation, transport and read-out (though a single electron reservoir) of individual electron spins in a linear array of three QDs hosted in GaAs/AlGaAs. In the same experiment, an electron has been shuttled back and forth in the QD array hundreds of times, covering a cumulative distance of 80 μm. This process had a negligible influence on the electron spin projection. Recently, this experiment has been extended to a 4QDs-array [unpublished].

Another approach [25] has shown that it is possible to generate a tunnel coupling between two distant quantum dots mediated by virtual occupation of an intermediate QD. One can envision the use of this cotunneling coupling for creating exchange gates between non nearest neighbours within clusters of QDs.

An approach to increase the capacitive coupling between not adjacent QDs is based on the realization of floating metallic (or superconducting) gates [26]. A capacitive coupling between QDs [27] or QD and charge sensor [28] via a floating metallic capacitor has been already demonstrated. Trifunovic et al. developed a new approach to achieve long-distance spin-spin coupling via a coupler built by a floating metal gate. According to this analysis, a long-range coupling with coupling strengths above the spin-decay rates can be achieved[2].

In [29], the same group developed, instead, a model to generate coherent coupling

[1] Even if still possible to implement error correction scheme with 1D qubit arrays, the required error rates are much lower (~ 10^{-5}) if compared to 2D arrays.

[2] On the other end, big concerns are still open about the extra charge noise introduced by this extra floating gates, strongly capacitively coupled with the QDs.

of distant spin qubits intermediated by a piece of ferromagnetic material between them to which both of them couple by magnetic dipolar interactions. They demonstrated that a dog-bone shape of the ferromagnet is the best compromise since it allows both strong coupling of the qubits to the ferromagnet and long-distance coupling because of its slowly decaying 1D spin-spin susceptibility. From their simulation, an interaction strength of ~10 μeV, for both the singlet-triplet (S-T) and spin-1/2 qubits, can be achieved. Furthermore, decoherence effects induced by the coupling to the ferromagnet, are estimated to be negligible.

Another possible strategy to couple distant spin qubits is based on the use of surface-acoustic waves (SAWs) to transport single electrons between distant quantum dots [30, 31][3]. From the electron point of view, the SAW represents a traveling electrostatic potential with a series of moving minima (at the velocity of the sound of the substrate), where it can get trapped and shuttled. By building a SAW channel next to a QD, controlling the electrochemical potential and tunnel barriers of the QD it is possible to selectively load a single electron onto a moving potential minimum. In the same way, by placing another QD in close proximity to the same SAW channel, it has been shown that the same single electron (transported by a SAW potential minima) can be trapped in this second static QD. The electron shuttling is operated by the SAW train at the sound velocity (typically ~3000 m/s), therefore it is possible to cover micron distances on the nanosecond timescales.

Recently, the Meunier group [32] moved a step further, demonstrating that spin information can be transferred between distant quantum dots using either one or two electrons. Spin polarization and spin read-out of the electron spin state are performed in static dots whereas the transfer is mediated by moving quantum dots generated with SAWs in a long depleted channel. The fidelity of the spin transfer reaches 30% and is believed to be limited by the depolarization prior and after the transfer in the static dots.

Inspired by the success of the circuit QED (cQED) experiments, different groups started to build and explore systems to couple MW photons, stored in a high-Q superconducting resonator, with the electrical dipole moment of a semiconductor qubit (mainly in the form of a DQD) [33–35]. A direct magnetic coupling between a single electron spin (electron's magnetic dipole moment) and a photon mode is currently too weak to be resolved in an experiment. On the contrary, different cQED-like experiments have been performed on N-spin ensemble systems, where a strong coupling can be realized thanks to the $\sqrt{N}$ enhancement of the coupling strength [36–38]. By realizing a coupling stronger than the decoherence time of the cavity and qubit system, it is possible to transfer the state of the qubit to a photon in the cavity, which could then in turn be transferred to the state of another qubit; this allows transmission of quantum information and the realization of a two-qubit gate over long distances. In this respect, a single electron spin hosted in Si is an ideal candidate due to its narrow line width (~600 kHz and ~1.2 kHz respectively in natural and isotopically purified Si).

Coupling of a single-spin qubit to the cavity electric field can be mediated by a nat-

[3] The application of a MW electric modulation on an interdigited transducer (IDT), realized on top of a piezoelectric substrate, generates a mechanical wave (due to the inverse piezoelectric effect) which also carries an electromagnetic field. The created surface acoustic waves is confined at the surface of a piezoelectric substrate and its frequency is determined by the spatial periodicity of the IDT (for a given substrate sound velocity).

ural or artificial spin-orbit coupling [39]. Achieving strong coupling in such hybrid systems has proved challenging due to the weak interaction between the zero-point fluctuations (ZPF) of conventional superconducting resonators and the quantum dot electrons. Even if charge-cavity coupling strengths of tens of MHz have been demonstrated [33, 34], the decoherence rate of a charge qubit is typically of the order of 0.1-1 GHz. In the same system, a spin-cavity coupling strengths of ~1 MHz is expected. Considering a single electron spin hosted in natural Si (~0.6 MHz dephasing time), a coupling of 1 MHz is on the boundary for strong coupling, not enough for fast spin qubit-qubit interactions. It is necessary, therefore, to improve significantly the coupling strength of this 'hybrid' system, for instance by using larger dipole (TQD instead of single or DQD).

In Chapter 9 we pursued another way to increase the coupling strength, focusing on the resonator performance. Traditionally, coplanar waveguide (CPW) resonators with characteristic impedance $Z_r \sim 50\ \Omega$ have been used as the staple cavity in cQED. However, by increasing (decreasing) Z_r, it is possible to enhance the ZPF of voltage (current), thus optimizing for electric (magnetic) dipole coupling to qubits.

Another challenge in incorporating superconducting resonators in spin-based systems is the typically poor performance of superconducting resonators at the magnetic fields required for the operation of such systems. Intrinsic quality factors $Q_1 > 10^6$ have been measured for the highest performance resonators in magnetically shielded cQED setups. However, strong magnetic fields induce vortices in the superconducting film, which move under the influence of microwave currents in the resonator, causing energy dissipation. In Chapter 9, we present microwave-frequency resonators based on NbTiN nanowires, displaying magnetic field resilience and promising stronger electrical coupling. We take advantage of the high kinetic inductance of the strongly disordered superconducting nanowires to increase its impedance up to $Z_r \approx 4\ \text{k}\Omega$, nearly two orders of magnitude higher than that of CPW resonators used in typical cQED devices. The corresponding $V_{ZPF}^{RMS} \approx 20\ \mu\text{V}$ makes these resonators well suited for coupling to systems with small electric dipole moments, such as electrons in single or double quantum dots. Moreover, the small nanowire cross section strongly suppresses vortex generation in a magnetic field, resulting in $Q_i > 2 \times 10^5$ at up to $B_{//} = 6$ T.

Another line of research has been recently proposed, based on the idea of coherent, long range interactions between individual qubits mediated by mechanical resonators. This coupling scheme is directly inspired to the cQED, with resonant phonons playing the role of cavity photons. Driven by two recent experiments [40, 41], where the coherent quantum nature of SAWs on a GaAs substrate has been explored, the authors of [42] proposed and analyzed SAW phonon modes in piezoactive materials as a universal mediator for long-range couplings between remote qubits. This approach involves qubits interacting with a localized SAW phonon mode, defined by a high-Q SAW resonator, which in turn can be coupled weakly to a SAW waveguide serving as a quantum bus. Recently two important steps in this direction have been realized in [43] and [44]. The first work shows the ability to create GHz SAW-resonators, on ST-quartz, with high quality factors in the quantum regime. Instead in the second work, authors realize already a prototype of a DQD in GaAs/AlGaAs, inside a SAW cavity and study the effect of the confined SAW on the DQD transport.

In the experiments realized on isotopically enriched Si at UNSW (Sydney), the spin

driving is realized magnetically, by a microstrip line built close to the confined electron [2, 3, 22]. This limits the Rabi frequencies obtained to around 100 kHz, a factor of 10 slower if compared to the electrical driving of our experiment (~1-5 MHz, in Chapter 5). On the other hand, the coherence time of a single electron confined ^{28}Si, is more than 100 times longer. Therefore, the averaged single qubit gate fidelities are around 99% and 99.95%, the respective measurements using natural [4] and isotopically purified [3, 45] Si systems.

The driving gradient component in our experiment is around 0.3 mT/nm (estimated by simulation, as reported in Chapter 5). From our simulations, we can predict that it can be increased to around 1-1.2 mT/nm by properly shaping the micromagnet and placing the electron in the right position, therefore gaining a factor of 4 in the Rabi frequency (compared to what we observed in the present experiment). Furthermore, as already reported in [46] (for a single electron confined in a GaAs/AlGaAs QD), a careful optimization of the electrical driving allows to reach a Rabi frequency up to 20-30 MHz (~10 times faster than what reported in Chapter 5). A similar experiment has been recently realized by the Tarucha group (Tokyo University, Japan) for a DQD device defined in natural SiGe/Si/SiGe quantum well (unpublished). In this case, the performance in terms of gate fidelity, for single electron spin confined in natural Si, can be comparable to what obtained in isotopically purified Si devices. Therefore, by combining the benefits of ultralong coherence time (coming from isotopically enriched silicon) with the fast Rabi frequency (coming from EDSR) we can further improve the fidelity of a single qubit gate.

REFERENCES

[1] J. R. Petta, A. C. Johnson, J. M. Taylor, E. A. Laird, A. Yacoby, M. D. Lukin, C. M. Marcus, M. P. Hanson, and A. C. Gossard, Science **309**, 2180 (2005).

[2] J. T. Muhonen, J. P. Dehollain, A. Laucht, F. E. Hudson, R. Kalra, T. Sekiguchi, K. M. Itoh, D. N. Jamieson, J. C. McCallum, A. S. Dzurak and A. Morello, Nature Nanotech. **9**, 986 (2014).

[3] M. Veldhorst, J. C. C. Hwang, C. H. Yang, A. W. Leenstra, B. de Ronde, J. P. Dehollain, J. T. Muhonen, F. E. Hudson, K. M. Itoh, A. Morello and A. S. Dzurak, Nature Nanotech. **9**, 981 (2014).

[4] E. Kawakami, T. Jullien, P. Scarlino, D. R. Ward, D. E. Savage, M. G. Lagally, V. V. Dobrovitski, Mark Friesen, S. N. Coppersmith, M. A. Eriksson, L. M. K. Vandersypen, 'Gate fidelity and coherence time of an electron spin in a Si/SiGe quantum dot', in preparation.

[5] J. Yoneda, T. Otsuka, T. Takakura, M. Pioro-Ladrière, R. Brunner, H. Lu, T. Nakajima, T. Obata, A. Noiri, C. J. Palmstrøm, A. C. Gossard and S. Tarucha, Applied Physics Express **8**, 084401 (2015).

[6] J. K. Gamble, M. A. Eriksson, S. N. Coppersmith, and M. Friesen, Phys. Rev. B **88**, 035310 (2013).

[7] Y. Tokura, W. van der Wiel, T. Obata, and S. Tarucha, Phys. Rev. Lett. **96**, 047202 (2006).

[8] R. Ferdous, P. Scarlino, E. Kawakami, M. Novak, D. E. Savage, M. G. Lagally, Mark Friesen, S. N. Coppersmith, M. A. Eriksson, L. M. K. Vandersypen, R. Rahman, 'Valley dependent g-factor anisotropy in Silicon quantum dots', in preparation.

[9] E. A. Laird, C. Barthel, E. I. Rashba, C. M. Marcus, M. P. Hanson, and A. C. Gossard, Semicond. Sci. Technol. **24**, 064004 (2009).

[10] F. Pei, E. A. Laird, G. A.Steele, L. P. Kouwenhoven, Nature Nanotech. **7**, 630 (2012).

[11] J. Stehlik, M. D. Schroer, M. Z. Maialle, M. H. Degani, and J. R. Petta, Phys. Rev. Lett. **112**, 227601 (2014).

[12] S. Nadj-Perge, V. S. Pribiag, J. W. G. van den Berg, K. Zuo, S. R. Plissard, E. P. A. M. Bakkers, S. M. Frolov, and L. P. Kouwenhoven, Phys. Rev. Lett. **108**, 166801 (2012).

[13] E. Kawakami, P. Scarlino, D. R. Ward, F. R. Braakman, D. E. Savage, M. G. Lagally, Mark Friesen, S. N. Coppersmith, M. A. Eriksson and L. M. K. Vandersypen, Nature Nanotech. **9**, 666 (2014).

[14] M. G. Borselli, et al., Appl. Phys. Lett. **98**, 123118 (2011).

[15] M. G. Borselli, et al., Appl. Phys. Lett. **99**, 063109 (2011).

[16] D. Culcer, A. L. Saraiva, B. Koiller, X. Hu and Das Sarma, Phys. Rev. Lett. **108**, 126804 (2012).

[17] M. Friesen and S. N. Coppersmith, Phys. Rev. B **81**, 115324 (2010).

[18] V. Srinivasa, K. C. Nowack, M. Shafiei, L. M. K. Vandersypen, and J. M. Taylor, Phys. Rev. Lett. **110**, 196803 (2013).

[19] V. N. Golovach, A. Khaetskii, and D. Loss, Phys. Rev. B **77**, 045328 (2008).

[20] V. Kornich, C. Kloeffel, and D. Loss, Phys. Rev. B **89**, 085410 (2014).

[21] K. C. Nowack, M. Shafiei, M. Laforest, G. E. D. K. Prawiroatmodjo, L. R. Schreiber, C. Reich, W. Wegscheider, L. M. K. Vandersypen, Science **333**, 1269 (2011).

[22] M. Veldhorst, C. H. Yang, J. C. C. Hwang, W. Huang, J. P. Dehollain, J. T. Muhonen, S. Simmons, A. Laucht, F. E. Hudson, K. M. Itoh, A. Morello and A. S. Dzurak, Nature **526**, 410 (2015).

[23] M. D. Shulman, O. E. Dial, S. P. Harvey, H. Bluhm, V. Umansky, A. Yacoby, Science **336**, 202 (2012).

[24] T. A. Baart, M. Shafiei, T. Fujita, C. Reichl, W. Wegscheider, L. M. K. Vandersypen, arXiv:1507.07991.

[25] F. R. Braakman, P. Barthelemy, C. Reichl, W. Wegscheider, L. M. K. Vandersypen, Nature Nanotech. **8**, 432 (2013).

[26] L. Trifunovic, O. Dial, M. Trif, J. R. Wootton, R. Abebe, A. Yacoby, D. Loss, Phys. Rev. X **2**, 011006 (2012).

[27] H. Chan, R. M. Westervelt, K. D. Maranowski, and A. C. Gossard, Appl. Phys. Lett. **80**, 1818 (2002).

[28] H. O. H. Churchill, A. J. Bestwick, J. W. Harlow, F. Kuemmeth, D. Marcos, C. H. Stwertka, S. K. Watson and C. M. Marcus, Nature Phys. **5**, 321 (2009).

[29] L. Trifunovic, F. L. Pedrocchi, D. Loss, Phys. Rev. X **3**, 041023 (2013).

[30] S.Hermelin, S. Takada, M. Yamamoto, S. Tarucha, A. D. Wieck, L. Saminadayar, C. Bäuerle, T. Meunier, Nature **477**, 435 (2011).

[31] R. P. G. McNeil, M. Kataoka, C. J. B. Ford, C. H. W. Barnes, D. Anderson, G. A. C. Jones, I. Farrer, D. A. Ritchie, Nature **477**, 439 (2011).

[32] B. Bertrand, S. Hermelin, S. Takada, M. Yamamoto, S. Tarucha, A. Ludwig, A. D. Wieck, C. Bäuerle, T. Meunier, arXiv:1508.04307.

[33] T. Frey, P. J. Leek, M. Beck, A. Blais, T. Ihn, K. Ensslin, and A. Wallraff, Phys. Rev. Lett. **108**, 046807 (2012).

[34] K. D. Petersson, L. W. McFaul, M. D. Schroer, M. Jung, J. M. Taylor, A. A. Houck, and J. R. Petta, Nature **490**, 380 (2012).

[35] J. J. Viennot, M. C. Dartiailh, A. Cottet, and T. Kontos, Science **349**, 408 (2015).

[36] D. I. Schuster, A. P. Sears, E. Ginossar, L. DiCarlo, L. Frunzio, J. J. L. Morton, H. Wu, G. A. D. Briggs, B. B. Buckley, D. D. Awschalom, and R. J. Schoelkopf, Phys. Rev. Lett. **105**, 140501 (2010).

[37] Y. Kubo, F. R. Ong, P. Bertet, D. Vion, V. Jacques, D. Zheng, A. Dréau, J. F. Roch, A. Auffeves, F. Jelezko, J. Wrachtrup, M. F. Barthe, P. Bergonzo, and D. Esteve, Phys. Rev. Lett. **105**, 140502 (2010).

[38] V. Ranjan, G. de Lange, R. Schutjens, T. Debelhoir, J. P. Groen, D. Szombati, D. J. Thoen, T. M. Klapwijk, R. Hanson, and L. DiCarlo, Phys. Rev. Lett. **110**, 067004 (2013).

[39] X. Hu, Yu-xi Liu, and F. Nori, Phys. Rev. B **86**, 035314 (2012).

[40] M. V. Gustafsson, P. V. Santos, G. Johansson, and P. Delsing, Nature Phys. **8**, 338 (2012).

[41] M. V. Gustafsson, T. Aref, A. F. Kockum, M. K. Ekström, G. Johansson, and P. Delsing, Science **346**, 207 (2014).

[42] M. J. A. Schuetz, E. M. Kessler, G. Giedke, L. M. K. Vandersypen, M. D. Lukin, and J. I. Cirac, Phys. Rev. X **5**, 031031 (2015).

[43] R. Manenti, M. J. Peterer, A. Nersisyan, E. B. Magnusson, A. Patterson, P. J. Leek, arXiv:1510.04965.

[44] J. C. H. Chen, Y. Sato, R. Kosaka, M. Hashisaka, K. Muraki and T. Fujisawa, Scientific Reports **5**, 15176 (2015).

[45] J. T. Muhonen, A. Laucht, S. Simmons, J. P. Dehollain, R. Kalra, F. E. Hudson, S. Freer, K. M. Itoh, D. N. Jamieson, J. C. McCallum, J. Phys. Condens. Matter. **27**, 154205 (2015).

[46] J. Yoneda, T. Otsuka, T. Nakajima, T. Takakura, T. Obata, M. Pioro-Ladrière, H. Lu, C. J. Palmstrøm, A. C. Gossard, and S. Tarucha, Phys. Rev. Lett. **113**, 267601 (2014).

A

DELFT FABRICATION RECIPE AND TEST STRUCTURES

What reported in this appendix has been developed in collaboration with F. Walvoort (Master thesis project) [1], following the indications of our collaborators at University of Wisconsin (M. Eriksson group).

A.1. FABRICATION PROCESS

1. Dice
   (a) Use S1813 resist
   (b) Dice material into 10 by 10 mm chips
2. Cleaning
   (a) Strip resist in fumic HNO_3 for 3 minutes
   (b) Rinse the samples with water
   (c) Put the samples in water. The samples can also be N_2 blown dry, but keeping them in water is simpler in light of the coming cleaning steps.
   (d) Perform RCA-1 cleaning. This removes any organic contaminants that are on the sample. Glass beakers can leach Na^+ ions at high pH that contaminate the sample. Instead, use teflon beakers and rinse them thoroughly (3x) before use.
      i. Heat bain-marie to 70 °C
      ii. Mix 50 ml H_2O and 10 ml 28% NH_4OH and place in bain-marie
      iii. After 10 minutes (the solution should be 70 °C by then), add 10 ml 31% H_2O_2. The solution might start bubbling within 2 minutes.
      iv. Place samples in the solution for 10 minutes

v. Contaminants can collect at the air-solution interface. To remove the samples, the interface needs to be broken. Place the beaker in a large dish, gently spray water into the solution until the beaker runs over and remove the samples.
vi. Place the samples in water

(e) Perform HF dip. The RCA-1 cleaning oxidized the samples. This step removes the oxide and any contaminants buried in the oxide.
i. Mix 190 ml H_2O and 10 ml 40% HF in a rinsed teflon beaker
ii. Put the samples in the solution for 2 minutes.
iii. Remove the samples through a broken interface (see above)
iv. Keep the samples in water

(f) Perform RCA-2 cleaning. This dissolves any metal impurities, particularly Fe and Na. Use rinsed teflon beakers.
i. Heat bain-marie to 70 °C (already done)
ii. Mix 50 ml H_2O and 10 ml 37% HCl and place in bain-marie
iii. After 10 minutes, add 10 ml 31% H_2O_2. The solution will start bubbling within 2 minutes.
iv. Place samples in the solution for 10 minutes
v. Remove the samples through a broken interface (see above)
vi. Place the samples in water

(g) Perform HF dip to remove the oxide formed by RCA-2 cleaning
i. Mix 190 ml H_2O and 10 ml 40% HF in a rinsed teflon beaker
ii. Put the samples in the solution for 2 minutes.
iii. Remove the samples through a broken interface (see above)
iv. Keep the samples in water
v. Blow dry the samples using N_2.

(h) The surface of the samples is now completely clean and oxide-free. The hydrogenated surface has to be protected permanently by covering it immediately with Al_2O_3.

3. Initial Al_2O_3 deposition

(a) Immediately after cleaning the samples, load them into the ALD machine

(b) Deposit 50 cycles (5 nm) Al_2O_3 at 300 °C. Do not use the oxygen plasma cleaning step, as this will oxidize the sample.

4. Alignment markers

(a) Use bi-layer resist (See standard procedures) (beam size 100 nm, dose 900 $\mu C/cm^2$)

(b) Sputter ~200 nm of NbTiN or ~130 nm of W

(c) Lift-off (See standard procedures)

5. Mesa etch
   (a) Use mono-layer resist A7 (See standard procedures) (beam size 100 nm, dose 1000 μC/cm^2)
   (b) Strip away Al_2O_3 and any native Si oxide in 7:1 BOE dip, 25 s
   (c) DI water rinse / gentle N_2 dry
   (d) RIE in Leybold-Heraeus F1: SF_6 (12.5 sccm) /O_2 (2.5 sccm) /He (1.0 sccm) etch, 40 W, 10 μbar. Etch rate ~80 nm/min. Minimum etch depth required is 50 nm.
   (e) Strip resist with lift-off procedure
6. Second Al_2O_3 deposition
   (a) Deposit 100 cycles (10 nm) Al_2O_3 at 300 °C. An oxygen cleaning can be performed.
7. Ion implantation
   (a) Use mono-layer resist A7 (beam size 10 nm, dose 1500 μC/cm^2 or 100 nm and 100 μC/cm^2)
   (b) Strip away Al_2O_3 and any native Si oxide in 7:1 BOE dip, 25 s
   (c) DI water rinse / gentle N_2 dry
   (d) Glue sample to support wafer using PMMA 950 A4 and bake for 10 minutes at 120 °C
   (e) Implant 31P+ (phosphorous) at 20 keV, $5 \cdot 10^{15}$ ions/cm^2, 7° tilt, room temperature
   (f) Acetone soak over several days, light sonication for multiple hours on the last day (30% power) at 50 °C. The PMMA is notoriously hard to remove, so sonication of several hours may be necessary as well as spraying with a syringe and swapping to clean acetone.
   (g) IPA rinse, N_2 dry
   (h) If needed, O_2 etch in Tepla stripper, 600 W, 1 mbar for 1−5 minutes
   (i) Rapid thermal anneal in forming gas, 700 °C for 15 s
8. Ohmic metallization
   (a) Use mono-layer resist A7 (beam size 10 nm, dose 1500 μC/cm^2 or 100 nm and 1000 μC/cm^2)
   (b) Strip away Al_2O_3 and any native Si oxide in 7:1 BOE dip, 25 s
   (c) DI water rinse / gentle N_2 dry
   (d) Immediately following BOE dip load into metal evaporator
   (e) Metal deposition
      i. Ti, 5 nm at 0.5 Å/s

ii. Au, 40 nm at 0.5 Å/s (Adjust thickness to resist residue height + 10 nm)

(f) Lift-off

9. Fine gates

(a) Use mono-layer resist A2 (See standard procedures) (beam size 2 nm, dose 1050 μC/cm^2)

(b) Metal deposition

i. Ti, 5 nm at 0.5 Å/s

ii. Au, 25 nm at 0.5 Å/s

(c) Lift-off

10. Large gates and pads

(a) Use bi-layer resist (beam size 100 nm, dose 700 μC/cm^2)

(b) Metal deposition

i. Ti, 5 nm at 0.5 Å/s

ii. Au, 100 nm at 1.0 Å/s (Adjust thickness to be mesa etch depth + 20 nm)

(c) Lift-off

11. Second Al_2O_3 layer

(a) Deposit 800 cycles (80 nm) Al_2O_3 at 300 °C

12. Fine accumulation gates

(a) Use mono-layer resist A2 (beam size 2 nm, dose 1050 μC/cm^2)

(b) Metal deposition

i. Ti, 5 nm at 0.5 Å/s

ii. Au, 30 nm at 0.5 Å/s

(c) Lift-off

13. Vias

(a) Use mono-layer resist A7 (beam size 100 nm, dose 1000 μC/cm^2)

(b) Bake at 175 °C for 1 minute

(c) Etch Al_2O_3 in 7:1 BOE, 45 s dip

(d) DI water rinse

(e) Gentle N_2 dry

} Repeat 3 times (total etch time 135 s)

(f) Acetone soak 1 hour

(g) IPA rinse, N_2 dry

14. Gate interconnects

(a) Use bi-layer resist (beam size 100 nm, dose 900 μC/cm^2)

(b) Metal deposition
   i. Ti, 5 nm at 0.5 Å/s
   ii. Au, 100 nm at 1.0 Å/s (Adjust thickness to be mesa etch depth + 20 nm)

(c) Lift-off

15. Micromagnets

(a) Deposit Al_2O_3 to isolate micromagnets from accumulation gates

(b) Use bi-layer resist (beam size 10 nm, dose 1550 $\mu C/cm^2$). To ensure proper lift-off, micromagnets should be larger than 200×600 nm^2

(c) Load into Leybold-Heraeus L560 evaporator with Co target

(d) Deposit 200 nm of Co at ~ 2 Å/s

(e) Lift-off

A.2. STANDARD PROCEDURES

A.2.1. BI-LAYER RESIST

1. Spin MMA/MAA copolymer 17.5% EL11 at 2500 rpm for 60 s (775 nm)
2. Bake at 175 °C for 10 minutes
3. Spin PMMA 950 A2 at 1500 RPM for 60 s (90 nm)
4. Bake at 175 °C for 10 minutes
5. E-beam lithography with specified beam size and dose
6. Develop sample in 3:1 IPA:MIBK (prepared manually) for 60 s
7. Rinse sample in IPA for 60 s
8. N_2 dry

A.2.2. MONO-LAYER RESIST S1813

1. Spin S1813 at 2000 rpm for 60 s (1900 nm)
2. Bake at 110 °C for 5 minutes

A.2.3. MONO-LAYER RESIST A2

1. Spin PMMA 950 A2 at 2000 rpm for 60 s (80 nm)
2. Bake at 175 °C for 10 minutes
3. E-beam lithography with specified beam size and dose
4. Develop sample in 3:1 IPA:MIBK (prepared manually) for 60 s
5. Rinse sample in IPA for 60 s
6. N_2 dry

A.2.4. MONO-LAYER RESIST A7

1. Spin PMMA 950 A7 at 3000 rpm for 60 s (700 nm)
2. Bake at 175 °C for 50 minutes
3. E-beam lithography with specified beam size and dose
4. Develop sample in 3:1 IPA:MIBK (prepared manually) for 90 s
5. Rinse sample in IPA for 60 s
6. N_2 dry

A.2.5. LIFT-OFF

1. Soak in acetone for at least one hour
2. Using a syringe, force acetone over the surface of the sample while in acetone. At some point the film will begin to tear due to the force of the acetone coming out of the syringe and you should be able to fully lift off the film.
3. Prior to making the tiniest gate features it is okay to use light sonication (maximum 30%) to help remove the films. Once there are nanoscale gates sonication risks damaging the wires.
4. Swap to clean acetone as needed
5. Rinse in IPA, N_2 dry

A.3. OHMIC CONTACTS AND CHARGE ACCUMULATION

To test the ion implantation-activation and the electron accumulation processes, we pattern and implant few cells of our Si/SiGe devices with the geometry reported in the lower right corner of Fig. 4.7(a)). The red lines represent the ion implanted regions, otherwise not visible in the figure because they are below the accumulation gate.

Table A.1: Test of the Ohmic contact (ion implantation) and accumulation of the quantum well. The letters refer to the contact pads as in Fig. 4.7(a).

Contact pads	Resistance	Remark
C–E	3.79 kΩ	—
B–F	5.68 kΩ	—
A–G	6.20 kΩ	—
F–G	5.06 GΩ	D on 0 V
F–G	7.02 kΩ	D on +2 V
E–F	6.38 GΩ	D on 0 V
E–F	6.24 GΩ	D on +2 V

These ion implanted lines will be used to perform three different preliminary measurements in a dipstick at 4 K to test the effectiveness of the ion implantation process (1), of the electron accumulation in the Si QW (2), and of the mesa-etching step (3):

1) To test the result of the ion implantation and successive rapid thermal annealing, resistances of the tree lines were measured in a two-point measurement. We recorded an ohmic behavior with the respective resistance values listed in the top part of Table A.1. The resistance increases linearly with line length according to the relationship

$$R = [0.006L(\mu m) + 2.150]\ k\Omega, \tag{A.1}$$

where 2.15 kΩ is a series resistance contribution that is related to the contact and the electronic instruments resistances.

The outcome of these measurements shows that the P-ions have been successfully implanted into the heterostructure and are properly activated by rapid thermal annealing (RTA). However, this measurement does not give insight of the implantation depth profile, so nothing can be yet concluded about the validity of the final optimized parameters (acceleration voltage, incidence angle, ions dose) and so about the functionality of the ohmic contacts of our QD structure. To properly achieve the latter, in fact, the implanted ions need to be concentrated around the the Si QW depth.

2) The next set of measurements consists in recording the resistance between gates F and G (see Fig. 4.7(a)) keeping the contacts A and B open. As we noticed[1], these two contacts are not directly connected by a low resistance path (there is not a direct P-ohmic connection between the two implanted lines), thus they are separated by an insulating region of the Si QW (at 4K there are not enough free carriers thermally generated inside the QW). The next step consists in the electrostatic accumulation of free electrons inside the Si QW. While keeping a constant voltage bias on gate G, the voltage on the accumulation gate D was gradually increased up to +2 V. For this specific heterostructure, around a voltage of +1.5 V (threshold voltage), the measured current starts to increase and it saturates around a voltage of +2 V (saturation voltage). A similar accumulation measurement is reported in Fig. 4.9(a). In this configuration (keeping the voltage on gate D fixed at +2 V) we estimate a resistance of ~ 7 kΩ between contacts F and G.
This simple measurement clearly shows that the accumulation gate can control the insulator-metal transition in the Si-QW below by modulating the electron density. Furthermore, no noticeable leakage current is measured from the accumulation gates to the P-implanted lines.

3) A final test on this structure consists in measuring the conductance between two implanted regions of the heterostructure separated by an etched grove (mesa etching represented by the black dotted line in Fig. 4.7(a)). Then, keeping a bias voltage on gate F, the accumulation voltage on gate D was increased gradually up to 2 V, while measuring the current through contact E (gates A, B, C and D kept open). No significant conductance increase has been registered during this measurement, indicating that the different regions of the heterostructure are effectively disconnected by etching locally grooves that make the QW accumulation process ineffective. Furthermore, a negligible leakage current has been measured from the top gate, which turns out to be well isolated by the 80 nm Al_2O_3 layer. This also confirms that the conduction between gates F and G observed in test (2) was indeed via electrons accumulated in the Si QW.

[1] by applying a voltage of +200 μV to G while measuring the current from gate F

A.4. ELECTRICAL LEAKAGE THROUGH DIELECTRIC

Compared to other deposition techniques, such as sputtering or electron-beam evaporation, atomic layer deposition produces dielectric films with much higher quality, with thickness control on atomic scale (for the Al_2O_3 we have ~ 0.1 nm for each ALD cycle). ALD Al_2O_3 is estimated to have a breakdown electric field of 10 MV/cm and a leakage current density of $10^{-10} - 10^{-9}$ A/cm^2 at zero bias [2]. To determine the quality of the deposited aluminium oxide, we realize capacitor-like test devices. They consist of a Si dummy wafer with gold gates deposited by evaporation and covered with 10 nm (100 cycles) of ALD Al_2O_3. This thickness would correspond to a breakdown voltage of ~ 10 V. A second set of gates is evaporated on top of the the Al_2O_3 layer, with different overlap areas with the gates buried below. We tested these devices in a room-temperature probe station, by applying voltages in the range $(-4, +4)$ V, which is well above the typical voltage range we use to apply to the fine gates. No measurable leakage current was observed.

A

A.5. UNDER-ETCHING TEST

Even if the wet etch process of the vias through the aluminum oxide has been optimized, an under-etching issue is still clearly visible (see dotted circle in Fig. 4.7(b) in correspondence of the under-etching halo). Therefore, we realize a test structure to ensure that the bigger diameter of the vias, due to the under-etching, would not short neighboring metallic leads once we fill the vias by evaporating metals (during the interconnection step). The test device consists of three gate structures, realized on a Si dummy wafer, reported in Fig. 4.7(b): one gate (labeled B) ends in a square with dimensions identical to those of the vias of the real device; the other gate (labeled A), wraps around the via. The separation between those two gates, around the position of the via, ranges from 6- – 16 μm, lower than the typical separation between gates at the via positions on a real device. Next, the sample was covered with 80 nm Al_2O_3 and the vias have been realized according to the iterative etching process (see the fabrication recipe in Appendix). Finally, a third gate (gate C) was deposited on top of the dielectric, to connect to gate B through the etched via.
The device was measured in a room-temperature probe station to detect possible electrical shorts. By measuring the current between gates B and C we found that they are properly connected (the etching through 80 nm Al_2O_3 works successfully). Furthermore, the test device shows a resistance in the GΩ range between gates A-B and A-C, from which we can conclude that, even if clearly present, the under-etching is sufficiently well localized in a small region around the via, preventing the issue of shorting between gates next to each other in a real device.

A.6. FINE GATES ALIGNMENT

Crucial to the QDs tuning process is the precision in the ebeam alignment for the fine depletion and accumulation gates. These, in fact, are separated by 80-30 nm of Al_2O_3 and have to be aligned relative to each other with high accuracy[2].

[2] For this purpose the marker positions are crucial; the alignment can be improved by making bigger markers closer to the micromesa.

To test our ability of making the fine gates well aligned on top of each other, a silicon dummy sample, covered with a mono-layer of PMMA A2, was exposed with the fine gates pattern, subsequently developed and covered with 5 nm Ti and 25 nm Au to define the fines gates. Everything, including the set of gold markers written in the same step[3] was subsequently covered with 80 nm aluminum oxide. Again, a monolayer of PMMA A2 has been patterned and exposed with the design for the fine accumulation gates. After development of the resist, 5 nm Ti and 30 nm Au were evaporated. Inspection with a SEM (see Fig. 4.8(d)) showed an almost perfect (within ~10 nm) horizontal alignment of the different sets of gates, proving the effectiveness of the markers, even through 80 nm of Al_2O_3. Despite that, on average we observe that 1 device out of 5 presents a non negligible misalignment (> 15 nm).

REFERENCES

[1] F. Walvoort, 'Fabrication and characterization of double quantum dots in an undoped Si-SiGe heterostructure', Master thesis, Delft University of Technology (2014).

[2] H. C. Lin, P. D. Ye and G. D. Wilk, Appl. Phys. Lett. **87**, 182904 (2005).

[3] those markers, buried by a thick dielectric, have to be properly identified by the electron beam in order to finalize the alignment process

ACKNOWLEDGEMENTS

If there is a single sentence to summarize what I learned during these fantastic but also quite challenging years, is the following: 'During a PhD, one has to work hard all of the time, almost never completely relaxing, in order to be always ready to get lucky.' Finding a working device is so rare that, once it is there, cold inside your cryostat, one has to be ready to get as much as possible out of it. What is very special in this amazing group (QT-QuTech) is the amount of possibilities and opportunities available to get lucky.
The concentration of different knowledge, expertise, facilities and especially the friendly and collaborative atmosphere that all the group leaders were able to build up during these years, made this group one of the leading place for mesoscopic physics (before) and quantum technology (nowadays). And I'm really proud to be part of this group, which, with the meaning of the above, I like to define a 'catalyst of luck'.
This special cocktail of diversified skills and interests makes this context so unique. This spirit is completely embodied by you, Lieven. I'm very grateful for this opportunity and especially for what, directly or indirectly, I have learned (or at least I hope to) from you about how to lead a research project and how to judge the following step of an experiment by balancing optimism and realism.

The experiments that I had the opportunity to realize during these years wouldn't have been possible without the very important contribution of many different people.

A special thanks is reserved to Erika who shared with me most of the work reported in this Thesis. I still clearly remember the day you were interviewed by our group. I had already been working on the SiGe project with Lars for 5 months and, after listening to your seminar I realized that you were really the right collaborator that I was wishing to have next to me for this project. Your deep knowledge in the spin physics, your passion and tenacity in interpreting the data, made you the perfect collaborator. I hope that in the near future we will manage to work together again. You are always very welcome to come to visit my place in Italy again whenever you want.
Mohammad and Lars, you have been my first direct supervisors during my Master thesis and beginning of PhD, respectively. I learned a lot from both of you. It was a lot of fun to realize the RF reflectometry technique together with you, Mohammad. Lars, you have been the pioneer, here in Delft, of the Si/Ge project. I am extremely grateful for all the time and patience you put into teaching me how to tune and interpret a device.
Floris, you are the scientist I shared and discussed new crazy scientific ideas with. I thank you in advance for all the times I will bother you now that I will move to Switzerland (kidding).
A special thanks also to Mark E., Sue and Mark F. . The collaboration with all of you has been extremely inspiring and important for all of the results reported in this thesis (and more). And especially thanks for being always so willing to share your knowledge and to

answer all of the questions.
Raymond S., I do not exaggerate when I say that you are the magical technician that every student dreams to meet, at least once in case of necessity. I feel extremely lucky I had the possibility to chat with you on a daily basis.
A very warm thank to Jelle, Remco, Bram, Mark. There is no problem or necessity that does not find a solution in less than half a day with you around, no matter how complex it may seem in the beginning. I will never forget the Guinness world record which consisted in rebuilding the lab in 1 week that we managed to realize thanks to your help Jelle! And Remco, I always knew that being “almost welcome” actually means being very welcome!
Yuki and Maria, thanks for always offering with a big smile your time and invaluable advices for every kind of necessity.
Finally, I want to thank all of my colleagues of the Spin qubit team, Pierre, Tim, Toivo, Nodar, Jelmer, Tom, Ferdy and all the QT group. You have been the solid substrate above which I built these splendid years of research and life in Delft.

CURRICULUM VITÆ

Pasquale SCARLINO

29-07-1986 Born in Gagliano del Capo (LE), Italy.

EDUCATION

2000–2005 Science High School
Liceo Scientidico Giulio Cesare Vanini, Casarano (LE), Italy.

2005–2008 Bachelor in Physics
University of Salento, Italy.

2008–2011 Master in Physics
University of Salento, Italy.

2011-2015 PhD. researcher, Delft University of Technology.
Subject: Spin and Valley Physics in a Si/SiGe Quantum Dot
Group: QuTech and Quantum Transport, Kavli Institute of Nanoscience.
Promotor: Prof. dr. ir. L. M. K. Vandersypen.

LIST OF PUBLICATIONS

8. E. Kawakami, **P. Scarlino**, L. R. Schreiber, J. R. Prance, D. E. Savage, M. G. Lagally, M. A. Eriksson, L. M. K. Vandersypen, *Excitation of a Si/SiGe quantum dot using an on-chip microwave antenna*, Appl. Phys. Lett. **103**, 132410 (2013).

7. E. Kawakami*, **P. Scarlino***, D. R. Ward, F. R. Braakman, D. E. Savage, M. G. Lagally, Mark Friesen, S. N. Coppersmith, M. A. Eriksson, L. M. K. Vandersypen, *Electrical control of a long-lived spin qubit in a Si/SiGe quantum dot*, Nature Nanotechnology **9**, 666–670 (2014).

6. **P. Scarlino**, E. Kawakami, P. Stano, M. Shafiei, C. Reichl, W. Wegscheider, L. M. K. Vandersypen, *Spin relaxation anisotropy in a GaAs quantum dot*, Phys. Rev. Lett. **113**, 256802 (2014).

5. **P. Scarlino**, E. Kawakami, D. R. Ward, D. E. Savage, M. G. Lagally, Mark Friesen, S. N. Coppersmith, M. A. Eriksson, L. M. K. Vandersypen, *Second Harmonic Coherent Driving of a Spin Qubit in a Si/SiGe Quantum Dot*, Phys. Rev. Lett. **115**, 106802 (2015).

4. N. Samkharadze, A. Bruno, **P. Scarlino**, G. Zheng, D. P. DiVincenzo, L. DiCarlo, and L. M. K. Vandersypen, *High Kinetic Inductance Superconducting Nanowire Resonators for Circuit QED in a Magnetic Field*, submitted.

3. **P. Scarlino**, E. Kawakami, D. R. Ward, D. E. Savage, M. G. Lagally, Mark Friesen, S. N. Coppersmith, M. A. Eriksson, L. M. K. Vandersypen, *Adiabatic and nonadiabatic nonlinear driving of a two-level system*, in preparation.

2. E. Kawakami, T. Jullien, **P. Scarlino**, D. R. Ward, D. E. Savage, M. G. Lagally, V. V. Dobrovitski, Mark Friesen, S. N. Coppersmith, M. A. Eriksson, L. M. K. Vandersypen, *Gate fidelity and coherence time of an electron spin in a Si/SiGe quantum dot*, in preparation.

1. R. Ferdous, **P. Scarlino**, E. Kawakami, M. Novak, D. E. Savage, M. G. Lagally, Mark Friesen, S. N. Coppersmith, M. A. Eriksson, L. M. K. Vandersypen, R. Rahman, *Valley dependent g-factor anisotropy in Silicon quantum dots*, in preparation.